UNIVERSITY OF TRENTO - Italy

International PhD program in Biomolecular Sciences

XXIX Cycle

Imaging Chloride Homeostasis in Neurons

Tutor

Mauro Dalla Serra

National Research Council of Italy

Ph.D. Thesis of

Daniele Arosio

National Research Council of Italy

University of Trento

Academic Year 2015–2016

Declaration

I, Daniele Arosio confirm that the work presented in this thesis is my own. Where information has been derived from other sources, I confirm that this has been indicated in the thesis.

Contents

List of Tables

List of Figures

Abstract

Intracellular chloride and pH are fundamental regulators of neuronal excitability and they are often co-modulated during excitation-inhibition activity. The study of their homeostasis requires simultaneous measurements in vivo in multiple neurons. Combining random mutagenesis screening, protein engineering and two-photon-imaging this thesis work led to the discovery of new chloride-sensitive GFP mutants and to the establishment of ratiometric imaging procedures for the quantitative combined imaging of intra-neuronal pH and chloride. These achievements have been demonstrated in vivo in the mouse cortex, in real-time monitoring the dynamic changes of ions concentrations during epileptic-like discharges, and in glioblastoma primary cells, measuring osmotic swelling responses to various drugs treatment.

1

Introduction

This chapter contains work adapted and improved from:

Twenty Years of Fluorescence Imaging of Intracellular Chloride

Arosio Daniele and Gian Michele Ratto; Frontiers in Cellular Neuroscience, 8 (2014)

The importance of chloride imaging stems from the many physiological role played by this anion in all living organisms and by the fact that it constitutes the only functional imaging technique to monitor the inhibitory circuits within the brain.

Chloride ion (Cl^-) homeostasis regulates charge balance in intracellular organelles like endosomes and lysosomes [1–3], drives fluid secretion and adsorption in epithelial cells [4], controls whole cell volumes [5,6]. Thanks to the balanced action of various Cl^- selective channels and Cl^- transporters, Cl^- is distributed in multicellular organism with a small transmembrane ratio of about 10:1 (extracellular-to-intracellular) [7–9]. For comparison, calcium distributes with a larger transmembrane ratio: about 10000:1 [10].

In humans, functional or genetic alterations of cellular factors that regulate the homeostasis of Cl^- then lead to a wide range of diseases; acquired or hereditary as diverse as cystic fibrosis, myotonia congenita, epilepsy, hyperekplexia, lysosomal storage disease, Bartter syndrome, deafness, renal salt loss, kidney stones and osteopetrosis [11–20]. Along with potassium channels, Cl^- selective channels are also emerging among the most active channels during tumor genesis [21–23].

1.1 Chloride regulation in brain cells

In the adult central nervous system, transient inhibitory activity is triggered by the synaptic release of GABA and glycine. The opening of the associated channels establishes a current, which is mainly sustained by the movement of Cl^- along their electrochemical gradient. Therefore, the intracellular concentration of Cl^- ($[Cl^-]_i$) determines the amplitude of the inhibitory currents. The interest in measuring directly $[Cl^-]_i$ increased with the dawning of the notion that GABA and glycine exert an excitatory action early during development due to the gradual

evolution of the reversal potential of Cl^- [24–29]. This discovery suggested a complexity of the mechanisms underlying the regulation of $[Cl^-]_i$ that was previously unsuspected [30]. In these studies, the development of Cl^- homeostasis was inferred by measuring the reversal potential of the $GABA_A$ current, rather than by a direct measurement of the concentration. Reverse potential measurements are still used to generate important insights in the field, but critical drawbacks are recognized to the adoption of this method:

1) measurements of the reversal potential provide an imperfect estimate of intracellular Cl^- because the GABAergic current contains a bicarbonate component (see later);

2) $[Cl^-]_i$ can be affected by the pipette content unless recording is performed in the perforated patch configuration, which is characterized by an inherently larger and more variable access resistance;

3) measurement of the reversal potential for GABAergic current *in vivo* (i.e. live brain) would be extremely challenging and labor-intensive to achieve.

Nevertheless, reverse potential methods allowed neuroscientists to shape our current knowledge on the regulation of Cl^- concentration within neurons: an equilibrium between passive fluxes through membrane conductance, and energy-dependent fluxes mediated by the cotransporters NKCC1 and KCC2 [31]. Passive fluxes follow the Cl^- electrochemical gradient, while the cotransporters are responsible for moving Cl^- away from equilibrium (Fig. 1.1) [32]. Both cotransporters are driven by ionic gradients, with NKCC1 using the sodium gradient to move potassium and Cl^- into the cell and KCC2 using the potassium gradient to move Cl^- out. In the immature brain, NKCC1 is the most abundant molecule determining high $[Cl^-]_i$ levels. During normal brain development, however, NKCC1 expression decreases meanwhile KCC2 expression increases. These concomitant

events decrease the $[Cl^-]_i$ to a level consistent with its inhibitory role in the adult brain [33–36]. An alternative view suggests that the Cl^- level is also affected by electrical charges arranged outside of the cell membrane in the extracellular matrix [37,38].

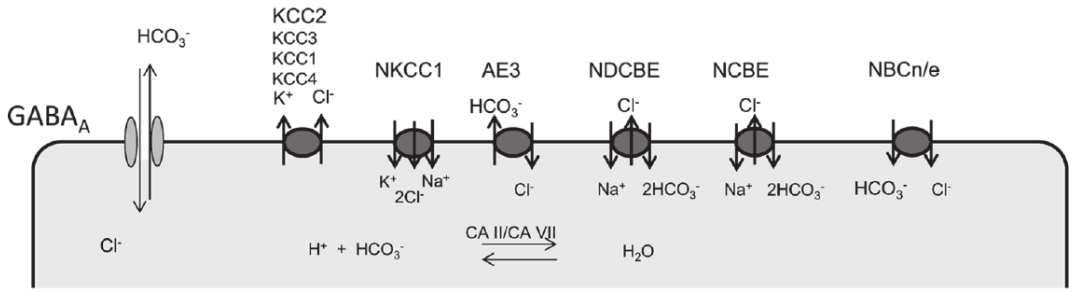

Figure 1.1: **Ion transporters involved in the regulation of neuronal Cl^- and bicarbonate levels.** GABA receptors are permeable for both Cl^- and bicarbonate. Several anion transporters are expressed in neurons and may thus also affect GABA signaling. Whereas NKCC1 is the main Cl^- accumulating transporter in most neurons, KCC2 is the most important Cl^- extruder. Anion-transporters of the SLC4A family of bicarbonate transporters can be sub-classified in Na+ dependent (NDCBE, NCBE) and Na+ independent anion exchangers (AE1,2,3). According to the stoichiometry Na+ coupled bicarbonate co-transports can be either electroneutral (NBCn) or electrogenic (NBCe). Although carbonic anhydrases cannot change the existing bicarbonate gradients, they promote anion transport by members of the SLC4A family and replenish bicarbonate levels. (Hubner 2013)

To date, also the activity of $GABA_A$ currents has been estimated by indirect methods. For example, in the immature cortex, depolarizing $GABA_A$ transmission can be unveiled by the opening of calcium voltage sensitive channels, which can be quantified by calcium imaging [39,40]. Voltage sensitive dyes can also be used to estimate GABAergic currents in slice preparations [41]. The steady state $[Cl^-]_i$ is given by the equilibrium between cotransporters, leakage, and tonic activation of $GABA_A$ conductance. The time modulation of $[Cl^-]_i$ concentration is caused by the incoming transient activation of synaptic $GABA_A$, in cortical neurons, or glycine receptors, in the spinal cord, basal forebrain, and retina. Interestingly, both the $GABA_A$ and the glycine ionotropic receptors are permeable to bicarbonate, which represents about 11 and 20% of the current flowing through the glycine receptor and $GABA_A$ conductance respectively [42,43]. Moreover, the flux of bicarbon-

ate modulates intracellular pH establishing a coupling between Cl^- fluxes and pH change; a fact with important physiological consequences, but also directly affecting imaging, since all genetically encoded Cl^- sensors are sensitive to pH changes.

1.2 Why measure intracellular chloride in brain cells?

Since its onset, fluorescent imaging of ionic concentration had a long love affair with neuroscience and it is easily argued that, in association with patch clamp, it has revolutionized our understanding of brain cell physiology. The key advantage of imaging is to allow the temporally and spatially resolved measurement of ionic concentration in brain cells in cultures, in acute or chronic slices and, by exploiting two photon excitation, also *in vivo*. The spatial resolution of these measures not only allows scientists to study different cells separately, but to image changes occurring in different sub cellular domains as minute as dendritic spines [44,45]. Most imaging studies have been performed with sensors for calcium, because of its essential role in the regulation of intracellular signaling and biochemistry. Furthermore, the dynamics of $[Ca]_i$ are considered as a proxy that reveals the underlying electrical activity of neurons: elevations in calcium are interpreted as evidence of net excitatory input and firing patterns can, at least in principle, be reconstructed from the time course of the somatic calcium changes [46]. Calcium increases are caused by the activation of voltage sensitive calcium channels that open in response to membrane depolarization. In the post-synaptic volume, calcium increases report both the activation of voltage sensitive channels and the incoming excitatory input though NMDA receptors

[47–49]. Thus, the spatially and temporally resolved imaging of calcium changes holds the key to decode the integration of excitatory synaptic inputs on a neuron. Just as calcium fluxes indicate neuronal firing and integration of excitatory inputs, Cl^- fluxes signal the activation of the ionotropic GABA currents, which are the main mediator of synaptic inhibition in the postnatal cortex. Therefore, imaging of Cl^- fluxes could well represent a crucial tool to understand the dynamic arrangement of ionotropic inhibitory inputs on neurons. The interpretation of the measures of intracellular concentration must take into account a fundamental difference between the electrochemical state of equilibrium for calcium and chloride. The reversal potential of calcium is so positive that it is outside the range of potentials experienced by cells, such that the opening of a calcium conductance always results in calcium influx. Furthermore, given the strong buffering of calcium, neuronal firing leads to only relatively modest increases in free calcium concentration under normal physiological conditions, and thus the driving force for calcium is only marginally dependent on activity. The situation is different for Cl^-: because its gradient is rather shallow, the Cl^- reversal potential is not strongly negative and depolarizes further when $[Cl^-]_i$ increases. If $[Cl^-]_i$ exceeds about 20–25 mM, the opening of $GABA_A$ channels depolarizes the membrane potential of a resting neuron toward the threshold potential for the activation of sodium channels. This dual role for GABA is often referred to as “hyperpolarizing” or “depolarizing” GABA [30]. It is clear that the switch between these two drastically different operation modes for $GABA_A$ action, depends critically on the absolute value of $[Cl^-]_i$, providing a paradigmatic example of the importance of directly measuring Cl^- concentration. In early embryonic and postnatal life, GABA acts as the primary excitatory neurotransmitter. This occurs because Cl^- concentration is so high that the opening of $GABA_A$ receptors brings neurons over the action potential threshold. As the glutamatergic transmission matures, $[Cl^-]_i$

decreases, opening of $GABA_A$ channels hyper-polarizes the neuron's membrane potential and thus Cl^- fluxes move into neurons; henceforth $GABA_A$ assumes its inhibitory role. The experimental evidences of this shift are extensive (see [30] for a review) and, although imaging measurements of the developmental shift of $[Cl^-]_i$ were obtained in neuronal cultures [50] and brain slices [37,51,52], a direct and pH independent measurement of Cl^- concentration *in vivo* during development has yet to be produced. Astrocytes are the second great family of cells in the brain. In the last two decades we have learned that they do not simply play a crucial role in the control of the extracellular homeostasis and on the coupling between brain and circulation but they also exert important modulatory effects on synaptic plasticity [53,54]. Although astrocytes do not possess a significant complement of voltage dependent conductances, they are endowed with a membrane that is enriched with a cohort of channels and transporters [55]; a fact that suggests a finely regulated intracellular environment. Indeed, in the last decade calcium imaging has revealed that astrocytes have a highly dynamic internal life, characterized by a complex spatiotemporal activity [56]. Astrocytes and neurons are engaged in a complex bidirectional dialog: synaptic activity modulates the internal state of astrocytes and, in turn, they release gliotransmitters that modulate neuronal function and synaptic transmission [53]. Although astrocytes are not excitable in a classic sense, they interact with the extracellular and extra synaptic environment through a multitude of mechanisms that are in many ways more complex than the ones operating in neurons. Ionic regulation in astrocytes is rather complex as underlined by the effects of neuronal activity on the intracellular concentration of calcium and sodium. Although the field has been little explored, the available biochemical evidences suggest that also Cl^- fluxes in astrocytes are coupled to neuronal activity. Cl^- in astrocytes is regulated by the concerted activity of cotransporters and Cl^- channels. The cotransporters for

GABA and glutamate are central to astrocyte function. Interestingly, the operation of glutamate and GABA transporters are coupled to fluxes of protons and Cl^-, respectively. Thus, we can expect to see changes in intracellular pH and Cl^- also in astrocytes during intense synaptic function and, hopefully, this will open a new window on the understanding of the activity dependent interplay between neurons and glia [57].

1.3 Chemical indicators

The earliest indicators for chloride imaging were synthetic dyes based on quinoline and they come in three variants: 6-methoxy-N-(3-sulfopropyl)quinolinium (SPQ), N-(ethoxycarbonylmethyl)-6-methoxyquinolinium bromide (MQAE)and 6-methoxy-N-ethylquinolinium iodide (MEQ). All these dyes share a similar mechanism of operation: an excited molecule by colliding with a chloride ion, returns to the fundamental state through a non-radioactive path. An increase in Cl^- concentration is thus signaled by a decrease in fluorescence without any change in either the excitation or emission spectra. This molecular process is commonly described as dynamic quenching of the sensor fluorescence. Chemical indicators are usually not ratiometric and thus cannot provide an absolute estimate of Cl^- concentration; in fact, their fluorescence intensity depends not only on Cl^- concentration but also on the dye concentration and optical thickness at each location. In principle it is possible to assemble a ratiometric dye by coupling the Cl^- sensitive molecule with a Cl^- insensitive dye. This type of chemical dyes are not currently available for experimentation, but the synthesis procedure has been successfully developed [58]. On the positive side, these dyes are rather insensitive to bicarbonate concentration and pH variations, moreover, their kinetics for Cl^- association is very fast. For indicators based on fluorescence dynamic

quenching, the Stern–Volmer equation (Eq. 1.1) describes the relationship between fluorescence and Cl^- concentration.

$$F([Cl^-]) = \frac{F_0}{1 + K_{SV}[Cl^-]} \tag{1.1}$$

The parameter F_0 indicates the fluorescence intensity in the absence of Cl^- and the Stern-Volmer constant K_{SV} corresponds to the Cl^- concentration at which $F = F_0/2$. Thus the Stern–Volmer constant defines the optimal working range of the chemical dye and it should be determined in the cells of interest because the variability in the cytosol environment – e.g. temperature, ionic strength and interaction with membrane structures – can affect substantially its value. Quinolinium-based dyes have their excitation peak at about 350 nm and emission at 440–460 nm; this is unfortunate since UV excitation is strongly prone to cause photodamage and it has a very limited penetration in deep tissues. These chemical indicators suffer from further experimental limitations that have curtailed their usefulness: their loading and stable retention are suboptimal especially at temperatures above 30 °C [59], and they are also prone to photobleaching [60,61].

Important results have been obtained with these dyes even if the calibration procedures and controls necessary to overcome their limitations can be rather complex and provide only limited quantitative control on the measurement – see [62] for an interesting analysis of MEQ signals. These early exploratory efforts at imaging the world of Cl^- distribution improved our understanding on both Cl^- regulation and the role of symporters in a variety of brain systems, including cortical neurons [60], rod retinal cells [63] and motoneurons [64]. These studies have also provided insights into pathological conditions that are affected by dysregulation of Cl^- homeostasis, a theme that is now in great development [65–68].

As a testimony of the ingenuity of the experimenters, chemical dyes have also provided an estimate of the changes occurring in the absolute Cl^- concentration during brain development, providing support to the depolarizing GABA model [59,62,69].

Most of these studies have employed conventional wide-field illumination, but chemical dyes can also be used with scanning microscopes. This application has lagged behind, likely because of the cost of the early UV lasers. The introduction of relatively low cost solid state blue and UV lasers might increase the potential usefulness of these dyes. In acute brain slices loaded with MEQ, UV laser-scanning confocal microscope revealed GABA-mediated changes of $[Cl^-]_i$ in single neurons [60]. The authors showed that pressure injection of muscimol, an agonist of the $GABA_A$ receptor, causes rapid Cl^- fluxes; demonstrating how chloride imaging can reveal transient inhibitory activity. More recently, an important step toward chloride imaging *in vivo* came with the demonstration that MQAE can be imaged by two photon excitation [70,71]. Here, the membrane permeable dye MQAE has been successfully loaded in acute brain slices and it was found that two photon excitation causes much less photodamage and photobleaching than UV illumination. This property enables longer recordings and measurements of Cl^- fluxes in dendrites. A quite interesting fact derives from the analysis of the collisional quenching mechanism that is involved in the operation of these dyes: the higher the concentration of Cl^-, the shorter the average time elapsing between collisions. If the concentration is high enough that the mean interval between collisions is shorter than the mean lifetime of fluorescence, the observed lifetime of the dye is shortened with increasing concentration of Cl^- [72]. The consequence of this is that the measurement of the fluorescence lifetime provides an absolute measure of Cl^- concentration that is free from the influence of sensor concentration. This property has been used: to measure the absolute

concentration of Cl^- in the olfactory epithelium and demonstrate the existence of a Cl^- concentration gradient between the sensory dendrites and the cell body [73]; to follow the maturation of Cl^- homeostasis in dorsal root ganglia [74]; and to monitor the effects of inflammatory processes on Cl^- regulation [75].

1.4 Genetically encoded indicators

Genetically encoded indicators are based on the green fluorescent protein (GFP) from the jellyfish *Aequorea victoria*. The potential of GFP as a molecular probe was first recognized when it was expressed heterologously in nematode to track gene expression in the sensory neurons [76]. Remarkably, the chromophore of GFP is formed by an auto catalytic, post-translational cyclization and oxidation of the polypeptide backbone; making the GFP fluorescence genetically encodable. Since then, GFP has been extensively engineered to improve folding and maturation in eukaryotes at 37 °C [77], to enhance fundamental fluorescence properties like brightness and photostability [78], and to expand the available color palette [79]. GFP and GFP homologous, discovered in species other than Aequorea victoria, have become essential probes in cell biology [80] and appreciated in a wide variety of applications [81,82]. While the pH dependence of GFP fluorescence was already known, the opportunity to quantify $[Cl^-]_i$ using GFP-based indicators arose when it was discovered that the fluorescence of the yellow fluorescent protein (YFP) – a GFP containing S65G, V68L, S72A, and T203Y mutations – strongly depends also on the environment concentration of halogens [83].

Probe	Cl^- K_d (mM)	I^- K_d (mM)	Selected reference

Table 1.1: Chloride and iodide affinity values for various probes at pH 7.35.

Probe	Cl^- K_d (mM)	I^- K_d (mM)	Selected reference
MQAE N-(6-methoxyquinolyl)[1]	13		[70]
acetoethyl ester[2][3]	40		[84]
SPQ 6-methoxy-N-(3-sulphopropyl)[4]	118	276	[85]
quinolinium	8.5		
YFP	777		[86]
YFP-H148Q	106	11	[87]
[5]	154.4	23.2	[86]
YFP-H148Q-I152L	85	1.9	[87]
YFP-H148Q-V163S	39	62	[87]
YFP-H148Q-V150A-I152L[6]	61	9	[87]
YFP-H148Q-V163T-F165Y[7]	55	5	[87]

On the one hand, point mutations were introduced into YFP to reduce its sensitivity to pH and anion-concentration changes leading to two well known FP: Citrine [88], which contains the Q69M mutation, and Venus [89], which contains the F46L, F64L, M153T, V163A, and S175G mutations. On the other hand, few pioneering studies recognized in the halogen sensitivity of YFP fluorescence an opportunity for developing novel methods to measure intracellular anion concentration [90,91]. In particular, it was found that the introduction of the H148Q

[1] Stern-Volmer constants
[2] Stern-Volmer constants
[3] Measured in cells
[4] Stern-Volmer constants
[5] Measured at pH=7.5
[6] Measured in bacterial lysate at pH=7.5
[7] Measured in bacterial lysate at pH=7.5

mutation into YFP produced a highly fluorescent protein with higher affinity for halides (Tbl. 1.1). Crystallographic analyses showed that YFP-H148Q contains a specific binding site for halides [86]. YFP-H148Q was successfully used to develop a cell-based high-throughput assay for screening of agonists against cystic fibrosis transmembrane conductance regulator (CFTR)-mediated halide transport [92,93]. In addition, YFP-H148Q was used as a starting template for generating random libraries of mutants that could have the potential for enhanced Cl^- affinity [87]. The analysis of 1536 clones resulted in the discovery that in YFP-H148Q Cl^- affinity can be improved by the introduction of hydrophilic amino acid at position 150 and 163 (Tbl. 1.1). A high-throughput screening based on the YFP-H148Q-I152L mutant was established for the screening of novel antagonists of $GABA_A$, $GABA_C$ and glycine receptors in HEK293 transfected cells (Kruger et al., 2005). The same YFP-H148Q-I152L mutant was also used for identifying inhibitors of a human calcium-activated Cl^- channel [94], engineering a cell-based imaging of sodium-iodide symporter activity [95], and developing a multiplexed high-throughput flow cytometry analysis of the glycine receptor (Gilbert et al., 2009). Among the YFP-H148Q mutants, YFP-H148Q-V163S has been recently tagged at the N- terminus with a palmitoylation sequence and used for monitoring of intracellular Cl^- changes in neuronal processes by live cell imaging of the midbrain [96]. Membrane targeting of this mutant was shown not to alter the high sensitivity for Cl^- and to be advantageous for stabilizing the fluorophore during whole-cell patch-clamp recordings. As with all genetically encoded sensors, GFP-based Cl^- probes show key advantages over chemical probes: (1) they can be targeted conditionally to specific cell types and to specific sub cellular compartments; (2) they are retained within cells allowing chronic repeated measurements *in vivo*; (3) they are generally more photostable than chemical dyes; (4) in contrast to chemical dyes, the thermodynamic and kinetic parameters for Cl^- binding to

GFP-based probes are concentration independent leading to more robust estimates of the calibration parameters. Furthermore, chemical dyes exhibit large variability in the Stern-Volmer constant when different calibration settings are used. For example, K_{SV} values for MQAE can vary from 185 M^{-1} *in vitro* to a range of values between 2 to 40 M^{-1} *in vivo* [73]. This large concentration-dependent variability is probably the result of self-quenching at high dye concentrations (>100 μM) and of dye interactions with other anions e.g., HPO_4^{2-} and HCO_3^- within cells.

1.5 Ratiometric chloride indicators

Cl^- indicators based on a single YFP provide a single optical signal (see sec. **??**) that cannot properly account for variations in local probe concentration, optical path length, light scattering, illumination intensity, and photobleaching. It has been repeatedly proven that these difficulties can be overcome by measuring the ratio between two optical signals that possess different dependency on the physiological parameter under study. Depending on the spectral properties of the sensor, these signals can be obtained by measuring two fluorescence emission bands or by changing the excitation wavelengths. Moreover, ratiometric methods allow accurate and precise measurement even in cells with complicated geometry such as neurons [97]. Indeed, a crucial development in genetically encoded Cl^- biosensors occurred with the development of the first ratiometric YFP-based Cl^- biosensor Clomeleon [50]. Clomeleon consists of two fluorescent proteins, CFP and Topaz, joined by a flexible polypeptide linker of 24 amino acids. Topaz is a YFP mutant, containing the H79R and L68V mutations (see alignment in Fig. 1.5), which is sensitive to Cl^-. Because of the spectral overlap between CFP emission and Topaz absorbance, and the close spatial proximity between

the two fluorophores, fluorescence resonance energy transfer (FRET) occurs. Cl^- binding to Topaz reduces its emission, and leads to a decrease in the degree of FRET or, in more simple words, a change in color from yellow to cyan of the emitted fluorescence. As the CFP fluorescence is free from the influence of Cl^- concentration, exciting the CFP (at 440 nm) and measuring the emission ratio of Topaz relative to CFP (485 ± 15 nm/530 ± 15 nm) provides an absolute measurement of the Cl^- concentration. Clomeleon allowed studies to image synaptic inhibition and $[Cl^-]_i$ in cultured neurons; and it has since been used in a wide range of applications both in slices and in culture. A line of transgenic mice that express Clomeleon under the control of the neuron-specific Thy1 promoter is available [51] and these mice have been used to demonstrate the spatiotemporal dynamics of inhibitory activity in various brain areas, from hippocampus to deep cerebellar nuclei [98]. Expressed in Arabidopsis, Clomeleon allowed chloride imaging in plants [99]. Clomeleon-based imaging was also demonstrated in a wide range of microscopy setup and techniques, including fluorescence lifetime imaging [100,101], 2-photon excitation microscopy [37,51,102,103] and confocal spinning-disk [51].

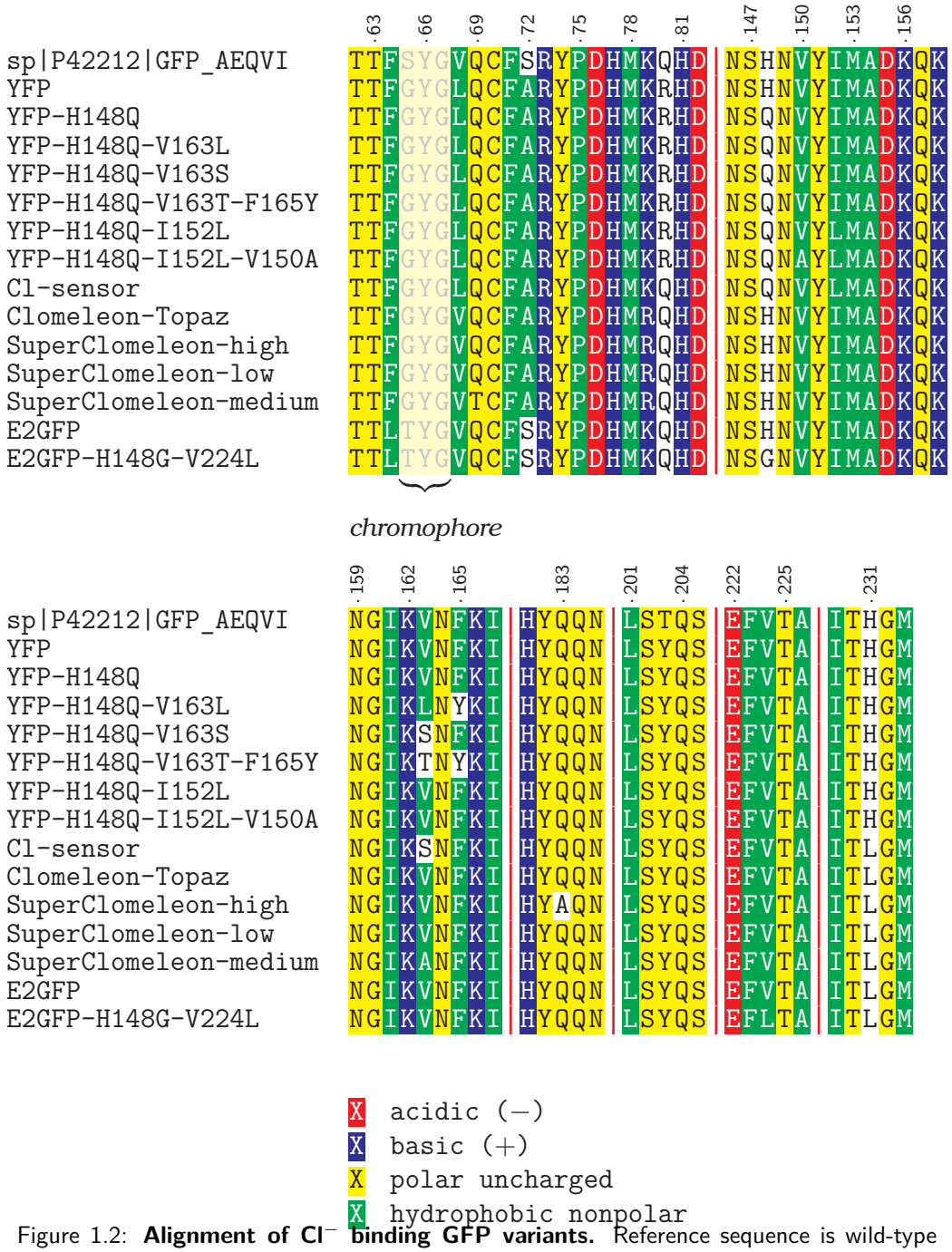

Figure 1.2: **Alignment of Cl^- binding GFP variants.** Reference sequence is wild-type GFP (UniProtKB entry P42212). Color-highlight indicates hydropathy index: discrimination between acidic and basic, polar uncharged and hydrophobic nonpolar residues are highlighted in the legend.

Clomeleon is unfortunately characterized by a few but significant limitations. Its signal displays substantial and complicated pH-dependence, and its Cl^- affinity is far from physiological $[Cl^-]_i$. Cl^- dissociation constant values from 87 to 167 mM were reported [50,51,103] whereas physiological $[Cl^-]_i$ lies within the range

from 3 to 60 mM. The large variability of the reported values for Cl^- K_d could be explained by the steep dependence of the Cl^- K_d on pH. In fact the apparent Cl^- K_d of Clomeleon spans two orders of magnitude in the pH range from 6 to 8 [10]. While it is well known that fluorescence emission intensity is substantially affected by pH variations, it is less recognized that pH variations can alter the degree of FRET reported by numerous FRET-based biosensors. In general, pH changes around physiological values influence both the acceptor and the donor fluorescences altering their excitation and emission spectra as well as their Forster distance, at which the efficiency of FRET is 50%. Assuming that the average donor-acceptor distance is predetermined by the design of the biosensor construct, a pH variation itself can modify the FRET efficiency of any GFP- derived donor-acceptor pair. In Clomeleon, pH changes perturb the FRET-based Cl^- measurement in a manner that is difficult to predict and correct. In particular, pH-dependent changes of (donor) CFP lifetime have been analyzed in a detailed study that successfully exploited Clomeleon in fluorescence lifetime imaging microscopy despite the complex multi-exponential pH-dependent fluorescence decay dynamics of the Clomeleon CFP donor [100] . For all these reasons, the development of ratiometric Cl^- biosensors with higher affinity for Cl^- and reduced pH- dependence was highly sought after. The first improvement on Clomeleon that enhanced the affinity for Cl^- was achieved by Cl-sensor [104], in which the Cl^- sensing fluorescent protein Topaz was substituted by the YFP-H148Q-I152L- V163S mutant. The YFP-H148Q-I152L-V163S mutant combines two mutations that were previously identified for their higher Cl^- affinities relative to YFP-H148Q (Tbl. 1.1). As in Clomeleon, YFP-H148Q-I152L-V163S is joined to CFP by a flexible 20-amino acid linker. Cl-sensor calibration in cells yielded a remarkable value of 30 mM for the Cl^- K_d , a value that matches the physiological $[Cl^-]_i$ optimally. The excitation spectra of Cl-sensor is characterized by

the presence of a Cl-independent isosbestic point at 465 nm, which is a useful feature for the recordings of Cl^- transients using conventional microscopes and rapid switching between excitation wavelengths. Borrowing the same design of Clomeleon, Cl-sensor displays the same subtle pH- dependence of the FRET read-out, which hinders precise and pH-independent Cl^- measurements. Recently, a line of transgenic mice expressing Cl-sensor under the Thy1 promoter has been generated [105]. The optimization of Clomeleon-based biosensors is a process not yet completed. By cell-free protein engineering methods, a random library of Clomeleon variants was recently synthesized and screened for improved Cl^- affinity and dynamic range [106]. This synthetic approach, which bypasses cloning steps, was used to investigate how the performance of Clomeleon is influenced by seven residues encompassing the halogen-binding site as defined by crystallographic analysis. This study found that the best signal-to-noise ratio in cellular imaging is obtained with YFP variants that remain highly fluorescent and exhibit Cl^- affinity that matches the $[Cl^-]_i$ at rest. At the end of their remarkable effort, the authors selected the double mutation Q69T-V163A, which possess a high affinity for Cl^- with a K_d of 21.2 ± 2.2 mM at pH = 7.1. Unfortunately, Q69T-V163A remains highly dependent on pH changes with a pKa value of 6.4 ± 0.1. This new variant was substituted in the original Clomeleon to obtain SuperClomeleon [106], in which three further optimizing modifications were introduced: (1) a brighter donor with the upgrade of CFP to Cerulean, (2) a shorter linker that optimizes the SNR of the biosensor in cultured neurons, and (3) the additional mutation S30R to enhance stability and brightness of both Cerulean donor and YFP-Q69T-V163A acceptor. Overall, SuperClomeleon exhibits a more than fourfold improvement in SNR over the original Clomeleon.

1.6 Chloride binding fluorescent proteins and their pH dependence

Many of the listed Cl^- biosensors e.g., Clomeleon, Cl-Sensor and SuperClomeleon exhibit relatively high sensitivity to pH. Indeed, all available Cl^- biosensors, either ratiometric or non ratiometric, are based on fluorescent proteins derived from the Aequorea victoria GFP. The common element is the T203Y mutation, which is present in all YFP and is required for Cl^- binding in GFP [107,108]. Unavoidably, fluorescence of all these YFP and GFP variants is pH-sensitive with acidification suppressing fluorescence emission and confounding the measurements of Cl^- concentration. At low $[Cl^-]_i$ (below 25 mM) the errors introduced by changes in intracellular pH values should be moderate, likely in the range from 10 to 20%. For instance, by loading the pH indicator BCECF-AM in YFP-H148Q-I152L expressing cells, variations of the fluorescence of YFP of about 15% were quantified for pH changes of 0.2 units around the physiological pH of 7.0 [95]. Nevertheless in the same study, the pH-dependence of the dissociation constant remains the main source of error with reported iodide K_d of 1.4, 2.0 and 2.4 mM at pH values of 6.8, 7.0 and 7.2, respectively. In agreement to Grynkiewicz equation [109], measured ion concentration is directly proportional to K_d ; so an undetected pH change from 7.0 to 6.8 would lead to an overestimation of $[Cl^-]_i$ of about 45%. These arguments suggest that the pH dependency of Cl^- biosensors is especially troublesome when shifts in intracellular pH are expected, e.g., during intense synaptic activity or epileptiform activity [110,111].

Measurement of the intracellular pH is thus needed to quantify the Cl^- affinity of YFP-based probes and ultimately to measure the exact $[Cl^-]_i$ value. This disadvantage of GFP based sensors also offers a great opportunity: if properly

designed, a GFP based Cl^- sensor would allow the simultaneous measurement of intracellular pH and Cl^- concentration. A response to this problem is provided by ClopHensor which was engineered to allow the simultaneous readout of pH and Cl^- [112]. Similar to the members of the Clomeleon family, ClopHensor is also a fusion construct linking two FP, DsRed-monomer and the EGFP-T203Y mutant, by a flexible 20-amino acid linker. EGFP-T203Y, also known as E^2GFP, is a highly accurate ratiometric pH biosensor – with a pKa of about 6.8 at 37 °C – with an isosbestic point in the excitation spectrum at 458 nm [113]. In EGFP, the single mutation T203Y introduces a specific halogen-binding site, which is located in a different position with respect to YFP-H148Q as shown by crystallographic analyses (pdb codes 1f09 and 2o2b). E^2GFP loses its fluorescence upon Cl^- binding because of static quenching. This fact allows accurate pH measurements free from the influence of $[Cl^-]_i$ variations, because the excitation and emission spectra remain unchanged through variations in Cl^- concentration. In the case of E^2GFP, the Cl^- K_d dependence on pH was thoroughly examined [108] revealing cooperative binding of Cl^- and protons that can be mathematically expressed in Eq. 1.2

$$K_d(pH) = K_d^1 \frac{1 + 10^{pK_a - pH}}{10^{pK_a - pH}} \tag{1.2}$$

where K_d^1 is the Cl^- K_d of the proton-ligated form of E^2GFP, and pK_a is the logarithm of the association constant of proton to chloride-free E^2GFP. DsRed-monomer fluorescence is insensitive to variation in either $[Cl^-]_i$ or pH and can be excited and detected in a separate region of the spectral range relative to E^2GFP. The red signal is used to compensate for changes in optical thickness, and provides an accurate reference signal to compute Cl^- concentration. Overall, ClopHensor spectral changes are ideally suited for ratiometric operation at

three excitation wavelengths: 488, 458, and 560 nm. $[Cl^-]_i$ measurements and chloride-independent pH measurements are derived from the ratios 458/560 and 488/458, respectively. In comparison to FRET based sensors, like Clomeleon, ClopHensor prevents the occurrence of subtle variations in the degree of FRET generated by pH-dependent variations of the GFP fluorescence. The cost of this is somewhat reduced time resolution, imposed by the need for sequential acquisition of three excitation wavelengths, and a less simple analysis. Cl^- concentration estimates in a region of interest must follow pH estimates and a corresponding calculation of the Cl^- K_d (according to Eq. 1.2). It has been recently reported that the expression of ClopHensor in hippocampal pyramidal neurons often results in highly heterogeneous DsRed intracellular aggregates. Substitution of tandem-Tomato for DsRed in ClopHensor yielded an improved version for neuronal imaging, ClopHensorN ; although at the cost of a 50% size increase [110,111]. ClopHensorN permitted measurements of activity-dependent ion dynamics in hippocampal neurons.

frontiers in
CELLULAR NEUROSCIENCE

REVIEW ARTICLE
published: 29 August 2014
doi: 10.3389/fncel.2014.00258

Twenty years of fluorescence imaging of intracellular chloride

Daniele Arosio [1,2] **** and Gian Michele Ratto*** [3,4] ******

[1] *Institute of Biophysics, National Research Council and Bruno Kessler Foundation, Trento, Italy*
[2] *Centre for Integrative Biology, University of Trento, Trento, Italy*
[3] *Nanoscience Institute, National Research Council of Italy, Pisa, Italy*
[4] *NEST, Scuola Normale Superiore, Pisa, Italy*

Edited by:
Graziella DiCristo, University of Montreal, Canada

Reviewed by:
Colin J. Akerman, University of Oxford, UK
Marco Canepari, Institut National de la Santé et de la Recherche Médicale, France

****Correspondence:***
Daniele Arosio, Institute of Biophysics, National Research Council and Bruno Kessler Foundation, Via alla Cascata 56, Trento, Italy
e-mail: daniele.arosio@cnr.it;
Gian Michele Ratto, NEST, Scuola Normale Superiore, Piazza San Silvertro 12, Pisa, Italy
e-mail: gianmichele.ratto@sns.it

Chloride homeostasis has a pivotal role in controlling neuronal excitability in the adult brain and during development. The intracellular concentration of chloride is regulated by the dynamic equilibrium between passive fluxes through membrane conductances and the active transport mediated by importers and exporters. In cortical neurons, chloride fluxes are coupled to network activity by the opening of the ionotropic $GABA_A$ receptors that provides a direct link between the activity of interneurons and chloride fluxes. These molecular mechanisms are not evenly distributed and regulated over the neuron surface and this fact can lead to a compartmentalized control of the intracellular concentration of chloride. The inhibitory drive provided by the activity of the $GABA_A$ receptors depends on the direction and strength of the associated currents, which are ultimately dictated by the gradient of chloride, the main charge carrier flowing through the $GABA_A$ channel. Thus, the intracellular distribution of chloride determines the local strength of ionotropic inhibition and influences the interaction between converging excitation and inhibition. The importance of chloride regulation is also underlined by its involvement in several brain pathologies, including epilepsy and disorders of the autistic spectra. The full comprehension of the physiological meaning of GABAergic activity on neurons requires the measurement of the spatiotemporal dynamics of chloride fluxes across the membrane. Nowadays, there are several available tools for the task, and both synthetic and genetically encoded indicators have been successfully used for chloride imaging. Here, we will review the available sensors analyzing their properties and outlining desirable future developments.

Keywords: chloride imaging, inhibitory and excitatory neurotrasmission, Clomeleon, chloride binding site, intracellular chloride

CHLORIDE REGULATION IN BRAIN CELLS

In the adult central nervous system, transient inhibitory activity is expressed by the synaptic release of GABA and glycine and by the activation of the relevant ionotropic receptors. The opening of the associated channels allows the flux of a current mainly carried by chloride ions moving along their electrochemical gradient and therefore, the intracellular concentration of chloride ($[Cl]_i$) determines the amplitude of the inhibitory currents. The interest in measuring directly $[Cl]_i$ increased with the dawning of the notion that GABA and glycine exert an excitatory action early during development due to the gradual evolution of the reversal potential of chloride (Obata et al., 1978; Ben-Ari et al., 1989; Cherubini et al., 1990; Wu et al., 1992; Kandler and Friauf, 1995; Ehrlich et al., 1999). This discovery suggested a complexity of the mechanisms underlying the regulation of $[Cl]_i$ that was previously unsuspected (Ben-Ari, 2002). In all these studies, the development of chloride homeostasis was inferred by measuring the reversal potential of the $GABA_A$ current, rather than by a directly measuring the concentration. This method continues to produce important insights in the field, but it has some drawbacks: (a) measurements of the reversal potential provide an imperfect estimate of intracellular chloride because the GABAergic current contains a bicarbonate component (see later); (b) $[Cl]_i$ can be affected by the pipette content unless recording is performed in the perforated patch configuration which is characterized by an inherently larger and more variable access resistance; (c) measurements of the reversal potential of the GABAergic current *in vivo* would be extremely challenging and labor-intensive.

Regardless, these studies have paved the way to the present understanding of $[Cl]_i$ regulation: an equilibrium between passive fluxes through membrane conductance, and energy-dependent fluxes mediated by the cotransporters NKCC1 and KCC2 (Delpire, 2000). Passive fluxes follow the chloride electrochemical gradient, while the cotransporters are responsible for moving chloride away from equilibrium. Both cotransporters are driven by ionic gradients, with NKCC1 using the sodium gradient to move potassium and chloride into the cell and KCC2 using the potassium gradient to move chloride out. In the immature brain, NKCC1 is the most abundant molecule determining high $[Cl]_i$ levels. During normal brain development, however, NKCC1 expression decreases meanwhile KCC2 expression increases. These concomitant events decrease the $[Cl]_i$ to a level consistent with its inhibitory role in the adult brain (Plotkin et al., 1997; Clayton et al., 1998; Lu et al., 1999;

Rivera et al., 1999) – see also (Glykys et al., 2014) for an alternative view.

The activity of $GABA_A$ currents has been estimated by indirect methods. For example, in the immature cortex, depolarizing $GABA_A$ transmission can be unveiled by the opening of calcium voltage sensitive channels, which can be quantified by calcium imaging (Canepari et al., 2000; Ganguly et al., 2001). Also voltage sensitive dyes can be used to estimate GABAergic currents in slice preparations (Canepari et al., 2010).

The steady state concentration of intracellular chloride is given by the equilibrium between cotransporters, leakage, and tonic activation of $GABA_A$ conductance. The time modulation of chloride concentration is caused by the incoming transient activation of synaptic $GABA_A$, in cortical neurons, or glycine receptors, in the spinal cord, basal forebrain, and retina. Interestingly, both the $GABA_A$ and the glycine ionotropic receptors are permeable to bicarbonate, which represents about 11 and 20% of the current flowing through the glycine receptor and $GABA_A$ conductance respectively (Bormann et al., 1987; Kaila et al., 1993). Moreover, the flux of bicarbonate modulates intracellular pH establishing a coupling between chloride fluxes and pH change; a fact with important physiological consequences, but also directly affecting imaging, since all genetically encoded chloride sensors are sensitive to pH changes.

WHY MEASURE INTRACELLULAR CHLORIDE IN BRAIN CELLS?

Since its onset, fluorescent imaging of ionic concentration had a long love affair with the neurosciences and it is easily argued that, in association with patch clamp, it has revolutionized our understanding of brain cell physiology. The key advantage of imaging is to allow the temporally and spatially resolved measurement of ionic concentration in brain cells in cultures, in acute or chronic slices and, by exploiting two photon excitation, also *in vivo*. The spatial resolution of these measures not only allows scientists to study different cells separately, but to image changes occurring in different sub cellular domains as minute as dendritic spines (Guthrie et al., 1991; Müller and Connor, 1991). Most imaging studies have been performed with sensors for calcium, because of this ion's essential role in the regulation of intracellular signaling and biochemistry. Furthermore, the dynamics of $[Ca]_i$ are considered as a proxy that reveals the underlying electrical activity of neurons: elevations in calcium are interpreted as evidence of net excitatory input and firing patterns can, at least in principle, be reconstructed from the time course of the somatic calcium changes (Smetters et al., 1999). Calcium increases are caused by the activation of voltage sensitive calcium channels that open in response to membrane depolarization. In the post-synaptic volume, calcium increases report both the activation of voltage sensitive channels and the incoming excitatory input though NMDA receptors (Yuste and Denk, 1995; Yuste et al., 1999; Noguchi et al., 2005). Thus, the spatially and temporally resolved imaging of calcium changes holds the key to decode the integration of excitatory synaptic inputs on a neuron. Just as calcium fluxes indicate neuronal firing and integration of excitatory inputs, chloride fluxes signal the activation of the ionotropic GABA currents, which are the main mediator of synaptic inhibition in the postnatal cortex. Therefore, imaging of chloride fluxes could well represent a crucial tool to understand the dynamic arrangement of ionotropic inhibitory inputs on neurons.

The interpretation of the measures of intracellular concentration must take into account a fundamental difference between the electrochemical state of equilibrium for calcium and chloride. The reversal potential of calcium is so positive that it is outside the range of potentials experienced by cells, such that the opening of a calcium conductance always results in calcium influx. Furthermore, given the strong buffering of calcium, neuronal firing leads to only relatively modest increases in free calcium concentration under normal physiological conditions, and thus the driving force for calcium is only marginally dependent on activity. The situation is different for chloride: because its gradient is rather shallow, the chloride reversal potential is not strongly negative and depolarizes further when $[Cl]_i$ increases. If $[Cl]_i$ exceeds about 20–25 mM, the opening of $GABA_A$ channels depolarizes the membrane potential of a resting neuron toward the threshold potential for the activation of sodium channels. This dual role for GABA is often referred to as "hyperpolarizing" or "depolarizing" GABA (Ben-Ari, 2002). It is clear that the switch between these two drastically different operation modes for $GABA_A$ action, depends critically on the absolute value of $[Cl]_i$, providing a paradigmatic example of the importance of directly measuring chloride concentration. In early embryonic and postnatal life, GABA acts as the primary excitatory neurotransmitter. This occurs because chloride concentration is so high that the opening of $GABA_A$ receptors brings neurons over the action potential threshold. As the glutamatergic transmission matures, $[Cl]_i$ decreases, opening of $GABA_A$ channels hyperpolarizes the neuron's membrane potential and chloride fluxes are directed into neurons; henceforth $GABA_A$ assumes its inhibitory role. The experimental evidences of this shift are extensive (see Ben-Ari, 2002 for a review) and, although imaging measurements of the developmental shift of $[Cl]_i$ were obtained in neuronal cultures (Kuner and Augustine, 2000) and brain slices (Berglund et al., 2006; Glykys et al., 2009, 2014), a direct and pH independent measurement of chloride concentration *in vivo* during development has yet to be produced.

Astrocytes are the second great family of cells in the brain. In the last two decades we have learned that they do not simply play a crucial role in the control of the extracellular homeostasis and on the coupling between brain and circulation but they also exert important modulatory effects on synaptic plasticity (Perea et al., 2009; Araque et al., 2014). Although astrocytes do not possess a significant complement of voltage dependent conductances, they are endowed with a membrane that is enriched with a cohort of channels and transporters (Kirischuk et al., 2012); a fact that suggests a finely regulated intracellular environment. Indeed, in the last decade calcium imaging has revealed that astrocytes have a highly dynamic internal life, characterized by a complex spatiotemporal activity (Zorec et al., 2012). Astrocytes and neurons are engaged in a complex bidirectional dialog: synaptic activity modulates the internal state of astrocytes and, in turn, they release gliotransmitters that modulate neuronal function and synaptic transmission (Perea et al., 2009). Although astrocytes are not excitable in a classic sense, they interact with the extracellular and

extrasynaptic environment through a multitude of mechanisms that are in many ways more complex than the ones operating in neurons. Ionic regulation in astrocytes is rather complex as underlined by the effects of neuronal activity on the intracellular concentration of calcium and sodium. Although the field has been little explored, the available biochemical evidences suggest that also chloride fluxes in astrocytes are coupled to neuronal activity. Chloride in astrocytes is regulated by the concerted activity of cotransporters and chloride channels. The cotransporters for GABA and glutamate are central to astrocyte function. Interestingly, the operation of glutamate and GABA transporters are coupled to fluxes of protons and chloride, respectively. Thus, we can expect to see changes in intracellular pH and chloride also in astrocytes during intense synaptic function and, hopefully, this will open a new window on the understanding of the activity dependent interplay between neurons and glia (Egawa et al., 2013).

CHEMICAL INDICATORS

The earliest indicators for chloride imaging were synthetic dyes based on quinoline and they come in three variants: 6-methoxy-*N*-(3-sulfopropyl)quinolinium (SPQ), *N*-(ethoxycarbonylmethyl)-6-methoxyquinolinium bromide (MQAE) and 6-methoxy-*N*-ethylquinolinium iodide (MEQ). All these dyes have a similar mechanism of operation: an excited molecule by colliding with a chloride ion, returns to the fundamental state through a non-radioactive path. An increase in chloride concentration is thus signaled by a decrease in fluorescence without any change in either the excitation or emission spectra. This molecular process is commonly described as dynamic quenching of the sensor fluorescence. Chemical indicators are usually not ratiometric and thus cannot provide an absolute estimate of chloride concentration; in fact, their fluorescence intensity depends not only on chloride concentration but also on the dye concentration and optical thickness at each location. In principle it is possible to assemble a ratiometric dye by coupling the chloride sensitive molecule with a chloride insensitive dye. This has been done by Jayaraman et al. (1999), but to our knowledge, this sensor is not commercially available. On the positive side, these dyes are rather insensitive to bicarbonate concentration and pH variations, moreover, their kinetics for chloride association is very fast. For indicators based on fluorescence dynamic quenching, the Stern–Volmer equation describes the relationship between fluorescence and chloride concentration:

$$F([Cl]) = \frac{F_0}{1 + K_{SV}[Cl]} \quad (1)$$

The constant K_{SV} is the chloride concentration that quenches half of the fluorescence and F_0 is the fluorescence in zero chloride. The Stern–Volmer constant K_{SV} is a key parameter which defines the optimal working range for each dye; it should be determined in the cells of interest since it can depend significantly on the chemical and physical characteristics of the cytosolic environment, e.g., temperature, ionic strength, and interaction with membrane structures. Quinolinium-based dyes have their excitation peak at about 350 nm and emission at 440–460 nm; this is unfortunate since UV excitation is strongly prone to cause photodamage and it has a very limited penetration in deep tissues. These chemical indicators suffer from further experimental limitations that have curtailed their usefulness: their loading and stable retention are suboptimal especially at temperatures above 30°C (Fukuda et al., 1998), and they are also prone to photobleaching (Inglefield and Schwartz-Bloom, 1997; Nakamura et al., 1997).

Notwithstanding these problems, important results have been obtained with these dyes even if the calibration procedures and controls necessary to overcome their limitations can be rather complex and provide only limited quantitative control on the measurement – see (Zhang et al., 2006) for an interesting analysis of MEQ signals. These early exploratory efforts at imaging the world of chloride distribution improved our understanding on both chloride regulation and the role of symporters in a variety of brain systems, including cortical neurons (Inglefield and Schwartz-Bloom, 1997), rod retinal cells (Thoreson et al., 2003) and motorneurons (Chub et al., 2006). These studies have also provided insights into pathological conditions that are affected by dysregulation of chloride homeostasis, a theme that is now in great development (White et al., 1997; Inglefield and Schwartz-Bloom, 1998; Sah and Schwartz-Bloom, 1999; Yamada et al., 2001). As a testimony of the ingenuity of the experimenters, chemical dyes have also provided an estimate of the changes occurring in the absolute chloride concentration during brain development, providing support to the depolarizing GABA model (Fukuda et al., 1998; Isomura et al., 2003; Zhang et al., 2006).

Most of these studies have employed conventional wide-field illumination, but chemical dyes can also be used with scanning microscopes. This application has lagged behind, likely because of the cost of the early UV lasers. The introduction of relatively low cost solid state blue and UV lasers might increase the potential usefulness of these dyes. In acute brain slices loaded with MEQ, UV laser-scanning confocal microscope revealed GABA-mediated changes of $[Cl]_i$ in single neurons (Inglefield and Schwartz-Bloom, 1997). The authors showed that pressure injection of muscimol, an agonist of the $GABA_A$ receptor, causes rapid chloride fluxes; demonstrating how chloride imaging can reveal transient inhibitory activity. More recently, an important step toward chloride imaging *in vivo* came with the demonstration that MQAE can be imaged by two photon excitation (Marandi et al., 2002; Kovalchuk and Garaschuk, 2012). Here, the membrane permeable dye MQAE has been successfully loaded in acute brain slices and it was found that two photon excitation causes much less photodamage and photobleaching than UV illumination. This property enables longer recordings and measurements of chloride fluxes in dendrites. A quite interesting fact derives from the analysis of the collisional quenching mechanism that is involved in the operation of these dyes: the higher the concentration of chloride ions, the shorter the average time elapsing between collisions. If the concentration is high enough that the mean interval between collisions is shorter than the mean lifetime of fluorescence, the observed lifetime of the dye is shortened with increasing concentration of chloride (Kaneko et al., 2002). The consequence of this is that the measurement of the fluorescence lifetime provides an

Table 1 | Chloride and iodide affinity for various probes at pH 7.5 and room temperature.

Probe	Cl^- K_d (mM)	I^- K_d (mM)	Selected reference
MQAE N-(6-methoxyquinolyl)	13* in cuvette		Marandi et al. (2002)
acetoethyl ester	40* in cells		
SPQ 6-methoxy-*N*-(3-sulphopropyl)	118*	276*	Krapf et al. (1988)
quinolinium	8.5		
YFP	777		Wachter et al. (2000)
YFP-H148Q	197	20	Galietta et al. (2001a),
	154.4	23.2	Wachter et al. (2000)
YFP-H148Q-I152L	88	3	Galietta et al. (2001a)
YFP-H148Q-V150A-I152L	61	9	Galietta et al. (2001a)
YFP-H148Q-V163S	62	107	Galietta et al. (2001a)
YFP-H148Q-V163T-F165Y	55	5	Galietta et al. (2001a)
YFP-H148Q-V163L	77	21	Galietta et al. (2001a)

**Values for the Stern–Volmer constant are reported in place of the dissociation constant values.*

absolute measure of chloride concentration that is free from the influence of sensor concentration. This property has been used: to measure the absolute concentration of chloride in the olfactory epithelium and demonstrate the existence of a chloride concentration gradient between the sensory dendrites and the cell body (Kaneko et al., 2004); to follow the maturation of chloride homeostasis in dorsal root ganglia (Gilbert et al., 2007); and to monitor the effects of inflammatory processes on chloride regulation (Funk et al., 2008).

GENETICALLY ENCODED INDICATORS

Genetically encoded indicators are based on the green fluorescent protein (GFP) from the jellyfish *Aequorea victoria*. The potential of GFP as a molecular probe was first recognized when it was expressed heterologously in nematode to track gene expression in the sensory neurons (Chalfie et al., 1994). Remarkably, the chromophore of GFP is formed by an auto catalytic, post-translational cyclization and oxidation of the polypeptide backbone; making the GFP fluorescence genetically encodable. Since then, GFP has been extensively engineered to improve folding and maturation in eukaryotes at 37°C (Cubitt et al., 1995), to enhance fundamental fluorescence properties like brightness and photostability (Heim et al., 1995), and to expand the available color palette (Heim and Tsien, 1996). GFP and GFP homols, discovered in species other than *Aequorea victoria*, have become essential probes in cell biology (Rizzo et al., 2009) and appreciated in a wide variety of applications (Day and Davidson, 2009; Chudakov et al., 2010).

While the pH dependence of GFP fluorescence was already known, the opportunity to quantify $[Cl]_i$ using GFP-based indicators arose when it was discovered that the fluorescence of the yellow fluorescent protein (YFP) – a GFP containing S65G, V68L, S72A, and T203Y mutations – strongly depends also on the environment concentration of halogens (Wachter and Remington, 1999). On the one hand, point mutations were introduced into YFP to reduce its sensitivity to pH and anion-concentration changes leading to two well known FP: Citrine (Griesbeck et al., 2001), which contains the Q69M mutation, and Venus (Nagai et al., 2002), which contains the F46L, F64L, M153T, V163A, and S175G mutations. On the other hand, few pioneering studies recognized in the halogen sensitivity of YFP fluorescence an opportunity for developing novel methods to measure intracellular anion concentration (Jayaraman et al., 2000). In particular, it was found that the introduction of the H148Q mutation into YFP produced a highly fluorescent protein with higher affinity for halides (**Table 1**). Crystallographic analyses showed that YFP-H148Q contains a specific binding site for halides (Wachter et al., 2000). YFP-H148Q was successfully used to develop a cell-based high-throughput assay for screening of agonists against cystic fibrosis transmembrane conductance regulator (CFTR)-mediated halide transport (Galietta et al., 2001b). In addition, YFP-H148Q was used as a starting template for generating random libraries of mutants that could have the potential for enhanced chloride affinity (Galietta et al., 2001a). The analysis of 1536 clones resulted in the discovery that in YFP-H148Q chloride affinity can be improved by the introduction of hydrophilic amino acid at position 150 and 163 (**Table 1**). A high-throughput screening based on the YFP-H148Q-I152L mutant was established for the screening of novel antagonists of $GABA_A$, $GABA_C$ and glycine receptors in HEK293 transfected cells (Kruger et al., 2005). The same YFP-H148Q-I152L mutant was also used for identifying inhibitors of a human calcium-activated chloride channel (De La Fuente et al., 2008), engineering a cell-based imaging of sodium-iodide symporter activity (Rhoden et al., 2007), and developing a multiplexed high-throughput flow cytometry analysis of the glycine receptor (Gilbert et al., 2009). Among the YFP-H148Q mutants, YFP-H148Q-V163S has been recently tagged at the N-terminus with a palmitoylation sequence and used for monitoring of intracellular chloride changes in neuronal processes by live-cell imaging of the midbrain (Watts et al., 2012). Membrane targeting of this mutant was shown not to alter the high sensitivity for chloride and to be advantageous for stabilizing the

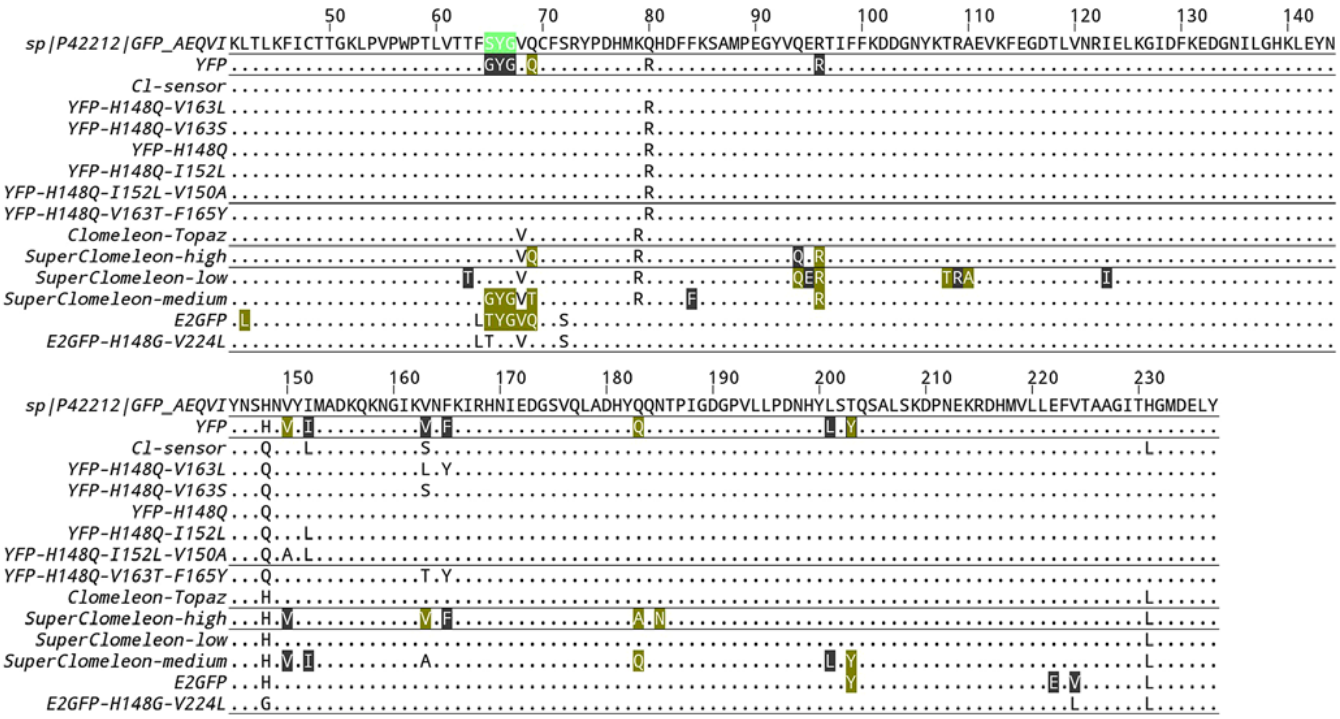

FIGURE 1 | Alignment of chloride binding GFP variants. Only residues that differ from the reference wild-type GFP sequence (UniProtKB entry P42212) are indicated. If the protein data bank contains structural information of a given GFP variant, the residues of the chloride binding site are boxed. Color highlight indicates a residue that forms either van-der-Walls or hydrogen bonds to the chloride ion. Gray highlight indicates a residue that is located within a radius of 5 Å around the chloride ion without forming any specific type of bond.

fluorophore during whole-cell patch-clamp recordings. As with all genetically encoded sensors, GFP-based chloride probes show key advantages over chemical probes: (1) they can be targeted conditionally to specific cell types and to specific sub cellular compartments; (2) they are retained within cells allowing chronic repeated measurements *in vivo;* (3) they are generally more photostable than chemical dyes; (4) in contrast to chemical dyes, the thermodynamic and kinetic parameters for chloride binding to GFP-based probes are concentration independent leading to more robust estimates of the calibration parameters. Dyes like MQAE, in fact, display large changes of the Stern–Volmer constant between calibration *in vitro*, $K_{SV} = 185\ M^{-1}$, and *in vivo*, K_{SV} from 2 to 40 M^{-1} (Kaneko et al., 2004). This large concentration-dependent variability is probably a result of self-quenching at high dye concentrations (>100 μM) and of dye interactions with other anions, e.g., HPO_4^{2-} and HCO_3^-, within cells (Kaneko et al., 2004).

RATIOMETRIC CHLORIDE INDICATORS

Chloride indicators based on a single (Y)FP provide a single optical signal that cannot properly account for variations in local probe concentration, optical path length, light scattering, illumination intensity, and photobleaching. It has been repeatedly proven that these difficulties can be overcome by measuring the ratio between two optical signals that possess different dependency on the physiological parameter under study. Depending on the spectral properties of the sensor, these signals can be obtained by measuring two fluorescence emission bands or by changing the excitation wavelengths. Moreover, ratiometric methods allow accurate and precise measurement even in cells with complicated geometry such as neurons (Bullen and Saggau, 1999).

Indeed, a crucial development in genetically encoded chloride biosensors occurred with the development of the first ratiometric YFP-based chloride biosensor Clomeleon (Kuner and Augustine, 2000). Clomeleon consists of two fluorescent proteins, CFP and Topaz, joined by a flexible polypeptide linker of 24 amino acids. Topaz is a YFP mutant, containing the H79R and L68V mutations (see alignment in **Figure 1**), which is sensitive to chloride ions. Because of the spectral overlap between CFP emission and Topaz absorbance, and the close spatial proximity between the two fluorophores, fluorescence resonance energy transfer (FRET) occurs. Chloride binding to Topaz reduces its emission, and leads to a decrease in the degree of FRET or, in more simple words, a change in color from yellow to cyan of the emitted fluorescence. As the CFP fluorescence is free from the influence of chloride concentration, exciting the CFP (at 440 nm) and measuring the emission ratio of Topaz relative to CFP (485 ± 15 nm/530 ± 15 nm) provides an absolute measurement of the chloride concentration. Clomeleon allowed studies to image synaptic inhibition and $[Cl]_i$ in cultured neurons; and it has since been used in a wide range of applications both in slices and in culture. A line of transgenic mice that express Clomeleon under the control of the neuron-specific thy1 promoter is available (Berglund et al., 2006) and these mice have been

used to demonstrate the spatiotemporal dynamics of inhibitory activity in various brain areas, from hippocampus to deep cerebellar nuclei (Berglund et al., 2008). Expressed in *Arabidopsis*, Clomeleon allowed chloride imaging in plants (Lorenzen et al., 2004). Clomeleon-based imaging was also demonstrated in a wide range of microscopy setup and techniques, including fluorescence lifetime imaging (Jose et al., 2007), 2-photon excitation microscopy (Berglund et al., 2006; Duebel et al., 2006; Dzhala et al., 2012; Glykys et al., 2014) and confocal spinning-disk (Berglund et al., 2006).

Clomeleon is unfortunately characterized by a few but significant limitations. Its signal displays substantial and complicated pH-dependence, and its chloride affinity is far from physiological $[Cl]_i$. Chloride dissociation constant values from 87 to 167 mM were reported (Kuner and Augustine, 2000; Berglund et al., 2006; Dzhala et al., 2012) whereas physiological $[Cl]_i$ lies within the range from 3 to 60 mM. The large variability of the reported values for chloride K_d could be explained by the steep dependence of the chloride K_d on pH. In fact the apparent chloride K_d of Clomeleon spans two orders of magnitude in the pH range from 6 to 8 (Bregestovski and Arosio, 2011). While it is well known that fluorescence emission intensity is substantially affected by pH variations, it is less recognized that pH variations can alter the degree of FRET reported by numerous FRET-based biosensors. In general, pH changes around physiological values influence both the acceptor and the donor fluorescences altering their excitation and emission spectra as well as their Forster distance, at which the efficiency of FRET is 50%. Assuming that the average donor-acceptor distance is predetermined by the design of the biosensor construct, a pH variation itself can modify the FRET efficiency of any GFP-derived donor-acceptor pair. In Clomeleon, pH changes perturb the FRET-based chloride measurement in a manner that is difficult to predict and correct. In particular, pH-dependent changes of (donor) CFP lifetime have been analyzed in a detailed study that successfully exploited Clomeleon in fluorescence lifetime imaging microscopy despite the complex multiexponential pH-dependent fluorescence decay dynamics of the Clomeleon CFP donor (Jose et al., 2007).

For all these reasons, the development of ratiometric chloride biosensors with higher affinity for chloride and reduced pH-dependence was highly sought after. The first improvement on Clomeleon that enhanced the affinity for chloride was achieved by Cl-sensor (Markova et al., 2008), in which the chloride sensing fluorescent protein Topaz was substituted by the YFP-H148Q-I152L-V163S mutant. The YFP-H148Q-I152L-V163S mutant combines two mutations that were previously identified for their higher chloride affinities relative to YFP-H148Q (**Table 1**). As in Clomeleon, YFP-H148Q-I152L-V163S is joined to CFP by a flexible 20-amino acid linker. Cl-sensor calibration in cells yielded a remarkable value of 30 mM for the chloride K_d, a value that matches the physiological $[Cl]_i$ optimally. The excitation spectra of Cl-sensor is characterized by the presence of a Cl-independent isosbestic point at 465 nm, which is a useful feature for the recordings of chloride transients using conventional microscopes and rapid switching between excitation wavelengths. Borrowing the same design of Clomeleon, Cl-sensor displays the same subtle pH-dependence of the FRET readout, which hinders precise and pH-independent chloride measurements. Recently, a line of transgenic mice expressing Cl-sensor under the Thy1 promoter has been generated (Batti et al., 2013).

The optimization of Clomeleon-based biosensors is a process not yet completed. By cell-free protein engineering methods, a random library of Clomeleon variants was recently synthesized and screened for improved chloride affinity and dynamic range (Grimley et al., 2013). This synthetic approach, which bypasses cloning steps, was used to investigate how the performance of Clomeleon is influenced by seven residues in the crystallographically defined halogen-binding site. This study found that the best signal-to-noise ratio in cellular imaging is obtained with YFP variants that remain highly fluorescent and exhibit chloride affinity that matches the $[Cl]_i$ at rest. At the end of their remarkable effort, the authors selected the double mutation Q69T-V163A, which possess a high affinity for chloride with a K_d of 21.2 ± 2.2 mM at pH = 7.1. Unfortunately, Q69T-V163A remains highly dependent on pH changes with a pK_a value of 6.4 ± 0.1. This new variant was substituted in the original Clomeleon to obtain SuperClomeleon (Grimley et al., 2013), in which three further optimizing modifications were introduced: (1) a brighter donor with the upgrade of CFP to Cerulean, (2) a shorter linker that optimizes the SNR of the biosensor in cultured neurons, and (3) the additional mutation S30R to enhance stability and brightness of both Cerulean donor and YFP-Q69T-V163A acceptor. Overall, SuperClomeleon exhibits a more than fourfold improvement in SNR over the original Clomeleon.

CHLORIDE BINDING FLUORESCENT PROTEINS AND THEIR pH DEPENDENCE

Many of the listed chloride biosensors e.g., Clomeleon, Cl-Sensor and SuperClomeleon exhibit relatively high sensitivity to pH. Indeed, all available chloride biosensors, either ratiometric or non-ratiometric, are based on fluorescent proteins derived from the *Aequorea victoria* GFP. The common element is the T203Y mutation, which is present in all YFP and is required for chloride binding in GFP (Arosio et al., 2007). Unavoidably, fluorescence of all these YFP and GFP variants is pH-sensitive with acidification suppressing fluorescence emission and confounding the measurements of chloride concentration.

At low $[Cl]_i$ (below 25 mM) the errors introduced by changes in intracellular pH values should be moderate, likely in the range from 10 to 20%. For instance, by loading the pH indicator BCECF-AM in YFP-H148Q-I152L expressing cells, variations of the fluorescence of YFP of about 15% were quantified for pH changes of 0.2 units around the physiological pH of 7.0 (Rhoden et al., 2007). Nevertheless in the same study, the pH-dependence of the dissociation constant remains the main source of error with reported iodide K_d of 1.4, 2.0 and 2.4 mM at pH values of 6.8, 7.0 and 7.2, respectively. In agreement to Grynkiewicz equation (Grynkiewicz et al., 1985), measured ion concentration is directly proportional to K_d; so an undetected pH change from 7.0 to 6.8 would lead to an overestimation of $[Cl]_i$ of about 45%. These arguments suggest that the pH dependency of chloride biosensors is especially troublesome when shifts in intracellular pH are expected, e.g., during intense synaptic activity or epileptiform activity (Raimondo et al., 2012).

Measurement of the intracellular pH is thus needed to quantify the chloride affinity of YFP-based probes and ultimately to measure the exact $[Cl]_i$ value. This disadvantage of GFP based sensors also offers a great opportunity: if properly designed, a GFP based chloride sensor would allow the simultaneous measurement of intracellular pH and chloride concentration. A response to this problem is provided by ClopHensor which was engineered to allow the simultaneous readout of pH and chloride (Arosio et al., 2010). Similar to the members of the Clomeleon family, ClopHensor is also a fusion construct linking two FP, DsRed-monomer and the EGFP-T203Y mutant, by a flexible 20-amino acid linker. EGFP-T203Y, also known as E^2GFP, is a highly accurate ratiometric pH biosensor – with a pK_a of about 6.8 at 37°C – with an isosbestic point in the excitation spectrum at 458 nm (Bizzarri et al., 2006). In EGFP, the single mutation T203Y introduces a specific halogen-binding site, which is located in a different position with respect to YFP-H148Q as shown by crystallographic analyses (pdb codes 1f09 and 2o2b). E^2GFP loses its fluorescence upon chloride binding because of static quenching. This fact allows accurate pH measurements free from the influence of $[Cl]_i$ variations, because the excitation and emission spectra remain unchanged through variations in chloride concentration. In the case of E^2GFP, the chloride K_d dependence on pH was thoroughly examined (Arosio et al., 2007) revealing cooperative binding of chloride and protons that can be mathematically expressed as follows:

$$K_d = K_d^1 \frac{1 + 10^{pK_a - pH}}{10^{pK_a - pH}} \quad (2)$$

where $K_d{}^1$ is the chloride K_d the proton-ligated form of E^2GFP, and pK_a is the logarithm of the association constant of proton to chloride-free E^2GFP. DsRed-monomer fluorescence is insensitive to variation in either $[Cl]_i$ or pH and can be excited and detected in a separate region of the spectral range relative to E^2GFP. The red signal is used to compensate for changes in optical thickness, and provides an accurate reference signal to compute chloride concentration. Overall, ClopHensor spectral changes are ideally suited for ratiometric operation at three excitation wavelengths: 488, 458, and 560 nm. $[Cl]_i$ measurements and chloride-independent pH measurements are derived from the ratios 458/560 and 488/458, respectively. In comparison to FRET based sensors, like Clomeleon, ClopHensor prevents the occurrence of subtle variations in the degree of FRET generated by pH-dependent variations of the GFP fluorescence. The cost of this is somewhat reduced time resolution, imposed by the need for sequential acquisition of three excitation wavelengths, and a less simple analysis. Chloride estimates in a region of interest must follow pH estimates and a corresponding calculation of the chloride K_d (according to Eq. 2).

It has been recently reported that the expression of ClopHensor in hippocampal pyramidal neurons often results in highly heterogeneous DsRed intracellular aggregates. Substitution of tandem-Tomato for DsRed in ClopHensor yielded an improved version for neuronal imaging, **ClopHensorN**; although at the cost of a 50% size-increase (Raimondo et al., 2013). ClopHensorN permitted measurements of activity-dependent ion dynamics in hippocampal neurons.

CALIBRATION

The sensor calibration is one of the most critical aspects for measuring absolute changes in $[Cl]_i$. The precision and accuracy of measurements of $[Cl]_i$ are determined by the parameters set during calibration. Calibration parameters can be divided into two groups, either those that are dependent on the optical setup or those that are dependent on the indicator chloride binding thermodynamic. Setup-dependent parameters account for different optical filters, detector gains, excitation intensity and general optical efficiency of the imaging setup. The experimenter should also be aware that the illuminated field is never uniform and generally dependent on excitation wavelength with both wide-field and laser-scanning microscopes. Indicator-dependent parameters should be absolute intrinsic properties of the molecular indicator accounting for the thermodynamics of chloride binding, namely chloride K_d and its dependence on pH. In cell culture, intracellular – *in situ* – calibration of chloride indicators is generally performed using the ionophores nigericin and trybutyltin in buffer containing high concentration of potassium (from 100 to 150 mM) and a titrated concentration of chloride (Krapf et al., 1988). The addition of some other ionophores has been reported; e.g., monensin and ionomycin for clamping intracellular milieu at fixed values of sodium concentration (Harootunian et al., 1989) and the protonophore CCCP for controlling pH (Kneen et al., 1998). Alternative methods for *in situ* calibration in cell cultures were proposed by permeabilizing the cell membrane with digitonin (Kneen et al., 1998) or natural surfactants like the triterpenoid saponin, β-escin (Black et al., 2004; Nausch et al., 2008; Waseem et al., 2010). Although calibration procedures using β-escin and the ionophores nigericin and trybutyltin have been reported to yield encouragingly equivalent results (Watts et al., 2012), it is likely that the many variables potentially affecting *in situ* calibration will produce less precise estimates of the intrinsic molecular parameters when compared to spectroscopy measurements performed in a cuvette. GFP-based biosensors can be abundantly purified as recombinant proteins and the biosensor intrinsic parameters can be measured with high accuracy in a spectrofluorometer, under the same temperature, pH and concentration conditions of the final microscopy specimen. The same experiment with the purified biosensor can also be replicated using the microscope to confirm both setup-dependent and intrinsic biosensor parameters. For instance, ClopHensor is intrinsically characterized by two molecular parameters, the pK_a and the chloride K_d^1 of the fully protonated form (see Eq. 2). In the original work these two parameters were determined, using the recombinant construct in cuvette, to be $pK_a = 6.81 \pm 0.05$ and $K_d^1 = 13.1 \pm 0.5$ mM, and validated by *in situ* calibration on cell lines with reported pK_a ranging from 6.78 to 6.84 and a chloride K_d^1 estimate of 14.4 ± 2.0 mM (Arosio et al., 2010). The good agreement between the calibration *in situ* and in cuvette suggests small effects of ionic strength and molecular crowding on the intrinsic parameters of ClopHensor. Yet, significantly different calibration parameters were reported for *in situ* calibrations of ClopHensor (**Table 2**), a difference that may lie in the calibration procedures.

Table 2 | Properties of ratiometric indicators.

Biosensor name and main reference	Chloride K_d (mM)	Ratiometric	Excitation (nm)	Emission (nm)	pKa
Clomeleon (Kuner and Augustine, 2000)	167 *in vitro* 137 *in vitro* Berglund et al. (2006) 87 in cultured hippocampal neurons	Emission	440	485 (15)/530 (15)	5.2
Cl-sensor (Markova et al., 2008)	28 ± 5 48.9 in cultured spinal neurons Waseem et al. (2010)	Excitation	440/480	535 (30)	7.1 at 4 mM KCl
SuperClomeleon (Grimley et al., 2013)	8.1 ± 0.5 21.2 ± 2.2 *in vitro*	Emission	440	485 (15)/530 (15)	6.4 ± 0.1
ClopHensor (Arosio et al., 2010)	49 ± 5*	Excitation	488/458 458/561	525 (25) 640 (60)	6.78 ± 0.04 in HEK 293 cells
ClopHensor-H148G (Mukhtarov et al., 2013)	21.4 ± 4.8 in CHO cells		488/458 458/545	535 (15) 632 (30)	7.3 in CHO cells
ClopHensorN (Raimondo et al., 2013)	39 ± 27	Excitation	488/458 458/594	525 (25) 675 (25)	7.45 ± 0.16 in hippocampal slices

**Propagating the error for the reported estimates of $k_d = 6.81 \pm 0.05$; $pK_a = 13.1 \pm 0.5$.*

FUTURE PERSPECTIVES AND OPEN ISSUES

We are entering the golden age of chloride imaging. New tools are being developed at an increasing rate and the technological efforts are encouraged by the understanding that the role of chloride homeostasis on the physiopathology of the brain is wider than expected. In this context, it is likely that the field will develop greatly and there are several issues that we can envision will be addressed. As our knowledge on the molecular determinants of chloride binding in GFP accumulates, we will be able to engineer ever improved biosensor variants that will optimally match $[Cl]_i$. Many YFP variants were developed during the last decade (**Table 1**), while very few chloride binding GFP variants were reported (Arosio et al., 2010; Mukhtarov et al., 2013). We expect that new E^2GFP variants will be developed, and it is likely that a chloride binding site will be inserted into other fluorescent proteins with different colors. The currently available ratiometric chloride biosensors are either based of the FRET between CFP and YFP variants or on the fluorescence emission ratio between GFP and RFP variants. New ratiometric design could be engineered to exploit alternative fluorescent proteins.

The substitution of the red fluorescence moiety in ClopHensor was demonstrated to improve substantially the ClopHensor potential in neuronal imaging and we envision substitution of the RFP with brighter and more photostable proteins in the future. The ideal RFP should be: a stable monomer not inclined to aggregate; pH independent with low pK_a; and with high brightness, possibly even using 2-photon excitation. TagRFP-T (**Table 3**) appears to offer the potential for greater photostability (but not brightness) compared to existing ClopHensor-based indicators. Finally, another factor that can be considered in ratiometric biosensors based on the fusion between two FP is the photobleaching rate. If two FP are bleached at the same rate, their ratio would be unaffected.

$GABA_A$ activity leads to bicarbonate flux that, in principle, brings about a pH change inside the cell. As we have seen this tight connection between chloride and pH is also mirrored by the dual sensitivity of the fluorescent sensors. Presently, most of the available sensors do not allow the correction of chloride measurement for pH. The exception is ClopHensor, which allows the combined measurement of both ion species. In particular, it was recently demonstrated that ClopHensorN can be used to measure pH and chloride simultaneously in neurons (Raimondo et al., 2013). If one were interested only in chloride concentration, it might be a better choice to employ a sensor with pH independent fluorescence and pH independent chloride affinity. This would simplify the measurement and calibration processes, and ultimately should lead to a more accurate estimate of the absolute chloride concentration.

IN VIVO IMAGING OF CHLORIDE CONCENTRATION IN ANESTHETIZED AND BEHAVING MICE

As occurred in the field of calcium imaging, the development of tools to measure chloride *in vivo*, where neural circuitry are fully preserved, will represent a dramatic improvement in our understanding of chloride regulation and of the mechanisms of $GABA_A$ mediated inhibitory activity. This is especially relevant since many factors relative to slice preparation and maintenance might have profound effects on chloride regulation (Dzhala et al., 2012; Puskarjov et al., 2012). The availability of genetically encoded sensors will make it possible to target imaging to specific cell classes, and to perform longitudinal recordings on anesthetized and behaving mice. This is an especially relevant issue considering the potential effects that anesthesia might have on chloride concentration. Indeed, it is surprising that even when Clomeleon mice have been available for several years, there are no reports on chloride imaging *in vivo* yet. We can expect that the accurate measurement of chloride concentration *in vivo* would encounter

Table 3 | Alternative red fluorescent proteins and their thermodynamic and photo-physical properties.

FP	*pKa*	Excitation and emission (nm)	Relative brightness (%)	Relative photostability (%)	Selected reference
DsRed-monomer	4.5	556/586	10.3	9.2	Shaner et al. (2005)
mCherry	<4.5	587/610	47.0	55.2	Shaner et al. (2005)
tdTomato	4.7	554/581	279.4	56.3	Shaner et al. (2005)
mStrawberry	<4.5	574/596	76.5	8.6	Shaner et al. (2005)
mPlum	<4.5	590/649	12.1	30.5	Shaner et al. (2005)
TagRFP	3.1	555/584	142	21.3	Merzlyak et al. (2007), Day and Davidson (2009)
TagRFP-T	4.6		99	193.7	Shaner et al. (2008)
mKate2	5.4	588/633	74		Chudakov et al. (2010)
LSS-mKate2	2.7	453/605			Piatkevich et al. (2010)

Photo-stability and brightness are reported as relative values with respect to EGFP.

some difficulties due to the sample thickness: to compute the chloride concentration with the available sensors it is necessary to measure the fluorescence emitted and/or excited at different wavelengths and to compare these results with calibration data obtained *in vitro*. Brain tissue is not transparent and both excitation and emission are attenuated in a wavelength dependent way. For example, at a depth of 150 μm, the photon flux is attenuated by a factor of 1.42 when the excitation is shifted from 950 nm to 800 nm, and the corresponding variation in fluorescence emitted greater than a factor of 2 (Brondi et al., 2012). Wavelength-dependent attenuation of excitation and emitted fluorescence does not affect our capacity of detecting relative changes of chloride *in vivo*, but it drastically affects the numerical accuracy of the estimate of absolute concentration. In spite of these problems, the importance for *in vivo* imaging of chloride homeostasis in the intact brain is obvious. Most measures of chloride dynamics have been performed during periods of abnormally large inhibitory activity, such as in the presence of epileptiform activity. *In vivo* imaging might reveal more subtle chloride fluxes that are activated in dendrites or in the soma by physiological activity. Up to now, an accurate mapping of intracellular chloride in cortical neurons has yet to be produced and it will be of obvious interest to image chloride compartmentalization within the dendritic tree and the cell body. Compartmentalization might arise by localized changes in homeostasis (Szabadics et al., 2006; Khirug et al., 2008), possibly linked to phosphorylation of KCC2 (Fiumelli et al., 2005; Kahle et al., 2013) and this might drastically affect the efficacy of inhibitory inputs placed in different neuronal compartments. Finally, sensory cortices offer the opportunity to study incoming GABAergic activity in response to physiological stimuli in regions where the functional architecture is well known.

Chloride imaging is playing a growing role in the understanding of brain diseases. Epilepsy is the most obvious pathology that involves an alteration in GABAergic transmission and, in fact, several studies have begun to dissect chloride regulation during seizures (Dzhala et al., 2005, 2010; Glykys et al., 2009; Lillis et al., 2012; Kaila et al., 2014). All these studies have been performed in slices, and hopefully, the next wave of studies will be performed on preparations that allow a better preservation of circuitry, perhaps by utilizing *in vivo* imaging of the hippocampus (see, for example, Mizrahi et al., 2004; Navarrete et al., 2012). While epilepsy and chloride homeostasis is certainly a very important field, it is becoming clear that the involvement of chloride regulation in brain physiopathology is far more extensive. The spectra of brain pathologies associated with defective inhibition is very wide including both acute situations such as ischemia or traumatic injury (Pond et al., 2006; Dzhala et al., 2012) and conditions such as fragile X and autism, (He et al., 2014; Tyzio et al., 2014) reviewed in (Pizzarelli and Cherubini, 2011; Deidda et al., 2014). It can be argued that dysregulation of chloride homeostasis might play an important part in any pathology associated to a defective equilibrium between excitation and inhibition. The availability of diuretics that alter the activity of chloride cotransporters and have a long clinical track record makes the modulation of chloride homeostasis an attractive target for pharmacological intervention (Löscher et al., 2013; Deidda et al., 2014; Puskarjov et al., 2014). Since the genetically encoded biosensors can be efficiently transfected during late fetal life (dal Maschio et al., 2012), it will also be feasible to screen different murine models of brain pathologies for alterations in the development of chloride regulation. In summary, *in vivo* imaging will likely offer a powerful pre-translational tool for the direct testing of drugs acting on chloride homeostasis in different models of brain diseases. A luminous future for chloride imaging is about to begin.

ACKNOWLEDGMENT

The financial support of Telethon – Italy (Grant no. GGP10138D and GGP12265) is gratefully acknowledged.

REFERENCES

Araque, A., Carmignoto, G., Haydon, P. G., Oliet, S. H. R., Robitaille, R., and Volterra, A. (2014). Gliotransmitters travel in time and space. *Neuron* 81, 728–739. doi: 10.1016/j.neuron.2014.02.007

Arosio, D., Garau, G., Ricci, F., Marchetti, L., Bizzarri, R., Nifosì, R., et al. (2007). Spectroscopic and structural study of proton and halide ion cooperative binding to GFP. *Biophys. J.* 93, 232–244. doi: 10.1529/biophysj.106.102319

Arosio, D., Ricci, F., Marchetti, L., Gualdani, R., Albertazzi, L., and Beltram, F. (2010). Simultaneous intracellular chloride and pH measurements using a GFP-based sensor. *Nat. Methods* 7, 516–518. doi: 10.1038/nmeth.1471

Batti, L., Mukhtarov, M., Audero, E., Ivanov, A., Paolicelli, R. C., Zuborg, S., et al. (2013). Transgenic mouse lines for non-invasive ratiometric monitoring of intracellular chloride. *Front. Mol. Neurosci.* 6:11. doi: 10.3389/fnmol.2013.00011

Ben-Ari, Y. (2002). Excitatory actions of gaba during development: the nature of the nurture. *Nat. Rev. Neurosci.* 3, 728–739. doi: 10.1038/nrn920

Ben-Ari, Y., Cherubini, E., Corradetti, R., and Gaiarsa, J. L. (1989). Giant synaptic potentials in immature rat CA3 hippocampal neurones. *J. Physiol.* 416, 303–325.

Berglund, K., Schleich, W., Krieger, P., Loo, L. S., Wang, D., Cant, N. B., et al. (2006). Imaging synaptic inhibition in transgenic mice expressing the chloride indicator, Clomeleon. *Brain Cell Biol.* 35, 207–228. doi: 10.1007/s11068-008-9019-6

Berglund, K., Schleich, W., Wang, H., Feng, G., Hall, W. C., Kuner, T., et al. (2008). Imaging synaptic inhibition throughout the brain via genetically targeted Clomeleon. *Brain Cell Biol.* 36, 101–118. doi: 10.1007/s11068-008-9031-x

Bizzarri, R., Arcangeli, C., Arosio, D., Ricci, F., Faraci, P., Cardarelli, F., et al. (2006). Development of a novel GFP-based ratiometric excitation and emission pH indicator for intracellular studies. *Biophys. J.* 90, 3300–3314. doi: 10.1529/biophysj.105.074708

Black, D. J., Tran, Q. K., and Persechini, A. (2004). Monitoring the total available calmodulin concentration in intact cells over the physiological range in free Ca^{2+}. *Cell Calcium* 35, 415–425. doi: 10.1016/j.ceca.2003.10.005

Bormann, J., Hamill, O. P., and Sakmann, B. (1987). Mechanism of anion permeation through channels gated by glycine and gamma-aminobutyric acid in mouse cultured spinal neurones. *J. Physiol.* 385, 243–286.

Bregestovski, P., and Arosio, D. (2011). "Green fluorescent protein-based chloride ion sensors for in vivo imaging," in *Fluorescent Proteins II,* ed. G. Jung (Berlin, Heidelberg: Springer Berlin Heidelberg), 99–124.

Brondi, M., Sato, S. S., Rossi, L. F., Ferrara, S., and Ratto, G. M. (2012). Finding a needle in a haystack: identification of EGFP tagged neurons during calcium imaging by means of two-photon spectral separation. *Front. Mol. Neurosci.* 5:96. doi: 10.3389/fnmol.2012.00096

Bullen, A., and Saggau, P. (1999). "Optical recording from individual neurons in culture," in *Modern Techniques in Neuroscience Research,* eds U. Windhorst and H. Johansson (Berlin: Springer), 89–126.

Canepari, M., Mammano, F., Kachalsky, S. G., Rahamimoff, R., and Cherubini, E. (2000). GABA- and glutamate-mediated network activity in the hippocampus of neonatal and juvenile rats revealed by fast calcium imaging. *Cell Calcium* 27, 25–33. doi: 10.1054/ceca.1999.0086

Canepari, M., Willadt, S., Zecevic, D., and Vogt, K. E. (2010). Imaging inhibitory synaptic potentials using voltage sensitive dyes. *Biophys. J.* 98, 2032–2040. doi: 10.1016/j.bpj.2010.01.024

Chalfie, M., Tu, Y., Euskirchen, G., Ward, W. W., and Prasher, D. C. (1994). Green fluorescent protein as a marker for gene expression. *Science* 263, 802–805. doi: 10.1126/science.8303295

Cherubini, E., Rovira, C., Gaiarsa, J. L., Corradetti, R., and Ari, Y. B. (1990). GABA mediated excitation in immature rat CA3 hippocampal neurons. *Int. J. Dev. Neurosci.* 8, 481–490. doi: 10.1016/0736-5748(90)90080-L

Chub, N., Mentis, G. Z., and O'Donovan, M. J. (2006). Chloride-sensitive MEQ fluorescence in chick embryo motoneurons following manipulations of chloride and during spontaneous network activity. *J. Neurophysiol.* 95, 323–330. doi: 10.1152/jn.00162.2005

Chudakov, D. M., Matz, M. V., Lukyanov, S., and Lukyanov, K. A. (2010). Fluorescent proteins and their applications in imaging living cells and tissues. *Physiol. Rev.* 90, 1103–1163. doi: 10.1152/physrev.00038.2009

Clayton, G. H., Owens, G. C., Wolff, J. S., and Smith, R. L. (1998). Ontogeny of cation–Cl- cotransporter expression in rat neocortex. *Dev. Brain Res.* 109, 281–292. doi: 10.1016/S0165-3806(98)00078-9

Cubitt, A. B., Heim, R., Adams, S. R., Boyd, A. E., Gross, L. A., and Tsien, R. Y. (1995). Understanding, improving and using green fluorescent proteins. *Trends Biochem. Sci.* 20, 448–455. doi: 10.1016/S0968-0004(00)89099-4

dal Maschio, M., Ghezzi, D., Bony, G., Alabastri, A., Deidda, G., Brondi, M., et al. (2012). High-performance and site-directed in utero electroporation by a triple-electrode probe. *Nat. Commun.* 3:960. doi: 10.1038/ncomms1961

Day, R. N., and Davidson, M. W. (2009). The fluorescent protein palette: tools for cellular imaging. *Chem. Soc. Rev.* 38, 2887–2921. doi: 10.1039/b901966a

Deidda, G., Bozarth, I. F., and Cancedda, L. (2014). Modulation of GABAergic transmission in development and neurodevelopmental disorders: investigating physiology and pathology to gain therapeutic perspectives. *Front. Cell. Neurosci.* 8:119. doi: 10.3389/fncel.2014.00119

De La Fuente, R., Namkung, W., Mills, A., and Verkman, A. S. (2008). Small-molecule screen identifies inhibitors of a human intestinal calcium-activated chloride channel. *Mol. Pharmacol.* 73, 758–768. doi: 10.1124/mol.107.043208

Delpire, E. (2000). Cation-chloride cotransporters in neuronal communication. *Physiology* 15, 309–312.

Duebel, J., Haverkamp, S., Schleich, W., Feng, G., Augustine, G. J., Kuner, T., et al. (2006). Two-photon imaging reveals somatodendritic chloride gradient in retinal ON-type bipolar cells expressing the biosensor Clomeleon. *Neuron* 49, 81–94. doi: 10.1016/j.neuron.2005.10.035

Dzhala, V. I., Kuchibhotla, K. V., Glykys, J. C., Kahle, K. T., Swiercz, W. B., Feng, G., et al. (2010). Progressive NKCC1-dependent neuronal chloride accumulation during neonatal seizures. *J. Neurosci.* 30, 11745–11761. doi: 10.1523/JNEUROSCI.1769-10.2010

Dzhala, V. I., Talos, D. M., Sdrulla, D. A., Brumback, A. C., Mathews, G. C., Benke, T. A., et al. (2005). NKCC1 transporter facilitates seizures in the developing brain. *Nat. Med.* 11, 1205–1213. doi: 10.1038/nm1301

Dzhala, V., Valeeva, G., Glykys, J., Khazipov, R., and Staley, K. (2012). Traumatic alterations in GABA signaling disrupt hippocampal network activity in the developing brain. *J. Neurosci.* 32, 4017–4031. doi: 10.1523/JNEUROSCI.5139-11.2012

Egawa, K., Yamada, J., Furukawa, T., Yanagawa, Y., and Fukuda, A. (2013). Cl- homeodynamics in gap junction-coupled astrocytic networks on activation of GABAergic synapses. *J. Physiol.* 591, 3901–3917. doi: 10.1113/jphysiol.2013.257162

Ehrlich, I., Löhrke, S., and Friauf, E. (1999). Shift from depolarizing to hyperpolarizing glycine action in rat auditory neurones is due to age-dependent Cl– regulation. *J. Physiol.* 520, 121–137. doi: 10.1111/j.1469-7793.1999.00121.x

Fiumelli, H., Cancedda, L., and Poo, M. (2005). Modulation of GABAergic transmission by activity via postsynaptic Ca^{2+}-dependent regulation of KCC2 function. *Neuron* 48, 773–786. doi: 10.1016/j.neuron.2005.10.025

Fukuda, A., Tanaka, M., Yamada, Y., Muramatsu, K., Shimano, Y., and Nishino, H. (1998). Simultaneous optical imaging of intracellular Cl– in neurons in different layers of rat neocortical slices: advantages and limitations. *Neurosci. Res.* 32, 363–371. doi: 10.1016/S0168-0102(98)00099-6

Funk, K., Woitecki, A., Franjic-Würtz, C., Gensch, T., Möhrlen, F., and Frings, S. (2008). Modulation of chloride homeostasis by inflammatory mediators in dorsal root ganglion neurons. *Mol. Pain* 4:32. doi: 10.1186/1744-8069-4-32

Galietta, L. J., Haggie, P. M., and Verkman, A. S. (2001a). Green fluorescent protein-based halide indicators with improved chloride and iodide affinities. *FEBS Lett.* 499, 220–224. doi: 10.1016/S0014-5793(01)02561-3

Galietta, L. V., Jayaraman, S., and Verkman, A. S. (2001b). Cell-based assay for high-throughput quantitative screening of CFTR chloride transport agonists. *Am. J. Physiol. Cell Physiol.* 281, C1734–C1742.

Ganguly, K., Schinder, A. F., Wong, S. T., and Poo, M. (2001). GABA itself promotes the developmental switch of neuronal GABAergic responses from excitation to inhibition. *Cell* 105, 521–532. doi: 10.1016/S0092-8674(01)00341-5

Gilbert, D., Franjic-Würtz, C., Funk, K., Gensch, T., Frings, S., and Möhrlen, F. (2007). Differential maturation of chloride homeostasis in primary afferent neurons of the somatosensory system. *Int. J. Dev. Neurosci.* 25, 479–489. doi: 10.1016/j.ijdevneu.2007.08.001

Gilbert, D. F., Wilson, J. C., Nink, V., Lynch, J. W., and Osborne, G. W. (2009). Multiplexed labeling of viable cells for high-throughput analysis of glycine receptor function using flow cytometry. *Cytometry A* 75, 440–449. doi: 10.1002/cyto.a.20703

Glykys, J., Dzhala, V., Egawa, K., Balena, T., Saponjian, Y., Kuchibhotla, K. V., et al. (2014). Local impermeant anions establish the neuronal chloride concentration. *Science* 343, 670–675. doi: 10.1126/science.1245423

Glykys, J., Dzhala, V. I., Kuchibhotla, K. V., Feng, G., Kuner, T., Augustine, G., et al. (2009). Differences in cortical versus subcortical GABAergic signaling: a candidate mechanism of electroclinical uncoupling of neonatal seizures. *Neuron* 63, 657–672. doi: 10.1016/j.neuron.2009.08.022

Griesbeck, O., Baird, G. S., Campbell, R. E., Zacharias, D. A., and Tsien, R. Y. (2001). Reducing the environmental sensitivity of yellow fluorescent protein. *J. Biol. Chem.* 276, 29188–29194. doi: 10.1074/jbc.M102815200

Grimley, J. S., Li, L., Wang, W., Wen, L., Beese, L. S., Hellinga, H. W., et al. (2013). Visualization of synaptic inhibition with an optogenetic sensor developed by cell-free protein engineering automation. *J. Neurosci.* 33, 16297–16309. doi: 10.1523/JNEUROSCI.4616-11.2013

Grynkiewicz, G., Poenie, M., and Tsien, R. Y. (1985). A new generation of Ca^{2+} indicators with greatly improved fluorescence properties. *J. Biol. Chem.* 260, 3440–3450.

Guthrie, P. B., Segal, M., and Kater, S. B. (1991). Independent regulation of calcium revealed by imaging dendritic spines. *Nature* 354, 76–80. doi: 10.1038/354076a0

Harootunian, A. T., Kao, J. P., Eckert, B. K., and Tsien, R. Y. (1989). Fluorescence ratio imaging of cytosolic free Na+ in individual fibroblasts and lymphocytes. *J. Biol. Chem.* 264, 19458–19467.

Heim, R., Cubitt, A. B., and Tsien, R. Y. (1995). Improved green fluorescence. *Nature* 373, 663–664. doi: 10.1038/373663b0

Heim, R., and Tsien, R. Y. (1996). Engineering green fluorescent protein for improved brightness, longer wavelengths and fluorescence resonance energy transfer. *Curr. Biol.* 6, 178–182. doi: 10.1016/S0960-9822(02)00450-5

He, Q., Nomura, T., Xu, J., and Contractor, A. (2014). The developmental switch in GABA polarity is delayed in fragile X mice. *J. Neurosci.* 34, 446–450. doi: 10.1523/JNEUROSCI.4447-13.2014

Inglefield, J. R., and Schwartz-Bloom, R. D. (1997). Confocal imaging of intracellular chloride in living brain slices: measurement of $GABA_A$ receptor activity. *J. Neurosci. Methods* 75, 127–135. doi: 10.1016/S0165-0270(97)00054-X

Inglefield, J. R., and Schwartz-Bloom, R. D. (1998). Optical imaging of hippocampal neurons with a chloride-sensitive dye: early effects of in vitro ischemia. *J. Neurochem.* 70, 2500–2509. doi: 10.1046/j.1471-4159.1998.70062500.x

Isomura, Y., Sugimoto, M., Fujiwara-Tsukamoto, Y., Yamamoto-Muraki, S., Yamada, J., and Fukuda, A. (2003). Synaptically activated Cl– accumulation responsible for depolarizing GABAergic responses in mature hippocampal neurons. *J. Neurophysiol.* 90, 2752–2756. doi: 10.1152/jn.00142.2003

Jayaraman, S., Biwersi, J., and Verkman, A. S. (1999). Synthesis and characterization of dual-wavelength Cl-sensitive fluorescent indicators for ratio imaging. *Am. J. Physiol.* 276, C747–C757.

Jayaraman, S., Haggie, P., Wachter, R. M., Remington, S. J., and Verkman, A. S. (2000). Mechanism and cellular applications of a green fluorescent protein-based halide sensor. *J. Biol. Chem.* 275, 6047–6050. doi: 10.1074/jbc.275.9.6047

Jose, M., Nair, D. K., Reissner, C., Hartig, R., and Zuschratter, W. (2007). Photophysics of Comeleon by FLIM: discriminating excited state reactions along neuronal development. *Biophys. J.* 92, 2237–2254. doi: 10.1529/biophysj.106.092841

Kahle, K. T., Deeb, T. Z., Puskarjov, M., Silayeva, L., Liang, B., Kaila, K., et al. (2013). Modulation of neuronal activity by phosphorylation of the K–Cl cotransporter KCC2. *Trends Neurosci.* 36, 726–737. doi: 10.1016/j.tins.2013.08.006

Kaila, K., Ruusuvuori, E., Seja, P., Voipio, J., and Puskarjov, M. (2014). GABA actions and ionic plasticity in epilepsy. *Curr. Opin. Neurobiol.* 26, 34–41. doi: 10.1016/j.conb.2013.11.004

Kaila, K., Voipio, J., Paalasmaa, P., Pasternack, M., and Deisz, R. A. (1993). The role of bicarbonate in GABAA receptor-mediated IPSPs of rat neocortical neurones. *J. Physiol.* 464, 273–289.

Kandler, K., and Friauf, E. (1995). Development of glycinergic and glutamatergic synaptic transmission in the auditory brainstem of perinatal rats. *J. Neurosci.* 15, 6890–6904.

Kaneko, H., Putzier, I., Frings, S., and Gensch, T. (2002). Determination of intracellular chloride concentration in dorsal root ganglion neurons by fluorescence lifetime imaging. *Calcium Activated Chloride Channels* 167–189. doi: 10.1016/S1063-5823(02)53033-7

Kaneko, H., Putzier, I., Frings, S., Kaupp, U. B., and Gensch, T. (2004). Chloride accumulation in mammalian olfactory sensory neurons. *J. Neurosci.* 24, 7931–7938. doi: 10.1523/JNEUROSCI.2115-04.2004

Khirug, S., Yamada, J., Afzalov, R., Voipio, J., Khiroug, L., and Kaila, K. (2008). GABAergic depolarization of the axon initial segment in cortical principal neurons is caused by the Na-K-2Cl cotransporter NKCC1. *J. Neurosci.* 28, 4635–4639. doi: 10.1523/JNEUROSCI.0908-08.2008

Kirischuk, S., Parpura, V., and Verkhratsky, A. (2012). Sodium dynamics: another key to astroglial excitability? *Trends Neurosci.* 35, 497–506. doi: 10.1016/j.tins.2012.04.003

Kneen, M., Farinas, J., Li, Y., and Verkman, A. S. (1998). Green fluorescent protein as a noninvasive intracellular pH indicator. *Biophys. J.* 74, 1591–1599. doi: 10.1016/S0006-3495(98)77870-1

Kovalchuk, Y., and Garaschuk, O. (2012). Two-photon chloride imaging using MQAE in vitro and in vivo. *Cold Spring Harb. Protoc.* 2012, 778–785. doi: 10.1101/pdb.prot070037

Krapf, R., Berry, C. A., and Verkman, A. S. (1988). Estimation of intracellular chloride activity in isolated perfused rabbit proximal convoluted tubules using a fluorescent indicator. *Biophys. J.* 53, 955–962. doi: 10.1016/S0006-3495(88)83176-X

Kruger, W., Gilbert, D., Hawthorne, R., Hryciw, D. H., Frings, S., Poronnik, P., et al. (2005). A yellow fluorescent protein-based assay for high-throughput screening of glycine and $GABAa_A$ receptor chloride channels. *Neurosci. Lett.* 380, 340–345. doi: 10.1016/j.neulet.2005.01.065

Kuner, T., and Augustine, G. J (2000). A genetically encoded ratiometric indicator for chloride: capturing chloride transients in cultured hippocampal neurons. *Neuron* 27, 447–459. doi: 10.1016/S0896-6273(00)00056-8

Lillis, K. P., Kramer, M. A., Mertz, J., Staley, K. J., and White, J. A. (2012). Pyramidal cells accumulate chloride at seizure onset. *Neurobiol. Dis.* 47, 358–366. doi: 10.1016/j.nbd.2012.05.016

Lorenzen, I., Aberle, T., and Plieth, C. (2004). Salt stress-induced chloride flux: a study using transgenic *Arabidopsis* expressing a fluorescent anion probe. *Plant J.* 38, 539–544. doi: 10.1111/j.0960-7412.2004.02053.x

Löscher, W., Puskarjov, M., and Kaila, K. (2013). Cation-chloride cotransporters NKCC1 and KCC2 as potential targets for novel antiepileptic and antiepileptogenic treatments. *Neuropharmacology* 69, 62–74. doi: 10.1016/j.neuropharm.2012.05.045

Lu, J., Karadsheh, M., and Delpire, E. (1999). Developmental regulation of the neuronal-specific isoform of K-CL cotransporter KCC2 in postnatal rat brains. *J. Neurobiol.* 39, 558–568. doi: 10.1002/(SICI)1097-4695(19990615)39:4<558::AID-NEU9>3.0.CO;2-5

Marandi, N., Konnerth, A., and Garaschuk, O. (2002). Two-photon chloride imaging in neurons of brain slices. *Pflugers Arch.* 445, 357–365. doi: 10.1007/s00424-002-0933-7

Markova, O., Mukhtarov, M., Real, E., Jacob, Y., and Bregestovski, P. (2008). Genetically encoded chloride indicator with improved sensitivity. *J. Neurosci. Methods* 170, 67–76. doi: 10.1016/j.jneumeth.2007.12.016

Merzlyak, E. M., Goedhart, J., Shcherbo, D., Bulina, M. E., Shcheglov, A. S., Fradkov, A. F., et al. (2007). Bright monomeric red fluorescent protein with an extended fluorescence lifetime. *Nat. Methods* 4, 555–557. doi: 10.1038/nmeth1062

Mizrahi, A., Crowley, J. C., Shtoyerman, E., and Katz, L. C. (2004). High-resolution in vivo imaging of hippocampal dendrites and spines. *J. Neurosci.* 24, 3147–3151. doi: 10.1523/JNEUROSCI.5218-03.2004

Mukhtarov, M., Liguori, L., Waseem, T., Rocca, F., Buldakova, S., Arosio, D., et al. (2013). Calibration and functional analysis of three genetically encoded Cl-/pH sensors. *Front. Mol. Neurosci.* 6:9. doi: 10.3389/fnmol.2013.00009

Müller, W., and Connor, J. A. (1991). Dendritic spines as individual neuronal compartments for synaptic Ca^{2+} responses. *Nature* 354, 73–76. doi: 10.1038/354073a0

Nagai, T., Ibata, K., Park, E. S., Kubota, M., Mikoshiba, K., and Miyawaki, A. (2002). A variant of yellow fluorescent protein with fast and efficient maturation for cell-biological applications. *Nat. Biotechnol.* 20, 87–90. doi: 10.1038/nbt0102-87

Nakamura, T., Kaneko, H., and Nishida, N. (1997). Direct measurement of the chloride concentration in newt olfactory receptors with the fluorescent probe. *Neurosci. Lett.* 237, 5–8. doi: 10.1016/S0304-3940(97)00794-5

Nausch, L. W. M., Ledoux, J., Bonev, A. D., Nelson, M. T., and Dostmann, W. R. (2008). Differential patterning of cGMP in vascular smooth muscle cells revealed by single GFP-linked biosensors. *Proc. Natl. Acad. Sci. U.S.A.* 105, 365–370. doi: 10.1073/pnas.0710387105

Navarrete, M., Perea, G., de Sevilla, D. F., Gómez-Gonzalo, M., Núñez, A., Martín, E. D., et al. (2012). Astrocytes mediate in vivo cholinergic-induced synaptic plasticity. *PLoS Biol.* 10:e1001259. doi: 10.1371/journal.pbio.1001259

Noguchi, J., Matsuzaki, M., Ellis-Davies, G. C. R., and Kasai, H. (2005). Spine-neck geometry determines NMDA receptor-dependent Ca^{2+} signaling in dendrites. *Neuron* 46, 609–622. doi: 10.1016/j.neuron.2005.03.015

Obata, K., Oide, M., and Tanaka, H. (1978). Excitatory and inhibitory actions of GABA and glycine on embryonic chick spinal neurons in culture. *Brain Res.* 144, 179–184. doi: 10.1016/0006-8993(78)90447-X

Perea, G., Navarrete, M., and Araque, A. (2009). Tripartite synapses: astrocytes process and control synaptic information. *Trends Neurosci.* 32, 421–431. doi: 10.1016/j.tins.2009.05.001

Piatkevich, K. D., Hulit, J., Subach, O. M., Wu, B., Abdulla, A., Segall, J. E., et al. (2010). Monomeric red fluorescent proteins with a large stokes shift. *Proc. Natl. Acad. Sci. U.S.A.* 107, 5369–5374. doi: 10.1073/pnas.0914365107

Pizzarelli, R., and Cherubini, E. (2011). Alterations of GABAergic signaling in autism spectrum disorders. *Neural Plast.* 2011:e297153. doi: 10.1155/2011/297153

Plotkin, M. D., Snyder, E. Y., Hebert, S. C., and Delpire, E. (1997). Expression of the Na-K-2Cl cotransporter is developmentally regulated in postnatal rat brains: a possible mechanism underlying GABA's excitatory role in immature brain. *J. Neurobiol.* 33, 781–795. doi: 10.1002/(SICI)1097-4695(19971120)33:6<781::AID-NEU6>3.0.CO;2-5

Pond, B. B., Berglund, K., Kuner, T., Feng, G., Augustine, G. J., and Schwartz-Bloom, R. D. (2006). The chloride transporter Na^+-K^+-Cl- cotransporter isoform-1 contributes to intracellular chloride increases after in vitro ischemia. *J. Neurosci.* 26, 1396–1406. doi: 10.1523/JNEUROSCI.1421-05.2006

Puskarjov, M., Ahmad, F., Kaila, K., and Blaesse, P. (2012). Activity-dependent cleavage of the K-Cl cotransporter KCC2 mediated by calcium-activated protease calpain. *J. Neurosci.* 32, 11356–11364. doi: 10.1523/JNEUROSCI.6265-11.2012

Puskarjov, M., Kahle, K. T., Ruusuvuori, E., and Kaila, K. (2014). Pharmacotherapeutic targeting of cation-chloride cotransporters in neonatal seizures. *Epilepsia* 55, 806–818. doi: 10.1111/epi.12620

Raimondo, J. V., Irkle, A., Wefelmeyer, W., Newey, S. E., and Akerman, C. J. (2012). Genetically encoded proton sensors reveal activity-dependent pH changes in neurons. *Front. Mol. Neurosci.* 5:68. doi: 10.3389/fnmol.2012.00068

Raimondo, J. V., Joyce, B., Kay, L., Schlagheck, T., Newey, S. E., Srinivas, S., et al. (2013). A genetically-encoded chloride and pH sensor for dissociating ion dynamics in the nervous system. *Front. Cell. Neurosci.* 7:202. doi: 10.3389/fncel.2013.00202

Rhoden, K. J., Cianchetta, S., Stivani, V., Portulano, C., Galietta, L. J., and Romeo, G. (2007). Cell-based imaging of sodium iodide symporter activity with the yellow fluorescent protein variant YFP-H148Q/I152L. *Am. J. Physiol. Cell Physiol.* 292, C814–C823. doi: 10.1152/ajpcell.00291.2006

Rivera, C., Voipio, J., Payne, J. A., Ruusuvuori, E., Lahtinen, H., Lamsa, K., et al. (1999). The K+/Cl co-transporter KCC2 renders GABA hyperpolarizing during neuronal maturation. *Nature* 397, 251–255. doi: 10.1038/16697

Rizzo, M. A., Davidson, M. W., and Piston, D. W. (2009). Fluorescent protein tracking and detection: fluorescent protein structure and color variants. *Cold Spring Harb. Protoc.* 2009:pdb.top63. doi: 10.1101/pdb.top63

Sah, R., and Schwartz-Bloom, R. D. (1999). Optical imaging reveals elevated intracellular chloride in hippocampal pyramidal neurons after oxidative stress. *J. Neurosci.* 19, 9209–9217.

Shaner, N. C., Lin, M. Z., McKeown, M. R., Steinbach, P. A., Hazelwood, K. L., Davidson, M. W., et al. (2008). Improving the photostability of bright monomeric orange and red fluorescent proteins. *Nat. Methods* 5, 545–551. doi: 10.1038/nmeth.1209

Shaner, N. C., Steinbach, P. A., and Tsien, R. Y. (2005). A guide to choosing fluorescent proteins. *Nat. Methods* 2, 905–909. doi: 10.1038/nmeth819

Smetters, D., Majewska, A., and Yuste, R. (1999). Detecting action potentials in neuronal populations with calcium imaging. *Methods* 18, 215–221. doi: 10.1006/meth.1999.0774

Szabadics, J., Varga, C., Molnár, G., Oláh, S., Barzó, P., and Tamás, G. (2006). Excitatory effect of GABAergic axo-axonic cells in cortical microcircuits. *Science* 311, 233–235. doi: 10.1126/science.1121325

Thoreson, W. B., Bryson, E. J., and Rabl, K. (2003). Reciprocal interactions between calcium and chloride in rod photoreceptors. *J. Neurophysiol.* 90, 1747–1753. doi: 10.1152/jn.00932.2002

Tyzio, R., Nardou, R., Ferrari, D. C., Tsintsadze, T., Shahrokhi, A., Eftekhari, S., et al. (2014). Oxytocin-mediated GABA inhibition during delivery attenuates autism pathogenesis in rodent offspring. *Science* 343, 675–679. doi: 10.1126/science.1247190

Wachter, R. M., and Remington, S. J. (1999). Sensitivity of the yellow variant of green fluorescent protein to halides and nitrate. *Curr. Biol.* 9, R628–R629. doi: 10.1016/S0960-9822(99)80408-4

Wachter, R. M., Yarbrough, D., Kallio, K., and Remington, S. J. (2000). Crystallographic and energetic analysis of binding of selected anions to the yellow variants of green fluorescent protein1. *J. Mol. Biol.* 301, 157–171. doi: 10.1006/jmbi.2000.3905

Waseem, T., Mukhtarov, M., Buldakova, S., Medina, I., and Bregestovski, P. (2010). Genetically encoded Cl-sensor as a tool for monitoring of Cl-dependent processes in small neuronal compartments. *J. Neurosci. Methods* 193, 14–23. doi: 10.1016/j.jneumeth.2010.08.002

Watts, S. D., Suchland, K. L., Amara, S. G., and Ingram, S. L. (2012). A sensitive membrane-targeted biosensor for monitoring changes in intracellular chloride in neuronal processes. *PLoS ONE* 7:e35373. doi: 10.1371/journal.pone.0035373

White, H. S., Brown, S. D., Woodhead, J. H., Skeen, G. A., and Wolf, H. H. (1997). Topiramate enhances GABA-mediated chloride flux and GABA-evoked chloride currents in murine brain neurons and increases seizure threshold. *Epilepsy Res.* 28, 167–179. doi: 10.1016/S0920-1211(97)00045-4

Wu, W. L., Ziskind-Conhaim, L., and Sweet, M. A. (1992). Early development of glycine- and GABA-mediated synapses in rat spinal cord. *J. Neurosci.* 12, 3935–3945.

Yamada, Y., Fukuda, A., Tanaka, M., Shimano, Y., Nishino, H., Muramatsu, K., et al. (2001). Optical imaging reveals cation–Cl- cotransporter-mediated transient rapid decrease in intracellular Cl- concentration induced by oxygen–glucose deprivation in rat neocortical slices. *Neurosci. Res.* 39, 269–280. doi: 10.1016/S0168-0102(00)00221-2

Yuste, R., and Denk, W. (1995). Dendritic spines as basic functional units of neuronal integration. *Nature* 375, 682–684. doi: 10.1038/375682a0

Yuste, R., Majewska, A., Cash, S. S., and Denk, W. (1999). Mechanisms of calcium influx into hippocampal spines: heterogeneity among spines, coincidence detection by NMDA receptors, and optical quantal analysis. *J. Neurosci.* 19, 1976–1987.

Zhang, L.-L., Pathak, H. R., Coulter, D. A., Freed, M. A., and Vardi, N. (2006). Shift of intracellular chloride concentration in ganglion and amacrine cells of developing mouse retina. *J. Neurophysiol.* 95, 2404–2416. doi: 10.1152/jn.00578.2005

Zorec, R., Araque, A., Carmignoto, G., Haydon, P. G., Verkhratsky, A., and Parpura, V. (2012). Astroglial excitability and gliotransmission: an appraisal of Ca^{2+} as a signalling route. *ASN Neuro* 4, 103–119. doi: 10.1042/AN20110061

Conflict of Interest Statement: The authors declare that the research was conducted in the absence of any commercial or financial relationships that could be construed as a potential conflict of interest.

Received: 04 June 2014; accepted: 12 August 2014; published online: 29 August 2014.
*Citation: Arosio D and Ratto GM (2014) Twenty years of fluorescence imaging of intracellular chloride. Front. Cell. Neurosci. **8**:258. doi: 10.3389/fncel.2014.00258*
This article was submitted to the journal Frontiers in Cellular Neuroscience.

2

Methods

2.1 Site-directed Mutagenesis

All mutants were obtained by site-directed mutagenesis using QuickChange II XL Site-Directed Mutagenesis Kit (Stratagene). Primers were synthesized by the Sigma-Aldrich company. PCRs were performed according to manufacturer's instructions using pPR-IBA2-D3GFP or pPR-IBA2-E2GFP plasmid as template and appropriate primers. Digestion of PCR reaction was carried out by Dpn1 digestion in order to eliminate template DNA and amplified mutated DNA was purified using Wizard SV Gel and PCR Clean-up System kit (Promega). E. coli XL10-Gold ultracompetent cells (Novagen) were transformed with plasmid after clean-

up according kit instructions and grown overnight on LB plates supplemented with 50mg/L ampicilin (amp) at 37°C. Positive colonies were picked and grown overnight in 2mL LB-amp and miniprep were performed using Wizard Plus SV Minipreps DNA Purification System (Promega). We checked for effective mutations by DNA sequencing (done by BMR Genomics).

2.2 Recombinant protein expression and purification

E. coli BL21 cells (Novagen) were transformed with plasmid carrying the mutated GFP gene using one-shot transformation kit and grown overnight in LB medium supplemented with 100 mg/mL ampicillin at 37°C. Bacterial cultures were pelleted 24 hours after induction with 1 mM isopropyl 6-D-1-thiogalactopyranoside (IPTG) (Sigma Aldrich) at 30°C. Purification by affinity was carried out using HIS-Select^{TM} Cartridges (Sigma Aldrich) or Strep-Tactin 5mL Superflow column (IBA Technology) following the manufacturer's instructions. Chloride-free buffers were used in all the chromatography steps ensuring the absence of Cl^- from all preparations. If necessary, protein preparations were concentrated using centrifugal filter devices (Amicon Ultra-15, Millipore) Bacterial pellets were typically resuspended in 5 ml of halide-free chromatography washing buffer (20mM diethanolamine DEA, 50mM K2SO4 , pH 8.5), supplemented with 2% of 50X cocktail of protease inhibitor (Roche). Lysis was performed with Ultrasonic Processor (Cole Parmer) (10 cycle of 30sec output 6W, interrupted by 10sec cooling). FPLC was performed on AKTA Basic10 FPLC system (GE Healthcare). Filtrated lysate was loaded without loop and flow rate was set up at 3mL/min. Elution of bound strep tagged-GFP was total with 25% of washing buffer supplemented with desthiobiotin. Protein concentration was estimated performing a Coomassie blue after 12% SDS PAGE and comparing with BSA scale standards. After pu-

rification protein was concentrated 3X by centrifugation using Amicon Ultra-4 centrifugal filter unit with 10kDa cut-off (Millipore).

2.3 Bioinformatics design of 3D structures

All figures showing 3D structure were obtained using the site- directed mutagenesis wizard tools of PyMOL Molecular Graphics System v.1.4 (Schrödinger, LLC) on the PDB file 2O2B.

2.4 Spectroscopy analysis of proteins *in vitro*

Absorption spectra were recorded using a steady-state spectrophotometer (model V-550 UV/VIS, Jasco, Inc.) equipped with a temperature-controlled cell holder. Fluorescence steady-state data were measured using an EnSpire spectral scanning multimode reader fluorometer (PerkinElmer) with 96-well black bottom plates (PerkinElmer, catalog # 6005279). Temperature was set at 20°C and 37°C and well volume was kept at 300 µL. Fluorescence intensities were collected with 100 numbers of flashes. Emission spectra were realized with excitation wavelength of 458 or 488 nm. Excitation spectra were recorded with an emission wavelength of 520 nm. Excitation and emission bandwidths were set both at 10 nm. Fluorescence spectra for pH titration were collected at 37°C using a Fluoromax-4 fluorescence spectrophotometer (Horiba) with excitation and emission bandwidths set at 5 nm.

We assumed the same extinction coefficient at 280 nm for all variants and E^2GFP so that the relative brightness (η/ηE2GFP) of a new variant could be calculated according to the following equation (Eq. 2.1).

$$\frac{\eta_{variant}}{\eta_E^2 GFP} = \frac{F^{variant}}{F^{E^2GFP}} \frac{A_{280nm}^{E^2GFP}}{A_{280nm}^{variant}} \tag{2.1}$$

2.5 Random mutagenesis

Plasmid DNA was purified from overnight cultures by using Wizard® Plus SV Minipreps DNA Purification System ("Promega", USA). PCR products were purified with reagent kit "Wizard SV Gel and PCR Wizard SV Gel and PCR Clean Up System from Promega Clean Up System" ("Promega", USA). Restriction endonucleases were purchased from Thermoscientific and New England Biolabs. The GeneMorph II Random Mutagenesis Kit ("Agilent", USA) was used for PCR random mutagenesis of gene E2GFP-S202N. 0.5 ng and 5 ng of plasmid pPR-IBA2-E2GFP-S202N were mixed with 1 μl of Mutazyme II DNA Polymerase, 5 μl of 10x Mutazyme II reaction buffer, 0.5 μl of 10 mkM primers: 5'-CGCCATATGGCTAGCTGGAGCCACC-3' and 5'-GGGAAGCTTAGTTAGATATCACTTGTACAGC-3', 1 μl of 40 mM dNTPs mix and water to a final volume of 50 μl and cycled following protocol. PCR-product cloned in translation vector pPR-IBA2 vector ("IBA", Germany) at NdeI and HindIII sites. Ligated plasmids were transformed in E.coli strain BL21-Gold (DE3) ("Agilent", USA) as outlined by [114].

2.6 Screening of GFP libraries

After transformation, bacterial clones were prescreened on LB-plates with 0.1 mg/ml of ampicillin and 0.5 mM of IPTG with using of UV-transilluminator 2000 with long-wave UV-lamp ("BioRad", USA). Single fluorescent colonies were se-

lected by visual screening and streaked out on LB agar plates with 0.1 mg/ml of ampicillin and 0.5 mM of IPTG. Plates were incubated overnight at 37 °C. After 12 hours, 30 µl of at least 80 wells were inoculated in corresponding position of new 96 deep-well plates containing 1.5 ml of LB medium with 0.1 mg/ml of ampicillin and grown at 37 °C under shaking condition; the remaining wells were used for controls like buffer, E^2GFP-V224Q (pK_a 8.0), E^2GFP (pK_a 6.8) and E^2GFP-V224L (pK_a 6.3) following a standard scheme as in Fig. 3.5.

	01	02	03	04	05	06	07	08	09	10	11	12
A	D3											D3
B	VQ											E2
C	E2											Buf
D	Buf											Buf
E	Buf											Buf
F	Buf											E2
G	E2											VQ
H	D3											D3

Figure 2.1: **Scheme of 96-well for pH titration assay.** Part of the wells were used to measure controls, samples with known pK_a, and buffer, whose fluorescence intensities were averaged and subtracted from all plate wells.

After 4 hours, when the OD at 600 nm reached approximately 0.6, GFP expression was induced by adding 0.5 mM of IPTG (Sigma-Aldrich). Cells were incubated for 30 hours at 30°C. Bacterial cells were pelleted and resuspended in 0.1 ml of lysis buffer containing 1 mg/ml of lysozyme, 1x solution of protease inhibitor cocktail tablets (Roche, Switzerland), 25 mM K2SO4, 2 mM EDTA, 0.1% Triton X-100, 50 mM Tris-HCl, pH 7.7, and incubated for 1 hour at 37°C. 1 ml of buffer containing 25 mM K2SO4, 2 mM EDTA, 0.1% Triton X-100, 50 mM Tris-HCl, pH 7.7 was added in each well. Lysed cells were centrifuged and then loaded on strep-well HT filter plates (IBA) placed above strep-well HT purification plates (IBA) previously equilibrated in buffer following the manufacturer's protocol (IBA,

Germany) and using the TECAN Evo 200 robot. Five cycles of 1' of vacuum at 200 mbar were applied to filter the solution of lysed cells and then purification plates were washed by two following steps of 1 ml with Buffer W. Proteins were eluted with 100 µl of Buffer at pH=9.0 and collected in black opaque 96-well Optiplates (PerkinElmer). Tecan M200 plate reader was used to measure, in fluorescence-top-reading mode, fluorescence emitted at 535 nm (bandwidth=25 nm) after exciting at both 400 and 485 nm (excitation bandwidths of 20 and 25 nm, respectively); 10 flashes, 20 µs integration time, and gain manually adjusted from 52 to 100. For pK_a measurement, fluorescence was measured at 25 °C starting at pH=9.0 and after each 2-µl addition of 1.9% H_2SO_4 until a pH value of about 5.3 was reached. The 6 additions that were commonly needed to span the pH range from 9 to 5 were robotically dispensed using EL406 Microplate Washer Dispenser (BioTek, USA). pH values were measured in triplicate after each addition using a pH-meter (GLP22, Crison Instruments, Spain) and microelectrode Minitrode (Hamilton, Switzerland). For measurement of chloride-dependent fluorescence 1 M NaCl in 50 mM acetic acid was added in each well spanning a $[Cl^-]$ range from 18 to 450 mM.

2.7 LSSmClopHensor constructs and cloning

Nucleotide sequence for LSSmKate2, fused at the N-term to the polypeptide linker "ASGGGGGLVPRGSASGA", was codon-optimized for expression in mammalian cells using the OptimumGene algorithm (GenScript, Inc.), and cloned into pUC57 plasmid between BamHI and XbaI unique restriction sites (see Supplementary Information). The mammalian expression vector pcDNA3-LSSmClopHensor was obtained by subcloning the BamHI-XbaI fragment into pcDNA3-ClopHensor (Addgene #25938) to replace DsRed-

monomer. The bacterial expression vector pET21-LSSmClopHensor was obtained by PCR amplification from pcDNA3-LSSmClopHensor using the primers NheI-E2-fw (5'-CTAGCTAGCGTGAGCAAGGGCGAGGA-3') and XhoI-LSS-rv (5'-CCGCTCGAGGCGATGGCCCAGCTT-3') for insertion into the multiple cloning site of pET21b vector (Novagen). Digestions with NheI and XhoI restriction enzymes were performed following the manufacturer's instructions (New England Biolabs). Bacterial expression vector for LSSmKate2 was prepared according the following procedure: sequence encoding LSSmKate2 was PCR-amplified from the pUC57-E2GFPLSSmKate2 plasmid using primers NheI-LSS-fw (5'-CTAGCTAGCGTGAGCGAACTGATTAAGGAG-3') and XhoI-LSS-rv (5'-CCGCTCGAGGCGATGGCCCAGCTT-3'). The insert was digested with NheI and XhoI restriction enzymes following the manufacturer's instructions (New England Biolabs).

2.8 pH and chloride imaging analysis

The combined pH and Cl^- ratio analysis was based on the acquisition of three fluorescence signals: cyan channel with excitation at 458 ± 10 nm and emission at 525 ± 25 nm; green channel with excitation at 482 ± 18 nm and emission at 525 ± 25 nm; and red channel with excitation at 458 ± 10 nm and emission at 610 ± 30 nm. For the calculation of Cl^- concentration and pH values two ratios were defined: R_{Cl} as red-over-cyan and R_{pH} as green-over-cyan. Ratio imaging analysis was performed as previously described [115] with the difference that no correction for fluctuation in the excitation intensity were required in this study, because a single light source (xenon lamp or argon laser) was used with a 3-channel (cyan, green and red) image acquired within brief intervals (1-2 s). Briefly, to estimate the pK_a of LSSmClopHensor from pH titration data we used

the following equation:

$$R_{pH} = \frac{R_B + R_A 10^{pK_a - pH}}{1 + 10^{pK_a - pH}} \tag{2.2}$$

where R_A and R_B are the plateau values for R_{pH} at acidic and basic conditions, respectively. To estimate K_d from Cl^- titration data, we used equation (3)

$$R_{Cl} = \frac{R^0_{Cl}}{1 + \frac{[Cl]}{K_d}} \tag{2.3}$$

where R^0_{Cl} is the value of R_{Cl} at $[Cl^-] = 0$, a pH-independent and setup-dependent parameter. Accordingly, pH and Cl^- concentration maps were computed pixel-by-pixel using respectively the following equations 4 and 5.

$$pH = pK_a + \log(\frac{R_{pH} - R_A}{R_B - R_{pH}}) \tag{2.4}$$

$$[Cl] = K_d(pH)\frac{R^0_{[Cl]} - R_{Cl}}{R_{Cl}} \tag{2.5}$$

To remove bleed-through in every channel, we calculated the intensity ratio of bleed-through in every emission channel using E^2GFP and LSSmKate2 proteins separately in independent experiments and varying intracellular pH in the range from 5.2 to 7.9 (Supplementary Figures S13, S14 and Table S1). The resulting images, corrected for bleed-through were then used to perform ratio analysis.

2.9 Fluorescence microscopy and image analysis

Images from cultured cells were recorded using a wide field microscope (iMIC, Till Photonics). Specimens were sequentially excited using a high stability 150 W xenon lamp (Oligochrome, Till Photonics) equipped with a fast filter switching device and the two required excitation filters: FF02-482/18-25 (Semrock), and the laser clean-up filter z 458/10x (Chroma). A dual band dichroic mirror Di01-R488/561 (Semrock) was hosted in the filter cube. Emitted fluorescence was collected from 1.2 NA, 60X water immersion objective and split (at about 560 nm) into green and red channels using a single band dichroic mirror (FF560-Di01, Semrock) mounted into a dichrotome device (Till Photonics). The split channels were then simultaneously projected onto half of the electron multiplied charged-coupled device (Ixon Ultra 897; Andor Technologies). The three channels required by ratiometric analysis were thus recorded alternating between two excitation filters. Imaging of rat cortical brain slices was performed using a confocal laser scanning microscope (TCS SP5-RS, Leica) with a time frame acquisition of 0.995 s (seven line average). Excitation wavelengths were sequentially switching between 458 an 488 nm; emission bands were set from 498 to 560 nm and from 560 to 720 nm for the green and red channels, respectively. The setup was also equipped with a CCD camera for differential interference contrast images. All experiments were performed in layer II/III.

Image processing was performed using custom Fiji macros. Images were filtered with Gaussian filter (sigma=1.5). Mean background fluorescence was measured in empty regions and subtracted to all images. Images were semi-automatically segmented on the basis of pixel intensity using the isodata algorithm (*getAutoThreshold* method). Masked images were then used to discriminate regions of interest (cells) and prevent artifacts arising from dividing background by back-

ground values.

2.10 Brain slice preparations and *in utero* electroporation

All experiments involving animals were carried out in strict accordance with the guidelines established by the European Communities Council Directive and approved by the National Council on Animal Care of the Italian Ministry of Health. The number of animals used was reduced to the minimum necessary for an adequate statistical analysis.

Coronal cortico-hippocampal slices were prepared from postnatal day 16–22 electroporated Wistar rats. Briefly, rats were deeply anesthetized with intraperitoneal injected Zoletil (40 mg/kg; Virbac). After decapitation, the brain was removed and transferred to ice-cold cutting solution containing (in mM): NaCl, 120; KCl, 3.2; KH_2PO_4, 1; $NaHCO_3$, 26; $MgCl_2$, 2; $CaCl_2$, 1; glucose, 10; Na-pyruvate, 2; and ascorbic acid, 0.6; at pH 7.4 (with 5% CO_2/95% O_2). Coronal slices were obtained by using a Leica vibratome VT1000S in the presence of the ionotropic glutamate receptor inhibitor kynurenic acid (2 mM). Slices were recovered for 20 min at 32°C and then kept at room temperature.

Standard in utero electroporation of layer II/III of the somatosensory cortex was performed as previously described [116]. Briefly, E17 timed-pregnant Sprague-Dawley rats were anesthetized with isoflurane (induction, 3.5%; surgery, 2.5%), and the uterine horns were exposed by laparotomy. The day of confirmation of vaginal plug was defined as E0, and the day of birth was defined as P0. The DNA (0.15-1.5 μg/μl in water) together with the dye Fast Green (0.3 mg/ml; Sigma) was injected (5-6 μl) through the uterine wall into one of the lateral ventricles of

each embryo using a 30G needle (Pic indolor). Embryo's head was carefully held between tweezer-type circular electrodes (10 mm diameter; Nepa Gene) that were wet with PBS while held across the uterine wall. For the electroporation protocol, 5 electrical pulses (amplitude, 50 V; duration, 50 ms; intervals, 150 ms) were delivered with a square-wave electroporation generator (CUY21EDIT; Nepa Gene). After electroporation, the uterine horns were returned into the abdominal cavity, and the embryos were allowed to continue their normal development.

2.11 Electrophysiology and induction of epileptic activity

Brain slices were continuously perfused in a submerged chamber (Warner Instruments) at a rate of 3-4 ml min-1 with (in mM): NaCl, 120; KCl, 3.2; KH_2PO_4, 1; $NaHCO_3$, 26; $MgCl_2$, 0.5; $CaCl_2$, 2; glucose, 10; pH 7.4 (with 5% CO_2/95% O_2). Seizure like events were evoked in the presence of 4-AP (50-100 µM). Bath temperature was maintained at 30-32°C by an in-line solution heater and temperature controller (TC-324B, Warner Instruments). A pressure ejection unit (PDES, NPI Electronics) was used to apply a single or double pulse to NMDA (1 mM, Sigma Aldrich)-containing pipettes with a 3 s interval, a pressure of 4–10 psi, and a duration of 200-600 ms. Typical pipette resistance was 2–3 MΩ. The NMDA glass pipette included an $AgCl_2$ electrode for extracellular local field potential recordings. Field potential signals were filtered at 1 kHz, amplified by an AM-1800 amplifier (AM-systems) and sampled at 10 KHz with a Digidata 1440s interface and pClamp software (version 10, Molecular Devices). Spectrograms of local field potential recording, were performed with an algorithm written in Matlab (version R2008b) using logarithmic wavelet windows.

2.12 Statistical methods

Calibration parameters were defined by global fitting to eq. 2.2 and eq. 2.3 using QtiPlot Software (http://www.qtiplot.com). Statistical tests were performed using Scipy (http://scipy.org). P-values were calculated using either the two-sample Kolmogorov-Smirnov test for statistical difference in distributions or the two-tailed Student's t test. Cumulative frequency distribution plots were prepared using Seaborn (http://stanford.edu/~mwaskom/software/seaborn).

2.13 Cell culture and calibration

HEK 293 cells and SK-N-SH cells were cultured in Dulbecco's modified Eagle's medium (DMEM) (Sigma-Aldrich) supplemented with 10% Fetal Bovine Serum (FBS) (Sigma-Aldrich), 2 mM L-glutamine (Sigma-Aldrich), 100U/mL penicillin (Sigma-Aldrich) and 100mg /mL streptomycin (Sigma-Aldrich) in a humidified 5% CO_2 incubator at 37°C. All cells were transfected using Effectene reagent (Qiagen) following manufacturer protocol. For differentiation, SK-N-SH cells were seeded to a confluence of approximately 30% in DMEM supplemented with 5% FBS, 2 mM L-glutamine, 100 U/mL penicillin, 100 mg/mL streptomycin and 10 μM retinoic acid (Sigma-Aldrich). The medium was changed every two days adding fresh retinoic acid. Differentiation was usually completed in 6 to 8 days when cell soma assumed a fusiform to triangular shape and elongation of slender neuritic processes was observed [117]. For SK-N-SH cell transfection the manufacturer protocol was adapted as follows: we doubled the amount of DNA and incubated transfection cocktail overnight in DMEM containing FBS (5%) and retinoic acid (10 μM).

Calibration in cells was realized as previously described [115]. The desired [Cl^-]

and pH were controlled by equilibrating extra- and intracellular ion concentrations using the K^+/H^+ exchanger nigericin (5 µM), the protonophore carbonyl cyanide p-chlorophenylhydrazone (CCCP) (5 µM), the K^+ ionophore valinomycin (5 µM) and the Cl^-/OH^- exchanger tributyltin chloride (10 µM) in the presence of high-K^+ 20 mM HEPES buffer containing 0.6 mM $MgSO_4$, 38 mM sodium gluconate and 100 mM potassium gluconate. Specified amount of gluconate anion was replaced by Cl^-; pH was adjusted with aliquots of NaOH. To avoid CO_2 dependent pH shifts during calibrations, cells were maintained in CO_2 free atmosphere at 37°C. Medium was replaced with proper buffer and changed five times every two minutes to ensure stabilization of intracellular ionic concentrations.

The sensor calibration is indeed one of the most critical aspects for measuring absolute changes in $[Cl^-]_i$. The precision and accuracy of measurements of $[Cl^-]_i$ are determined by the parameters set during calibration. For a discussion of alternatives procedures see [118].

2.14 Calcein-AM-based Cell Volume Measurements

Cell volume change was determined using calcein as a marker of intracellular water volume, which was established previously [119]. Briefly, cells on coverslips either coated with poly-L-lysine (50 µg/ml) (GC22) or polyornitin (50 µg/ml) and laminin (5 µg/ml) (GBM43) were incubated with 0.5 µM calcein-AM for 30 min at 37°C. The cells were placed in a heated (37°C) imaging chamber (Warner Instruments) on a Nikon Ti Eclipse inverted epifluorescence microscope equipped with perfect focus, a 40X Super Fluor oil immersion objective lens, and a Princeton Instruments MicroMax CCD camera. Calcein fluorescence was monitored using a FITC filter set (excitation 480 nm, emission 535 nm, Chroma Technology).

Images were collected every 60 sec with MetaFluor image-acquisition software (Molecular Devices). Regions of interest (0.5 μm in diameter) were selected in the cytoplasm of 5~15 cells. Baseline drift resulting from photobleaching and dye leakage was corrected as described before. The fluorescence change was plotted as a function of the reciprocal of the relative osmotic pressure and the resulting calibration curve applied to all subsequent experiments as previously described REFF(71). The HEPES buffered isotonic solution contained (in mM, pH 7.4): 100 NaCl, 5.4 KCl, 1.3 CaCl2, 0.8 MgSO4, 20 HEPES, 5.5 glucose, 0.4 NaHC03, and 70 sucrose with 310 mOsm determined using an osmometer (Advanced Instruments). Anisosmotic solutions (262 and 432 mOsm) were prepared by removal or addition of sucrose to the above solution.

2.15 Use of ClopHensor for chloride imaging in GBM cells

ClopHensor is based on a chloride-sensitive GFP and can be combined with real-time optical detection of Cl^- fluxes in living cells. Electroporation of the ClopHensor plasmid was used to induce ClopHensor expression into cultured GBM cells. Cells were maintained in a humidified atmosphere at 37 °C containing 5% CO2 during microscopy analysis. Wide field fluorescence images were acquired using a customized iMIC (Till Photonics) microscope equipped with a 0.65 NA plan-N 40X air objective (Olympus), a high stability xenon lamp and a 14-bit CCD camera (Stingray F145B-30fps, Allied Vision Technologies). Excitation filters 458/10 (Chroma), 482/18 (BrightLine HC) and 563/9 (Semrock) were mounted on the lamp fast filter switching device, and a dual channel filter set (dichroic: HC-Beamsplitter BS R488/561, emitter: Brightline HC 523/610, Semrock) was used

in the filter cube. Thus, cyan, green and red channels were respectively acquired with excitation (emission) wavelengths at 458 ± 10 (525 ± 25), 482 ± 18 (525± 25), and 563 ± 9 (610 ± 30) nm. Intracellular Cl^- concentration was measured in time-lapse from cells exposed to hypertonic stress in the following sequence: 5 min isotonic HEPES-MEM (317 mOsm), 20 min hypertonic HEPES-MEM (432 mOsm), and 10 isotonic HEPES-MEM. Cells were preincubated for 10 minutes in isotonic condition before starting time-lapse acquisition. BMT (10 μM) and AF peptide (5 μg/ml) were pre-incubated and present throughout the experiment. Solution osmolarity was measured using a cryoscopic osmometer (Osmomat 030, Gonotec GmbH). Three-channel images were acquired every 60 s and ratio analysis was performed as previously described (Sec. 2.13), where Cl^- concentration and pH are calculated from the cyan-over-red (Cl^-) and the green-over-cyan (pH) ratios.

2.16 In vivo two-photon imaging

In vivo two-photon imaging and spectroscopy were performed on a Prairie Ultima Multiphoton microscope (Prairie technologies) equipped with a mode-locked Ti:Sapphire laser (Chameleon Ultra II, Coherent). For each field, a set of images was acquired at different excitation wavelengths (ranging in number from 5 to 11). Acquisition was performed with a water immersion lens (Olympus, 60x, 1.00 NA) at a resolution of 512 x 512 pixels and at zoom 2, leading to a field of 102 x 102 μm and a nominal linear resolution of 0.2 μm per pixel. Before each imaging session we measured the power of the excitation laser at the optic bench and at the output of the objective lens at each wavelength. This conversion function is required to be able to infer the power at the sample, which is not accessible once the mouse is placed under the objective, from the power measured on the optic bench. The power was measured with a radiometer (Melles Griot). We ob-

tained imaging data by selecting the fields on the basis of the intensity of the fluorescence and of the mechanical stability of the preparation. Since the measure required the acquisition of images at different excitation wavelength, the dimensional consistency of the imaging sequence was of great importance. Time lapse imaging was performed by alternating the excitation from two Ti-Sapphire lasers (Coherent chameleon UltraII and Coherent Mira) tuned at 960 and 910 nm respectively. The polarization of the beams has been crossed by means of an half wave plate and they are steered to a polarizing beam splitter for combination. Two different sets of mirrors allow for the alignment of the beams and lenses have been used to equalize beam divergence and to ensure a similar illumination of the objective back aperture. The alternation was provided by fast electromechanical shutters controlled by an Arduino based controller synchronized to the microscope scanning unit. The resulting imaging data were analyzed by a custom ImageJ macro.

2.17 Calibration and processing of imaging data

Images were analysed with ImageJ (http://imagej.nih.gov/ij/). The images were processed as follow:

1) Dark subtraction. Dark image were acquired in both G and R channels with the excitation beam switched off. Since the dark image from a scanning microscope does not contain any spatial structure (as opposed to what happens with a CCD or CMOS sensor), the dark image was averaged and the mean value was subtracted from imaging data.

2) Flat calibration. Regardless of the quality of alignment of the optic bench, the illumination of the imaging field it is never uniform and it varies with excitation

wavelength. To compensate for this we acquired a library of flat field images that were dark subtracted, normalized to 1 and used to correct the imaging data. For each wavelength, the flat is an image obtained by the mean of 50 frames of a solution of a broadband emitting fluorophore (Rhodamine 6G, 1 µM) loaded in the spectroscopy chambers. Imaging data were therefore calibrated following the equation:

$$\mathbf{I}_{\text{cal}} = (\mathbf{I}_{\text{raw}} - dark)/\mathbf{F} \tag{2.6}$$

where *dark* is the mean dark signal and $\boldsymbol{F}$ is the dark-subtracted flat field image obtained at the same excitation wavelength and at the same scanning zoom. The ratio is computed pixel by pixel. We verified that it was critical to obtain a new flat library each time the optic bench was realigned. We noticed that the relative gain of the two acquisition channels was subject to small changes from one imaging session to the other. Of course these changes would affect both the Cl^- measurement and the correction for the emission in the G and R channels. The flat data are also used to correct for changes in the relative gain of the two detection channels.

3) Normalisation of each image to the square of the excitation power on the sample (since two-photon fluorescence is quadratic with power intensity);

4) Alignment of the images for random translations occurring during the acquisition because of motion artefacts. Normally we used the Stackreg plugin of imageJ;

5) Design of a region of interest (ROI) for each cell and measurement of the mean intensity at each wavelength. For each cell in each optical section we obtained a spectral series that was analyzed by custom software that implements the com-

putation pipeline described. Alternatively, we developed an imageJ macro that computes the maps of both pH_i and $[Cl^-]_i$ applying equations listed in Sec. 4.2.

3

Biosensor protein engineering

In this chapter various protein engineering approaches are exploited to design novel biosensors and to improve present Cl^- sensing schemes. At the molecular level the design principles of biomolecules involve fundamental principles of physical-chemistry, thermodynamics and kinetics. In particular the following specific goals are pursued: increasing GFP Cl^- affinity, reducing the pH dependence of GFP fluorescence and simplify the ratiometric measurement and calculations. New knowledge on the molecular determinants of GFP protonation were achieved along with a better description of Cl^- binding thermodynamics. The usefulness of new biosensor constructs is demonstrated in eukaryotic cells and in neurons.

This chapter is organized into three main sections encompassing: the rational design of improved GFP mutants (sec. 3.1); the screening of random GFP libraries (sec. 3.2); and a new sensing scheme based on long Stokes' shift fluorescence property (sec. 3.3).

My contribution to these work concerns the design of all single-site mutants and of all strategies for random library construction, data analysis of fluorescence spectroscopy measurements, data analysis for Cl^- and pH quantification, design of the sensors, manuscript writing and editing.

3.1 The rational mutagenesis

This work has been adapted and expanded from:

Calibration and functional analysis of three genetically encoded Cl–/pH sensors

Mukhtarov, M., Liguori, L., Waseem, T., Rocca, F., Buldakova, S., Arosio, D., and Bregestovski, P. Front. Mol. Neurosci 6, 9 (2013)

As a consequence of the cooperative binding of proton and halide ions to GFP-T203Y mutants [10,108], GFP- and YFP-based Cl^- biosensors exhibit a strong increase of the Cl^- K_d at pH values >= pK_a.

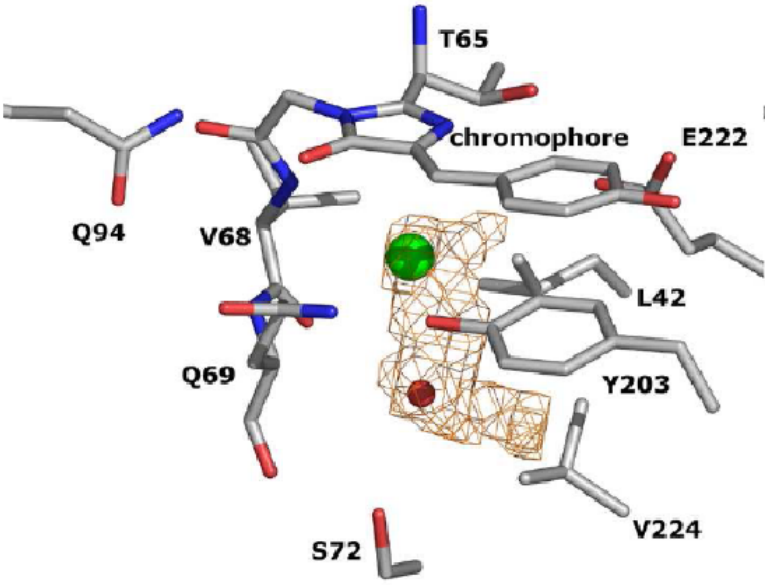

Figure 3.1: **Cl^- binding pocket** In the Cl^- binding cavity (volume 10 Å^3) a single buried water molecule is present (Wat252 in pdb:2o24; red sphere), H-bonded to the Cl^- (green sphere). V224 residue clearly localizes near the water molecule.

The X-ray structure of E^2GFP·Cl complex reveals the presence of a water molecule (Wat252 in pdb:2o24). Remarkably, the structure of the CLC chloride channel from E. coli shows that the selective flow of Cl- ions across cell membrane is due to a specific halogen binding site where the halogen is coordinated by two main-chain amide nitrogen atoms and by the side-chain oxygen atoms from a tyrosine and a serine [120]. Similar Cl^- coordination geometry can also be found in the structures of myeloperoxidase, hydrolase in the presence of a water molecule and of mymochrome IV in the absence of any water molecule. Moreover, iodide complex (pdb:2o2b) did not show the presence of any solvent molecule, possibly because of iodide ion larger size (iodide ionic radius = 2.06 Å ; chloride ionic radius = 1.67 Å). Since the affinity of E^2GFP for iodide is substantially higher than for Cl^-, we decided to determine the influence of Wat252 on the halide binding site

energetics. So, we designed the mutation V224L to reduce solvent accessibility to the E^{2}GFP halide binding cavity (Fig. 3.1) and maintaining the same charge distribution around the chromophore.

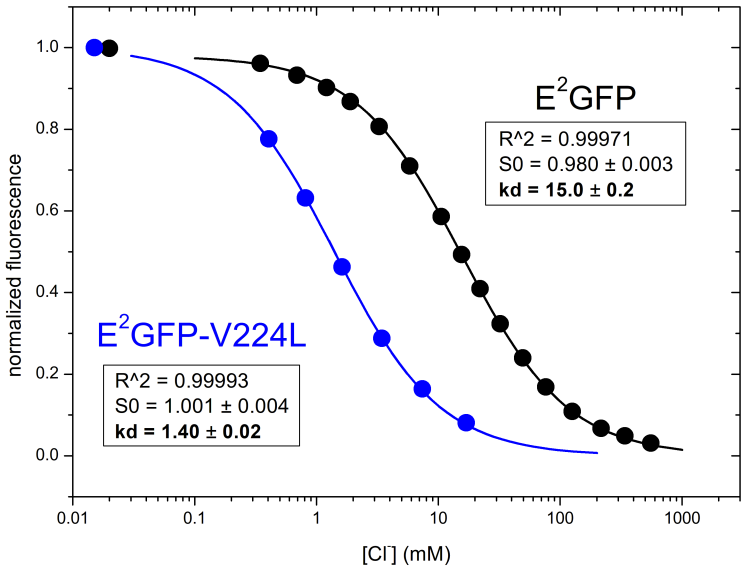

Figure 3.2: **Cl^- affinity of E^{2}GFP.** Comparison between E^{2}GFP (solid circles) E^{2}GFP-V224L (solid square) Cl^- binding curves of the fully protonated forms. Fittings to simple Langmuir isotherms are reported.

Titration measurements revealed a remarkable improvements of Cl^- affinity in the V224L variant with an improvement of one order of magnitude in the Cl^- affinity (Fig. 3.2). Fluorescence spectroscopy at various pH values also revealed a substantial effect of the V224L substitution of the chromophore protonation suggesting changes in the hydrogen bond patterns within the chromophore (Fig. 3.3).

Furthermore, Van't Hoff analysis of Cl^- binding to E^{2}GFP-V224L disclosed an entropic origin for the improved affinity. In fact, the entropy of binding increased from -0.29 cal/mol K in E^{2}GFP to -2.58 cal/mol K in the new variant, probably, as a consequence of the water molecule displacement.

We then attempted to insert a polar and longer side chain (glutamine) at the position 224. Bioinformatics structure prediction indicated a complete filling of

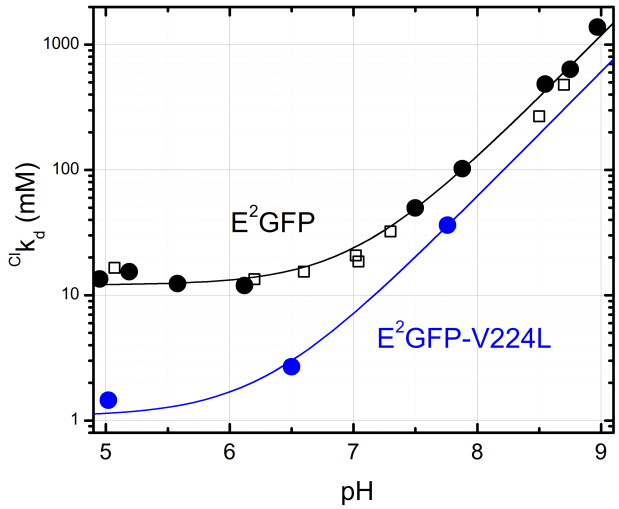

Figure 3.3: **pH dependence of Cl^- affinity for E^{2}GFP-V224L.** Cl^- dissociation constant ($^{Cl}K_d$) dependence on pH for E^{2}GFP-V224L (open blue circles) compared to E^{2}GFP. The plotted apparent K_d values are derived by fluorescence Cl^- titration experiments performed in solution at T = 37 °C, 1M ionic strength and pH values as reported on the x-axis marks.

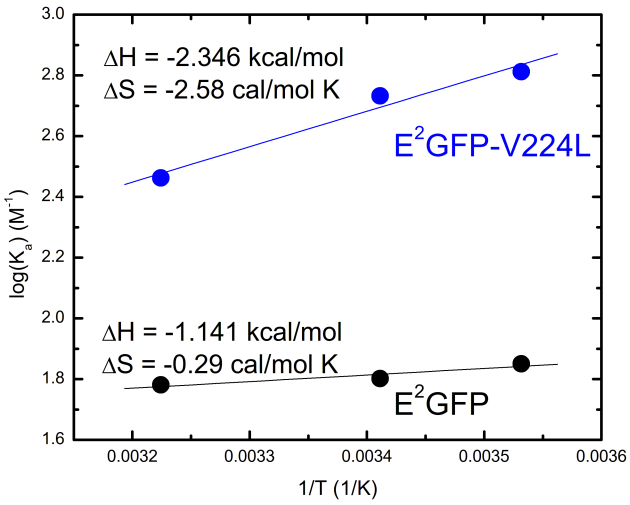

Figure 3.4: **Van't Hoff analysis of Cl^- binding to E^{2}GFP-V224L.** Van't Hoff analysis of Cl^- binding to E^{2}GFP-V224L (blue circles) and E^{2}GFP (black circles). Derived enthalpy and entropy contributions to the free energy of binding are reported.

the water-occupied volume. Although the V224Q variant was insensitive to Cl^-, its protonation pK_a was remarkably increased to a value of about 8.5, making this variant very pH-insensitive in the physiological pH range. On the basis of previous reports [121,122], we also explored the influence of the position 148, substituting the histidine with either aspartic acid or glycine in combination to either valine or leucine at the position 224. The results are summarized in Tbl. 3.1.

The combined mutations H148G and V224L exhibited high Cl^- affinity and reduced pH dependence; so, it was selected for further testing in vivo, reported in the following paper.

Table 3.1: Spectroscopic and thermodynamic properties of GFP variants.

	E^2GFP	V224L	V224Q	H148G	H148G/V224L	H148D/V224L
λ_{em} (nm)	523	515	510	518	520	520
$\lambda_{ex,neutral}$ (nm)	425	410	415	400	410	440
$\lambda_{ex,anionic}$ (nm)	510	510	510	500	510	510
$\lambda_{abs,neutral}$ (nm)	410	-	410	-	400	-
$\lambda_{abs,anionic}$ (nm)	510	-	508	-	507	-
$\lambda_{isosbestic}$ (nm)	458	-	453	493[1]	-	457[2]
pK_a	6.9 ±0.1	6.3 ±0.15	8.8 ±0.15	8.0 ±0.1	7.2 ±0.1	7.7 ±0.1
K_d (mM)	13 ± 2	1.3 ±0.2	> 1000	120 ± 8	15 ±1	280 ±45

[1] Isosbestic point in emission.
[2] In the limited pH range from 6.7 to 8.2.

frontiers in
MOLECULAR NEUROSCIENCE

METHODS ARTICLE
published: 18 April 2013
doi: 10.3389/fnmol.2013.00009

Calibration and functional analysis of three genetically encoded Cl^-/pH sensors

M. Mukhtarov[1,2], L. Liguori[3], T. Waseem[1,4], F. Rocca[3,5], S. Buldakova[1], D. Arosio[3]* and P. Bregestovski[1]*

[1] Brain Dynamics Institute, Inserm UMR1106, Aix-Marseille University, Marseille, France
[2] Laboratory of Neurobiology, Institute of Fundamental Medicine and Biology, Kazan Federal University, Kazan, Russia
[3] Institute of Biophysics, National Research Council and FBK, Trento, Italy
[4] Institute of Biophysics and Cell Engineering, National Academy of Sciences, Minsk, Belarus
[5] Physics Department, University of Trento, Trento, Italy

Edited by:
Pau Gorostiza, Catalan Institution for Research and Advanced Studies, Spain

Reviewed by:
Colin J. Akerman, University of Oxford Academic Research Fellow, UK
Alexandre Mourot, Université Pierre et Marie Curie, France

***Correspondence:**
D. Arosio, Institute of Biophysics, National Research Council and FBK, Trento, Italy.
e-mail: daniele.arosio@cnr.it;
P. Bregestovski, Brain Dynamics Institute, Inserm UMR1106, Aix-Marseille University, 27 Boulevard Jean Moulin, 13385 Marseille Cedex 05, France.
e-mail: piotr.bregestovski@univmed.fr

Monitoring of the intracellular concentrations of Cl^- and H^+ requires sensitive probes that allow reliable quantitative measurements without perturbation of cell functioning. For these purposes the most promising are genetically encoded fluorescent biosensors, which have become powerful tools for non-invasive intracellular monitoring of ions, molecules, and enzymatic activity. A ratiometric CFP/YFP-based construct with a relatively good sensitivity to Cl^- has been developed (Markova et al., 2008; Waseem et al., 2010). Recently, a combined Cl^-/pH sensor (ClopHensor) opened the way for simultaneous ratiometric measurement of these two ions (Arosio et al., 2010). ClopHensor was obtained by fusion of a red-fluorescent protein (DsRed-monomer) to the E^2GFP variant that contains a specific Cl^--binding site. This construct possesses $pK_a = 6.8$ for H^+ and K_d in the 40–50 mM range for Cl^- at physiological pH (~7.3). As in the majority of cell types the intracellular Cl^- concentration ($[Cl^-]_i$) is about 10 mM, the development of sensors with higher sensitivity is highly desirable. Here, we report the intracellular calibration and functional characterization of ClopHensor and its two derivatives: the membrane targeting PalmPalm-ClopHensor and the H148G/V224L mutant with improved Cl^- affinity, reduced pH dependence, and pK_a shifted to more alkaline values. For functional analysis, constructs were expressed in CHO cells and $[Cl^-]_i$ was changed by using pipettes with different Cl^- concentrations during whole-cell recordings. K_d values for Cl^- measured at 33°C and pH ~7.3 were, respectively, 39, 47, and 21 mM for ClopHensor, PalmPalm-ClopHensor, and the H148G/V224L mutant. PalmPalm-ClopHensor resolved responses to activation of Cl^--selective glycine receptor (GlyR) channels better than did ClopHensor. Our observations indicate that these different ClopHensor constructs are promising tools for non-invasive measurement of $[Cl^-]_i$ in various living cells.

Keywords: fluorescent biosensors, intracellular chloride, intracellular pH, non-invasive monitoring, optogenetics

INTRODUCTION

Beginning with the pioneer studies by Tsien and co-authors on measurements of intracellular calcium concentration in intact lymphocytes (Tsien et al., 1982), non-invasive monitoring of different intracellular ions (Ca^{2+}, Mg^{2+}, Cl^-, and H^+) has became a powerful direction of research for functional analysis of neurons and other cell types under normal and pathophysiological conditions.

Among several methods proposed for monitoring intracellular Cl^- concentration ($[Cl^-]_i$), the most promising is the use of genetically encoded Cl^--sensitive probes (Bregestovski et al., 2009; Mancuso et al., 2011). The first generation of probes named "Clomeleon" (Kuner and Augustine, 2000) and "Cl-Sensor" (Markova et al., 2008) was based on the Cl^--sensitive yellow-fluorescent protein (YFP) linked with Cl^--insensitive cyan-fluorescent protein (CFP), which was the reference fluorescence molecule. These indicators have opened the way for non-invasive monitoring and ratiometric measurement of $[Cl^-]_i$ in different cell types *in vitro* (Pellegrino et al., 2011; Bertollini et al., 2012; Friedel et al., 2013). Expressed in neurons of transgenic mice, they have allowed imaging of Cl^- dynamics in inhibitory circuits of different brain areas, including hippocampus, cerebellum, and deep cerebellar nuclei (Berglund et al., 2008, 2011), as well as in intact hippocampus (Dzhala et al., 2012) and a dorsal root ganglia preparation (Batti et al., 2013). Producing a construct consisting of a glycine receptor (GlyR) with Cl-Sensor incorporated into the long cytoplasmic domain (BioSensor-GlyR) provided a tool for non-invasive monitoring activity of these Cl^--selective receptor-operated channels (Mukhtarov et al., 2008).

The recently proposed combined Cl^-/pH sensor (ClopHensor) opened the way for simultaneous ratiometric measurement of these two ions (Arosio et al., 2010). ClopHensor is obtained by fusion of a red-fluorescent protein (DsRed-monomer) to the E^2GFP variant that contains a specific Cl^--binding site. This construct is particularly promising as it allows simultaneous monitoring of $[Cl^-]_i$ and intracellular pH (pH_i) in the same cells (Arosio et al., 2010; Bregestovski and Arosio, 2011; Raimondo et al., 2012). At physiological pH (~7.3), ClopHensor possesses $pK_a = 6.8$ for H^+ and K_d in the 40–50 mM range for Cl^-. As in the majority of cell types the intracellular Cl^- concentration is about 10 mM (Khirug et al., 2008; Tyzio et al., 2008; Bregestovski et al., 2009), development of sensors with higher sensitivity is necessary.

Here, we present calibration and functional analysis of ClopHensor and two of its derivatives: (i) PalmPalm-ClopHensor, which should have preferable membrane targeting and thus allow near-membrane measurement of $[Cl^-]_i$ and pH_i; and (ii) ClopHensor with mutations H148G and V224L aimed to increase the affinity of this probe for Cl^- and change the pH-sensing properties. It has been previously demonstrated that the V224L mutation increases the affinity for Cl^- by an order of magnitude (Arosio et al., 2011), while the H148G mutation increases the pK_a value by 1 pH unit in YFP (Elsliger et al., 1999) as well as in GFP (Hanson et al., 2002). Here, we combined the H148G and the V224L mutations in E^2GFP in order to: (1) shift the K_d for Cl to the lower mM range, and (2) increase the pK_a of the GFP sensing element to more alkaline values.

For these three constructs, calibrations determining their sensitivity to Cl^- and H^+ in living cells were obtained. Also presented are the distributions of these probes in cells and simultaneous recording of changes in $[Cl^-]_i$ and pH_i during activation of Cl^--selective GlyR channels.

MATERIALS AND METHODS

PRODUCING AND CLONING OF ClopHensor VARIANTS

The ClopHensor, E^2GFP-DsRedm, construct was mutated at two residues, H148G and V224L, of the GFP domain. Two sequential site-directed mutagenesis were performed using QuickChange II XL Site-Directed Mutagenesis Kit (Stratagene) following the manufacturer's protocol. Complementary primers were synthesized by Sigma-Aldrich with the following sequences: H148G-fw GAGTACAACTACAACAGCGG CAACGTCTATA TCATGG; H148G-rv CCATGATATAGACGTTGCCGCTGTTGT AGTTGTACTC; V224L-fw CTGCTGGAGTTCCTGAACGC CGCCG; V224L-rv CGGCGGCGTTCAGGAACTCCAGCAG and were used to amplify the entire plasmid in a PCR reaction using high-fidelity polymerase. To eliminate template, the PCR reaction was digested with Dpn1. The amplified mutated DNA was purified using Wizard SV Gel and the PCR Clean-up System kit (Promega), and transformed into *Escherichia coli* XL10-Gold ultracompetent cells (Novagen), which were then grown overnight on LB plates supplemented with 50 mg/l ampicillin at 37°C.

Four positive colonies were picked and grown overnight in 3 ml of LB-ampicillin at 37°C under shaking for mini prep DNA extraction (Wizard®*Plus* SV Minipreps DNA Purification; Promega). All the constructs were verified by sequencing the entire insert. Finally, plasmids used for transfection were prepared using the QIAGEN Plasmid *Plus* Maxi kit.

EXPRESSION AND PURIFICATION OF THE H148G/V224L MUTANT

The recombinant GFP variant was expressed as Strep-tagged protein in *Escherichia coli* BL21 (Novagen) and harvested 20 h after induction with 1 mM IPTG at 30°C. Purification by affinity was carried out using Strep-Tactin Superflow 5-ml cartridges (IBA, GmbH, Germany), following the manufacturer's instructions, at 4°C in an AKTA Basic10 FPLC system (GE Healthcare Europe, Milan, Italy) with continuous monitoring of optical densities at 280 nm. The use of Cl^--free buffers in the final purification step ensured the complete removal of Cl^- from the preparation. Diethanolamine (DEA; 20 mM) in 50 mM K_2SO_4 adjusted to pH 8.5 was supplemented with a cocktail of protease inhibitors (Roche). Lysis was performed with an Ultrasonic Processor (Cole Parmer) (10 cycles of 30 s, output 6W, and 10 s cooling). FPLC was performed on an AKTA Basic10 FPLC system (GE Healthcare) using a Strep-Tactin Superflow 5 ml column (IBA Technology). Filtered lysate was loaded without a loop, and the flow rate was set at 3 ml/min. Elution of bound strep-tagged GFP was obtained in 75% washing buffer 2.5 mM desthiobiotin. Protein Concentration was determined by BCA™ Protein Assay (Pierce Protein Biology Products, USA).

CELL CULTURE PREPARATION

For fluorescence analysis of $[Cl^-]_i$ and $[H^+]_i$, and also for immunocytochemistry and electrophysiology, ClopHensor constructs and human α1 GlyR subunits were expressed in CHO cells and in neurons of primary culture by means of Lipofectamin transfection.

Chinese hamster ovary (CHO-K1) cells were obtained from the American Type Tissue Culture Collection (ATCC, Molsheim, France) and maintained as previously described (Medina et al., 2000; Waseem et al., 2010). One day before the transfection, cells were plated onto coverslips (12–14 mm in diameter), which were placed inside 35-mm cell culture dishes with 2 ml of medium. CHO-K1 cells were transfected with approximately 1 μg/1μl cDNA of constructs, using the Lipofectamine 2000 transfection protocol (Life Technology, USA). Three hours after the initial exposure of the cells to the cDNAs, a fresh cDNA-containing solution replaced the old one.

Neurons of hippocampal culture from 18-day rat embryos were dissociated using trypsin and plated at a density of 70,000 cells cm^{-2} in minimal essential medium (MEM) supplemented with 10% NU serum (BD Biosciences, Le Pont de Claix, France), 0.45% glucose, 1 mM sodium pyruvate, 2 mM glutamine, and 10 IU ml^{-1} penicillin–streptomycin as previously described (Buerli et al., 2007). On days 7, 10, and 13 of culture incubation, half of the medium was changed to MEM with 2% B27 supplement (Invitrogen).

Transfections of neuronal cultures at 7–10 days *in vitro* (DIV) were performed as described previously (Buerli et al., 2007; Pellegrino et al., 2011). Cells were used in experiments 2–5 days after transfection.

INTRACELLULAR CL^- CALIBRATION OF ClopHensor VARIANTS

For Cl^- calibration we used whole-cell recordings with different Cl^- concentrations in recording pipettes. Whole-cell patch-clamp recordings on CHO cells were conducted 24–48 h after transfection, using an EPC-9 amplifier (HEKA Elektronik, Germany) at a holding potential −20 or −30 mV and at a temperature of 32–33°C. Cells were bathed in a solution containing (mM): NaCl 126; KCl 3.5; $CaCl_2$ 2; $MgCl_2$ 1.3; NaH_2PO_4 1.2; $NaHCO_3$ 25; and D-glucose 10; equilibrated at pH 7.4 with 95% O_2 and 5% CO_2; 320 mOsm. The patch pipette solution contained (mM): KCl (0–135) or K-gluconate (0–135); $MgCl_2$ 2; MgATP 2; HEPES/KOH 10; and BAPTA 1; pH 7.3, 300 mOsm. A combination of K-gluconate and KCl at a constant K^+ concentration of 135 mM were used for Cl^- calibration of ClopHensor constructs with six different Cl^- concentrations in the pipette solution ($[Cl^-]_p$): 4, 10, 20, 60, 100, and 135 mM. Calibration curves were obtained by recording from 5–7 cells for each $[Cl^-]_p$. The effectiveness of the cell dialysis and $[Cl^-]_i$ established after whole-cell penetration were checked by measurement of the reversal potential for glycine-induced currents. Glycine was applied locally using Picospritzer II (General Valve Corporation, USA) with a pipette positioned close to the soma of the recorded cell at different holding potentials.

All reagents were obtained from Sigma unless otherwise specified.

INTRACELLULAR pH CALIBRATION OF ClopHensor VARIANTS

For pH calibration b-escin permabilization method was used (Waseem et al., 2010). In more detail, a range of HEPES-based extracellular solutions (150 mM K-Gluconate, 20 mM HEPES, and 10 mM D-glucose) with different pH values was created by adding HEPES powder for acidification of the solution or 1 M NaOH for alkalization.

To increase the permeability of the cell membrane to ions, 80 μM β-escin (Sigma, St Louis, USA) was added to the bath solution. β-escin was dissolved in water and prepared freshly for each experiment. This suspension was stable for about 2 h. The coverslip with cultured cells was placed into the recording chamber and superfused with escin-containing bath solution until cells become swollen, indicating the dissipation of ion gradients and coupled membrane potential in treated cells. The perfusing solution was then switched to the escin-free bath solution in order to avoid lysis of the cells. Thereafter, the fluorescence responses of ClopHensor constructs corresponding to specified H^+ concentrations inside the cell were registered.

REAL-TIME FLUORESCENCE IMAGING

Fluorescence images were acquired using a customized digital imaging microscope. Excitation of cells at various wavelengths was achieved using a Polychrome V monochromator (Till Photonics, Germany). Light intensity was attenuated using neutral density filters. Emission wavelengths were controlled using a Lambda 10-3 controller (Sutter Instrument Company, USA). Fluorescence was visualized using an upright microscope Axioskop (Zeiss, Germany) equipped with a 60× water-immersion objective (n.a. 0.9; LumPlanFL, Olympus, USA). Fluorescent emitted light passed to a 16-bit digital camera Andor iXon EM+ (Andor Technology PLC, Northern Ireland). Images were acquired on a computer via a DMA serial transfer. All peripheral hardware control, image acquisition and image processing were achieved using Andor iQ software (Andor Technology PLC). The average fluorescence intensity of each region of interest (ROI) was measured.

Cells expressing ClopHensor variants were excited at three wavelengths: 458 and 488 nm for Cl^-/pH-sensitive E^2GFP excitation, and 545 nm for excitation of DsRed-monomer. Fluorescent signals were recorded using a dual-band GFP/DsRed 493/574 dichroic mirror (Semrock Inc., USA) and two emission filters: 535 ± 15 nm for E^2GFP emission and 632 ± 30 nm for emission of DsRed-monomer (both Chroma Technology Corporation, USA). The emission filters were mounted into the Lambda 10^{-3} Filter wheel (Sutter Instruments Company, Novato, USA).

The duration of excitation at each wavelength was usually 20 ms. The sampling interval was 5 s for the slow $[Cl^-]_i$ changes during the transition of the recorded cell in whole-cell configuration and was switched to 1 s for the fast $[Cl^-]_i$ transients in response to glycine application after establishing $[Cl^-]_i/[Cl^-]_p$ equilibrium.

IMMUNOCYTOCHEMISTRY

For immunodetection of constructs in CHO cells or hippocampal neurons, cells in culture on coverslips expressing ClopHensor or it derivatives were fixed in PFA 4% (wt/vol) in 0.1 M phosphate buffer (PBS), pH 7.4, at room temperature for 15 min. After fixation, the cells were rinsed three times in PBS. In each experimental procedure, control and experimental cells were processed together to eliminate potential bias due to inherent variations in the intensity of the immunohistochemical labeling. For further staining, neurons were pre-incubated in 4% (vol/vol) normal goat serum in PBS containing 0.5% Triton X-100 (vol/vol) for 1 h at room temperature to block secondary-antibody binding sites. Coverslips with neurons expressing ClopHensor were then incubated overnight at 4°C with rabbit anti-GFP polyclonal antibody (Invitrogen) diluted 1:4000 in PBS with 4% normal goat serum and mouse monoclonal anti-MAP2 antibodies (1:2000). Incubations with the primary antibodies were performed at room temperature and slow shaking for 1 h, then overnight at 4°C. Samples were rinsed three times in PBS. As secondary antibodies, either a Cy3-conjugated anti-rabbit IgG for detection of GFP or a Cy5-conjugated anti-mouse IgG for detection MAP2 (all 1:1500; Molecular Probes, Invitrogen) were used. Samples were then rinsed twice in PBS with one additional washing in PBS containing Hoechst 33342 (10 mg/ml; Sigma-Aldrich). Coverslips were mounted using Fluoromount™ (Sigma-Aldrich, St Louis, MO, USA).

Images were acquired using a Leica SP5C confocal microscope using 40–60× oil-immersion objectives. Micrographs shown here are digital composites of *Z*-series scans of 5–15 optical sections through a depth of 1–6 μm. Final images were constructed with ImageJ software.

In vitro ANALYSIS

In vitro characterization of H^+ and Cl^--binding properties was performed by analysing fluorescence spectra variations with a

multimodal plate reader (EnSpire; PerkinElmer) in 96-well plates. Acetic acid buffer (50 mM) was used to adjust the solution pH to around 5.2, 100 mM PBS was used for the pH range 5.2–8.0 and 20 mM DEA buffer was used for the pH range 8.0–8.5. Temperature was kept constant at 20 ± 0.5°C and fluorescence spectra were acquired with 1-nm steps. Protein concentration was always kept constant at about 1 μM throughout every pH and Cl titration.

The proton dissociation constant (pK_a) was obtained by fitting fluorescence data with the equation:

$$F = \frac{A_1 + A_2 10^{(pK_a - pH)}}{1 + 10^{(pK_a - pH)}}$$

which describes the effect of environmental proton concentration (pH) on chromophore fluorescence (F).

The chloride dissociation constant (K_d^{Cl}) was obtained by fitting data with a 1:1 Langmuir binding model (Arosio et al., 2007):

$$S = \frac{S_0 + S_1 \cdot [Cl]/K_d^{Cl}}{1 + [Cl]/K_d^{Cl}}.$$

RESULTS

DESCRIPTION OF THE CONSTRUCTS AND *in vitro* ANALYSIS

In this study we performed calibration and functional characterization of the original ClopHensor and doubly palmitoylated membrane-targeted constructs (Arosio et al., 2010), as well as a new ClopHensor variant with mutations designed to increase Cl^- affinity and shift pK_a to more alkaline values (**Figure 1B**).

ClopHensor was designed by linking two fluorescent proteins, E^2GFP ? EGFP-T203Y and DsRed-monomer by means of a flexible 20-amino-acid spacer. To target the sensor to the inner interface of the plasma membrane, we inserted the N-terminal 20 residues of GAP-43, which contain two palmitoylation sites, at the ClopHensor N-terminus (**Figure 1A**). DsRed fluorescence, which is not affected by pH or Cl^- changes, was shown to provide an excellent normalization signal leading to ratiometric Cl^- sensing, free from the influence of sensor concentration in living neurons.

Following purification of the E^2GFP-H148G-V224L mutant, Cl^--binding properties of the recombinant protein were investigated *in vitro* by measuring fluorescence spectra at constant pH and increasing Cl^- concentration, from 0 to 310 mM (**Figures 2A,B**). Because of the cooperative interaction between Cl^- and H^+ binding, Cl^- titrations were measured at various pH values (from 5.25 to 8.9) and K_d values were analyzed with an infinite cooperative model (Arosio et al., 2007; Bregestovski and Arosio, 2011) with two interacting binding sites, one for Cl^- and one for H^+:

$$K_d = \frac{K_d^0 \cdot \left(1 + 10^{(pK_a - pH)}\right)}{10^{(pK_a - pH)}}$$

containing two fitting parameters for the probe: pK_a and K_d^0, the Cl^- dissociation constant for the fully protonated form (present at pH ≤ 5).

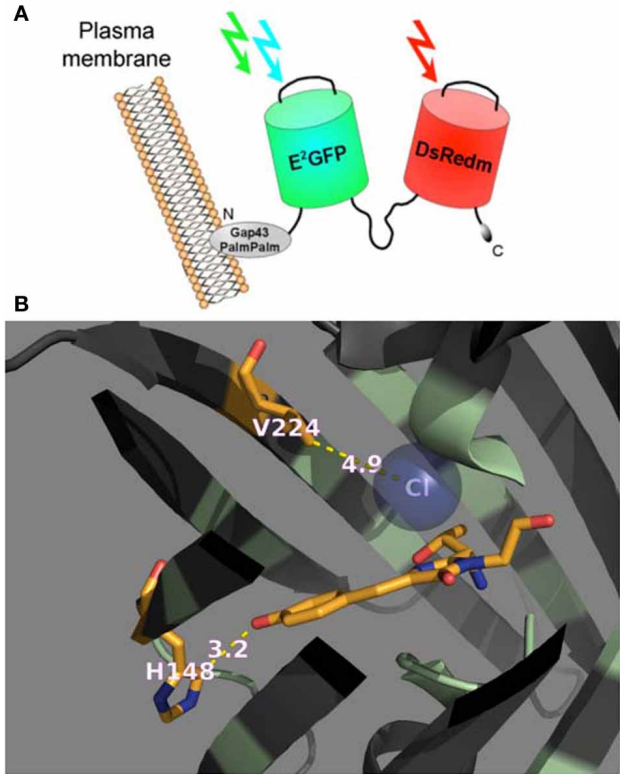

FIGURE 1 | Genetically encoded Cl^-/pH-sensors used in this study. **(A)** Schematic representation of PalmPalm-ClopHensor. **(B)** A cartoon representing the specific Cl^--binding site in the newly developed H148G/V224L/T203Y variant of E^2GFP. The residues in positions 148 and 224 as well as the chromophore are shown as stick models with the atoms colored as follow: C, orange; N, dark blue, and O, red. The Cl^- ion is shown as a sphere model in transparent blue.

The proton binding equilibrium was studied and the pK_a value was determined from spectra acquired at different pH buffer conditions, ranging from 5.25 to 8.9, in the absence of halogens (**Figures 2C,D**).

Precisely, the Cl^- and H^+ binding thermodynamic parameters for H148G/V224L were found to be $pK_a = 7.9 \pm 0.05$ (best-fit ± SD) and $K_d^0 = 19 \pm 1.5$ mM.

Overall, *in vitro* analysis at various pH and Cl^- conditions revealed that the H148G/V224L mutant is suited for Cl^- concentration measurements with reduced pH dependence in the physiological range. Indeed, in the pH range between 6.8 and 7.8 K_d changes were between 18 and 30 mM (**Figure 3**).

DISTRIBUTION OF THE CONSTRUCTS IN CELLS

To determine the intracellular distribution of ClopHensor constructs, we transiently expressed them in CHO cells and in neurons of dissociated hippocampal culture (see Materials and Methods). Expression was already observable 12 h after transfection and remained at high levels for at least 4 days. The fluorescence of the ClopHensor was distributed homogeneously throughout CHO cells (**Figures 4A,B**, *left*) and in neurons (**Figure 4C**). The fluorescence was bright with no preferential

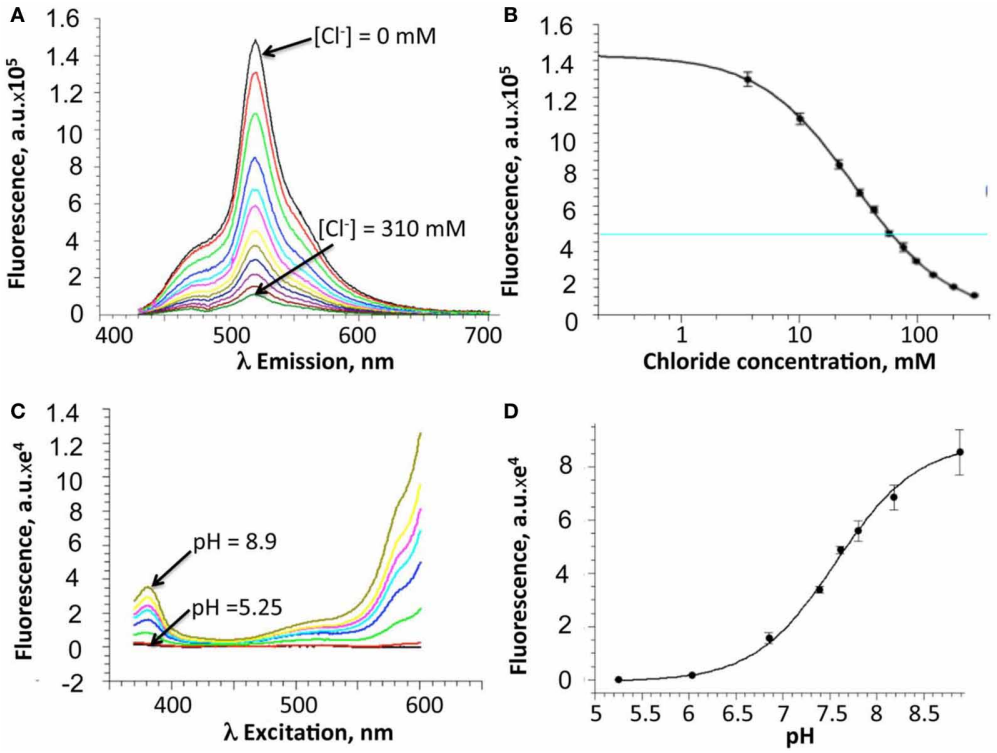

FIGURE 2 | *In vitro* properties of the H148G/V224L ClopHensor mutant. **(A)** Emission spectra at pH 7.0 for excitation at 415 nm, at increasing Cl^- concentrations from 0 mM (*top spectrum*) to 310 mM (*bottom spectrum*). Note the reduction in fluorescence intensity due to Cl^- binding-site quenching. **(B)** Dependence on Cl^- concentration of the fluorescence intensity recorded at 520 nm. **(C)** Excitation spectra, at different pH values, for emission at 520 nm, in buffer without chloride. *No isosbestic point is present.* **(D)** pH dependence of the fluorescence intensity recorded at 485 nm. For **(B)** and **(D)**, data are represented as mean ± SD from 3 independent measurements.

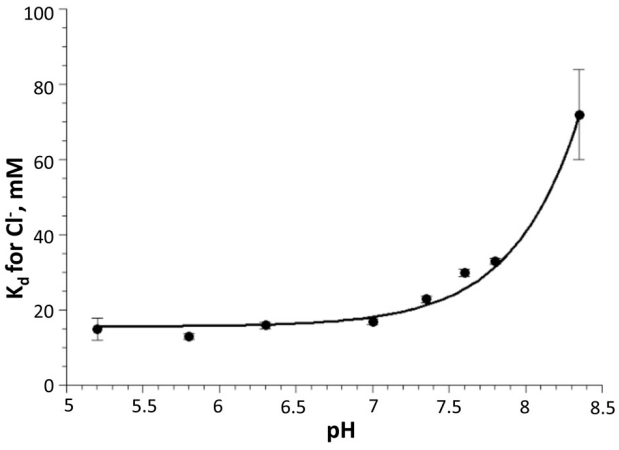

FIGURE 3 | Dependency of Cl^- dissociation constant K_d on pH for H148G/V224L mutant. Note the relatively small variations of K_d in the physiological pH range (7.0–7.5). Data are represented as mean ± SD from 3 independent measurements.

staining of membrane or intracellular organelles, as illustrated by the fluorescence profile (**Figure 4B**, *left*).

Distribution of the H148G/V224L mutant was also cytoplasmic, similar to those for ClopHensor (**Figures 4A,B**, *middle*). In contrast, the PalmPalm-ClopHensor typically showed near-membrane distribution; however, a small fraction of the probe could still be observed in the cytoplasm (**Figures 4A,B**, *right*).

These observations indicate that ClopHensor and H148G/V224L mutants exhibit cytoplasmic intracellular distributions while the PalmPalm-ClopHensor construct is typically localized to the plasma membrane and the Golgi region, as it was shown previously (McCabe and Berthiaume, 1999).

INTRACELLULAR CALIBRATION OF THE CONSTRUCTS

Calibration for Cl^-

In order to evaluate the dynamic range and sensitivity of constructs to ions, we co-expressed them in CHO cells with Cl^--selective GlyR channels and performed simultaneous monitoring of whole-cell currents and fluorescent signals. Whole-cell recordings were performed with different Cl^- concentrations in the pipette solution ($[Cl^-]_p$ = 4–135 mM). To activate GlyR channels, glycine was applied using pressure pulses. For this, a pipette containing 200 μM glycine dissolved in extracellular solution was advanced to within 30–50 μm of the recorded cell (**Figure 5A**).

For ratiometric monitoring, following the approach presented in Arosio et al. (2010) we used the ratio $R_{Cl} = F_{458}/F_{545}$ for measurement of intracellular Cl^- concentration ($[Cl^-]_i$), and for calculating intracellular pH values (pH_i) the ratio $R_{pH} = F_{488}/F_{458}$ was used.

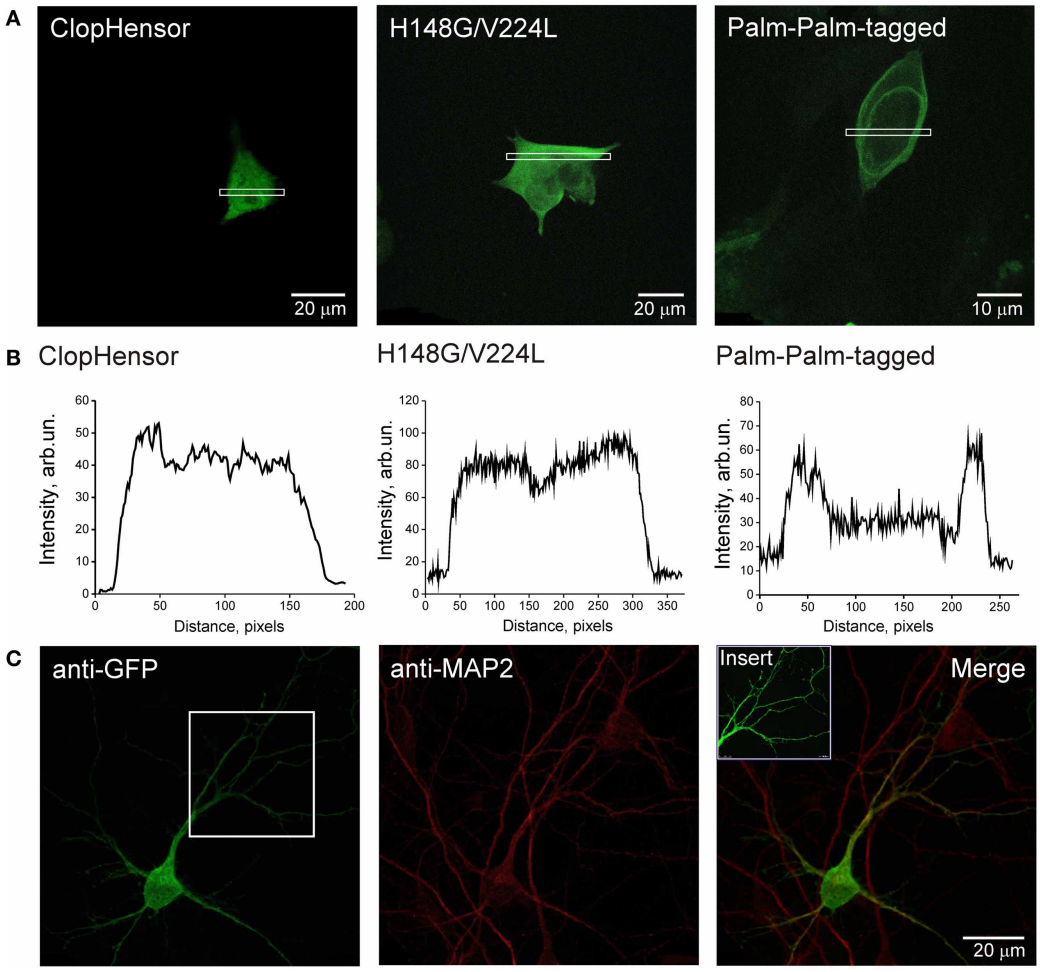

FIGURE 4 | Expression of ClopHensor and its derivatives in CHO cells and in hippocampal neurons. (A) Confocal micrographs of CHO cells expressing three genetically encoded probes and **(B)** illustrative profiles of signal intensity distribution within the corresponding selected area. Cells were transfected with ClopHensor (*left*), H148G/V224L mutant (*middle*), and PalmPalm-ClopHensor (*right*). Note the difference in distribution patterns being predominantly cytoplasmic for both the ClopHensor and H148G/V224L mutant and preferential membrane localization for PalmPalm-ClopHensor that is additionally confirmed by profiles of fluorescent signal distribution. **(C)** Confocal micrographs of ClopHensor expressed in a hippocampal neuron (DIV14). The probe spread well throughout the cell body and processes, thus providing a suitable tool for $[Cl^-]_i$ and pH_i monitoring in different regions of neurons.

Figure 5B illustrates relative changes in $[Cl^-]_i$ during whole-cell recordings from three cells, using pipettes with solutions containing different Cl^- concentrations. The graph represents changes in R_{Cl}/R_{Cl_0} with time, where R_{Cl_0} corresponds to $[Cl^-]_i$ in the cell-attached mode, i.e., to the native concentration of Cl^- in the cytoplasm of CHO cells. Obtaining the whole-cell configuration by rupturing the membrane with a pipette containing 135 mM Cl^- resulted in a strong decrease in R_{Cl}/R_{Cl_0}, corresponding to elevation of $[Cl^-]_i$. In contrast, on rupture of the membrane with the pipette containing 4 mM Cl^- an increase in R_{Cl}/R_{Cl_0} was observed. Transition to the whole-cell configuration with a pipette containing 20 mM Cl^- produced a short transient, increasing with stabilization of R_{Cl}/R_{Cl_0} at a level close to those in the cell-attached configuration. This reflects the fact that in the recorded cell the native value of $[Cl^-]_i$ in cytoplasm is close to the $[Cl^-]_p$ of 20 mM.

Simultaneous monitoring of relative pH changes (R_{pH}/R_{pH_0}) showed that after transition to the whole-cell configuration pH_i similarly decreased for all three cells recorded with different $[Cl^-]_p$ but with identical pH (**Figure 5C**).

Calibration curves for Cl^- obtained from six different $[Cl^-]_p$ in physiological conditions were best fitted by a Logistic Dose–Response Sigmoidal Fit using the OriginPro 8.5 program with the formula:

$$R_{Cl} = A2 + \frac{A1 - A2}{1 + \left(\frac{[Cl^-]i}{K_d}\right)^p}$$

where R_{Cl} is the fluorescence ratio for Cl^- (F_{458}/F_{545}), K_d is the dissociation constant for Cl^-binding, A1 and A2 are, respectively, the minimum and maximum asymptotic values of R_{Cl}, and p is the power value.

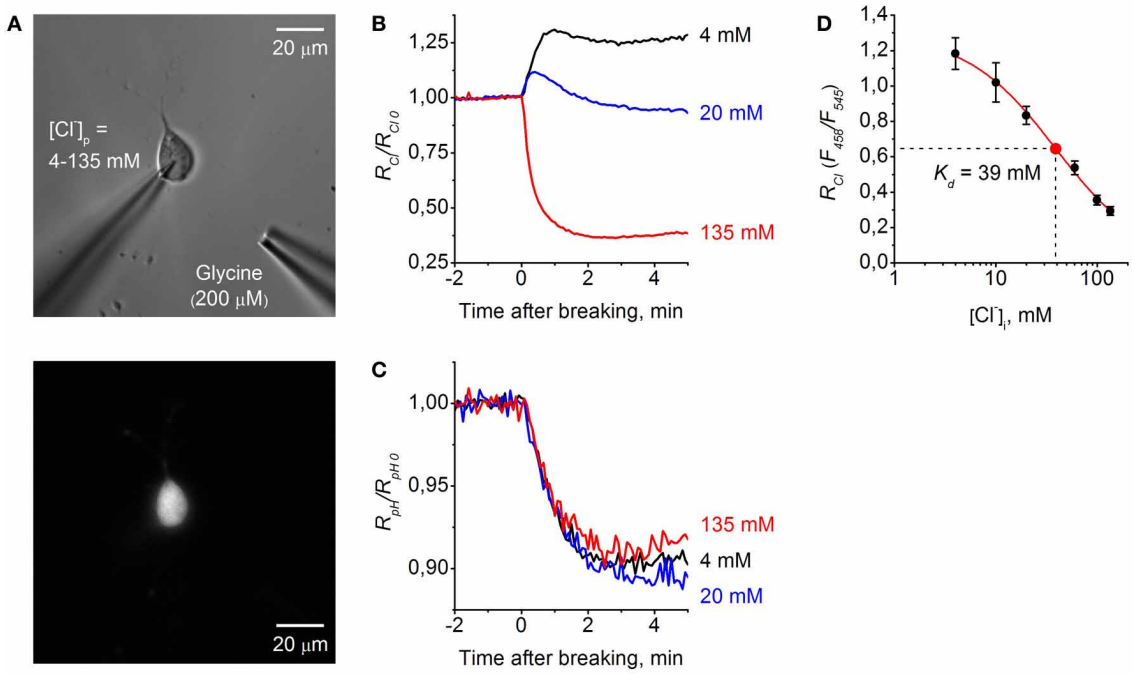

FIGURE 5 | Calibration of ClopHensor for Cl^-. (A) Micrographs of CHO cell co-transfected by ClopHensor and GlyR taken with white light (*top*) and 545 nm excitation (*bottom*). Note the patch pipette on the cell and puff pipette for glycine application at about 50 μm from the recorded cell. **(B)** Relative changes in R_{Cl} (F_{458}/F_{545}) measured in three cells during whole-cell recordings with different $[Cl^-]_p$: 4 mM (*black trace*), 20 mM (*blue trace*), and 135 mM (*red trace*). Each trace represents data from a single cell. Time = 0 corresponds to the moment the membrane breaks to give whole-cell mode. **(C)** Relative changes in R_{pH} (F_{488}/F_{458}) recorded simultaneously in the same cells as in **(B)** before and after cells transition into the whole-cell configuration. **(D)** Calibration curve for ClopHensor obtained by recording of R_{Cl} at six different $[Cl^-]_p$: 4, 10, 20, 60, 100, and 135 mM. $K_d = 38.9 \pm 6.5$ mM (mean ± s.e.m.). Data from 5–7 cells for each $[Cl^-]_p$ are presented. Note the approximately four-fold change in R_{Cl} when $[Cl^-]_i$ is adjusted from 4 to 135 mM.

From this formula we obtained the equation for $[Cl^-]_i$ values recalculation:

$$[Cl^-]_i = K_d \cdot \left(\frac{A1 - A2}{R_{\mathrm{Cl}} - A2} - 1\right)^{\frac{1}{P}}$$

For ClopHensor the values of constants obtained from fitting the curve were the following: $K_d = 38.9 \pm 6.5$ mM, A1 = 1.29, A2 = 0.01, and $p = 1$ (**Figure 5D**).

Similar analyses were performed for PalmPalm-ClopHensor and H148G/V224L mutants (**Figure 6**). They demonstrated that changes in R_{Cl}/R_{Cl_0} observed at transitions from cell-attached to whole-cell configuration in cells expressing PalmPalm-ClopHensor were similar to those for ClopHensor (**Figure 6A**). From the calibration curve for PalmPalm-ClopHensor the following fitting parameters were obtained: $K_d = 46.8 \pm 3.8$ mM, A1 = 1.15, A2 = 0.29, and $p = 1.02$ (**Figure 6B**). While this value of K_d was higher than for ClopHensor, the difference was non-significant ($P > 0.05$, *t*-Student).

For cells expressing the H148G/V224L mutant, R_{Cl}/R_{Cl_0} when recording with the pipette containing 20 mM of Cl^- was almost midway between values recorded with pipettes containing 135 and 4 mM (**Figure 6C**), suggesting higher sensitivity of the construct to Cl^-. This was confirmed by obtaining the calibration curve for the H148G/V224L mutant. The constants were the following: $K_d = 21.4 \pm 4.8$ mM, A1 = 1.58, A2 = 1.06, and $p =$ 1.51 (**Figure 6D**). Statistical analysis of K_d values for ClopHensor vs. H148G/V224L showed that they were significantly different ($P < 0.05$, *t*-Student) and for PalmPalm vs. H148G/V224L K_d values were also significantly different ($P < 0.01$, *t*-Student). The dynamic range of R_{Cl} changes for the mutant was, however, smaller than those for the ClopHensor, which reduces the benefits arising from the increased affinity.

Calibration for pH

As the H148G/V224L mutation caused a shift in the pK_a, we performed comparative pH calibrations of ClopHensor and H148G/V224L mutant. For pH calibration, the β-escin method was used (see Materials and Methods).

Sequential exchanging of bath solutions with different pH values produced corresponding shifts in the fluorescence pH ratio (**Figure 7**).

For pH calibration curves a Dose–Response Sigmoidal Fit (OriginPro 8.5) with the following formula was used:

$$R_{\mathrm{pH}} = B1 + \frac{B2 - B1}{1 + 10^{\mathrm{p}(\mathrm{p}K_a - \mathrm{pH_i})}}$$

where R_{pH} is the fluorescence ratio for pH (F_{488}/F_{458}), pK_a is the acid dissociation constant for H^+ binding, B1 and B2 are, respectively, the minimum and maximum asymptotic values of R_{pH}, and p is the power value.

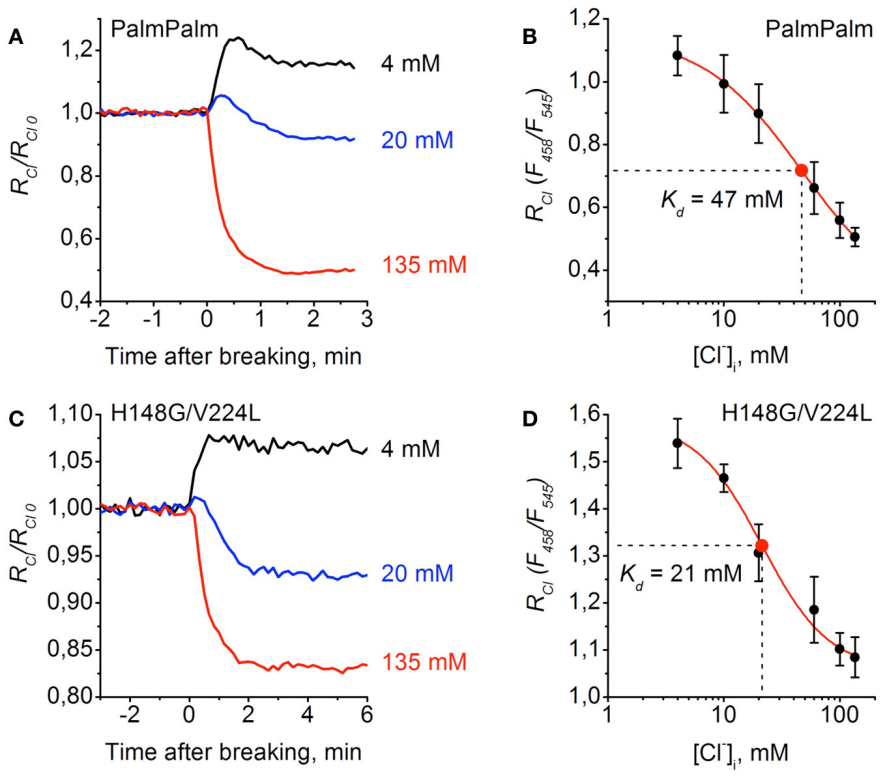

FIGURE 6 | Calibration of PalmPalm-ClopHensor and H148G/V224L mutant for Cl^-. (A) and **(C)** Relative changes in R_{Cl} (F_{458}/F_{545}) of PalmPalm-ClopHensor **(A)** and the H148G/V224L mutant **(C)** measured in three cells during whole-cell recordings with different $[Cl^-]_p$: 4 mM (*black trace*), 20 mM (*blue trace*), and 135 mM (*red trace*). Each trace represents the data from a single cell. Time = 0 corresponds to the moment the membrane breaks to give whole-cell mode. **(B)** and **(D)** Calibration curve for PalmPalm-ClopHensor **(B)** and H148G/V224L mutant **(D)** obtained by recording R_{Cl} at six different $[Cl^-]_p$: 4, 10, 20, 60, 100, and 135 mM. For PalmPalm-ClopHensor $K_d = 46.8 \pm 3.8$ mM and for H148G/V224L mutant $K_d = 21.4 \pm 4.8$ mM. Data from 5–7 cells for each $[Cl^-]_p$ are presented. Note the approximately two-fold changes in R_{Cl} for PalmPalm-ClopHensor when $[Cl^-]_i$ changed from 4 to 135 mM and the much smaller dynamic range of R_{Cl} for H148G/V224L mutant.

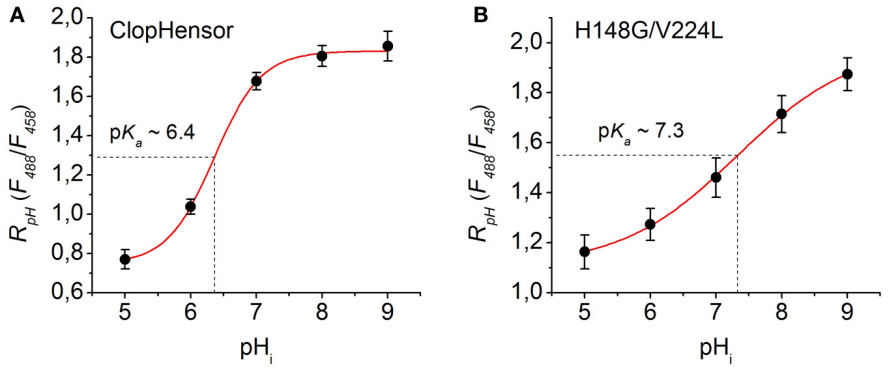

FIGURE 7 | Calibration of ClopHensor and H148G/V224L mutant for pH. (A) and **(B)** Changes in R_{pH} (F_{488}/F_{458}) of ClopHensor **(A)** and H148G/V224L mutant **(B)** measured in transfected partially permeabilized CHO cells perfused with bath medium of different pH values (see Materials and Methods for details).

From this formula we obtained the equation for pH_i values recalculation:

$$pH_i = pK_a - \frac{1}{p} \cdot \log\left(\frac{B2 - B1}{R_{pH} - B1} - 1\right)$$

Based on the fitting of the experimental curves the constants values obtained were: $pK_a = 6.36$, B1 = 0.75, B2 = 1.83, and $p = 1.21$ for ClopHensor (**Figure 7A**) and $pK_a = 7.32$, B1 = 1.11, B2 = 1.99, and $p = 0.49$ for the H148G/V224L mutant (**Figure 7B**). In comparison with ClopHensor, the dynamic range

of R_{pH} changes and the slope of the calibration curve characterizing by the constant p for the mutant were smaller, indicating its lower pH sensitivity.

Transients of $[Cl^-]_i$ and pH_i during activation glycine receptor channels

We further performed comparative analysis of the three variants of ClopHensor while monitoring $[Cl^-]_i$ and pH_i transients induced by activation of Cl^--selective GlyR channels in CHO cells.

Figure 8A illustrates changes in $[Cl^-]_i$ monitored from three CHO cells co-expressing ClopHensor with GlyR and recorded with different $[Cl^-]_p$: 4 mM (*black trace*), 20 mM (*blue trace*), and 135 mM (*red trace*). Values of $[Cl^-]_i$ recalculated from R_{Cl} (F_{458}/F_{545}) were obtained using the calibration curve in **Figure 5D**. The transition to whole-cell configuration (holding potential $V_h = -30$ mV) with a pipette containing 135 mM Cl^- caused a strong elevation of $[Cl^-]_i$. After peaking, $[Cl^-]_i$ slowly declined, presumably due to pumping out of Cl^-_i by transporters (see, for instance, Pellegrino et al., 2011) or through weakly activated Cl^--selective ionic channels (Friedel et al., 2013). Application of 200 μM glycine to the cell induced a transient decrease in $[Cl^-]_i$, the amplitude of which depended on the duration of the applied pulses of the agonist and values of V_h. The holding potential was transiently changed to the values indicated on the figure for each pulse of glycine. Application of the agonist for 1 s caused a decrease of 5–10 mM, while activation of GlyRs for 10 s resulted in decrease of about 60 mM (**Figure 8A**, *red trace*). After transiently diminishing, $[Cl^-]_i$ recovered to its initial steady-state level. Interestingly, for the cell recorded with $[Cl^-]_p = 135$ mM it was difficult to increase $[Cl^-]_i$ in conditions under which the glycine-induced current caused a strong influx of Cl^-, i.e., at $V_h = +60$ and even at +80 mV (**Figure 8A**, *asterisks*, *red trace*). In this cell the reversal potential (E_r) for I_{Gly} was about +5 mV, as predicted for symmetric intracellular–extracellular Cl^- concentrations.

Simultaneous recording of $[Cl^-]_i$ and ionic currents (**Figure 8C**) showed two main features. First, the kinetics of $[Cl^-]_i$ transients were much slower than those for glycine-induced currents. This is in accordance with previous observations from monitoring of Cl^- transients using MQAE-mediated fluorescence (Marandi et al., 2002) or BioSensor-GlyR (Mukhtarov et al., 2008). Second, $[Cl^-]_i$ amplitude increased both on elevation of the driving force for Cl^- and on prolongation of glycine applications. As illustrated in **Figure 8C**, the amplitude of $[Cl^-]_i$ transients induced by 1-s pulses of glycine increased in parallel with GlyR current amplitude at changes of V_h from −20 to 0 mV. At constant V_h (0 mV), prolongation of glycine pulses from 1 to 5 s caused an increase in $[Cl^-]_i$ amplitude although an increase in GlyR current amplitude was not observed.

When transition to whole-cell configuration ($V_h = -20$ mV) was produced with a pipette containing 20 mM Cl^- a brief transient decrease in $[Cl^-]_i$ with subsequent stabilization at a level close to that in the cell-attached configuration was observed (**Figure 8A**, *blue trace*). Even at short (100 ms) glycine applications, substantial transients in $[Cl^-]_i$, of about 5 mM, were

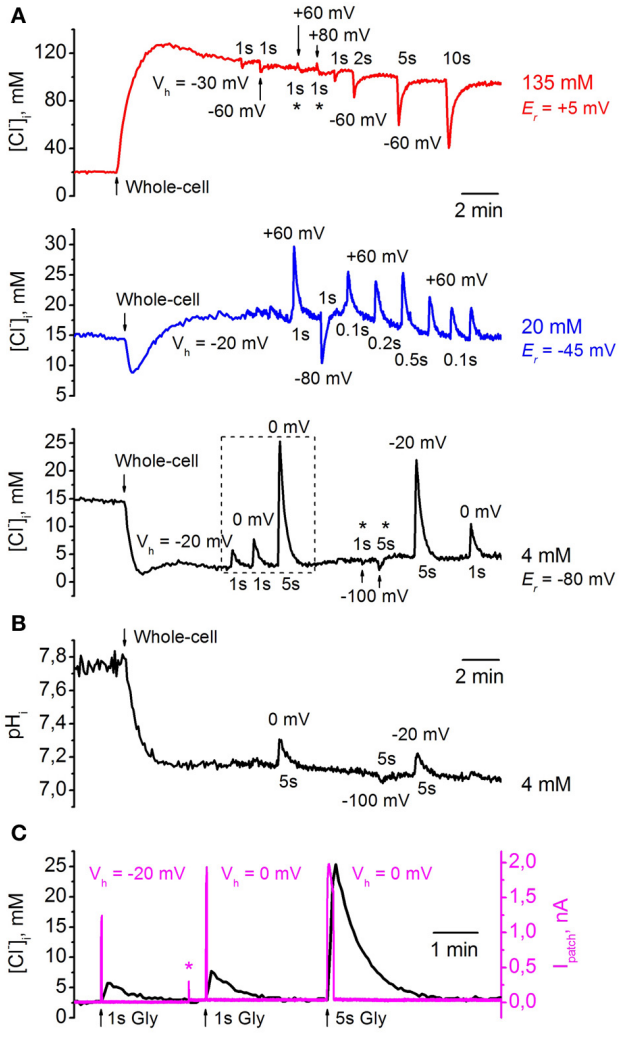

FIGURE 8 | Monitoring of transients of $[Cl^-]_i$ and pH_i during GlyR activation using ClopHensor. (A) Changes in $[Cl^-]_i$ monitored by ClopHensor in three CHO cells co-expressing GlyR and recorded with different $[Cl^-]_p$: 4 mM (*black trace*), 20 mM (*blue trace*), and 135 mM (*red trace*). Transients in $[Cl^-]_i$ on transition to whole-cell configuration and GlyR channel activation at different holding potentials (V_h) and different durations of glycine (200 μM) pulses are illustrated. Reversal potentials for glycine-induced currents (E_r) for each cell recorded with different $[Cl^-]_p$ are indicated. **(B)** Changes in pH_i monitored simultaneously with $[Cl^-]_i$ by ClopHensor in the same cell as in **(A)** (*black trace*) recorded with $[Cl^-]_p = 4$ mM. Note that only the long (5 s) glycine application produced noticeable pH_i changes of 0.1–0.2 units. **(C)** Simultaneous monitoring of whole-cell current (I_{patch}) and $[Cl^-]_i$ during glycine application in a cell co-expressing ClopHensor and GlyR and recorded with a $[Cl^-]_p$ of 4 mM. Responses from *dashed frame* in **(A)** (*black trace*) are illustrated. Note: (i) the kinetics of $[Cl^-]_i$ transients are much slower than those for corresponding glycine-induced currents (I_{Gly}); (ii) both amplitudes of I_{Gly} and $[Cl^-]_i$ changes increase with elevation of the driving force for Cl^- (recordings at $V_h = -20$ and 0 mV); (iii) $[Cl^-]_i$ amplitude increases with increasing GlyR channels activation from 1 to 5 s, while I_{Gly} amplitudes are similar ($V_h = 0$ mV). *Asterisk* on I_{patch} trace indicates the artifact when V_h changed from −20 to 0 mV. Because of the high input resistance of the cell, the steady-state shift in the current on changing the V_h is very weak in comparison with I_{Gly} amplitudes and is not visible on the record.

recorded with $V_h = +60$ mV; these reversed in direction when V_h was changed from +60 to −80 mV. E_r for glycine-induced currents in this cell was about −45 mV (**Figure 8A**, *blue trace*).

With a pipette containing 4 mM Cl^-, transition to whole-cell configuration ($V_h = -20$ mV), as predicted, caused a decrease in $[Cl^-]_i$ (**Figure 8A**, *black trace*). At $V_h = -20$ and 0 mV, application of 200 μM glycine induced strong $[Cl^-]_i$ transients whose amplitudes increased with prolongation of pulse duration; these increases were about 3–5 and 18–22 mM for glycine pulses of 1 and 5 s, respectively. Similarly to high $[Cl^-]_p$, for the cell recorded with a $[Cl^-]_p$ of 4 mM it was difficult to decrease $[Cl^-]_i$ in conditions under which glycine-induced current caused efflux of Cl^-, i.e., at $V_h = -100$ mV (**Figure 8A**, *asterisks*, *black trace*). E_r for glycine-induced currents in this cell was about −80 mV.

Simultaneous monitoring of pH_i in the same cell as that shown in **Figure 8A**, *black trace*, demonstrated a decrease in pH_i of about 0.6 units after transition to whole-cell configuration (**Figure 8B**). Values of pH_i recalculated from R_{pH} (F_{488}/F_{458}) were obtained using the calibration curve in **Figure 7A**. The changes in $[Cl^-]_i$ up to 5 mM (with 1-s glycine applications) did not produce marked changes in pH_i, while the changes in $[Cl^-]_i$ to ≥20 mM (with 5-s glycine applications) caused changes in pH_i of 0.1–0.2 units (**Figure 8B**).

These observations indicate that ClopHensor is a reliable tool for long-lasting simultaneous monitoring of intracellular Cl^- and pH in living cells.

Next we analysed the properties of ClopHensor derivatives: the membrane-targeted PalmPalm-ClopHensor and the H148G/V224L ClopHensor mutant.

Figure 9A illustrates simultaneous monitoring of $[Cl^-]_i$ (*top trace*) and pH_i (*bottom trace*) by PalmPalm-ClopHensor in CHO cells co-expressing GlyR and recorded with a $[Cl^-]_p$ of 4 mM. Values of $[Cl^-]_i$ recalculated from R_{Cl} (F_{545}/F_{458}) were obtained using the calibration curve in **Figure 6B**. The transition to whole-cell configuration ($V_h = -20$ mV) produced a decrease in $[Cl^-]_i$ similar to those monitored by ClopHensor. Short (100 ms) application of 200 μM glycine to the cell induced transient increases in $[Cl^-]_i$ that were dependent on the difference between the holding potential and the reversal potential of glycine-induced currents.

Transients in $[Cl^-]_i$ varied from about 10 mM at $V_h = 0$ mV to about 20 mM at $V_h = +60$ mV (**Figure 9A**, *top trace*). E_r for glycine-induced currents in this cell was about −75 mV. These changes were much higher than would be found when monitoring with ClopHensor at similar stimuli. This was confirmed on analysis of $[Cl^-]_i$ transients when recording from cells expressing these two sensors. As illustrated in **Figure 9B**, very similar GlyR currents induced $[Cl^-]_i$ transients whose amplitude appeared about 2.5-fold higher when monitored by PalmPalm-ClopHensor.

As the molecular organization of PalmPalm-ClopHensor is identical to that of ClopHensor, the recalculation of pH_i values from R_{pH} (F_{488}/F_{458}) was done using the calibration curve in **Figure 7A**. Similarly, after transition to whole-cell configuration, pH_i decreased by about 0.5 units (**Figure 9A**, *bottom trace*). Very weak pH_i transients were observed (**Figure 9A**, *bottom trace*) with short (100 ms) glycine applications even at $V_h = +60$ mV, while the transient increase in $[Cl^-]_i$ in this cell was about 20 mM (**Figure 9A**, *top trace*).

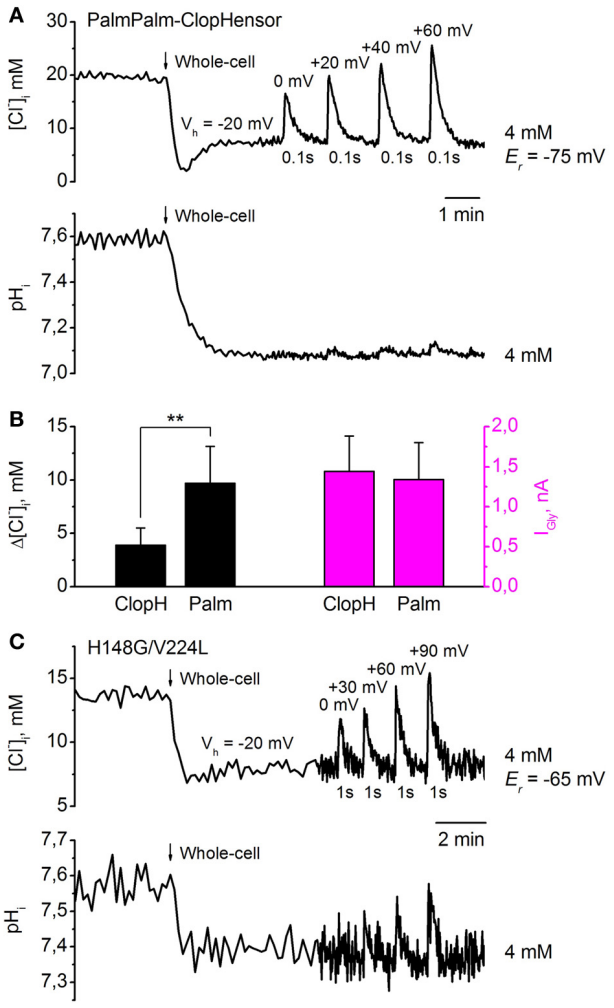

FIGURE 9 | Monitoring of transients in $[Cl^-]_i$ and pH_i in response to GlyR activation, using PalmPalm-ClopHensor and the H148G/V224L mutant. (A) Changes in $[Cl^-]_i$ (*top trace*) and pH_i (*bottom trace*) monitored simultaneously by PalmPalm-ClopHensor in a CHO cell co-expressing GlyR and recorded with $[Cl^-]_p = 4$ mM. Transients in $[Cl^-]_i$ and pH_i upon whole-cell penetration and GlyR activation by pressure application of 200 μM glycine to the cell at different V_h and 100 ms duration of agonist application are illustrated. The reversal potential for glycine-induced currents (E_r) is indicated. Note the very small pH_i changes at short (100 ms) glycine application (*bottom trace*). **(B)** Averaged glycine-induced current (I_{Gly}) amplitudes (*magenta columns, right*) and corresponding $[Cl^-]_i$ changes (*black columns, left*) in response to 1-s glycine applications. Whole-cell recordings from CHO cells with pipettes containing $[Cl^-]_p = 4$ mM. Cells expressed either ClopHensor (*ClopH*) or PalmPalm-ClopHensor (Palm). Note that for very similar I_{Gly}, transients of $[Cl^-]_i$ are about 2.5-fold higher when monitored by PalmPalm-ClopHensor than by ClopHensor. Data from seven cells for each sensor are illustrated. $^{**}P < 0.01$ (ANOVA). **(C)** Changes in $[Cl^-]_i$ (*top trace*) and pH_i (*bottom trace*) monitored by the H148G/V224L mutant of ClopHensor in a CHO cell co-expressing GlyR and recorded with a $[Cl^-]_p$ of 4 mM. Transients in $[Cl^-]_i$ upon whole-cell penetration and GlyR activation by pressure application of 200 μM glycine to the cell at different V_h and 1-s duration of agonist application are illustrated. Note the evident pH_i changes of about 0.1 units only under conditions of substantial difference between V_h and E_r and relatively long (1-s) glycine application. Different baseline noise in the two traces resulted from changes in acquisition frequency from 0.2 to 1 Hz.

When the H148G/V224L mutant of ClopHensor was co-expressed with GlyR in CHO cells recorded with $[Cl^-]_p = 4$ mM, a decrease in $[Cl^-]_i$ on transition to whole-cell configuration ($V_h = -20$ mV) was also observed (**Figure 9C**, *top trace*). Values of $[Cl^-]_i$ recalculated from $R_{Cl}(F_{545}/F_{458})$ were obtained using the calibration curve in **Figure 6D**. Again, glycine-induced transient increases in $[Cl^-]_i$ depended on the difference between V_h and E_r. Transients in $[Cl^-]_i$ with 1-s glycine application varied from about 5 mM at $V_h = 0$ mV to about 10 mM at $V_h = +90$ mV. E_r for glycine-induced currents in this cell was about −65 mV.

Simultaneous monitoring of pH_i in the same cell reveal that the $[Cl^-]_i$ transients below 5 mM did not produce marked changes in pH_i. The recalculation of pH_i values from $R_{pH}(F_{488}/F_{458})$ was done using the calibration curve in **Figure 7B**. An evident pH_i increase (of about 0.1 units) was recorded only when there was a substantial difference between V_h and E_r and relatively long (1-s) glycine application, which induced a $[Cl^-]_i$ elevation of about 10 mM (**Figure 9C**, *bottom trace*).

These results demonstrate that PalmPalm-ClopHensor, which has preferable membrane targeting, could be of interest for near-membrane measurement of intracellular Cl^- and pH changes. Another construct, the H148G/V224L mutant of ClopHensor, with a higher affinity for Cl^-, possesses the smallest dynamic range of R_{Cl} (F_{458}/F_{545}) changes and this could be a limiting factor in some cases due to lower signal/noise ratio.

DISCUSSION

Development of genetically encoded probes for non-invasive monitoring of ions and protein function has opened powerful routes for the analysis of a variety of physiological problems and functions of various cell types under different experimental conditions. These probes are non-toxic, capable of remaining stable in cells for a long time, can be expressed in specific cellular compartments and are suitable for production of transgenic models.

Here, we describe the calibration in living cells, the cytoplasmic distribution, and examples of simultaneous monitoring of intracellular Cl^- and H^+ of three genetically encoded sensors: (1) ClopHensor; (2) its variant designed to have preferential membrane targeting due to the addition to the N-terminus of a short peptide containing two palmitoylation sites (PalmPalm-ClopHensor) (Arosio et al., 2010), and (3) ClopHensor containing mutations of E^2GFP (H148G/V224L) aimed at increasing the Cl^- affinity of the sensor.

Following transient expression in CHO cells, ClopHensor and the H148G/V224L mutant exhibit cytoplasmic intracellular distribution while the PalmPalm-ClopHensor construct, as expected, is preferentially localized in the vicinity of membranes. Upon transfection of rat dissociated hippocampal cultures with cDNA of ClopHensor, the probe shows a strong cytoplasmically distributed fluorescence in the soma and neuronal processes. These observations indicate that all three sensors can be easily expressed in various cell types and detected in different, even very small, areas of cells.

Calibration analysis performed on CHO cells using patch pipettes containing different concentrations of Cl^-, and also β-escin permeabilization with bath medium having different pH (Waseem et al., 2010) revealed that the constructs exhibit different sensitivity to Cl^- and H^+. While ClopHensor and PalmPalm-ClopHensor probes demonstrated K_d for Cl^- of about 40 mM, for the H148G/V224L mutant this value was about 20 mM, indicating its higher affinity. However, the mutant exhibits a smaller dynamic range of R_{Cl}, which could be a limiting factor for monitoring Cl^- in cells containing low $[Cl^-]_i$ or with small changes in Cl^- concentration. Poor dynamic range could be, at least partially, explained by different spectral properties of H148G/V224L mutant (**Figures 2A,C**) from those for ClopHensor (Arosio et al., 2010). In the present study, for all constructs including the H148G/V224L mutant, the calibration measurements were performed using the same excitation wavelengths, GFP/DsRed dichroic mirror and emission filters (see Materials and Methods). We suggest that this range can be considerably extended in the future by better selection of excitation and emission parameters.

Calibration of pH in CHO cells using the β-escin method showed that the pK_a for the H148G/V224L mutant is strongly shifted to alkaline values. This is consistent with *in vitro* measurements: $pK_a = 7.9 \pm 0.05$. *In vitro* analysis also demonstrated that K_d for Cl^- of the H148G/V224L mutant exhibits relatively small pH dependency over a wide pH range: from about 18 mM at pH 6.5 to about 30 mM at pH 7.8. This suggests that the H148G/V224L mutant is a useful tool for $[Cl^-]_i$ measurements in experimental models with high pH variations.

Our previous observations demonstrated that when using the CFP/YFP-based Cl-Sensor, long or frequent acquisition causes strong "bleaching" of Cl^--sensitive YFP resulting in changes in fluorescence parameters during ratiometric measurement of $[Cl^-]_i$. This problem is discussed in detail in the paper by Friedel et al. (2013, this issue). In contrast, E^2GFP-DsRedm-based ClopHsensor exhibits remarkable stability (see, for instance, **Figures 8**, **9**), providing an excellent tool for long-lasting reliable monitoring and with variable acquisition rate.

Our observations of the effects of activation of Cl^--selective GlyR channels on $[Cl^-]_i$ indicate that it is a highly dynamic parameter, which can be strongly changed by over-activation of Cl^--selective channels or activity of other proteins involved in regulation and determination of physiological $[Cl^-]_i$ in living systems. Indeed, activation of GlyRs for several seconds caused changes in $[Cl^-]_i$ of more than 10–20 mM (**Figures 8**, **9**).

Together our experiments demonstrate that these three ClopHensor constructs are suitable tools for stable, long-lasting, non-invasive monitoring of $[Cl^-]_i$ and pH_i in different cell types.

ACKNOWLEDGMENTS

We are grateful to Dr. Paul A. Heppenstal for critical reading of the manuscript. This study was supported for M. Mukhtarov by the European Union Seventh Framework Programme under grant agreement no. HEALTH-F2-2008-202088 ("Neurocypres" Project), for L. Liguori by Telethon n. GGP10138D and for T. Waseem by Federation of European Biochemical Societies (FEBS) Short Term Fellowship.

REFERENCES

Arosio, D., Beltram, F., Ricci, F., and Marchetti, L. (2011). Novel pH- and anion concentration-responsive GFP mutant, a chimeric protein comprising such a mutant and a method for the combined assaying of the pH and anion concentration. *Eur. Pat. Appl.* 08165 522.7–1212.

Arosio, D., Garau, G., Ricci, F., Marchetti, L., Bizzarri, R., Nifosì, R., et al. (2007). Spectroscopic and structural study of proton and halide ion cooperative binding to gfp. *Biophys. J.* 93, 232–244.

Arosio, D., Ricci, F., Marchetti, L., Gualdani, R., Albertazzi, L., and Beltram, F. (2010) Simultaneous intracellular chloride and pH measurements using a GFP-based sensor. *Nat. Methods* 7, 516–518.

Batti, L., Mukhtarov, M., Audero, E., Ivanov, A., Paolicelli, R., Zurborg, S., et al. (2013). Transgenic mouse lines for non-invasive ratiometric monitoring of intracellular chloride. *Front. Mol. Neurosci.*

Berglund, K., Kuner, T., Feng, G., and Augustine, G. J. (2011). Imaging synaptic inhibition with the genetically encoded chloride indicator Clomeleon. *Cold Spring Harb. Protoc.* 2011, 1492–1497.

Berglund, K., Schleich, W., Wang, H., Feng, G., Hall, W. C., Kuner, T., et al. (2008). Imaging synaptic inhibition throughout the brain via genetically targeted Clomeleon. *Brain Cell Biol.* 36, 101–118.

Bertollini, C., Murana, E., Mosca, L., D'Erme, M., Scala, F., Francioso, A., et al. (2012) Transient increase in neuronal chloride concentration by neuroactive aminoacids released from glioma cells. *Front. Mol. Neurosci.* 5:100. doi: 10.3389/fnmol.2012.00100

Bregestovski, P., and Arosio, D. (2011). "Green fluorescent protein-based chloride ion sensors for *in vivo* imaging," in *Fluorescent Proteins, Springer Ser Fluoresc*, ed G. Jung (Berlin, Heidelberg: Springer-Verlag), 90–124.

Bregestovski, P., Waseem, T., and Mukhtarov, M. (2009). Genetically encoded optical sensors for monitoring of intracellular chloride and chloride-selective channel activity. *Front. Mol. Neurosci.* 2:15. doi: 10.3389/neuro.02.015.2009

Buerli, T., Pellegrino, C., Baer, K., Lardi-Studler, B., Chudotvorova, I., Fritschy, J. M., et al. (2007). Efficient transfection of DNA or shRNA vectors into neurons using magnetofection. *Nat. Protoc.* 2, 3090–3101.

Dzhala, V., Valeeva, G., Glykys, J., Khazipov, R., and Staley, K. (2012). Traumatic alterations in GABA signaling disrupt hippocampal network activity in the developing brain. *J. Neurosci.* 32, 4017–4031.

Elsliger, M. A., Wachter, R. M., Hanson, G. T., Kallio, K., and Remington, S. J. (1999) Structural and spectral response of green fluorescent protein variants to changes in pH. *Biochemistry* 38, 5296–5301.

Friedel, P., Bregestovski, P., and Medina, I. (2013). Improved method for efficient imaging of intracellular Cl^- with Cl^- Sensor using conventional fluorescence set up. *Front. Mol. Neurosci.* 6:7. doi: 10.3389/fnmol.2013.00007

Hanson, G. T., McAnaney, T. B., Park, E. S., Rendell, M. E., Yarbrough, D. K., Chu, S., et al. (2002). Green fluorescent protein variants as ratiometric dual emission pH sensors. 1. Structural characterization and preliminary application. *Biochemistry* 41, 15477–15488.

Khirug, S., Yamada, J., Afzalov, R., Voipio, J., Khiroug, L., and Kaila, K. (2008). GABAergic depolarization of the axon initial segment in cortical principal neurons is caused by the Na-K-2Cl cotransporter NKCC1. *J. Neurosci.* 28, 4635–4639.

Kuner, T., and Augustine, G. J. (2000). A genetically encoded ratiometric indicator for chloride: capturing chloride transients in cultured hippocampal neurons. *Neuron* 27, 447–459.

Mancuso, J. J., Kim, J., Lee, S., Tsuda, S., Chow, N. B., and Augustine, G. J. (2011). Optogenetic probing of functional brain circuitry. *Exp. Physiol.* 96, 26–33.

Marandi, N., Konnerth, A., and Garaschuk, O. (2002). Two-photon chloride imaging in neurons of brain slices. *Pflugers Arch.* 445, 357–365.

Markova, O., Mukhtarov, M., Real, E., Jacob, Y., and Bregestovski, P. (2008). Genetically encoded chloride indicator with improved sensitivity. *J. Neurosci. Methods* 170, 67–76.

McCabe, J. B., and Berthiaume, L. G. (1999). Functional roles for fatty acylated amino-terminal domains in subcellular localization. *Mol. Biol. Cell* 10, 3771–3786.

Medina, I., Krapivinsky, G., Arnold, S., Kovoor, P., Krapivinsky, L., and Clapham, D. E. (2000). A switch mechanism for G beta gamma activation of I(KACh). *J. Biol. Chem.* 275, 29709–29716.

Mukhtarov, M., Markova, O., Real, E., Jacob, Y., Buldakova, S., and Bregestovski, P. (2008). Monitoring of chloride and activity of glycine receptor channels using genetically encoded fluorescent sensors. *Philos. Transact. A Math. Phys. Eng. Sci.* 366, 3445–3462.

Pellegrino, C., Gubkina, O., Schaefer, M., Becq, H., Ludwig, A., Mukhtarov, M., et al. (2011) Knocking down of the KCC2 in rat hippocampal neurons increases intracellular chloride concentration and compromises neuronal survival. *J. Physiol.* 589, 2475–2496.

Raimondo, J. V., Irkle, A., Wefelmeyer, W., Newey, S. E., and Akerman, C. J. (2012). Genetically encoded proton sensors reveal activity-dependent pH changes in neurons. *Front. Mol. Neurosci.* 5:68. doi: 10.3389/fnmol.2012.00068

Tsien, R. Y., Pozzan, T., and Rink, T. J. (1982) Calcium homeostasis in intact lymphocytes: cytoplasmic free calcium monitored with a new, intracellularly trapped fluorescent indicator. *J. Cell Biol.* 94, 325–334.

Tyzio, R., Minlebaev, M., Rheims, S., Ivanov, A., Jorquera, I., Holmes, G. L., et al. (2008). Postnatal changes in somatic gamma-aminobutyric acid signalling in the rat hippocampus. *Eur. J. Neurosci.* 27, 2515–2528.

Waseem, T., Mukhtarov, M., Buldakova, S., Medina, I., and Bregestovski, P. (2010). Genetically encoded Cl-Sensor as a tool for monitoring of Cl-dependent processes in small neuronal compartments. *J. Neurosci. Methods* 193, 14–23.

Conflict of Interest Statement: The authors declare that the research was conducted in the absence of any commercial or financial relationships that could be construed as a potential conflict of interest.

Received: 01 February 2013; accepted: 02 April 2013; published online: 18 April 2013.

Citation: Mukhtarov M, Liguori L, Waseem T, Rocca F, Buldakova S, Arosio D and Bregestovski P (2013) Calibration and functional analysis of three genetically encoded Cl^-/pH sensors. Front. Mol. Neurosci. ***6****:9. doi: 10.3389/fnmol.2013.00009*

3.2 Random mutagenesis

Here, through a combination of random and targeted site-saturation mutagenesis and accumulating beneficial mutations over multiple generations, we developed novel chloride-sensitive GFP variants with high pK_a values, of about ≥ 8.0. Random GFP library were iteratively produced following random mutagenesis by error-prone PCR [123,124]. We then set up protocols and analysis pipeline for the screening of GFP variants based on their pK_a, Cl^- K_d and fluorescence properties (Fig. 3.5).

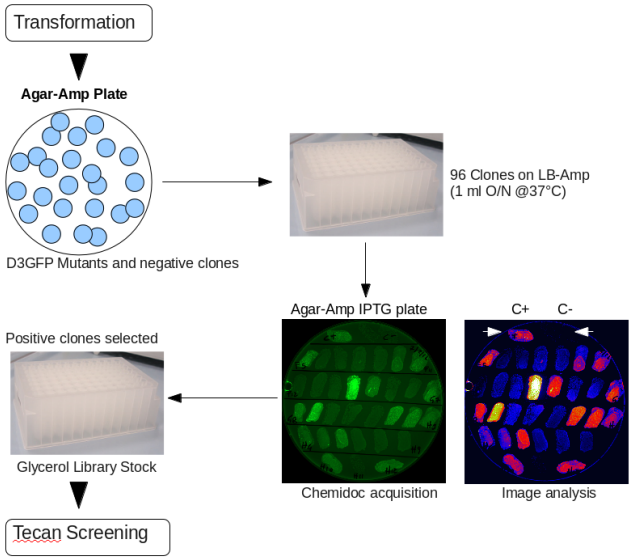

Figure 3.5: **Schematic diagram of the random mutagenesis screening.** Following transformation selected colonies were picked and grown overnight at 37°C in 1 ml LB-Amp. Bacteria (from each well) were then spread on LB-AMP-IPTG plate and grown for 24 hours at 30°C. Only brightly fluorescent clones were grown, stored and purified for automated measurement of pK_a and Cl^- K_d.

We aimed to produce library of GFP variants carrying 1-3 mutations. To this aim we optimized the use of the GeneMorph® II Random Mutagenesis Kit (Stratagene, La Jolla, CA) by testing various amount of template DNA (from 0.5 to 240 ng) and various number of PCR amplification cycles (from 25 to 35). We adopted 5 ng of template DNA and 30 PCR cycles as reported in Tbl. 3.2. PCR primers were designed for cloning into the pPR-IBA2 vector (IBA, Germany): **NdeI-fw** CGC-

CATATGgctagctggagccacc (25 bp; 66 °C) and **HindIII-rv** GGGAAGCTTagttagaTATCACTTGTACAGC (28 bp; 64 °C). Details can be found in Sec. 2.5.

Table 3.2: PCR program for random mutagenesis.

number of cycles	T °C	duration
1	95	20 min
30	95	30 sec
	62	30 sec
	72	3 min
1	72	10 min

After transformation, colonies were picked and grown in 1 ml LB-Amp at 37°C under shacking overnight in a 96 deep well plate. Positive (E^2GFP clone) and negative (empty vector clone) controls were added. Few micro liters from each well were then spread on a LB-amp-IPTG 0.1 mM agar plate and incubated 24 hours at 30°C to induce protein expression in BL21 cells. Various degree of fluorescence brightness were observed. Clones with fluorescence intensity higher than the negative controls were selected and incubated in 1 ml LB-Amp into a new 96 deep well plate for storage at -80°C upon addition of 50% Glycerol.

After expression, libraries were purified using Strep-Well HT 50 purification plates ("IBA", Germany) and a Tecan EVO 200 robot (Sec. 2.6) with an average yield of about 2 ug of protein per well. Libraries of purified GFP variants were then assayed for determining the chromophore protonation pK_a and possibly in the same plate for the Cl^- dissociation constant K_d.

To cover the pH range from 9.0 to about 5.0, we screened various buffer systems for reproducibility and identified the following buffer being able to maintain stable

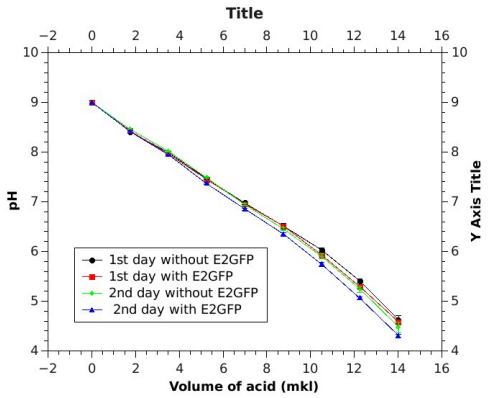

Figure 3.6: **Stability of buffer for automated pH titration assay.** Reproducibility of pH values upon addition of 2 ul 1.9% sulfuric acid into 100 ul buffer: 50 mM Tris base, 50 mM Bis Tris, 25 mM citric acid, 1 mM EDTA, 2.5 mM dDTB, 150 mM Na_2SO_4. Titrated pH values were stable over day and independent of the presence of protein in solution.

pH values upon addition of small aliquots of 1.9% sulfuric acid in the desired range over days (Fig. 3.6). Composition of the starting buffer at pH=9.0 was: 50 mM Tris base, 50 mM Bis Tris, 25 mM citric acid, 1 mM EDTA, 2.5 mM dDTB, 150 mM Na2SO4.

Fluorescence pH-titrations were collected at 2 excitation band peaked at 400 and 485 nm using a filter based plate reader (Sec. 2.6). Titration data were extracted and analysed using a software pipeline (source code available in a Bitbucket repository https://bitbucket.org/darosio/prtecan). A representative pH-titration example is reported in Fig. 3.7 and the Cl^--titration for the same well in Fig. 3.8.

Fig. 3.9 compares results between a library produced at the beginning and one produced after few rounds of random-mutagenesis improvement of GFP variant pK_a.

The best hits from our analyses were sent for sequencing and results are summarized in Tbl. 3.3. Interestingly, our approach identified mutation at position

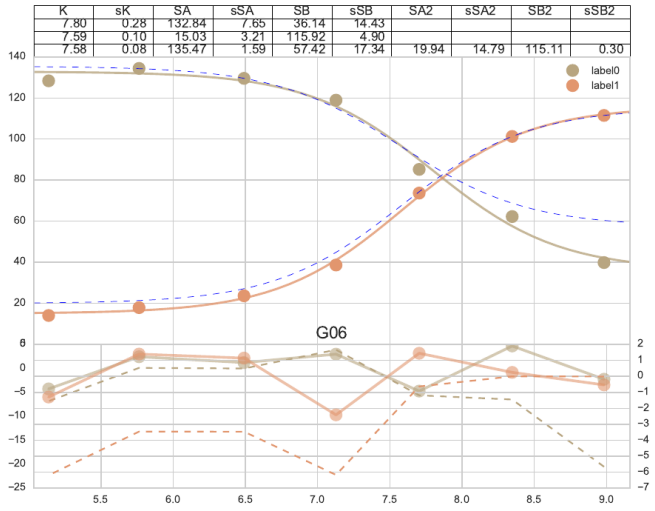

Figure 3.7: **Automated pH-titration analysis.** Titration data collected using 2 excitation bands peaked at 400 (label0) and 485 (label1) nm. Data were subtracted for average buffer fluorescence intensity and corrected for dilution generated by titrating additions. Fit to the single band data are reported (solid colored lines) using the following equation: $S = \frac{S_B + S_A 10^{pK_a - pH}}{1 + 10^{pK_a - pH}}$. Global fitting to both dataset for estimating a global pK_a parameter is also reported (dashed blue lines).

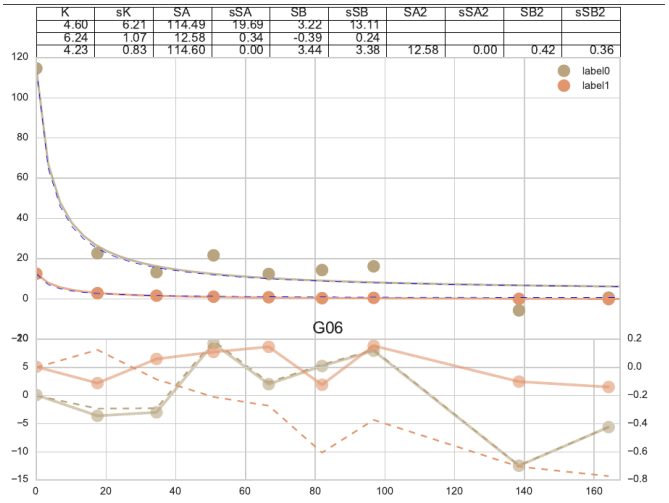

Figure 3.8: **Automated Cl-titration analysis.** Titration data collected using 2 excitation bands peaked at 400 (label0) and 485 (label1) nm. Data were subtracted for average buffer fluorescence intensity and corrected for dilution generated by titrating additions. Fit to the single band data are reported (solid colored lines) using the following equation: $S = \frac{S_A + S_B [Cl]/K_d}{1 + [Cl]/K_d}$. Global fitting to both dataset for estimating a global K_d parameter is also reported (dashed blue lines).

69 lowering the pK_a value in agreement to published results for citrine fluorescent protein [88]. To confirm pK_a and K_d results (from the automated screening analysis) and to assess other spectral and biophysical properties, protein purification of the best candidate was scaled up. An aliquot of BL21 cells, stocked in glycerol, corresponding to the clones of interest were first grown in 2 ml of LB medium-Amp at 37 °C overnight and then protein production induced in 250 ml cultures. For this cases, Tbl. 3.3 reports also pK_a values measured at 20 and 37 °C.

Table 3.3: Selected hits from the random mutagenesis.

template	well	lib	pKa	Kd (mM)	mutations
E2GFP-S202N	A04	1	6.4 ± .8		T65S M153R
	A10	1	6.9 ± .7		D46E G61D V68M A206V
	B06	1	6.8 ± .7		D173E S205T
	G09	1	6.9 ± .5		S2G
	H11	1	7.1 ± .2		E6K
E2GFP-S202N	D03	2	6.8 ± .2		D190V
E2GFP-S202N	A08	3	7.0 ± .1	6.1 ± 0.2	V93I
	B03	3	6.8 ± .1	8.8 ± 0.3	N144K
	B09	3	7.0 ± .1	9.1 ± 1.0	N149D

template	well	lib	pKa	Kd (mM)	mutations
	D09	3	6.8 ± .1	9.4 ± 0.2	S2I
	F09	3	6.6 ± .1	10.0 ± 1.1	I167T D197N
	G09	3	6.9 ± .2	5.0 ± 0.1	V16I
	G10	3	6.8 ± .2	8.7 ± 0.3	E6D
E2GFP-S202N	A11	4	7.6 ± .2 7.15[a]	0.0 ± 2.5	K14ON
	E06	4	5.4 ± .2	1.8 ± 0.1	Q69H K131M
	G02	4	7.6 ± .1 7.8[a] 7.65[b]	5.6 ± 0.2	A87T N185T
	G06	4	6.0 ± .2	2.5 ± 1.8	Q69H
	B05	4	6.8 ± .1	7.4 ± 0.6	V120L
	B02	4	6.9 ± .1	9.1 ± 0.7	E11Q R168L
	A10	4	6.9 ± .1	6.2 ± 0.4	H81Y N198T shiftN200
	A05	4	6.9 ± .1	7.0 ± 0.9	E5D T97S K166M
	B04	4	6.9 ± .1	9.7 ± 1.9	Q80H

template	well	lib	pKa	Kd (mM)	mutations
	B06	4	6.8 ± .1	8.4 ± 0.7	K140N
	B03	4	7.0 ± .1	10.6 ± 1.1	P187L shiftN206
	A03	4	7.1 ± .1	10.6 ± 0.5	H81Y
	A09	4	6.8 ± .1	10.3 ± 1.2	E90D N144K
	A04	4	6.8 ± .1	10.0 ± 0.4	D133N
	A02	4	6.9 ± .2	8.8 ± 0.8	H25L T50S Q184Y L207M
	A07	4	7.0 ± .1	7.2 ± 0.9	K126M
	A06	4	6.9 ± .1	10.3 ± 0.9	E172V
	A08	4	6.8 ± .1	7.4 ± 1.6	E32K K52R A154T
E2GFP-S202N	D02	5	7.0 ± .1		R73H H81V T118I Y182F L201M
	G02	5	7.3 ± .1		A87V K156T
	G10	5	7.3 ± .1		F99I G116C Y203C
E2GFP-S202N	D07	6	6.7 ± .1		L201M
	B03	6	6.6 ± .1		S30F N105K

template	well	lib	pKa	Kd (mM)	mutations
E2GFP-	E05	7	7.7 ± .3	1.1 ±	Y151C N198I
A87T-				1.5	
N185T-	H11	7	7.8 ± .1	11.5 ±	Q94L
S202N				1.6	
	B03	8	7.6 ± .1	6.4 ±	S2N
				0.3	
	B11	8	7.8 ± .2 8.0[a] 7.66[b]	1.2 ±	D21Y
				1.3	
E2GFP-	A04	10	7.8 ± .1 8.2[a] 7.76[b]	3.8 ±	D21H
A87T-				0.6	
N185T-	A05	10	8.1 ± .1 8.2[a] 7.8[b]	11.0 ±	I167V
S202N				1.3	
	A06	10	7.7 ± .1 8.16[a] 7.77[b]	4.2 ±	E115V
				0.9	
	A07	10	7.7 ± .2 8.0[a] 7.6[b]	10.3 ±	V150I
				1.8	
	A09	10	7.8 ± .3	4.0 ±	R215C
				0.6	
	A11	10	7.9 ± .7 8.0[a] 7.6[b]	5.4 ±	31
				0.9	
	B09	10	7.6 ± .2	5.5 ±	L7R
				1.2	
	B11	10	7.7 ± .7 8.1[a]] 7.7[b]	5.2 ±	C48S N105Y
				0.7	
	D06	10	8.0 ± .4	4.2 ±	A226G
				0.4	

template	well	lib	pKa	Kd (mM)	mutations
	D07	10	7.7 ± .1	4.5 ± 0.3	Q80L
	E04	10	7.9 ± .1 8.4[a] 7.9[b]	24.1 ± 3.4	I47V I167V Q184E
	G03	10	8.1 ± .1 8.4[a] 7.9[b]	12.7 ± 0.6	I47V I167V Q184E
	E06	10	7.7 ± .1	7.1 ± 1.8	I149C N198I
	E08	10	7.8 ± .2 8.15[a] 7.75[b]	4.0 ± 0.3	N170D
	F06	10	7.7 ± .2	8.7 ± 1.2	D103E

Correlating pK_a values with sequences data, we finally identified key positions within GFP structure which can strongly affect the GFP protonation equilibria (Fig. 3.10) and might be targeted by saturation mutagenesis.

3.3 Chloride imaging simplified by Long Stokes Shift fluorescent protein

This work has been adapted from:

Synchronous Bioimaging of Intracellular pH and Chloride Based on LSS Fluorescent Protein

Paredes, J. M., Idilli, A. I., Mariotti, L., Losi, G., Arslanbaeva, L. R., Sato, S. S., Artoni, P., Szczurkowska, J., Cancedda, L., Ratto, G. M., Carmignoto, G., and Arosio, D. ACS Chem. Biol. 11, 1652–1660 (2016)

Cl^- biosensors can be based on the fluorescence resonance energy transfer (FRET) between a CFP variant and a chloride-binding YFP variant; in this case, they are ratiometric in emission. Unfortunately, FRET-based Cl^- measurements are biased by a strong pH dependency - present in all the YFP and GFP variants adopted in chloride-sensing applications - of both the Cl^- binding affinity and the emitted fluorescence. Precise Cl^- measurements require therefore independent estimation of the intracellular pH or, alternatively, the simultaneous measurement of intracellular Cl^- and pH combined into a single construct. ClopHensor prevents the intricate pH dependency of FRET signals and provides both a chloride-independent ratiometric measurement of the intracellular pH and an accurate measurement of the intracellular Cl^- concentration. ClopHensor is ratiometric in excitation and requires, for its operation, sequential illumination with three wavelengths to excite the pH isosbestic point at exactly 458 nm, the green anionic form at about 488 – 500 nm and the red component at about 540 – 560 nm (see Sec. 1.5).

To simplify setup requirements and allow a wider adoption of quantitative chloride imaging with the correct analysis of concomitant pH changes, we reasoned whether it was possible to substitute DsRed-monomer with a FP with a large (> 100 nm) Stokes shift. Red fluorescence proteins with a large distance between excitation and emission maxima could allow the ratiometric operation using a single excitation wavelength that is optimal for both the green and red proteins. This, we tested LSSmKate2 [125,126] as a partner of E^2GFP. We named the new biosensor LSSmClopHensor, and demonstrated its ability to perform dynamic measurement of concomitant changes of intracellular H^+ and Cl^- concentration in neurons.

3.3.1 Development of LSSmClopHensor

LSSmKate2 shows favorable properties to replace DsRed-monomer in ClopHensor. LSSmKate2 excitation maximum at 460 nm matches E^2GFP isosbestic point at 458 nm [113,115] Fig. 3.11; compared to DsRed-monomer, LSSmKate2 shows faster maturation rate and higher pH stability (pK_a = 2.7) with unaltered brightness.

To examine whether the fluorescence of LSSmKate2 was also stable over changes of Cl^- concentration, we purified recombinant LSSmKate2 from bacterial lysate and measured fluorescence properties. Emission spectra collected in a wide range of Cl^- concentration (from 0 to 1 M) Fig. 3.12 and pH values (from 5.2 to 8.4) Fig. 3.13 resulted superimposed indicating high Cl^- stability over a wide pH range.

Using recombinant LSSmKate2, we also surveyed its brightness - as the product of absorption and quantum yield - relative to E^2GFP and obtained a value of 0.57 ± 0.05; a substantial improvement over the corresponding value of 0.13 for DsRed-monomer [127], which should lead to numerically more stable ratio calculation. Motivated by the large Stokes shift and the high pH and Cl^- stability of LSSmKate2, we then decided to replace DsRed-monomer with LSSmKate2 and generate LSSmClopHensor, a new chimeric protein linking E^2GFP with LSSmKate2 (panel a). We expressed and purified recombinant LSSmClopHensor to check whether the chimeric protein conserved the fluorescence properties E^2GFP. The excitation wavelength (isosbestic point) that produces a pH-independent fluorescence intensity was present in the same position of E^2GFP (panel b). Therefore, excitation of LSSmClopHensor at 458 nm shall continue to provide the pH-independent fluorescence signal, which turned out convenient for the simultaneous ratiometric measurement of pH and Cl^- con-

centration [115]. We performed a pH titration of recombinant LSSmClopHensor in the range from 5.6 to 8.7. The ratio (488-over-458) of the emission spectra integrated from 500 to 550 nm and collected using excitation bands peaking at 488 nm (panel c) and 458 nm (panel d) defined the R_{pH} ratio (panel e) of Fig. 3.14. Notably, the R_{pH} ratio is not affected by changes in Cl^- concentration, follows a single site binding curve (Methods, Eq. 2.2) and thus allows for accurate pH measurements independently of Cl^- and LSSmClopHensor concentrations.

We then calculated the emission ratio R_{Cl} between the green (from 500 to 550 nm) and red (from 580 to 640 nm) fluorescence at increasing Cl^- concentrations using a single excitation band (Fig. 3.14, panel f). Increasing amount of Cl^- quenched the green fluorescence because of the static quenching mechanism that regulates Cl^- binding to the E^2GFP moiety. Red fluorescence instead remained constant thanks to the chloride-independent fluorescence of LSSmKate2. Overall, chloride titrations at various pH values demonstrated a high sensitivity for Cl^- within the physiological pH range (Fig. 3.14, panel g and Supplementary Figure S6). Finally, we investigated the ion shield effects on our measurements. In the cellular environment, in fact, biological processes produce continuous changes of the local ion concentrations, which can prevent correct pH measurements by altering the apparent pK_a of the sensor [128,129]. We measured the apparent pK_a of LSSmClopHensor at increasing ionic strength and observed only a slight decrease, from 6.74 ± 0.02 to 6.57 ± 0.04, when moving from low (1 mM) to high (2 M) salt concentration (Fig. 3.15). This assured us that LSSmClopHensor can report intracellular pH accurately even in the presence of the largest physiological changes of ion concentration.

3.3.2 Chloride imaging in live cells

We first expressed LSSmClopHensor in human embryonic kidney 293 (HEK293) and in human neuroblastoma (SK-N-SH) [130,131] cells. Protein expression showed a uniform distribution pattern within all cell compartments without observable aggregates for both cell lines as well as for differentiated SK-N-SH cells - adopting neuronal-like phenotype (Fig. 3.16).

By ionophore clamping cells at values encompassing a wide range of pH and Cl^- concentrations, we performed an *in situ* calibration. Two excitation wavelengths, 488 and 458 nm, and two emission bands, green and red, provided the three channels (cyan, green and red) required for ratio analyses (detailed in Sec. 2.8). Global fitting (using Eq. 2.2) of R_{pH} values obtained from both cell lines provided a unique pH calibration curve (Fig. 3.17, a).

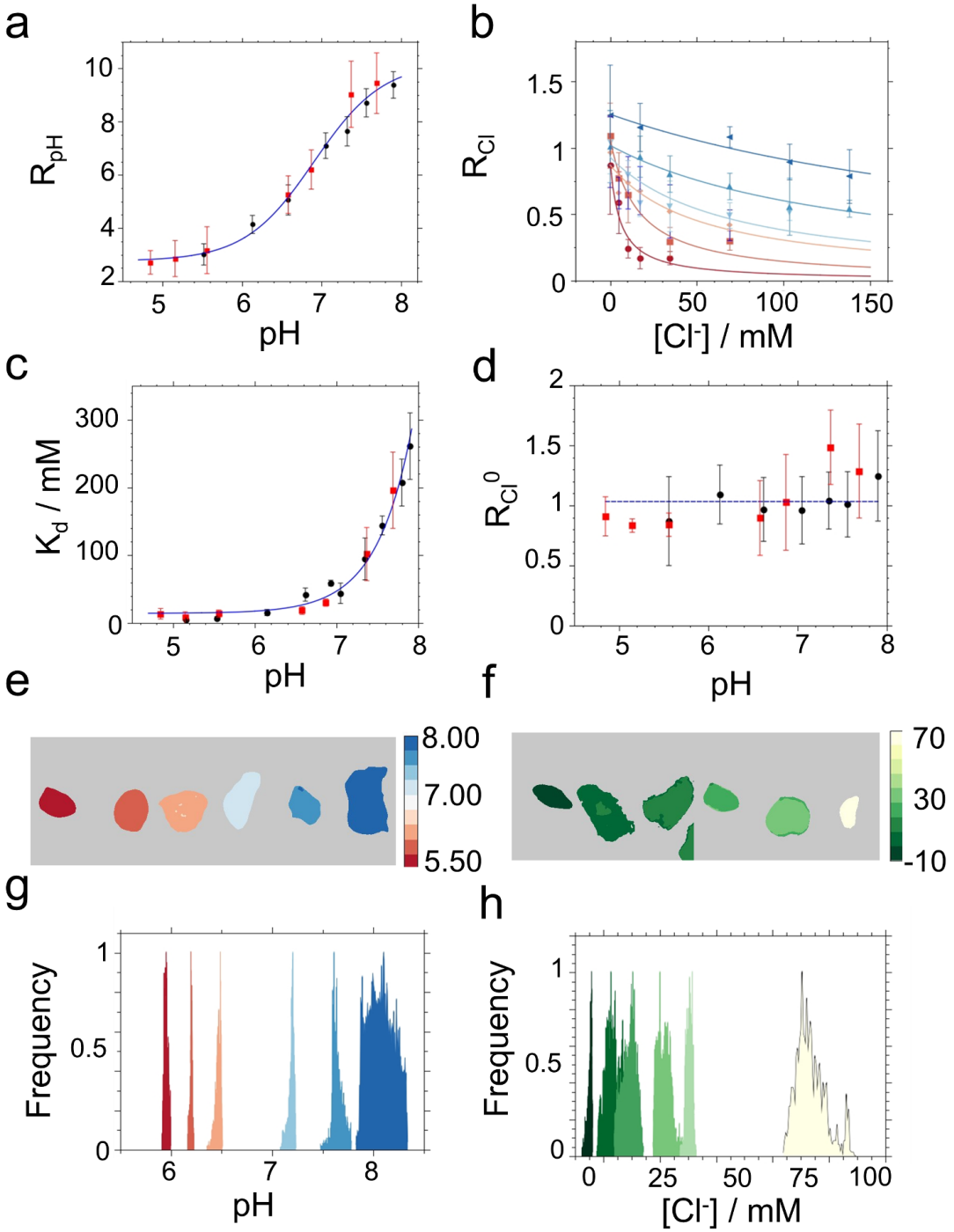
a
R_{pH}
pH
b
R_{Cl}
[Cl-] / mM
c
K_d / mM
pH
d
R_{Cl}^0
pH
e
8.00
7.00
5.50
f
70
30
-10
g
Frequency
pH
h
Frequency
[Cl-] / mM

Figure 3.17: **pH and chloride imaging calibration in cells.** (a) Green-to-cyan R_{pH} ratio values vs. pH for LSSmClopHensor expressed in HEK293 (black circles) and SK-N-SH (red squares) cells. Global fitting curve was drawn for the two datasets using [@eq:rpH] in Methods and the following best fit parameters: $R_A = 2.75 \pm 0.11$, $R_B = 10.2 \pm 0.3$ and $pK_a = 6.89 \pm 0.06$. Error bars are cell-to-cell standard deviation (N = from 20 to 25 cells). (b) Cyan-to-red R_{Cl} ratio values vs. Cl^- concentration for LSSmClopHensor expressed in HEK293 cells at the pH values of 5.54, 6.15, 6.62, 7.35, 7.56 and 7.90, in the direction indicated by the arrow. Fitting curves were drawn using [@eq:rcl] in Methods. (c) Cl^- dissociation constant K_d, determined as exemplified in b, vs. pH for LSSmClopHensor expressed in HEK293 (black circles) and SK-N-SH (red squares) cells. Fitting curve was drawn using [@eq:kd] with the following best-fit parameters: $pK_a = 6.64 \pm 0.12$ and chloride $K_d = 14.27 \pm 3.5$ mM. Error bars represent the best fit uncertainties. (d) R^0_{Cl} of HEK293 (black circles) and SK-N-SH (red squares) cell lines clamped at various pH values and $[Cl^-] = 0$ mM. Error bars represent the best fit uncertainties. (e) Representative pH maps of HEK293 cells clamped at $[Cl^-] = 0$ mM and various pH values. (f) Representative $[Cl^-]$ maps of HEK293 cells clamped at pH = 6.6 and various $[Cl^-]$ values. (g) Distributions of pH values corresponding to cells reported in e. (h) Distributions of $[Cl^-]$ values corresponding to cells reported in f.

Because chloride K_d of GFP-based biosensor is strongly pH-dependent, different Cl^- calibration reference curve are obtained at different pH values. Using the single 458-nm excitation, we acquired R_{Cl} values in HEK293 (Fig. 3.17, panel b) and in SK-N-SH (Fig. 3.18) cells at increasing amount of Cl^- concentration for various pH values.

By fitting LSSmClopHensor Cl^- titration with Eq. 2.3, we determined the dependence of chloride K_d on pH, which can be modeled according to the cooperative binding of H^+ and Cl^- to E^2GFP-based biosensors [115,132] as follows.

$$K_d(pH) = K_d^1 \frac{1 + 10^{pK_a - pH}}{10^{pK_a - pH}}$$

where K_d^1 is the Cl^- dissociation constant of the fully protonated form of LSSmClopHensor; an intrinsic property of the sensor that together with the pK_a characterize the binding equilibria of LSSmClopHensor in solution. Using data from both cell lines for a global fit, we obtained a reference function for the dependence of the chloride K_d on pH (Fig. 3.17, panel c). Finally, the last parameter required by our calibration scheme was the setup dependent parameter R^0_{Cl}, estimated by

clamping cells at [Cl^-] = 0 mM. We recorded R^0_{Cl} values in a wide pH range for both cell lines and obtained a weighed average value of 1.03 ± 0.19 (Fig. 3.17, panel d). Following the determination of three setup-dependent (R^0_{Cl}, R_A and R_B) and two LSSmClopHensor intrinsic (pK_a = 6.64 ± 0.12 and K^1_d = 14 ± 3 mM) parameters, the following operational order settled pH and Cl^- concentration maps: for each pixel of segmented cells (1) we assigned a pH value using the measured R_{pH} value and the pH calibration curve in Fig. 3.17, panel a; (2) then we calculated a chloride K_d value using Eq. 1.2; and finally (3) we assigned a Cl^- concentration value using the measured R_{Cl} value and Eq. 2.3 (Fig. 3.17, panel e and f). The narrow pixel-by-pixel distribution reveals the precision of LSSmClopHensor for pH and Cl^- measurements (Fig. 3.17, panel g and h).

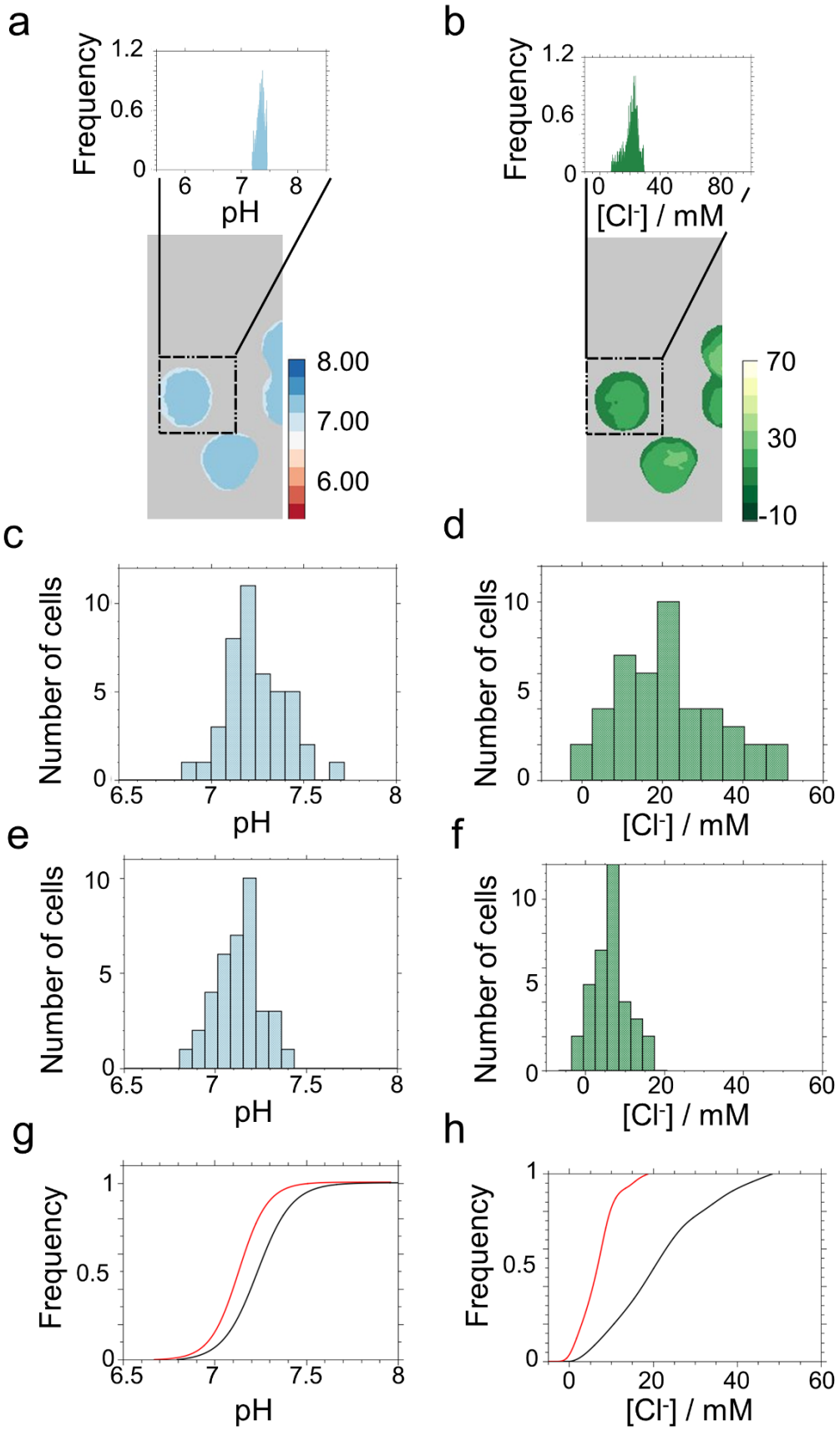
a
Frequency
1.2
0.6
0
6
7
8
pH
8.00
7.00
6.00
b
Frequency
1.2
0.6
0
0
40
80
[Cl-] / mM
70
30
-10
c
Number of cells
10
5
0
6.5
7
7.5
8
pH
d
Number of cells
10
5
0
0
20
40
60
[Cl-] / mM
e
Number of cells
10
5
0
6.5
7
7.5
8
pH
f
Number of cells
10
5
0
0
20
40
60
[Cl-] / mM
g
Frequency
1
0.5
0
6.5
7
7.5
8
pH
h
Frequency
1
0.5
0
0
20
40
60
[Cl-] / mM

Figure 3.19: **pH and chloride imaging calibration in cells.** LSSmClopHensor measures physiological changes in intracellular pH and Cl^- concentrations. (a) Representative pH map for SK-N-SH cells. The inserts show the distribution (pixel-by-pixel) of pH values for the highlighted cells. (b) Representative [Cl^-] map for SK-N-SH cells. (c) Cell-by-cell distribution of pH w values for SK-N-SH cells (top) and HEK293 cells (middle) represented with histograms and kernel density estimate curves. Black (HEK293) and red (SK-N-SH) lines were drawn from the best fit to a Gaussian distribution. Comparison of the cumulative distribution functions for the examined cell populations (bottom) indicated that the average pH of SK-N-SH cells is distributed in a range of significantly ($p = 0.005$ in a Kolmogorov-Smirnov test for statistical difference in distributions) smaller pH values. Two-sided t-test indicated an average pH significantly different between the cell lines ($p = 0.0009$; and using Welch's t-test $p = 0.0007$ for different sample variances). (d) Cell-by-cell distribution of [Cl^-] values for SK-N-SH cells (top) and HEK293 cells (middle) represented with histograms and kernel density estimate curves. Black (HEK293) and red (SK-N-SH) lines were drawn from the best fit to a Gaussian distribution. Comparison of the cumulative distribution functions for the examined cell populations (bottom) indicated that the distribution of intracellular Cl^- concentration was significantly different between SK-N-SH and HEK293 cells ($p = 1.6\times10^{-10}$ in a Kolmogorov-Smirnov test between distributions).

We next investigated how the Cl^- is distributed both in cellular compartments and from cell to cell. We performed direct measurements of intracellular Cl^- concentration and pH in model neuronal SK-N-SH cells under physiological conditions (Fig. 3.19). Distribution of Cl^- concentrations was narrow in SK-N-SH cells, peaking at 8.0 ± 4.1 mM (mean ± SD, N=37). On the contrary, we observed a broader distribution of intracellular Cl^- concentration in HEK293 cells (24 ± 12 mM, N=44). Intracellular pH values were 7.17 ± 0.13 (mean ± SD, N=37 cells) and 7.29 ± 0.18 (N=44 cells) for SK-N-SH and HEK293 cells, respectively. Our finding showing a lower Cl^- concentration in SK-N-SH than in HEK293 cells is in agreement with intracellular Cl^- values reported for neuronal cell lines [111,133,134] and other renal cell lines [6,133], and suggest the presence of mechanisms for a tight control of intracellular Cl^- in model neuronal cells.

In conclusion, I have shown that LSSmClopHensor can be used to quantify simultaneously intracellular pH and Cl^- concentration in cell lines. Using a red long Stokes shift (LSS) FP and a chloride-sensitive green FP, we have successfully developed a new genetically encodable chloride biosensor, LSSmClopHensor. We proved that a single excitation band is sufficient to optimally excite both green

and red FP and exploit the ratio between their emissions for measuring intracellular Cl^-. The use of LSS FP in FRET-based biosensors will prove useful in the development of future biosensor, which will avoid biases in FRET efficiency calculations generated by changes in intracellular pH.

ACS chemical biology

Articles

pubs.acs.org/acschemicalbiology

Synchronous Bioimaging of Intracellular pH and Chloride Based on LSS Fluorescent Protein

Jose M. Paredes,[*,†,§] Aurora I. Idilli,[†] Letizia Mariotti,[‡] Gabriele Losi,[‡] Lyaysan R. Arslanbaeva,[†,▽] Sebastian Sulis Sato,[∥] Pietro Artoni,[⊥] Joanna Szczurkowska,[#] Laura Cancedda,[#] Gian Michele Ratto,[∥,⊥] Giorgio Carmignoto,[‡] and Daniele Arosio[*,†,▽]

[†]Institute of Biophysics, CNR, Via alla Cascata 56/C, 38123 Trento, Italy

[‡]Neuroscience Institute, CNR, Viale G. Colombo 3, 35121 Padova, Italy

[§]Bruno Kessler Foundation, Via Sommarive 18, 38123 Trento, Italy

[∥]Nanoscience Institute, CNR, Pisa, Italy

[⊥]Scuola Normale Superiore, Pisa, Italy

[#]Istituto Italiano di Tecnologia, Genoa, Italy

[▽]CIBIO, University of Trento, Via delle Regole 101, 38123 Trento, Italy

Supporting Information

ABSTRACT: Ion homeostasis regulates critical physiological processes in the living cell. Intracellular chloride concentration not only contributes in setting the membrane potential of quiescent cells but it also plays a role in modulating the dynamic voltage changes during network activity. Dynamic chloride imaging demands new tools, allowing faster acquisition rates and correct accounting of concomitant pH changes. Joining a long-Stokes-shift red-fluorescent protein to a GFP variant with high sensitivity to pH and chloride, we obtained LSSmClopHensor, a genetically encoded fluorescent biosensor optimized for the simultaneous chloride and pH imaging and requiring only two excitation wavelengths (458 and 488 nm). LSSmClopHensor allowed us to monitor the dynamic changes of intracellular pH and chloride concentration during seizure like discharges in neocortical brain slices. Only cells with tightly controlled resting potential revealed a narrow distribution of chloride concentration peaking at about 5 and 8 mM, in neocortical neurons and SK-N-SH cells, respectively. We thus showed that LSSmClopHensor represents a new versatile tool for studying the dynamics of chloride and proton concentration in living systems.

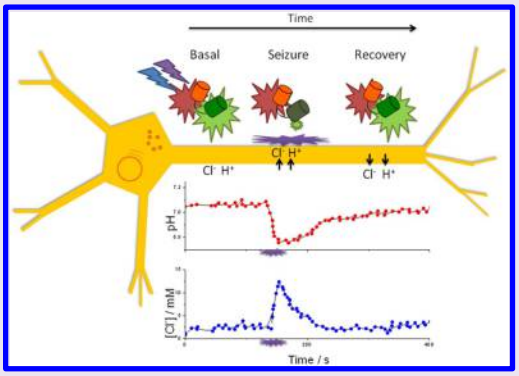

Electrochemical proton (H^+) gradients represent a ubiquitous source of energy in live cells. The chloride ion (Cl^-), the most abundant anion in organisms, controls pH within cell compartments by shunting the effects of H^+ charge accumulation on membrane potential.[1−3] The importance of Cl^- in cell functions was not fully recognized until recently, yet Cl^- and H^+ play coordinated roles in physiological processes including control of membrane potential,[4] regulation of cell volume,[5,6] growth and migration of neurons,[7−9] and synaptic signaling in both the depolarizing and hyperpolarizing directions.[10,11] Intracellular Cl^- concentration is tightly regulated by the interaction of energy-dependent transporters with passive-diffusion channels so that a gradient of varying intensity over time is established across the plasma membrane.[12] Cl^- homeostasis is of high significance in the physiopathology of many human diseases such as cystic fibrosis, myotonia, epilepsy, lysosomal storage diseases,[13] and neurodevelopmental disorders[14] including autism,[15] fragile X syndrome,[16] and Down syndrome.[17] Therefore, understanding the regulatory mechanisms of Cl^- homeostasis is of fundamental importance.

Development of experimental noninvasive means—mainly optogenetics—to monitor and manipulate intracellular Cl^- in live cells is a flourishing field with a growing number of different approaches reported in the recent literature.[18−20] The measurement of Cl^- in living cells has experienced an extraordinary development following the adoption of methods based on imaging techniques. Organic fluorescent dyes and later genetically encoded fluorescent proteins (FP) replaced the use of ion-selective electrodes.[21,22] It was the discovery of Cl^- sensitivity of yellow fluorescent protein (YFP)[23] which triggered this intense development. Combining two fluorescence proteins with distinct colors into a single construct, ratiometric biosensors were developed with the advantage of

Received: February 1, 2016
Accepted: March 31, 2016

DOI: 10.1021/acschembio.6b00103
ACS Chem. Biol. XXXX, XXX, XXX−XXX

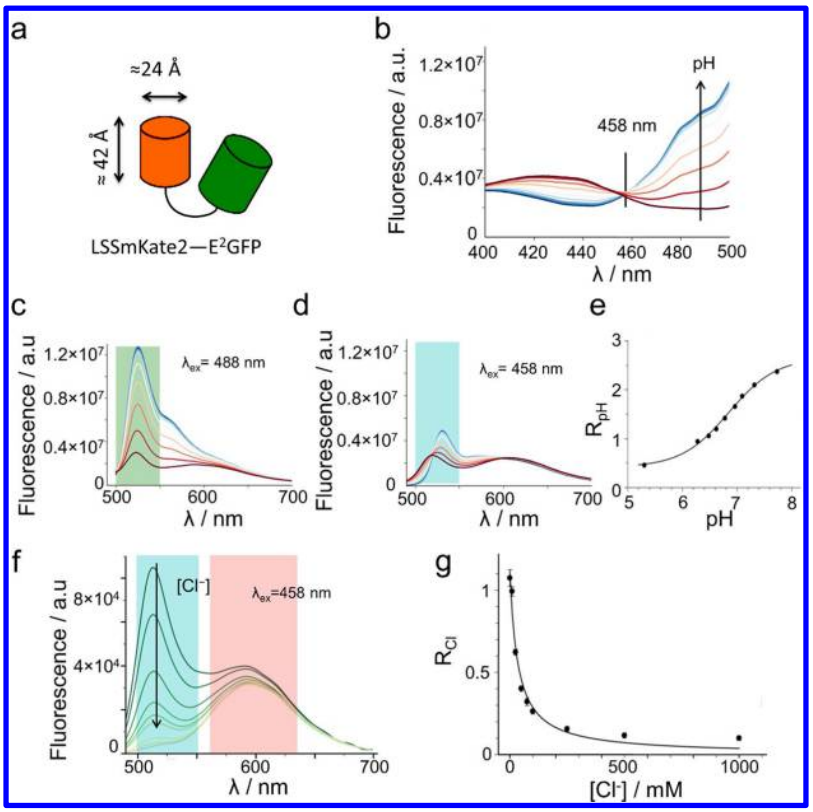

Figure 1. Spectroscopy characterization of purified LSSmClopHensor. (a) Schematic representation of LSSmClopHensor. Monomer LSSmKate2 dimensions are derived from structural data (PDB code: 3nt3). (b) Excitation spectra at pH values 5.59, 6.01, 6.40, 6.71, 7.12, 7.54, 7.98, 8.42, and 8.72 (color coded from red to blue in the direction indicated by the arrow). Emission wavelength set at 520 nm, $[Cl^-]$ = 0 mM, and temperature at 37 °C. The presence of a single isosbestic point was unambiguously identified at 458 nm. (c, d) Emission spectra collected at the same pH values, from 5.59 to 8.72; excitation wavelength set at 488 (in c) and 458 (in d) nm, $[Cl^-]$ = 0 mM, and temperature at 37 °C. Color-shaded areas represent the spectral bands used in the analysis. (e) pH ratio values calculated after integration of emission spectra from 500 to 550 nm (shaded spectral range in c and d). Fitting curve was drawn using eq 2 in Methods and the following best fit parameters: $R_A = 0.41 \pm 0.03$, $R_B = 2.66 \pm 0.04$, and $pK_a = 6.86 \pm 0.03$. (f) Emission spectra at the $[Cl^-]$ values of 0, 10, 25, 50, 75, 100, 250, 500, and 1000 mM; excitation wavelength set at 458 nm, the isosbestic point, pH = 6.5, and temperature at 37 °C. The arrow indicates increases in the $[Cl^-]$. (g) Chloride ratio values corresponding to the data and spectral ranges reported in f. Fitting curve was drawn using eq 3 in Methods and the following best fit ± SD (from fit) parameters: $R^0_{Cl} = 1.12 \pm 0.06$ and $K_d = 33.6 \pm 5.0$ mM.

being free from the influence of local probe concentration, thickness of the specimen, light scattering, illumination intensity fluctuation, and photobleaching.[24] Chloride biosensors can be based on the fluorescence resonance energy transfer (FRET) between a CFP variant and a chloride-binding YFP variant; in this case, they are ratiometric in emission.[24−26] Unfortunately, FRET-based Cl^- measurements are biased by a strong pH dependency—present in all the YFP and GFP variants adopted in chloride-sensing applications—of both the Cl^- binding affinity and the emitted fluorescence.[27] Precise Cl^- measurements require therefore independent estimation of the intracellular pH[28,29] or, alternatively, the simultaneous measurement of intracellular Cl^- and pH combined into a single construct.[30] On the basis of the pH and Cl^- independent fluorescence of DsRed-monomer, ClopHensor prevents the intricate pH dependency of FRET signals and provides both a chloride-independent ratiometric measurement of the intracellular pH and an accurate measurement of the intracellular Cl^- concentration. ClopHensor is ratiometric in excitation and requires, for its operation, sequential illumination with three wavelengths to excite the pH isosbestic point at exactly 458 nm, the green anionic form at about 488−500 nm and the red component at about 540−560 nm. The requirement of three excitation wavelengths limited the use of ClopHensor to dedicated setups despite the increasing interest in accurate mapping of Cl^- fluxes in the dendritic tree and cell body of neurons in an intact brain both under physiological conditions[31,32] and in animal models of neuronal disorders.[33,34]

To simplify setup requirements and allow a wider adoption of quantitative chloride imaging with the correct analysis of concomitant pH changes, we reasoned whether it was possible to substitute DsRed-monomer with a FP with a large (>100 nm) Stokes shift. Red fluorescence proteins with a large distance between excitation and emission maxima could allow the ratiometric operation using a single excitation wavelength that is optimal for both the green and red proteins. Here, we tested LSSmKate2[35,36] as a partner of E^2GFP, a GFP variant that contains a highly specific Cl^- binding site.[37] We named the new biosensor LSSmClopHensor and demonstrated its ability to perform dynamic measurement of concomitant changes of intracellular H^+ and Cl^- concentration in neurons.

RESULTS AND DISCUSSION

Development of LSSmClopHensor. LSSmKate2 shows favorable properties to replace DsRed-monomer in ClopHensor. LSSmKate2 excitation maximum at 460 nm matches the E^2GFP isosbestic point at 458 nm[30,38] (Supporting Information Figure S1); compared to DsRed-monomer, LSSmKate2 shows

DOI: 10.1021/acschembio.6b00103
ACS Chem. Biol. XXXX, XXX, XXX−XXX

faster maturation rate and higher pH stability (pK_a = 2.7) with unaltered brightness.

To examine whether the fluorescence of LSSmKate2 was also stable over changes of Cl^- concentration, we purified recombinant LSSmKate2 from bacterial lysate and measured fluorescence properties. Emission spectra collected in a wide range of Cl^- concentration (from 0 to 1 M) and pH values (from 5.2 to 8.4) resulted in being superimposed (Supporting Information Figures S2 and S3), indicating high Cl^- stability over a wide pH range. Using recombinant LSSmKate2, we also surveyed its brightness—as the product of absorption and quantum yield—relative to E^2GFP and obtained a value of 0.57 ± 0.05 (Supporting Information Figures S4 and S5), a substantial improvement over the corresponding value of 0.13 for DsRed-monomer,[39] which should lead to numerically more stable ratio calculation. Motivated by the large Stokes shift and the high pH and Cl^- stability of LSSmKate2, we then decided to replace the DsRed-monomer with LSSmKate2 and generate LSSmClopHensor, a new chimeric protein linking E^2GFP with LSSmKate2 (Figure 1a). We expressed and purified recombinant LSSmClopHensor to check whether the chimeric protein conserved the fluorescence properties E^2GFP. The excitation wavelength (isosbestic point) that produces a pH-independent fluorescence intensity was present in the same position of E^2GFP (Figure 1b). Therefore, excitation of LSSmClopHensor at 458 nm shall continue to provide the pH-independent fluorescence signal, which turned out convenient for the simultaneous ratiometric measurement of pH and Cl^- concentration.[30] We performed a pH titration of recombinant LSSmClopHensor in the range from 5.6 to 8.7. The ratio (488:458) of the emission spectra integrated from 500 to 550 nm and collected using excitation bands peaking at 488 nm (Figure 1c) and 458 nm (Figure 1d) defined the R_{pH} ratio (Figure 1e). Notably, the R_{pH} ratio is not affected by changes in Cl^- concentration, follows a single site binding curve (Methods, eq 2), and thus allows for accurate pH measurements independently of Cl^- and LSSmClopHensor concentrations.

We then calculated the emission ratio R_{Cl} between the green (from 500 to 550 nm) and red (from 580 to 640 nm) fluorescence at increasing Cl^- concentrations using a single excitation band (Figure 1f). An increasing amount of Cl^- quenched the green fluorescence because of the static quenching mechanism that regulates Cl^- binding to the E^2GFP moiety. Red fluorescence instead remained constant thanks to the chloride-independent fluorescence of LSSmKate2. Overall, chloride titrations at various pH values demonstrated a high sensitivity for Cl^- within the physiological pH range (Figure 1g and Supporting Information Figure S6). Finally, we investigated the ion shield effects on our measurements. In the cellular environment, in fact, biological processes produce continuous changes of the local ion concentrations, which can prevent correct pH measurements by altering the apparent pK_a of the sensor.[40,41] We measured the apparent pK_a of LSSmClopHensor at increasing ionic strength and observed only a slight decrease, from 6.74 ± 0.02 to 6.57 ± 0.04, when moving from low (1 mM) to high (2 M) salt concentration (Supporting Information Figure S7). This assured us that LSSmClopHensor can report intracellular pH accurately even in the presence of the largest physiological changes of ion concentration.

Chloride Imaging in Live Cells. We first expressed LSSmClopHensor in human embryonic kidney 293 (HEK293) and in human neuroblastoma (SK-N-SH)[42,43] cells. Protein expression showed a uniform distribution pattern within all cell compartments without observable aggregates for both cell lines as well as for differentiated SK-N-SH cells—adopting neuronal-like phenotype (Supporting Information Figures S8–S10). By ionophore clamping cells at values encompassing a wide range of pH and Cl^- concentrations, we performed an *in situ* calibration. Two excitation wavelengths, 488 and 458 nm, and two emission bands, green and red, provided the three channels (cyan, green, and red) required for ratio analyses (detailed in Methods). Global fitting (Methods, eq 2) of R_{pH} values obtained from both cell lines provided a unique pH calibration curve (Figure 2a). Instead, Cl^- calibration could not be

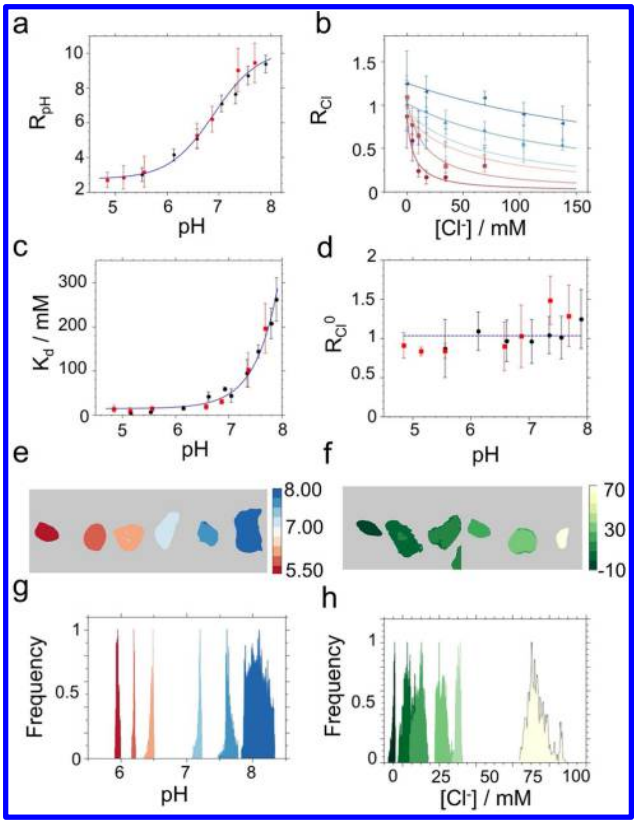

Figure 2. pH and chloride imaging calibration in cells. (a) Green-to-cyan R_{pH} ratio values vs pH for LSSmClopHensor expressed in HEK293 (black circles) and SK-N-SH (red squares) cells. The global fitting curve was drawn for the two data sets using eq 2 in the Methods and the following best fit parameters: R_A = 2.75 ± 0.11, R_B = 10.2 ± 0.3, and pK_a = 6.89 ± 0.06. Error bars are cell-to-cell standard deviation (N = from 20 to 25 cells). (b) Cyan-to-red R_{Cl} ratio values vs Cl^- concentration for LSSmClopHensor expressed in HEK293 cells at the pH values of 5.54, 6.15, 6.62, 7.35, 7.56, and 7.90, in the direction indicated by the arrow. Fitting curves were drawn using eq 3 in the Methods. (c) Cl^- dissociation constant K_d, determined as exemplified in b, vs pH for LSSmClopHensor expressed in HEK293 (black circles) and SK-N-SH (red squares) cells. A fitting curve was drawn using eq 1 with the following best-fit parameters: pK_a = 6.64 ± 0.12 and chloride K_d = 14.27 ± 3.5 mM. Error bars represent the best fit uncertainties. (d) R_{Cl}^0 of HEK293 (black circles) and SK-N-SH (red squares) cell lines clamped at various pH values and [Cl^-] = 0 mM. Error bars represent the best fit uncertainties. (e) Representative pH maps of HEK293 cells clamped at [Cl^-] = 0 mM and various pH values. (f) Representative [Cl^-] maps of HEK293 cells clamped at pH = 6.6 and various [Cl^-] values. (g) Distributions of pH values corresponding to cells reported in e. (h) Distributions of [Cl^-] values corresponding to cells reported in f.

DOI: 10.1021/acschembio.6b00103
ACS Chem. Biol. XXXX, XXX, XXX–XXX

parametrized into a single reference curve, because chloride K_d of GFP-based biosensor is strongly pH-dependent.[22] Using the single 458 nm excitation, we acquired R_{Cl} values in HEK293 (Figure 2b) and in SK-N-SH (Supporting Information Figure S11) cells at increasing amount of Cl^- concentration for various pH values. By fitting LSSmClopHensor Cl^- titration with eq 3, we determined the dependence of chloride K_d on pH, which can be modeled according to the cooperative binding of H^+ and Cl^- to E^2GFP-based biosensors[30,37] as follows.

$$K_d\,(\mathrm{pH}) = K_d^1 \frac{1 + 10^{\mathrm{p}K_a - \mathrm{pH}}}{10^{\mathrm{p}K_a - \mathrm{pH}}} \quad (1)$$

where K_d^1 is the Cl^- dissociation constant of the fully protonated form of LSSmClopHensor; an intrinsic property of the sensor that together with the pK_a characterize the binding equilibria of LSSmClopHensor in solution. Using data from both cell lines for a global fit, we obtained a reference function for the dependence of the chloride K_d on pH (Figure 2c). Finally, the last parameter required by our calibration scheme was the setup dependent parameter R_{Cl}^0, estimated by clamping cells at $[Cl^-]$ = 0 mM. We recorded R_{Cl}^0 values in a wide pH range for both cell lines and obtained a weighed average value of 1.03 ± 0.19 (Figure 2d). Following the determination of three setup-dependent (R_{Cl}^0, R_A, and R_B) and two LSSmClopHensor intrinsic (pK_a = 6.64 ± 0.12 and K_d^1 = 14 ± 3 mM) parameters, the following operational order settled pH and Cl^- concentration maps: for each pixel of segmented cells, (1) we assigned a pH value using the measured R_{pH} value and the pH calibration curve in Figure 2a; (2) then we calculated a chloride $K_d$value using eq 1; and finally (3), we assigned a Cl^- concentration value using the measured R_{Cl} value and eq 3 (Figure 2e and f). The narrow pixel-by-pixel distribution reveals the precision of LSSmClopHensor for pH and Cl^- measurements (Figure 2g and h).

We next investigated how the Cl^- is distributed both in cellular compartments and from cell to cell. We performed direct measurements of intracellular Cl^- concentration and pH in model neuronal SK-N-SH cells under physiological conditions (Figure 3). Distribution of Cl^- concentrations was narrow in SK-N-SH cells, peaking at 8.0 ± 4.1 mM (mean ± SD, N = 37). On the contrary, we observed a broader distribution of intracellular Cl^- concentration in HEK293 cells (24 ± 12 mM, N = 44). Intracellular pH values were 7.17 ± 0.13 (mean ± SD, N = 37 cells) and 7.29 ± 0.18 (N = 44 cells) for SK-N-SH and HEK293 cells, respectively. Our finding showing a lower Cl^- concentration in SK-N-SH than in HEK293 cells is in agreement with intracellular Cl^- values reported for neuronal cell lines[21,44,45] and other renal cell lines,[21,46] and suggests the presence of mechanisms for a tight control of intracellular Cl^- in model neuronal cells.

Dynamic Chloride Imaging in Neocortical Brain Slices. Last, we extended the use of LSSmClopHensor to monitor dynamic changes of Cl^- and H^+ concentration in neocortical neuron networks in *ex vivo* preparations. Electroporation *in utero* was performed in Sprague–Dawley rats at embryonic day 17 targeting progenitors of pyramidal neurons committed to layers II/III of the cortex. LSSmClopHensor showed a sustained and uniform expression—driven by the CMV early enhancer/chicken β actin (CAG) promoter—in the target neurons (Figure 4a; Supporting Information Figures S12).

Neuronal somas and processes were imaged while performing synchronous electrophysiological recordings of local field potentials (LFP). We monitored pH and Cl^- concentration in real time during spontaneous and induced epileptic seizure like discharges (SLDs). Epileptiform activity was induced with 4-

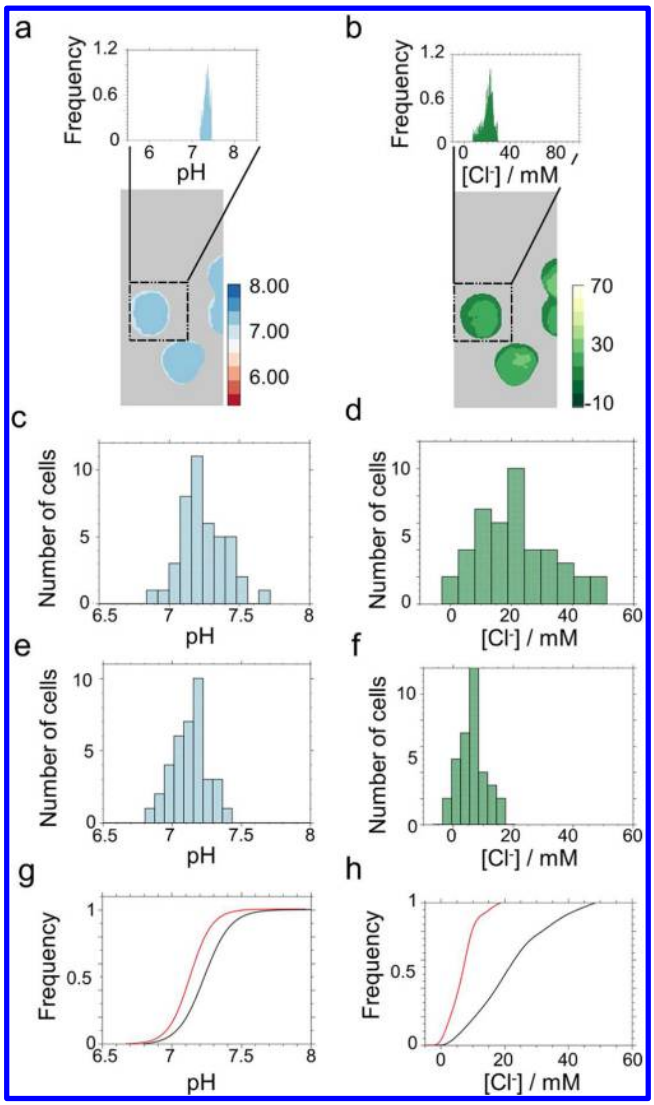

Figure 3. LSSmClopHensor measures physiological changes in intracellular pH and Cl^- concentrations. (a) Representative pH map for SK-N-SH cells. The insets show the distribution (pixel-by-pixel) of pH values for the highlighted cells. (b) Representative $[Cl^-]$ map for SK-N-SH cells. (c) Cell-by-cell distribution of pH with values for SK-N-SH cells (top) and HEK293 cells (middle) represented with histograms and kernel density estimate curves. Black (HEK293) and red (SK-N-SH) lines were drawn from the best fit to a Gaussian distribution. Comparison of the cumulative distribution functions for the examined cell populations (bottom) indicated that the average pH of SK-N-SH cells is distributed in a range of significantly (p = 0.005 in a Kolmogorov–Smirnov test for statistical difference in distributions) smaller pH values. Two-sided t test indicated an average pH significantly different between the cell lines (p = 0.0009; and using Welch's t test p = 0.0007 for different sample variances). (d) Cell-by-cell distribution of $[Cl^-]$ values for SK-N-SH cells (top) and HEK293 cells (middle) represented with histograms and kernel density estimate curves. Black (HEK293) and red (SK-N-SH) lines were drawn from the best fit to a Gaussian distribution. Comparison of the cumulative distribution functions for the examined cell populations (bottom) indicated that the distribution of intracellular Cl^- concentration was significantly different between SK-N-SH and HEK293 cells ($p = 1.6 \times 10^{-10}$ in a Kolmogorov–Smirnov test between distributions).

DOI: 10.1021/acschembio.6b00103
ACS Chem. Biol. XXXX, XXX, XXX–XXX

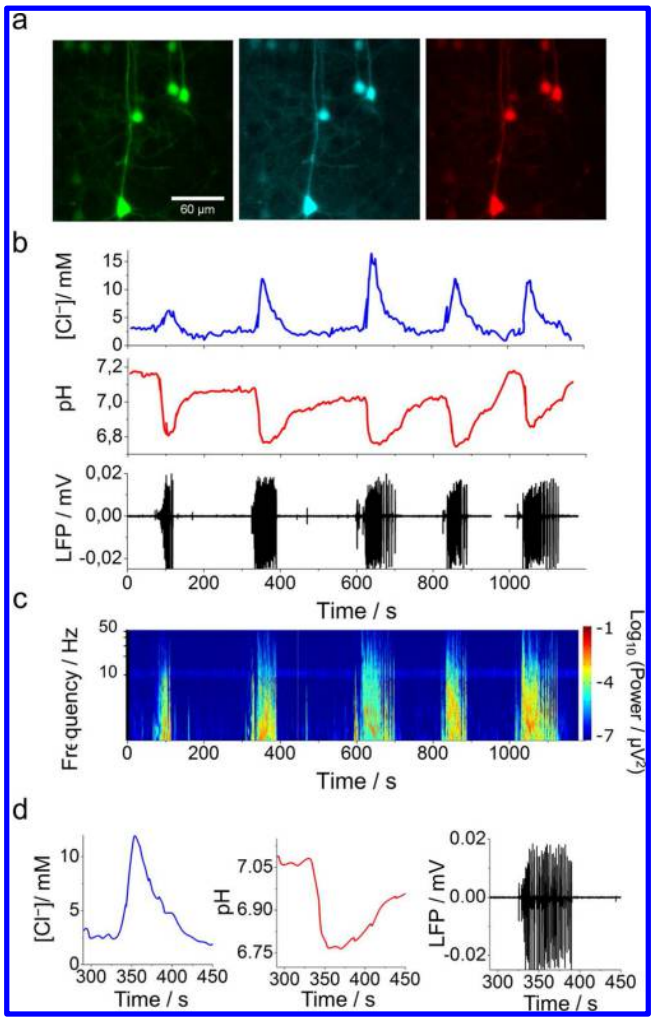

Figure 4. pH and chloride imaging and simultaneous LFP recording during epileptiform activity. (a) Fluorescence images of pyramidal neurons in layer II/III of temporal cortex expressing LSSmClopHensor showing E^2GFP emission (green), E^2GFP emission with excitation at isosbestic point (cyan), and LSSmKate2 emission (red). Scale bar 10 μm. (b) Measurements of Cl^- concentration (blue trace) and pH (red trace) changes over time from a neuronal dendrite expressing LSSmClopHensor. The black trace displays the LFP of five consecutive SLDs recorded during the imaging session. Cl^- concentration and pH values were recorded with a time interval of 990 ms and calculated as reported in the Methods. (c) Spectrogram of the recorded LFP representing the dominant frequency during epileptic activity. (d) Zoomed traces from the second SLD of panel b.

aminopyridine (4-AP; 50−100 μM), reduced Mg^{2+} (0.5 mM), and local NMDA brief applications as previously reported.[47−49] A total of seven somas and 14 dendrites were imaged during successive SLDs from nine slices. Figure 4 shows a typical experiment with the pH and Cl^- concentration calculated in a neuronal dendrite during five consecutive SLDs. Data showed an initial pH value close to 7.15 and a Cl^- concentration below 5 mM, in accordance with values from the SK-N-SH cells and from neurons.[44] SLDs produced an alteration in the fluxes of H^+ and Cl^- at the plasma membrane, causing an intracellular acidification and Cl^- accumulation in the imaged neurons. This observation, in line with previously reported data,[29,44,50] pointed out the power of LSSmClopHensor for intracellular pH and Cl^- concentration measurements *in ex vivo* brain tissue. We measured changes of intracellular pH and Cl^- concentration during different SLDs. We calculated pH decreases of (mean ± SD, N = 21 recordings from nine biological replicates) 0.31 ± 0.06 and Cl^- concentration increases of 8.9 ± 3.8 mM (Figure 4).

Overall, our data revealed that, compared to current methods to measure intracellular Cl^-, LSSmClopHensor represents a substantial advancement in several regards. Current electrophysiological methods provide only indirect estimates of Cl^- concentrations by measuring the reversal potential; they are invasive and difficult to use *in vivo*. Noninvasive chemical indicators have been widely used to measure Cl^- homeostasis, but their loading in living cells is difficult and is retained within the cells for only brief periods.[51] On the contrary, biosensors, which currently are all based on GFP variants with high affinity for Cl^-, can be targeted to specific subcellular compartments and permanently retained within cells. The broadly used Clomeleon[24] and improved variants are all based on the FRET occurring between a cyan donor and a chloride-sensitive acceptor YFP. Therefore, local pH changes impair their accuracy by altering the Cl^- affinity of the YFP moiety as well as the FRET efficiency. Changes in pH indeed affect the brightness of donors and acceptors, and thus make it difficult to predict the effect on the efficiency of the FRET process.[52] In neuronal cells, Cl^- fluxes are closely linked to the pH changes caused by the opening of GABA and glycine receptors generating activity-dependent fluxes of bicarbonate.[50,53] For this reason, all Clomeleon-derived biosensors need independent means to correct measured Cl^- concentration for concomitant pH variations. Unfortunately, this also applies to the recently developed SuperClomeleon, optimized for improved Cl^- affinity and signal-to-noise in cells.[26] On the contrary, LSSmClopHensor allows for precise quantification of intracellular Cl^- by measuring and removing pH bias on a cell-by-cell basis like the original ClopHensor. Furthermore, ClopHensor expression in neural cells can result in highly heterogeneous intracellular red aggregates, probably, as a consequence of DsRed aggregation in the cytosol and subsequent transport into lysosomes.[54] This problem has been recently circumvented by the substitution of DsRed with tandem dimer tomato (tdTomato), a bright dimer (66 kDa) red fluorescence protein, and the generation of ClopHensorN.[44] LSSmClopHensor maintains the same size of the original ClopHensor by using a monomeric red FP. Moreover, LSSmClopHensor allows for faster than ClopHensorN acquisition rates, thanks to the use of a single pH-independent excitation wavelength (458 nm) to measure Cl^- concentration. Thus, the Cl^- ratio of LSSmClopHensor is also free from the biases resulting from intensity fluctuations in the excitation light source, an advantage that up to now was recognized only in sensors ratiometric in emission like Clomeleon.

Conclusions. Using a red long Stokes shift (LSS) FP and a chloride-sensitive green FP, we have successfully developed a new genetically encodable chloride biosensor, LSSmClopHensor. We proved that a single excitation band is sufficient to optimally excite both green and red FP and exploit the ratio between their emissions for measuring intracellular Cl^-. The use of LSS FP in FRET-based biosensors will prove useful in the development of future biosensors, which will avoid biases in FRET efficiency calculations generated by changes in intracellular pH.

We have shown that LSSmClopHensor can be used to quantify simultaneously intracellular pH and Cl^- concentration in cell lines. Next, we were able to monitor the dynamic

DOI: 10.1021/acschembio.6b00103
ACS Chem. Biol. XXXX, XXX, XXX−XXX

changes of intracellular Cl^- (accumulation) and pH (acidification) during epileptiform activity in *ex vivo* cortical brain slices. Thus, we expect LSSmClopHensor to have wide use in imaging studies, in *ex vivo* and potentially also in *in vivo*, investigating the role of Cl^- and H^+ in the cellular physiology and physiopathology.

METHODS

DNA Constructs and Cloning. The nucleotide sequence for LSSmKate2, fused at the N-term to the polypeptide linker "ASGGGGGLVPRGSASGA," was codon-optimized for expression in mammalian cells using the OptimumGene algorithm (GenScript, Inc.) and cloned into the pUC57 plasmid between *Bam*HI and XbaI unique restriction sites (see Supporting Information). The mammalian expression vector pcDNA3-LSSmClopHensor was obtained by subcloning the *Bam*HI-XbaI fragment into pcDNA3-ClopHensor (Addgene #25938) to replace DsRed-monomer. The bacterial expression vector pET21-LSSmClopHensor was obtained by PCR amplification from pcDNA3-LSSmClopHensor using the primers NheI-E2-fw (5′-CTAGCTAGCGTGAGCAAGGGCGAGGA-3′) and XhoI-LSS-rv (5′-CCGCTCGAGGCGATGGCCCAGCTT-3′) for insertion into the multiple cloning site of pET21b vector (Novagen). Digestions with NheI and XhoI restriction enzymes were performed following the manufacturer's instructions (New England Biolabs). The bacterial expression vector for LSSmKate2 was prepared according the following procedure: the sequence encoding LSSmKate2 was PCR-amplified from the pUC57-E2GFPLSSmKate2 plasmid using primers NheI-LSS-fw (5′-CTAGCTAGCGTGAGCGAACTGATTAAGGAG-3′) and XhoI-LSS-rv (5′-CCGCTCGAGGCGATGGCCCAGCTT-3′). The insert was digested with NheI and XhoI restriction enzymes following the manufacturer's instructions (New England Biolabs).

Spectroscopy Analysis of Proteins *in Vitro*. Recombinant LSSmClopHensor and LSSmKate2 were expressed in the *E. coli* BL21 (DE3) strain (Invitrogen) and purified by His-tagged affinity chromatography. Starter cultures were grown overnight in LB Broth (Sigma-Aldrich) containing 100 mg mL^{-1} of ampicillin (Sigma-Aldrich) at 37 °C. Bacterial cultures were pelleted 24 h after induction with 1 mM isopropyl β-D-1-thiogalactopyranoside (IPTG; Sigma-Aldrich) at 30 °C. Purification by affinity was carried out using HIS-Select Cartridges (Sigma-Aldrich) following the manufacturer's instructions and collecting elution in 2 mL fractions. Chloride-free buffers were used in all the chromatography steps ensuring the absence of Cl^- from all preparations. If necessary, protein preparations were concentrated using centrifugal filter devices (Amicon Ultra-15, Millipore)

Absorption spectra were recorded using a steady-state spectrophotometer (model V-550 UV/vis, Jasco, Inc.) equipped with a temperature-controlled cell holder. Fluorescence steady-state data were measured using an EnSpire spectral scanning multimode reader fluorometer (PerkinElmer) with 96-well black bottom plates (PerkinElmer, catalog # 6005279). The temperature was set at 20 and 37 °C, and the well volume was kept at 300 μL. Fluorescence intensities were collected with 100 flashes. Emission spectra were realized with an excitation wavelength of 458 or 488 nm. Excitation spectra were recorded with an emission wavelength of 520 nm. Excitation and emission bandwidths were both set at 10 nm. Fluorescence spectra for pH titration were collected at 37 °C using a Fluoromax-4 fluorescence spectrophotometer (Horiba) with excitation and emission bandwidths set at 5 nm.

pH and Chloride Imaging Analysis. The combined pH and chloride ratio analysis was based on the acquisition of three fluorescence signals: a cyan channel with excitation at 458 ± 10 nm and emission at 525 ± 25 nm, a green channel with excitation at 482 ± 18 nm and emission at 525 ± 25 nm, and a red channel with excitation at 458 ± 10 nm and emission at 610 ± 30 nm. For the calculation of Cl^- concentration and pH values, two ratios were defined: R_{Cl} as red-over-cyan and R_{pH} as green-over-cyan. Ratio imaging analysis was performed as previously described[30] with the difference that no correction for fluctuation in the excitation intensity was required in this study, because a single light source (xenon lamp or argon laser) was used with a three-channel (cyan, green, and red) image acquired within brief intervals (1−2 s). Briefly, to estimate the pK_a of LSSmClopHensor from pH titration data, we used the following equation:

$$R_{pH} = \frac{R_B + R_A 10^{pK_a - pH}}{1 + 10^{pK_a - pH}} \quad (2)$$

where R_A and R_B are the plateau values for R_{pH} at acidic and basic conditions, respectively. To estimate K_d from Cl^- titration data, we used eq 3

$$R_{Cl} = \frac{R^0_{Cl}}{1 + \frac{[Cl]}{K_d}} \quad (3)$$

where R^0_{Cl} is the value of R_{Cl} at $[Cl^-] = 0$, a pH-independent and setup-dependent parameter. Accordingly, pH and Cl^- concentration maps were computed pixel-by-pixel using respectively eqs 4 and 5.

$$pH = pK_a + \log\left(\frac{R_{pH} - R_A}{R_B - R_{pH}}\right) \quad (4)$$

$$[Cl] = K_d\,(pH)\frac{R^0_{[Cl]} - R_{Cl}}{R_{Cl}} \quad (5)$$

To remove bleed-through in every channel, we calculated the intensity ratio of bleed-through in every emission channel using E^2GFP and LSSmKate2 proteins separately in independent experiments and varying intracellular pH in the range from 5.2 to 7.9 (Supporting Information Figures S13 and S14 and Table S1). The resulting images, corrected for bleed-through, were then used to perform ratio analysis.

Fluorescence Microscopy and Image Analysis. Images from cultured cells were recorded using a wide field microscope (iMIC, Till Photonics). Specimens were sequentially excited using a high stability 150 W xenon lamp (Oligochrome, Till Photonics) equipped with a fast filter switching device and the two required excitation filters: FF02-482/18-25 (Semrock) and the laser cleanup filter z 458/10x (Chroma). A dual band dichroic mirror Di01-R488/561 (Semrock) was hosted in the filter cube. Emitted fluorescence was collected from 1.2 NA, using a 60× water immersion objective, and split (at about 560 nm) into green and red channels using a single band dichroic mirror (FF560-Di01, Semrock) mounted into a dichrotome device (Till Photonics). The split channels were then simultaneously projected onto half of the electron multiplied charged-coupled device (Ixon Ultra 897; Andor Technologies). The three channels required by ratiometric analysis were thus recorded alternating between two excitation filters. Imaging of rat cortical brain slices was performed using a confocal laser scanning microscope (TCS SP5-RS, Leica) with a time frame acquisition of 0.995 s (seven line average). Excitation wavelengths were sequentially switching between 458 an 488 nm; emission bands were set from 498 to 560 nm and from 560 to 720 nm for the green and red channels, respectively. The setup was also equipped with a CCD camera for differential interference contrast images. All experiments were performed in layer II/III.

Image processing was performed using custom Fiji macros. Images were filtered with Gaussian filter (sigma = 1.5). Mean background fluorescence was measured in empty regions and subtracted to all images. Images were semiautomatically segmented on the basis of pixel intensity using the isodata algorithm (*getAutoThreshold* method). Masked images were then used to discriminate regions of interest (cells) and prevent artifacts arising from dividing background by background values.

Cell Culture and Calibration. HEK 293 cells and SK-N-SH cells were cultured in Dulbecco's modified Eagle's medium (DMEM; Sigma-Aldrich) supplemented with 10% Fetal Bovine Serum (FBS; Sigma-Aldrich), 2 mM L-glutamine (Sigma-Aldrich), 100 U/mL penicillin (Sigma-Aldrich), and 100 mg/mL streptomycin (Sigma-Aldrich) in a humidified 5% CO_2 incubator at 37 °C. All cells were

DOI: 10.1021/acschembio.6b00103
ACS Chem. Biol. XXXX, XXX, XXX−XXX

transfected using Effectene reagent (Qiagen) following manufacturer protocol. For differentiation, SK-N-SH cells were seeded to a confluence of approximately 30% in DMEM supplemented with 5% FBS, 2 mM L-glutamine, 100 U/mL penicillin, 100 mg mL^{-1} streptomycin, and 10 μM retinoic acid (Sigma-Aldrich). The medium was changed every 2 days adding fresh retinoic acid. Differentiation was usually completed in 6 to 8 days when cell soma assumed a fusiform to triangular shape and elongation of slender neuritic processes was observed.[55] For SK-N-SH cell transfection, the manufacturer protocol was adapted as follows: we doubled the amount of DNA and incubated transfection cocktail overnight in DMEM containing FBS (5%) and retinoic acid (10 μM).

Calibration in cells was realized as previously described.[30] The desired [Cl^-] and pH were controlled by equilibrating extra- and intracellular ion concentrations using the K^+/H^+ exchanger nigericin (5 μM), the protonophore carbonyl cyanide *p*-chlorophenylhydrazone (CCCP; 5 μM), the K^+ ionophore valinomycin (5 μM), and the Cl^-/OH^- exchanger tributyltin chloride (10 μM) in the presence of high-K^+ 20 mM HEPES buffer containing 0.6 mM $MgSO_4$, 38 mM sodium gluconate, and 100 mM potassium gluconate. A specified amount of gluconate anion was replaced by Cl^-; pH was adjusted with aliquots of NaOH. To avoid CO_2-dependent pH shifts during calibrations, cells were maintained in a CO_2-free atmosphere at 37 °C. Medium was replaced with proper buffer and changed five times every 2 min to ensure stabilization of intracellular ionic concentrations.

Brain Slice Preparations and *in Utero* Electroporation. All experiments involving animals were carried out in strict accordance with the guidelines established by the European Communities Council Directive and approved by the National Council on Animal Care of the Italian Ministry of Health. The number of animals used was reduced to the minimum necessary for an adequate statistical analysis.

Coronal cortico-hippocampal slices were prepared from postnatal day 16–22 electroporated Wistar rats. Briefly, rats were deeply anesthetized with intraperitoneal injected Zoletil (40 mg/kg; Virbac). After decapitation, the brain was removed and transferred to an ice-cold cutting solution containing (in mM): NaCl, 120; KCl, 3.2; KH_2PO_4, 1; $NaHCO_3$, 26; $MgCl_2$, 2; $CaCl_2$, 1; glucose, 10; Na-pyruvate, 2; and ascorbic acid, 0.6 at pH 7.4 (with 5% CO_2/95% O_2). Coronal slices were obtained by using a Leica vibratome VT1000S in the presence of the ionotropic glutamate receptor inhibitor kynurenic acid (2 mM). Slices were recovered for 20 min at 32 °C and then kept at RT.

Standard *in utero* electroporation of layer II/III of the somatosensory cortex was performed as previously described.[56] Briefly, E17 timed-pregnant Sprague–Dawley rats were anesthetized with isoflurane (induction, 3.5%; surgery, 2.5%), and the uterine horns were exposed by laparotomy. The day of confirmation of vaginal plug was defined as E0, and the day of birth was defined as P0. The DNA (0.15–1.5 μg/μL in water) together with the dye Fast Green (0.3 mg mL^{-1}; Sigma) was injected (5–6 μL) through the uterine wall into one of the lateral ventricles of each embryo using a 30G needle (Pic indolor). The embryo's head was carefully held between tweezer-type circular electrodes (10 mm diameter; Nepa Gene) that were wet with PBS while held across the uterine wall. For the electroporation protocol, five electrical pulses (amplitude, 50 V; duration, 50 ms; intervals, 150 ms) were delivered with a square-wave electroporation generator (CUY21EDIT; Nepa Gene). After electroporation, the uterine horns were returned into the abdominal cavity, and the embryos were allowed to continue their normal development.

Electrophysiology and Induction of Epileptic Activity. Brain slices were continuously perfused in a submerged chamber (Warner Instruments) at a rate of 3–4 mL min^{-1} with (in mM): NaCl, 120; KCl, 3.2; KH_2PO_4, 1; $NaHCO_3$, 26; $MgCl_2$, 0.5; $CaCl_2$, 2; glucose, 10 at pH 7.4 (with 5% CO_2/95% O_2). Seizure-like events were evoked in the presence of 4-AP (50–100 μM). The bath temperature was maintained at 30–32 °C by an in-line solution heater and temperature controller (TC-324B, Warner Instruments). A pressure ejection unit (PDES, NPI Electronics) was used to apply a single or double pulse to NMDA (1 mM, Sigma-Aldrich)-containing pipettes with a 3 s interval, a pressure of 4–10 psi, and a duration of 200–600 ms. Typical pipet resistance was 2–3 MΩ. The NMDA glass pipet included an $AgCl_2$ electrode for extracellular local field potential recordings. Field potential signals were filtered at 1 kHz, amplified by an AM-1800 amplifier (AM-systems), and sampled at 10 kHz with a Digidata 1440s interface and pClamp software (version 10, Molecular Devices). Spectrograms of local field potential recording were performed with an algorithm written in Matlab (version R2008b) using logarithmic wavelet windows.

Statistical Methods. Calibration parameters were defined by global fitting to eq 2 and eq 3 using QtiPlot Software (http://www.qtiplot.com). Statistical tests were performed using Scipy (http://scipy.org). The reported *P* values were calculated using either the two-sample Kolmogorov–Smirnov test for statistical difference in distributions or the two-tailed Student's *t* test. Cumulative frequency distribution plots were prepared using Seaborn (http://stanford.edu/mwaskom/software/seaborn).

■ ASSOCIATED CONTENT

Supporting Information

The Supporting Information is available free of charge on the ACS Publications website at DOI: 10.1021/acschembio.6b00103.

Optimized sequence of LSSmKate2, amino acid sequence of LSSmClopHensor in pcDNA3.1+ and pET21b vectors, influence of the ionic strength over pK_a, supplementary Figures S1–S14, and supplementary Tables S1 and S2 (PDF)

■ AUTHOR INFORMATION

Corresponding Authors

*E-mail: jmparedes@ugr.es.

*Phone: +390461314607. E-mail: daniele.arosio@cnr.it.

Author Contributions

J.M.P., A.I.I., L.R.A., and D.A. designed the sensor and *in vitro* experiments. J.M.P., A.I.I., L.R.A., S.S.S., and P.A. prepared LSSmClopHensor constructs. A.I.I. performed calibrations. J.S. and L.C. performed the *in utero* electroporation. L.M. and G.L. performed electrophysiological recordings in brain slices and, with J.M.P. and A.I.I. performed the imaging in neurons. G.C. and G.M.R. designed the brain slice and imaging experiment. J.M.P. and D.A. wrote the manuscript. J.M.P. prepared Supporting Information. All authors reviewed the manuscript and participated in the discussion of the data.

Notes

The authors declare no competing financial interest.

■ ACKNOWLEDGMENTS

We gratefully acknowledge the financial support of Telethon Italy (Grant GGP10138), RESTATE Programme cofunded by the European Union under the FP7 COFUND Marie Curie Action - Grant agreement no. 267224 to J.M.P., MIUR (PRIN 2009XPTWM2) and University of Trento (Progetti di Ricerca 2014).

■ REFERENCES

(1) Faundez, V., and Hartzell, H. C. (2004) Intracellular Chloride Channels: Determinants of Function in the Endosomal Pathway. *Sci. Signaling 2004*, re8.

(2) Hartzell, H. C., and Ruppersburg, C. C. (2013) Functional reconstitution of a chloride channel bares its soul. *Proc. Natl. Acad. Sci. U. S. A. 110*, 19185–19186.

(3) Wolosker, H., de Souza, D. O., and de Meis, L. (1996) Regulation of glutamate transport into synaptic vesicles by chloride and proton gradient. *J. Biol. Chem. 271*, 11726–11731.

DOI: 10.1021/acschembio.6b00103
ACS Chem. Biol. XXXX, XXX, XXX–XXX

(4) Hodgkin, A. L., and Horowicz, P. (1959) The influence of potassium and chloride ions on the membrane potential of single muscle fibres. *J. Physiol. 148*, 127−160.
(5) Maeno, E., Ishizaki, Y., Kanaseki, T., Hazama, A., and Okada, Y. (2000) Normotonic cell shrinkage because of disordered volume regulation is an early prerequisite to apoptosis. *Proc. Natl. Acad. Sci. U. S. A. 97*, 9487−9492.
(6) Okada, Y., and Maeno, E. (2001) Apoptosis, cell volume regulation and volume-regulatory chloride channels. *Comp. Biochem. Physiol., Part A: Mol. Integr. Physiol. 130*, 377−383.
(7) Ransom, C. B., O'Neal, J. T., and Sontheimer, H. (2001) Volume-Activated Chloride Currents Contribute to the Resting Conductance and Invasive Migration of Human Glioma Cells. *J. Neurosci. 21*, 7674−7683.
(8) Schwab, A., Fabian, A., Hanley, P. J., and Stock, C. (2012) Role of Ion Channels and Transporters in Cell Migration. *Physiol. Rev. 92*, 1865−1913.
(9) Payne, J. A., Rivera, C., Voipio, J., and Kaila, K. (2003) Cation−chloride co-transporters in neuronal communication, development and trauma. *Trends Neurosci. 26*, 199−206.
(10) Owens, D. F., and Kriegstein, A. R. (2002) Is there more to gaba than synaptic inhibition? *Nat. Rev. Neurosci. 3*, 715−727.
(11) Rivera, C., Voipio, J., Payne, J. A., Ruusuvuori, E., Lahtinen, H., Lamsa, K., Pirvola, U., Saarma, M., and Kaila, K. (1999) The K+/Cll [minus]| co-transporter KCC2 renders GABA hyperpolarizing during neuronal maturation. *Nature 397*, 251−255.
(12) Alvarez-Leefmans, F. J. (2011) Intracellular Chloride Regulation. *Cell Physiology Source Book: Essentials of Membrane Biophysics*, 221−259.
(13) Planells-Cases, R., and Jentsch, T. J. (2009) Chloride channelopathies. *Biochim. Biophys. Acta, Mol. Basis Dis. 1792*, 173−189.
(14) Deidda, G., Bozarth, I. F., and Cancedda, L. (2014) Modulation of GABAergic transmission in development and neurodevelopmental disorders: Investigating physiology and pathology to gain therapeutic perspectives. *Front. Cell. Neurosci. 8*, DOI: 10.3389/fncel.2014.00119.
(15) Tyzio, R., Nardou, R., Ferrari, D. C., Tsintsadze, T., Shahrokhi, A., Eftekhari, S., Khalilov, I., Tsintsadze, V., Brouchoud, C., Chazal, G., Lemonnier, E., Lozovaya, N., Burnashev, N., and Ben-Ari, Y. (2014) Oxytocin-Mediated GABA Inhibition During Delivery Attenuates Autism Pathogenesis in Rodent Offspring. *Science 343*, 675−679.
(16) Lemonnier, E., Robin, G., Degrez, C., Tyzio, R., Grandgeorge, M., and Ben-Ari, Y. (2013) Treating fragile x syndrome with the diuretic bumetanide: A case report. *Acta Paediatr. 102*, e288−290.
(17) Deidda, G., Parrini, M., Naskar, S., Bozarth, I. F., Contestabile, A., and Cancedda, L. (2015) Excitatory GABAergic transmission impairs synaptic plasticity and memory in Down syndrome. *Int. J. Dev. Neurosci. 47*, 36.
(18) Glykys, J., Dzhala, V., Egawa, K., Balena, T., Saponjian, Y., Kuchibhotla, K. V., Bacskai, B. J., Kahle, K. T., Zeuthen, T., and Staley, K. J. (2014) Local Impermeant Anions Establish the Neuronal Chloride Concentration. *Science 343*, 670−675.
(19) Wietek, J., Wiegert, J. S., Adeishvili, N., Schneider, F., Watanabe, H., Tsunoda, S. P., Vogt, A., Elstner, M., Oertner, T. G., and Hegemann, P. (2014) Conversion of Channelrhodopsin into a Light-Gated Chloride Channel. *Science 344*, 409−412.
(20) Berndt, A., Lee, S. Y., Ramakrishnan, C., and Deisseroth, K. (2014) Structure-Guided Transformation of Channelrhodopsin into a Light-Activated Chloride Channel. *Science 344*, 420−424.
(21) Bregestovski, P., Waseem, T., and Mukhtarov, M. (2009) Genetically encoded optical sensors for monitoring of intracellular chloride and chloride-selective channel activity. *Front. Mol. Neurosci. 2*, 15.
(22) Bregestovski, P., and Arosio, D. (2011) Green Fluorescent Protein-Based Chloride Ion Sensors for In Vivo Imaging, in *Fluorescent Proteins II* (Jung, G., Ed.), pp 99−124, Springer, Berlin.
(23) Wachter, R. M., and Remington, S. J. (1999) Sensitivity of the yellow variant of green fluorescent protein to halides and nitrate. *Curr. Biol. 9*, R628−629.
(24) Kuner, T., and Augustine, G. J. (2000) A Genetically Encoded Ratiometric Indicator for Chloride: Capturing Chloride Transients in Cultured Hippocampal Neurons. *Neuron 27*, 447−459.
(25) Markova, O., Mukhtarov, M., Real, E., Jacob, Y., and Bregestovski, P. (2008) Genetically encoded chloride indicator with improved sensitivity. *J. Neurosci. Methods 170*, 67−76.
(26) Grimley, J. S., Li, L., Wang, W., Wen, L., Beese, L. S., Hellinga, H. W., and Augustine, G. J. (2013) Visualization of Synaptic Inhibition with an Optogenetic Sensor Developed by Cell-Free Protein Engineering Automation. *J. Neurosci. 33*, 16297−16309.
(27) Arosio, D., and Ratto, G. M. (2014) Twenty years of fluorescence imaging of intracellular chloride. *Front. Cell. Neurosci. 8*, 258.
(28) Pond, B. B., Berglund, K., Kuner, T., Feng, G., Augustine, G. J., and Schwartz-Bloom, R. D. (2006) The chloride transporter Na(+)-K(+)-Cl- cotransporter isoform-1 contributes to intracellular chloride increases after in vitro ischemia. *J. Neurosci. 26*, 1396−406.
(29) Lillis, K. P., Kramer, M. A., Mertz, J., Staley, K. J., and White, J. A. (2012) Pyramidal cells accumulate chloride at seizure onset. *Neurobiol. Dis. 47*, 358−366.
(30) Arosio, D., Ricci, F., Marchetti, L., Gualdani, R., Albertazzi, L., and Beltram, F. (2010) Simultaneous intracellular chloride and pH measurements using a GFP-based sensor. *Nat. Methods 7*, 516−U44.
(31) Navarrete, M., Perea, G., de Sevilla, D. F., Gómez-Gonzalo, M., Núñez, A., Martín, E. D., and Araque, A. (2012) Astrocytes Mediate In Vivo Cholinergic-Induced Synaptic Plasticity. *PLoS Biol. 10*, e1001259.
(32) Brondi, M., Sato, S. S., Rossi, L. F., Ferrara, S., and Ratto, G. M. (2012) Finding a Needle in a Haystack: Identification of EGFP Tagged Neurons during Calcium Imaging by Means of Two-Photon Spectral Separation. *Front. Mol. Neurosci. 5*, DOI: 10.3389/fnmol.2012.00096.
(33) Dzhala, V., Valeeva, G., Glykys, J., Khazipov, R., and Staley, K. (2012) Traumatic alterations in GABA signaling disrupt hippocampal network activity in the developing brain. *J. Neurosci. 32*, 4017−4031.
(34) Glykys, J., Dzhala, V. I., Kuchibhotla, K. V., Feng, G., Kuner, T., Augustine, G., Bacskai, B. J., and Staley, K. J. (2009) Differences in Cortical versus Subcortical GABAergic Signaling: A Candidate Mechanism of Electroclinical Uncoupling of Neonatal Seizures. *Neuron 63*, 657−672.
(35) Piatkevich, K. D., Malashkevich, V. N., Almo, S. C., and Verkhusha, V. V. (2010) Engineering ESPT Pathways Based on Structural Analysis of LSSmKate Red Fluorescent Proteins with Large Stokes Shift. *J. Am. Chem. Soc. 132*, 10762−10770.
(36) Piatkevich, K. D., Hulit, J., Subach, O. M., Wu, B., Abdulla, A., Segall, J. E., and Verkhusha, V. V. (2010) Monomeric red fluorescent proteins with a large Stokes shift. *Proc. Natl. Acad. Sci. U. S. A. 107*, 5369−5374.
(37) Arosio, D., Garau, G., Ricci, F., Marchetti, L., Bizzarri, R., Nifosi, R., and Beltram, F. (2007) Spectroscopic and structural study of proton and halide ion cooperative binding to GFP. *Biophys. J. 93*, 232−244.
(38) Bizzarri, R., Arcangeli, C., Arosio, D., Ricci, F., Faraci, P., Cardarelli, F., and Beltram, F. (2006) Development of a novel GFP-based ratiometric excitation and emission pH indicator for intracellular studies. *Biophys. J. 90*, 3300−3314.
(39) Shaner, N. C., Steinbach, P. A., and Tsien, R. Y. (2005) A guide to choosing fluorescent proteins. *Nat. Methods 2*, 905−909.
(40) Boens, N., Qin, W., Basarić, N., Orte, A., Talavera, E. M., and Alvarez-Pez, J. M. (2006) Photophysics of the fluorescent pH indicator bCECF. *J. Phys. Chem. A 110*, 9334−9343.
(41) Paredes, J. M., Crovetto, L., Rios, R., Orte, A., Alvarez-Pez, J. M., and Talavera, E. M. (2009) Tuned lifetime, at the ensemble and single molecule level, of a xanthenic fluorescent dye by means of a buffer-mediated excited-state proton exchange reaction. *Phys. Chem. Chem. Phys. 11*, 5400−5407.
(42) Ross, R. A., Spengler, B. A., and Biedler, J. L. (1983) Coordinate Morphological and Biochemical Interconversion of Human Neuroblastoma Cells. *J. Natl. Cancer Inst 71*, 741−747.

DOI: 10.1021/acschembio.6b00103
ACS Chem. Biol. XXXX, XXX, XXX−XXX

(43) Acosta, S., Lavarino, C., Paris, R., Garcia, I., de Torres, C., Rodríguez, E., Beleta, H., and Mora, J. (2009) Comprehensive characterization of neuroblastoma cell line subtypes reveals bilineage potential similar to neural crest stem cells. *BMC Dev. Biol. 9*, 12.
(44) Raimondo, J. V., Joyce, B., Kay, L., Schlagheck, T., Newey, S. E., Srinivas, S., and Akerman, C. J. (2013) A genetically-encoded chloride and pH sensor for dissociating ion dynamics in the nervous system. *Front. Cell. Neurosci. 7*, DOI: 10.3389/fncel.2013.00202.
(45) Dzhala, V. I., Kuchibhotla, K. V., Glykys, J. C., Kahle, K. T., Swiercz, W. B., Feng, G., Kuner, T., Augustine, G. J., Bacskai, B. J., and Staley, K. J. (2010) Progressive NKCC1-Dependent Neuronal Chloride Accumulation during Neonatal Seizures. *J. Neurosci. 30*, 11745.
(46) Miyazaki, H., Shiozaki, A., Niisato, N., and Marunaka, Y. (2007) Physiological significance of hypotonicity-induced regulatory volume decrease: Reduction in intracellular Cl- concentration acting as an intracellular signaling. *Am. J. Physiol Ren. Physiol 292*, F1411−F1417.
(47) Losi, G., Cammarota, M., Chiavegato, A., Gomez-Gonzalo, M., and Carmignoto, G. (2010) A new experimental model of focal seizures in the entorhinal cortex. *Epilepsia 51*, 1493−1502.
(48) Gómez-Gonzalo, M., Losi, G., Chiavegato, A., Zonta, M., Cammarota, M., Brondi, M., Vetri, F., Uva, L., Pozzan, T., de Curtis, M., et al. (2010) An excitatory loop with astrocytes contributes to drive neurons to seizure threshold. *PLoS Biol. 8*, 800.
(49) Cammarota, M., Losi, G., Chiavegato, A., Zonta, M., and Carmignoto, G. (2013) Fast spiking interneuron control of seizure propagation in a cortical slice model of focal epilepsy. *J. Physiol. 591*, 807−822.
(50) Kaila, K., Voipio, J., Paalasmaa, P., Pasternack, M., and Deisz, R. A. (1993) The role of bicarbonate in GABAA receptor-mediated IPSPs of rat neocortical neurones. *J. Physiol. 464*, 273−289.
(51) Fukuda, A., Tanaka, M., Yamada, Y., Muramatsu, K., Shimano, Y., and Nishino, H. (1998) Simultaneous optical imaging of intracellular Cl− in neurons in different layers of rat neocortical slices: Advantages and limitations. *Neurosci. Res. 32*, 363−371.
(52) Jose, M., Nair, D. K., Reissner, C., Hartig, R., and Zuschratter, W. (2007) Photophysics of Clomeleon by FLIM: Discriminating excited state reactions along neuronal development. *Biophys. J. 92*, 2237−2254.
(53) Bormann, J., Hamill, O. P., and Sakmann, B. (1987) Mechanism of anion permeation through channels gated by glycine and gamma-aminobutyric acid in mouse cultured spinal neurones. *J. Physiol. 385*, 243−286.
(54) Katayama, H., Yamamoto, A., Mizushima, N., Yoshimori, T., and Miyawaki, A. (2008) GFP-like proteins stably accumulate in lysosomes. *Cell Struct. Funct. 33*, 1−12.
(55) Gaitonde, S. V., Qi, W., Falsey, R. R., Sidell, N., and Martinez, J. D. (2001) Morphologic Conversion of a Neuroblastoma-derived Cell Line by E6-mediated p53 Degradation. *Cell Growth Differ 12*, 19−27.
(56) dal Maschio, M., Ghezzi, D., Bony, G., Alabastri, A., Deidda, G., Brondi, M., Sato, S. S., Zaccaria, R. P., Di Fabrizio, E., Ratto, G. M., and Cancedda, L. (2012) High-performance and site-directed in utero electroporation by a triple-electrode probe. *Nat. Commun. 3*, 960.

DOI: 10.1021/acschembio.6b00103
ACS Chem. Biol. XXXX, XXX, XXX−XXX

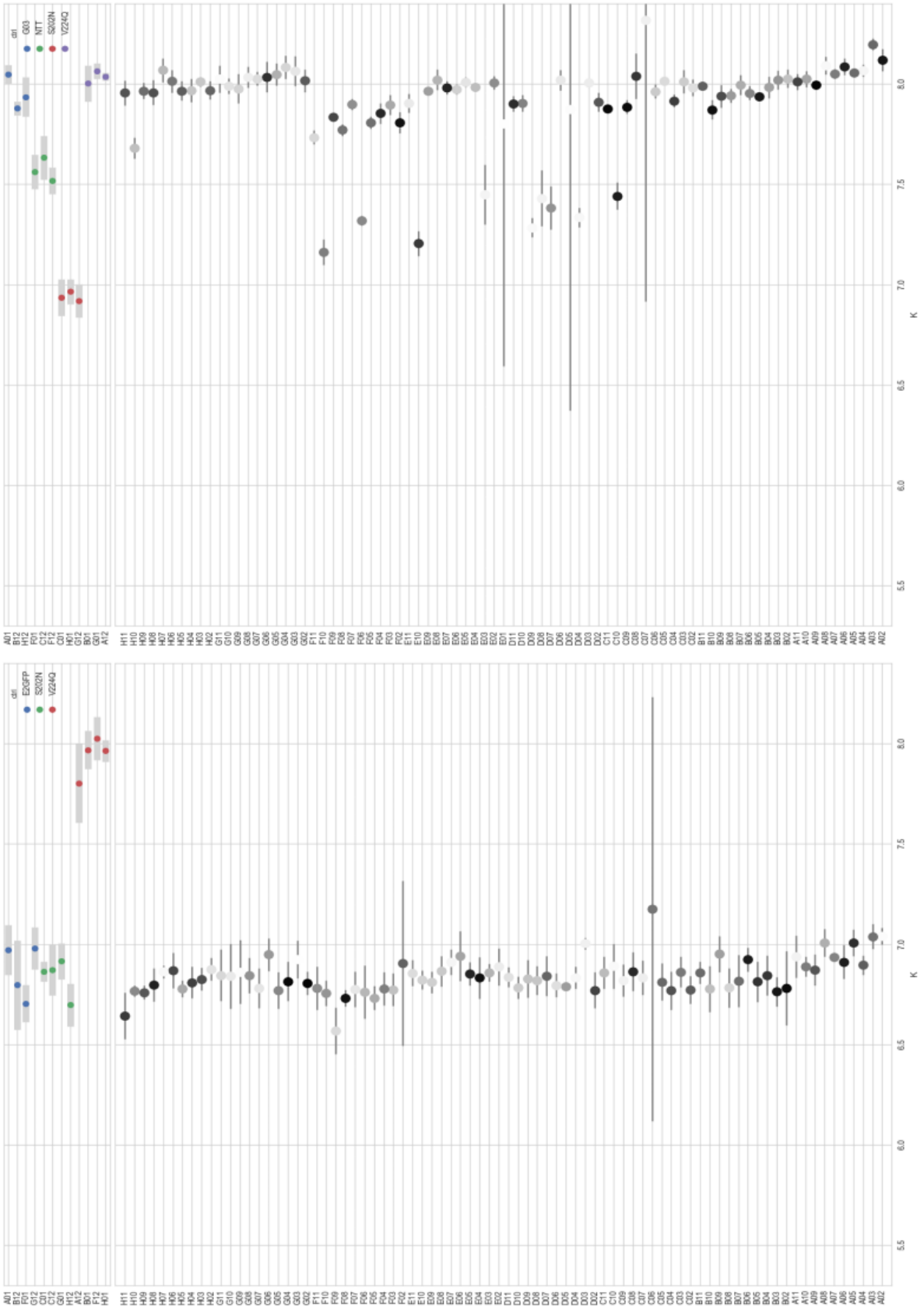

Figure 3.9: **Comparison of GFP library pK_a.** Comparison of pK_a values between early generation library, on the left part, and a later generation library, on the right part, showing an overall increase of the pK_a values. Controls are reported at the top in triplicate.

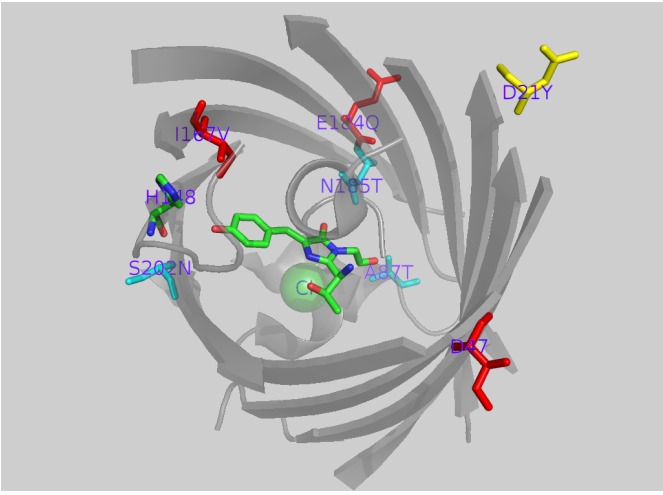

Figure 3.10: **Residues affecting GFP protonation equilibria.** 3D representation of key residues determining GFP pK_{α}.

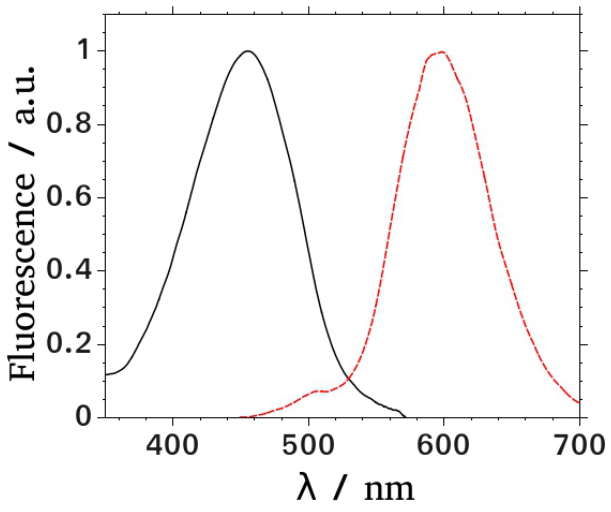

Figure 3.11: **LSSmKate2 excitation and emission spectra.** Excitation and emission spectra for recombinant LSSmKate2, respectively, at emission (605 nm) excitation maxima (460 nm).

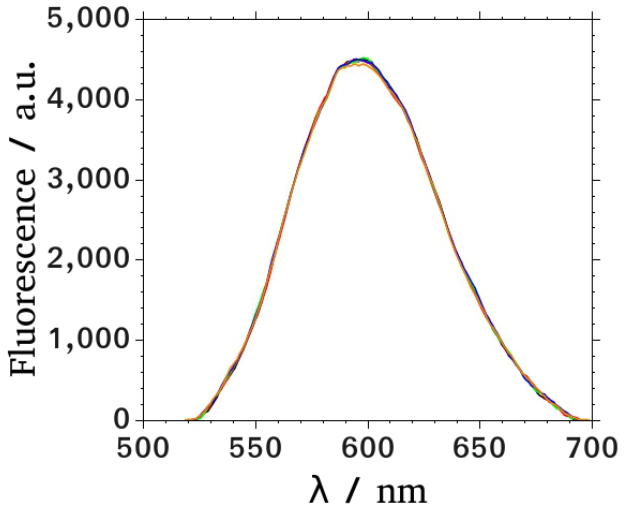

Figure 3.12: **Chloride dependence of LSSmKate2.** Emission spectra of recombinant LSSmKate2 collected at the [Cl^-] values of 0, 250, 500, 750 and 1000 mM (pH=7.2) with excitation wavelength set at 460 nm.

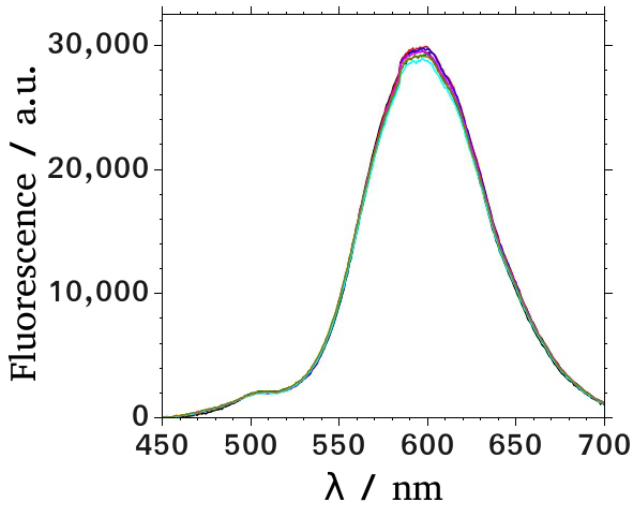

Figure 3.13: **pH dependence of LSSmKate2.** Emission spectra of recombinant LSSmKate2 collected at the pH values of 5.2, 6.2, 6.6, 7.0, 7.4, 7.6 and 8.4 ([Cl^-]=0) with excitation wavelength set at 460 nm.

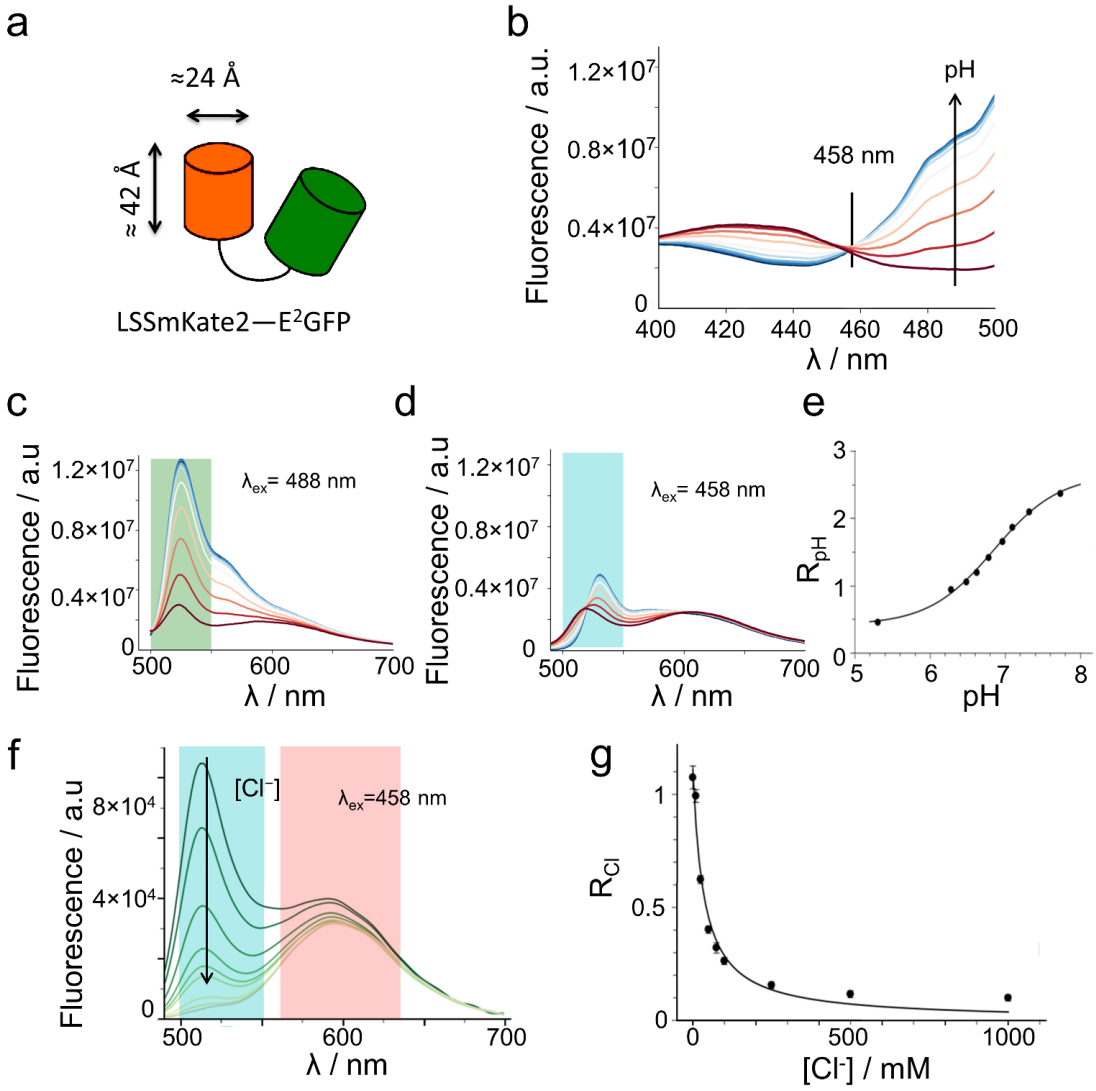

Figure 3.14: **Spectroscopy characterization of purified LSSmClopHensor.** (a) Schematic representation of LSSmClopHensor. Monomer LSSmKate2 dimensions are derived from structural data (PDB code: 3nt3). (b) Excitation spectra at pH values 5.59, 6.01, 6.40, 6.71, 7.12, 7.54, 7.98, 8.42 and 8.72 (color coded from red to blue in the direction indicated by the arrow). Emission wavelength set at 520 nm, $[Cl^-] = 0$ mM and temperature at 37°C. The presence of a single isosbestic point was unambiguously identified at 458 nm. (c, d) Emission spectra collected at the same pH values, from 5.59 to 8.72; excitation wavelength set at 488 (in c) and 458 (in d) nm, $[Cl^-] = 0$ mM and temperature at 37°C. Color shaded areas represent the spectral bands used in the analysis. (e) pH ratio values calculated after integration of emission spectra from 500 to 550 nm (shaded spectral range in c and d). Fitting curve was drawn using [@Eq:rpH] in Methods and the following best fit parameters: R A $= 0.41 \pm 0.03$, R B $= 2.66 \pm 0.04$ and $pK_a = 6.86 \pm 0.03$. (f) Emission spectra at the $[Cl^-]$ values of 0, 10, 25, 50, 75, 100, 250, 500 and 1000 mM; excitation wavelength set at 458 nm, the isosbestic point, pH $= 6.5$ and temperature at 37°C. The arrow indicates increases in the $[Cl^-]$. (g) Chloride ratio values corresponding to the data and spectral ranges reported in f. Fitting curve was drawn using [@Eq:rcl] in Methods and the following best fit ± SD (from fit) parameters: $R^0_{Cl} = 1.12 \pm 0.06$ and $K_d = 33.6 \pm 5.0$ mM.

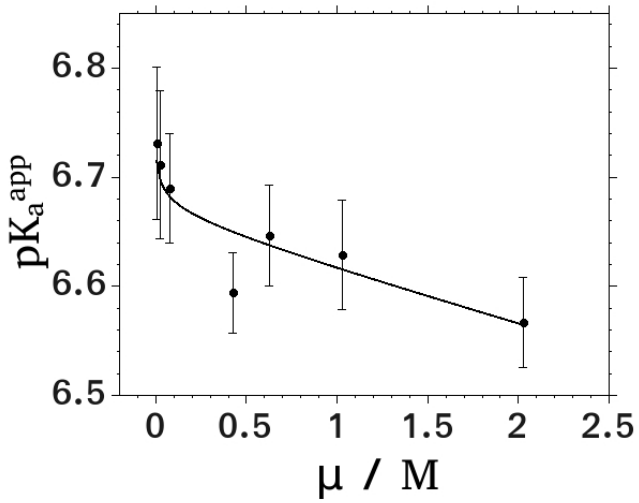

Figure 3.15: **Effects of ionic strength on E^{2}GFP pK_a.** E^{2}GFP pK_a values plotted vs. the solution ionic strength . pK_a values were calculated from E^{2}GFP emission spectra collected at various pH values, generally from 5 to 9. The theoretical curse was drawn (solid line) using the best-fit parameter pK_a = 6.74 ± 0.02 (see Appendix). The apparent pK_a of E^{2}GFP decreases moderately from 6.75 to 6.55 when ionic strength was increased from 0 to 1 M by the addition of sodium sulphate (Na_2SO_4). Because the prototropic species involved in the equilibrium own only few charges, the apparent pK_a is poorly sensitive to salt concentration; a great advantage for a fluorescent indicator.

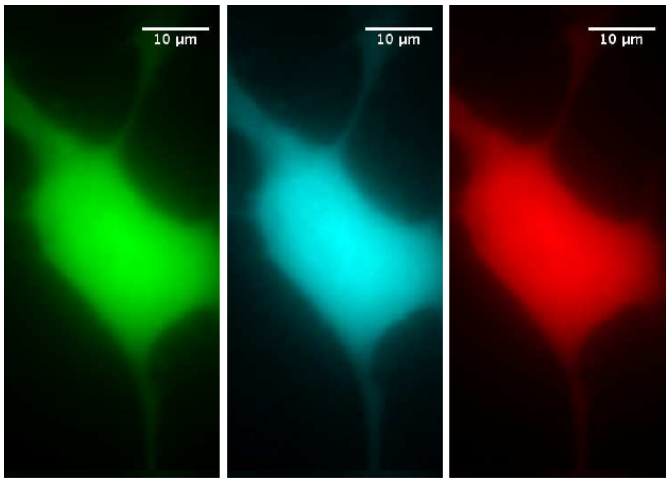

Figure 3.16: **LSSmClopHensor in SK-N-SH cells.** Micrograph of SK-N-SH cells expressing LSSmClopHensor. Green, cyan and red channel are left, middle and right panel, respectively.

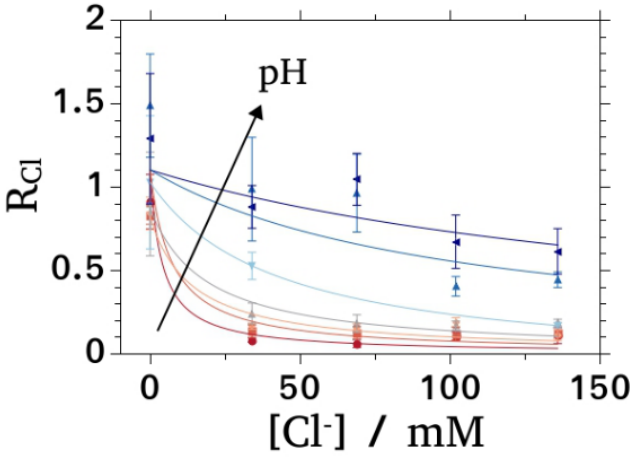

Figure 3.18: **LSSmClopHensor calibration in SK-N-SH cells.** Cyan to Red ratio (R_Cl) values of E^2GFP-LSSmKate2 expressed in SK-N-SH cells at the pH values of 4.85, 5.15, 5.56, 6.58, 6.87, 7.37 and 7.69 and chloride concentration from 0 to 1 M; best-fit curves are overlaid to data points. Error bars display standard deviations.

4

Intracellular chloride measurements

Intracellular chloride and pH are often co-modulated during activity and, since they are fundamental regulators of neuronal excitability, they exert wide ranging effects on synaptic plasticity and in disorders of the brain. The understanding of their homeostasis requires simultaneous measurements in vivo in multiple neurons by non-invasive tools.

Here, by exploiting the fluorescence properties of our sensors, I demonstrate methods for the combined measurement of chloride and pH in models epilepsy and glioblastoma diseases as well as in the mouse cortex in vivo.

My contribution to these work concerns the acquisition and analysis of fluorescence spectroscopy and microscopy data, the setting of transfection procedures

and of the osmotic stress assay in primary cells, the analysis and quantification of pH and Chloride traces in time-lapse and manuscript writing and editing.

4.1 Epilepsy model

The regulation of intracellular Chloride ($[Cl^-]_i$) is a crucial determinant of inhibitory neurotransmission in the brain. In adult neurons, the chloride Nerst equilibrium is close to the resting membrane potential, and GABAergic activity plays its inhibitory role by inducing an inward chloride flux through Cl^--permeable $GABA_A$ receptors. This current hyperpolarizes the membrane potential, keeping neurons away from the potential required to activate depolarizing conductances. In contrast, in the immature brain where GABA is the predominant neurotransmitter, GABA behaves as a depolarizing and mostly excitatory neurotransmitter. Indeed, in early development GABA exerts a key role in the maturation of neuronal networks by supporting network excitability and promoting the maintenance of spontaneous activity (ref). The importance of chloride homeostasis is highlighted by the growing evidences that link anomalous $[Cl]_i$ and the consequent impaired GABA-ergic transmission to a number of neurodevelopmental disorders, including epilepsy, Down syndrome and autism.

This part of the work was conducted in collaboration with Dr. Laura Cancedda, IIT Genova and Dr. Giorgio Carmignoto, Istituto Neuroscienze, CNR, Padova.

4.1.1 Dynamic chloride imaging in neocortical brain slices

Here, we extended the use of LSSmClopHensor to monitor dynamic changes of Cl^- and H^+ concentration in neocortical neuron networks in ex vivo preparations.

Electroporation *in utero* was performed in Sprague-Dawley rats at embryonic day 17 targeting progenitors of pyramidal neurons committed to layers II/III of the cortex. LSSmClopHensor showed a sustained and uniform expression - driven by the CMV early enhancer/chicken β actin (CAG) promoter - in the target neurons (Fig. 4.1).

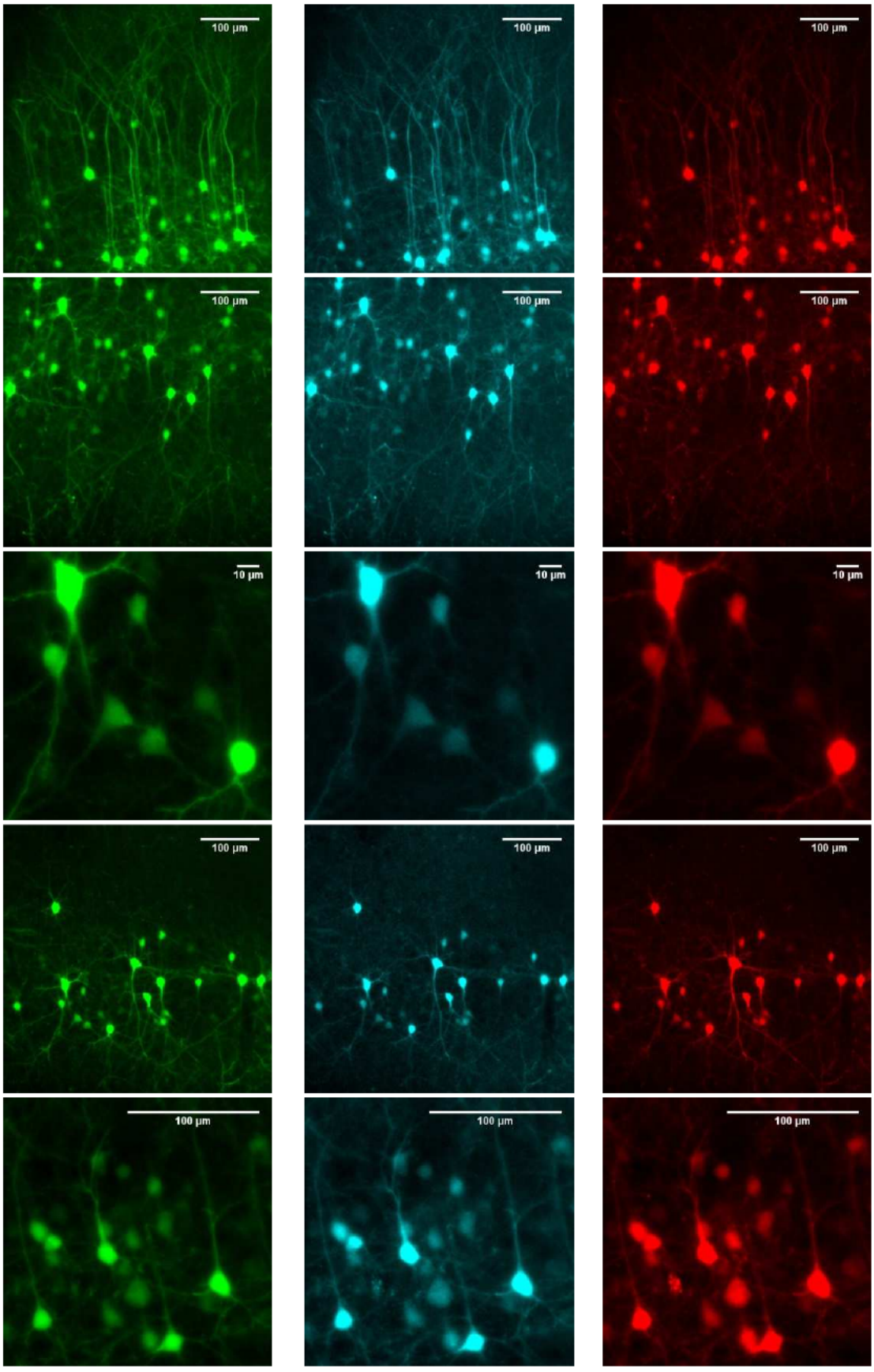
100 µm
100 µm
100 µm
100 µm
100 µm
100 µm
10 µm
10 µm
10 µm
100 µm
100 µm
100 µm
100 µm
100 µm
100 µm

Figure 4.1: **LSSmClopHensor expression in mice.** Neurons expressing LSSmClopHensor after in-utero electroporation. The biosensor presented a homogeneous expression and co-localization of the two fluorophores. Left panels show the green channel (E2GFP emission), middle panels show the cyan channel (E2GFP emission with excitation at isosbestic point) and right panels show the red channel (LSSmKate2 emission).

Neuronal somas and processes were imaged while performing synchronous electrophysiological recordings of local field potentials (LFP). We monitored pH and Cl^- concentration in real time during spontaneous and induced epileptic seizure like discharges (SLDs). Epileptiform activity was induced with 4-aminopyridine (4-AP; 50-100 µM), reduced Mg^{2+} (0.5 mM) and local NMDA brief applications as previously reported [135–137]. A total of 7 somas and 14 dendrites were imaged during successive SLDs from 9 slices. Figure 4 shows a typical experiment with the pH and Cl^- concentration calculated in a neuronal dendrite during 5 consecutive SLDs. Data showed an initial pH value close to 7.15 and a Cl^- concentration below 5 mM, in accordance with values from the SK-N-SH cells and from neurons [111]. SLDs produced an alteration in the fluxes of H^+ and Cl^- at the plasma membrane, causing an intracellular acidification and Cl^- accumulation in the imaged neurons. This observation, in line with previously reported data [43,111,138], pointed out the power of LSSmClopHensor for intracellular pH and Cl^- concentration measurements *in ex vivo* brain tissue. We measured changes of intracellular pH and Cl^- concentration during different SLDs. We calculated pH decreases of (mean ± SD, N=21 recordings from 9 biological replicates) 0.31 ± 0.06 and Cl^- concentration increases of 8.9 ± 3.8 mM (Fig. 4.2).

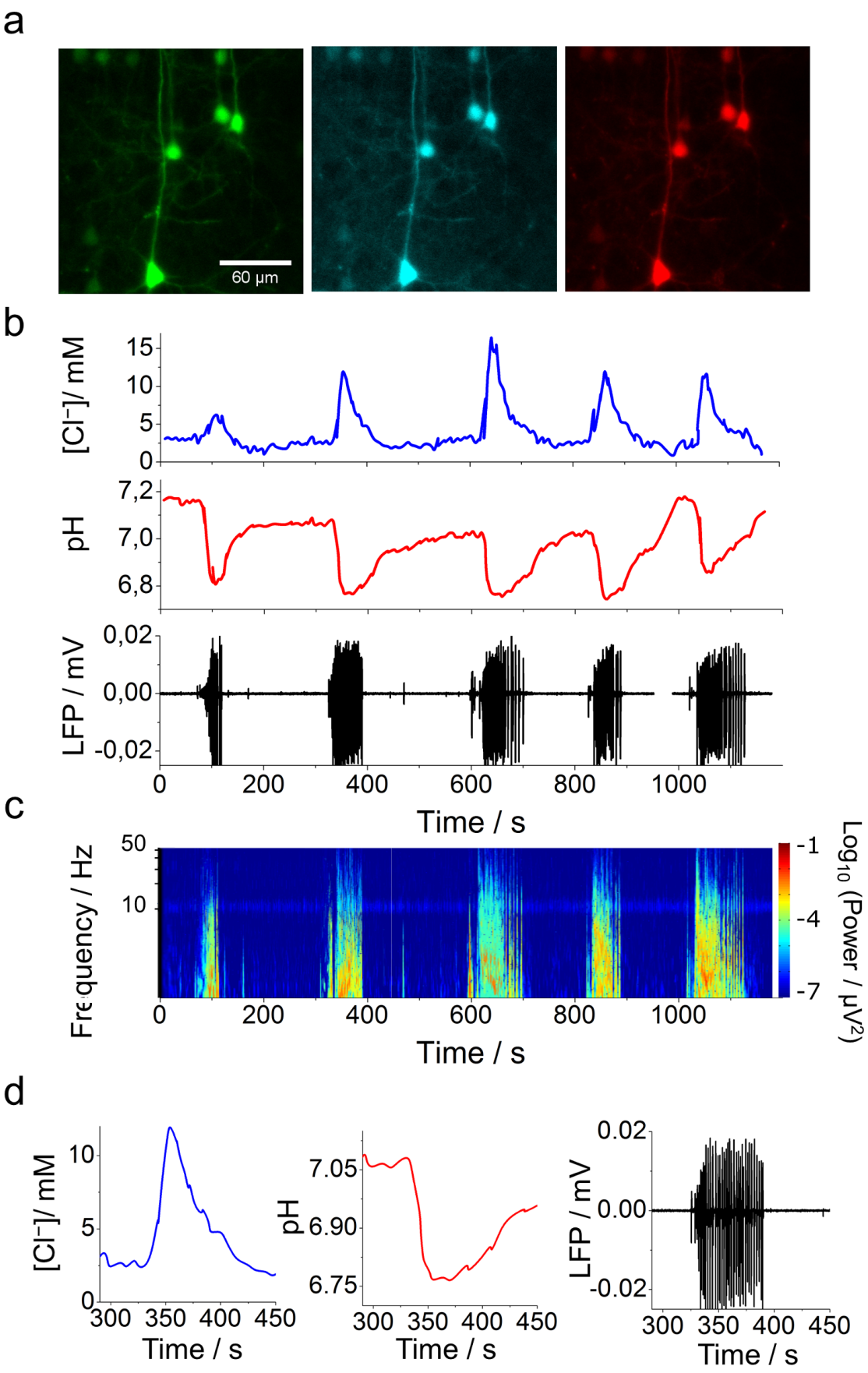
a
60 µm
b
[Cl⁻]/ mM
15
10
5
0
pH
7,2
7,0
6,8
LFP / mV
0,02
0,00
-0,02
0
200
400
600
800
1000
Time / s
c
Frequency / Hz
50
10
-1
-4
-7
Log10 (Power / µV²)
0
200
400
600
800
1000
Time / s
d
[Cl⁻]/ mM
10
5
0
300 350 400 450
Time / s
pH
7.05
6.90
6.75
300 350 400 450
Time / s
LFP / mV
0.02
0.00
-0.02
300 350 400 450
Time / s

Figure 4.2: **pH and chloride imaging and simultaneous LFP recording during epileptiform activity.** (a) Fluorescence images of pyramidal neurons in layer II/III of temporal cortex expressing LSSmClopHensor showing E^2GFP emission (green), E^2GFP emission with excitation at isosbestic point (cyan) and LSSmKate2 emission (red). Scale bar 10 µm. (b) Measurements of Cl^- concentration (blue trace) and pH (green trace) changes over time from a neuronal dendrite expressing LSSmClopHensor. The black trace displays the LFP of five consecutive SLDs recorded during the imaging session. Cl^- concentration and pH values were recorded with a time interval of 990 ms and calculated as reported in Methods. (c) Spectrogram of the recorded LFP representing the dominant frequency during epileptic activity. (d) Zoomed traces from the second SLD of panel b.

4.2 Chloride imaging using 2-photon microscopy in vivo

The intracellular concentration of Chloride ($[Cl]_i$) is regulated by the expression of two cation Cl- cotransporters, NKCC1 and KCC2, which move Cl^- in opposite directions. Their expression is regulated during development: NKCC1 is abundant in the pre and neonatal life, whereas KCC2 is mostly expressed in the adult (ref). This developmental pattern is predicted to cause a shift in $[Cl]_i$ between neonatal and adult brain but all available evidence have been obtained in slices and cultures by indirect means and no direct demonstration of a developmentally regulated change of $[Cl]_i$ has ever been provided. Given the ever increasing role of Cl regulation on development and on the pathophysiology of the brain, a quantitatively sound imaging method for the measure of intracellular Cl is a clear and present necessity. Furthermore, *in vivo* imaging not only allows to study different cells separately, but to image chloride changes occurring in different subcellular domains. Countless studies performed *in vivo* by two photon imaging have contributed to transform radically our understanding of brain operation and synaptic plasticity: just like calcium fluxes indicate neuronal firing and integration of excitatory inputs, chloride fluxes signal the activation of the ionotropic GABA currents. Therefore, imaging of chloride changes could well represent a crucial

tool to understand the dynamic arrangement of ionotropic inhibitory inputs on neurons and their activity dependent plasticity.

It is surprising that, even if mice expressing the fluorescent Cl sensor Clomeleon have been available for several years, there are no reports on chloride imaging *in vivo* yet. Attempts in this direction may have been frustrated by some severe difficulties that arise when converting the fluorescence data in chloride concentration by using calibration data set.

Here, we transfected LSSmClopHensor in utero in mice embryo and chloride imaging of layer 2/3 pyramidal neurons has been performed at various time after birth. We determined that a major confounding effect is due to the wavelength dependent scattering and absorption of both excitation and fluorescence that prevents the straightforward application of the calibration data to the in vivo data. We developed a quantitatively sound method to estimate and correct for these effects and we obtained the first direct measure of the developmental switch of intracellular chloride in vivo.

This part of the work was conducted in collaboration with Dr. Gian Michele Ratto, Istituto Nanoscienze, CNR, Pisa.

4.2.1 Two-photon excitation spectra

First, we characterized the two-photon excitation spectra and its dependency on pH and chloride. We performed the calibration of the purified sensor protein in experimental aqueous solutions where we were able to control pH and chloride concentration with great precision. Furthermore, given the free diffusion of the protein in the imaging chamber, this set of high quality spectra is completely unaffected by photobleaching and has optimal signal to noise ratio. Two-photon

excitation spectra of purified LSSmClopHensor were collected by providing the same number of photons at each wavelength (Fig. 4.3, panel A).

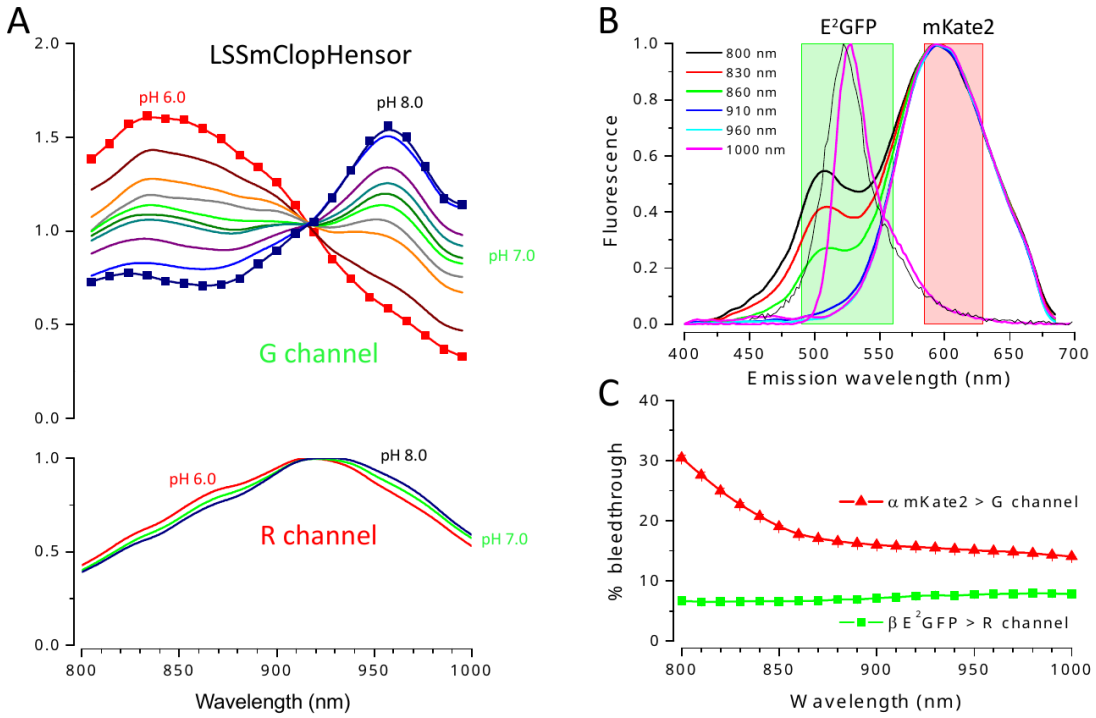

Figure 4.3: **Raw excitation spectra of LSSmClopHensor and fluorescence bleed-through between the acquisition channels.** A) Spectra have been obtained from purified protein in aqueous solution imaged under the two-photon microscope. Data have been normalized at the value of the red fluorescence at 910 nm. The red fluorescence showed an apparent dependency on pH. The symbols indicate the wavelengths at which the spectra have been sampled and have been omitted in most traces for clarity. The non labelled spectra of LSSmClopHensor have been obtained at pH values of 7.6, 7.4, 7.2, 7.1, 6.9, 6.8, 6.4. B) Emission spectra of E2GFP and LSSmKate2 depend on the wavelength of two-photon excitation. The green and red rectangles show the bandwidth of the emission filters of our imaging setup (G: 525/70 nm, R: 607/45 nm). E2GFP shows only a modest change of the emission spectrum which falls mostly inside the G detection channel. For clarity only the extremes spectra (excitation 800 and 1000 nm) are shown. In contrast, LSSmKate2 shows a drastic increase of fluorescence emitted in the G detection channel for wavelength shorter than 850 nm. C) The bleed- through coefficients α and β have been derived by measuring the fluorescence of each protein in the green and red channels. As expected from the emission spectra β is quite constant while α has a strong dependency on excitation below 850 nm.

Similarly, we measured the two-photon excitation spectra of ClopHensor. The excitation spectra of DsRed-monomer and E2GFP showed a poor overlap (Fig. 4.4), thus preventing imaging both proteins at the same wavelengths.

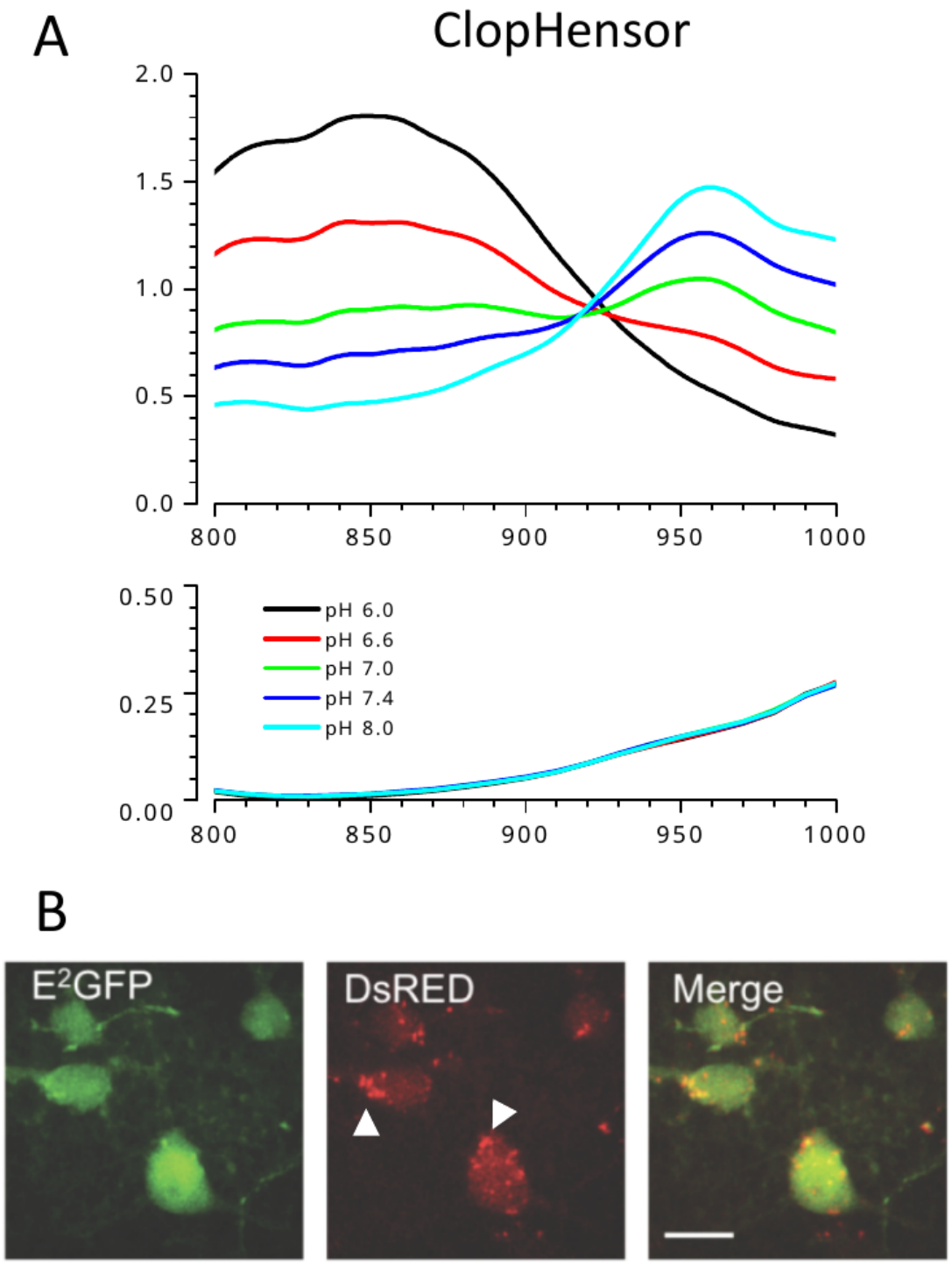

Figure 4.4: **ClopHensor is not suitable for in vivo two-photon imaging.** A) Two-photon excitation spectra of ClopHensor after correction for bleed-through and normalization on the DsRed signal. DsRed has very low fluorescence compared to LSSmKate2 and its excitation is mostly restricted to wavelengths longer than 900 nm. B) The imaging of ClopHensor in vivo shows the formation of red aggregates (arrowheads) which indicated a defective stoichiometry of the sensor, at least in these regions. Calibration bar 20 m.

As expected, the spectra measured in the green channel strongly depended on pH. The pH dependency was also observed in the red channel as a result of bleed-through of the E2GFP emission. The entity of bleed-through was determined by purifying separately the proteins composing the sensor (E2GFP and LSSmKate2, see Supplementary Methods for details) and by measuring their fluorescence in both emission channels (Fig. 4.3, panel B). These data provided the coefficients α(λ) and β(λ) that describe the cross talk between the emission channels (Fig. 4.3, panel C). The fluorescence of E2GFP and LSSmKate2 corrected for bleed-through are given by the following system of linear equations:

$$\begin{aligned} G_*(\lambda) &= G_{raw}(\lambda) - \alpha(\lambda) R_*(\lambda) \\ G_*(\lambda) &= R_{raw}(\lambda) - \beta(\lambda) G_*(\lambda) \end{aligned} \tag{4.1}$$

where G_{raw} and R_{raw} indicate the fluorescence measured in the green and red channels (after background subtraction and flat correction, see supplementary methods) and G_* and R_* indicate the fluorescence that originates from E2GFP and LSSmKate2, respectively. In order to compare the spectra obtained at different pH values we had to consider that different samples had slightly different protein concentrations. Since the optical properties of LSSmKate2 were independent on pH, we normalized each spectrum at the peak of R* and this normalization is used from here onward. The excitation spectrum of LSSmKate2 was pH-independent after correction for bleed-through, while the E2GFP spectra showed a well-defined isosbestic point at about 910 nm (Fig. 4.5, panels A and B).

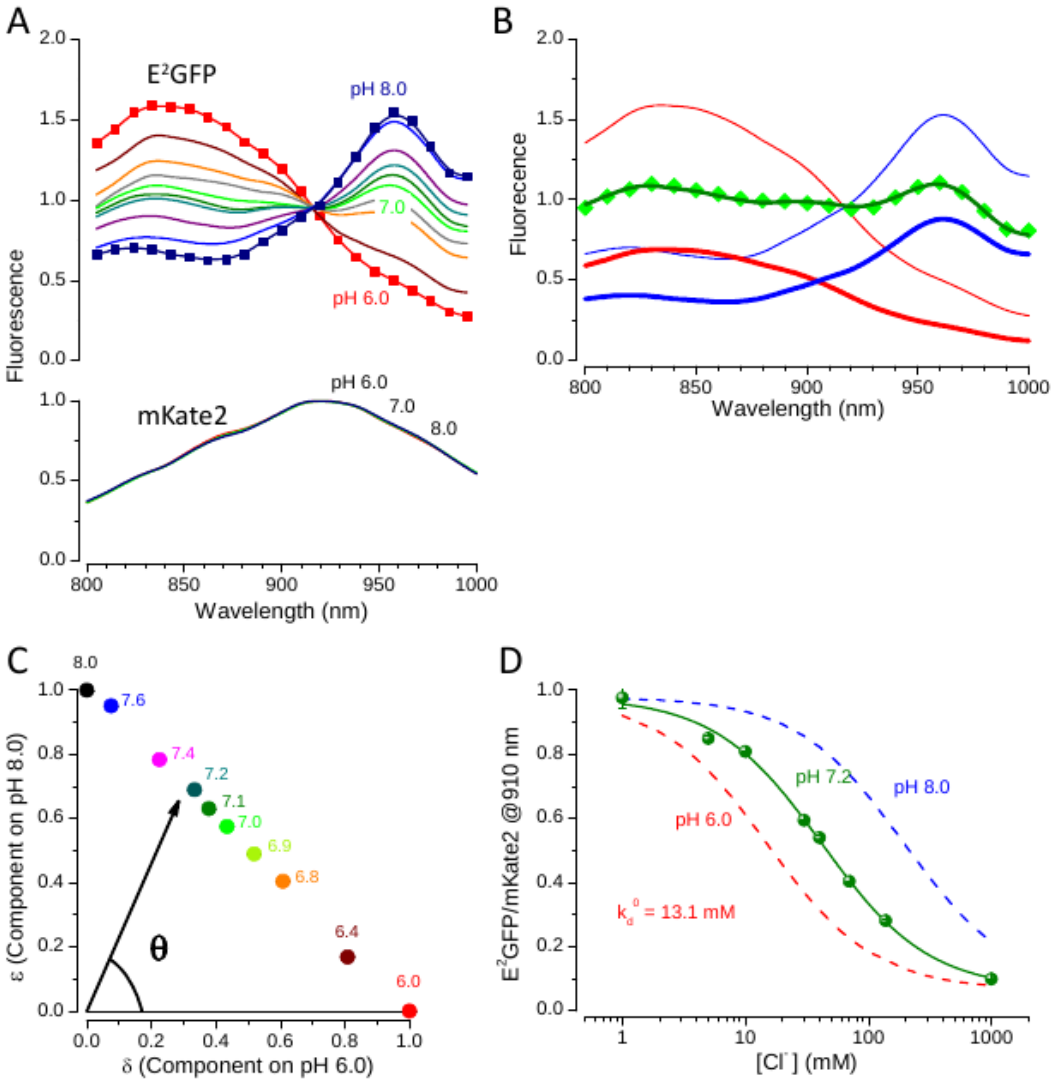

Figure 4.5: **Two-photon LSSmClopHensor spectroscopy.** A) Schematic diagram of the structure of the sensor. B) Two-photon excitation spectra of E2GFP and LSSmKate2 at different pH. Data have been corrected for bleed-through and were normalized on the peak of the LSSmKate2 emission. The excitation spectrum of LSSmKate2 is pH insensitive: the inset shows the difference between the spectra obtained at pH 8, 7 and 6, with the mean spectrum averaged on all pHs. The non labelled spectra of LSSmClopHensor have been obtained at pH values of 7.6, 7.4, 7.2, 7.1, 6.9, 6.8, 6.4. C) Example of liner decomposition of the spectrum obtained at pH 7.0 (green symbols) on the spectra obtained at pH 6.0 and 8.0 (red and blue thin lines respectively). The two components are represented by the thick red and blue curves and the line running through the experimental points is their sum. D) Symbols represent components of the linear decomposition for the set of calibration solutions whose spectra are shown in panel B. The ratio between the components identifies the angle , that is specific to each value of pH. The error bars are contained within the symbol size. E) Chloride determines the quenching of E2GFP fluorescence as shown by the loss of fluorescence measured at the isosbestic point. The chloride Kd depends on pH because chloride binds only the protonated form of LSSmClopHensor. Red and blue dashed lines are calculated for pH 6.0 and 8.0, respectively.

4.2.2 pH calibration

LSSmClopHensor was first used for the ratiometric determination of intracellular pH. Ratiometric measurements, here presented, were usually performed by computing the ratio of the fluorescence signal excited at two different wavelengths. It is however possible to obtain a reliable measurement by sampling the excitation spectra at several wavelengths. The excitation spectrum of LSSmClopHensor at a given pH can be described as the linear combination of the protonated ($G_{*6.0}$) and deprotonated ($G_{*8.0}$) spectra:

$$G_{*pH}\ (\lambda) = \delta G_{*6.0}(\lambda) + \varepsilon G_{*8.0}(\lambda) \tag{4.2}$$

This is a set of n equations where n is the number of sampled wavelengths. If n=2 the system can be solved analytically according to the standard ratiometric analysis. A larger set of excitation wavelengths provides a result that is less sensitive to errors, but the system is overdetermined and there is no analytical solution. δ and ε can then be determined by minimizing the sum of the residues R defined as follows.

$$R = \sum_{i=1}^{n} \left(G_{*pH}\left(\lambda_i\right) - \left(\delta G_{*6.0}(\lambda_i) + \varepsilon G_{*8.0}(\lambda_i)\right)\right)^2 \tag{4.3}$$

The size of the residue is an important indicator of the quality of the fit. We applied this procedure to the data set of Fig. 4.5, A. For each spectrum, the minimum of R determined δ and ε (see Appendix??? for details). Fig. 4.5, B shows the spectral decomposition of a spectral sequence. A calibration curve can be obtained by the relationship between the polar angle (θ=atan(ε / δ), Fig. 4.5, panel C) and the pH of the fitted spectra. The calibration is fitted with the following

sigmoidal function.

$$\theta = \theta_L + \frac{\theta_R - \theta_L}{1 + 10^{(\mathrm{pK}_a - \mathrm{pH})a}} \tag{4.4}$$

Tbl. 4.1 shows the values of the fit parameters at three different temperatures.

Table 4.1: LSSmClopHensor pH and Cl calibrations.

	24°C	31°C	36°C
$\mathrm{pK_a}$	6.88 ± 0.05	6.77 ± 0.05	6.67 ± 0.04
∂_{L}	-6.53 ± 0.16	-8.44 ± 0.24	-12.22 ± 0.24
∂_{R}	93.34 ± 0.11	92.29 ± 0.12	91.97 ± 0.09
a	1.31 ± 0.01	1.34 ± 0.01	1.30 ± 0.012
r(0)	0.98 ± 0.03	1.04 ± 0.03	1.11 ± 0.03

The corresponding functions are reported in Fig. 4.6, B. This calibration was repeated periodically in between *in vivo* experimental sessions and showed only minimal changes.

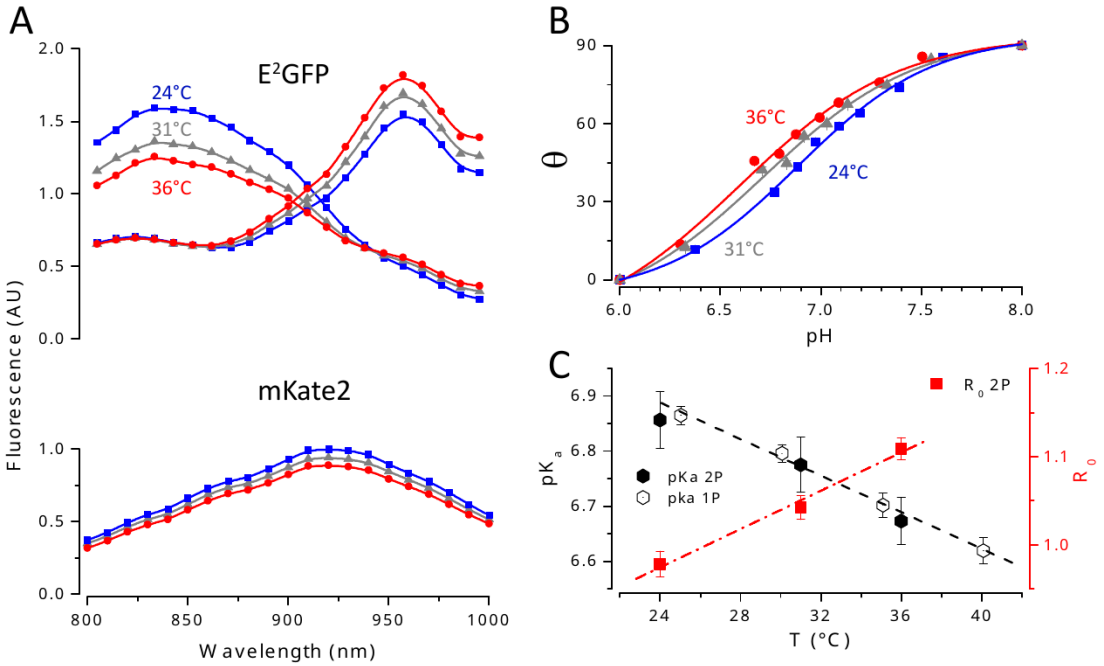

Figure 4.6: **Dependency of LSSmClopHensor calibration on temperature.** A) Excitation spectra at pH 6.0 and pH 8.0 (peaks at about 840 nm and 960 nm respectively) for three different temperatures as indicated in the labels. Notably, the temperature dependency is different for the protonated and deprotonated spectra. The LSSmKate2 spectra experience a slight fluorescence decrease with increasing temperature. B) Calibration curves for pH at three different temperatures. The parameter θ is computed by the spectral decomposition shown in Figure 1. C) Dependency of pKa and R 0 on temperature. The filled and empty black symbols report the pK a measured at 2 and 1 photon excitation, respectively.

This calibration set provides correct results only if the sensor behaves identically in solution and in the cytoplasm, or if one can account for the difference between solution and cellular environment. Since the optical properties of the chromophore are affected by the surrounding cellular environment [139] we repeated the pH calibration in HEK293T cells in presence of ionophores to allow equilibration of pH. Since the measured pH_i was rather variable among cells (Fig. 4.7, panel A), we used the median of the distribution to score the pH of each data set. We observed that the spectroscopic estimate of pH was systematically more acidic than the nominal value of the extracellular calibration media. These data (Fig. 4.7, panel B) allowed the correction of the calibration by accounting for the behavior of the sensor in the intracellular environment (Eq. 4.9).

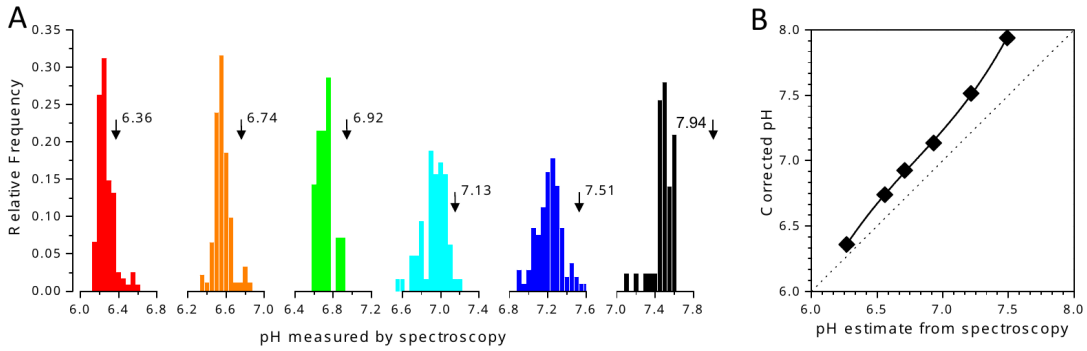

Figure 4.7: **Calibration of LSSmClopHensor *in situ*.** A) Effects of intracellular environment on LSSmClopHensor spectroscopy. HEK293T were transfected with LSSmClopHensor and imaged in zero chloride solution in presence of ionophores to allow equilibration of pH between cytosol and extracellular media. Each group of cells was imaged at 31°C in zero chloride at the pH indicated by the arrow. Each distribution shows the dispersion of the spectroscopic measure of intracellular pH at a given value of extracellular pH. The comparison of these data with the pH of the extracellular solution (vertical arrows), suggests that the spectroscopic readout performed with the reference spectra is systematically more acidic. This must be due to differences of the sensor optical properties when it is placed in aqueous solution or in the cellular environment. The difference between the observed and the expected pH values is used to produce the transformation that corrects the pH values obtained with the spectra measured in calibration solutions. The figure contains data measured from 704 cells. B) The spectroscopic estimate of pH is shifted towards acidic values and has to be corrected according to the empirical function shown here. Error bars (SE) are contained within the symbol size.

4.2.3 Computation of intracellular chloride

E^2GFP fluorescence is quenched upon chloride binding and, indeed, we found that an increase of chloride concentration led to a fluorescence drop (Fig. 4.5, panel D). The relationship between fluorescence change and $[Cl]_i$ is not straightforward: since E^2GFP can bind to chloride only when it is in the protonated state, only a fraction of the sensor fluorescence depends on chloride binding, and this fraction depends on pH. This is summarized by the Eq. 1.2 with the chloride affinity of the fully protonated form of E^2GFP K_d^0 = 13.1 mM. Finally, the intracellular chloride concentration was computed following the method described in Sec. 1.5 with R^0, the ratio between the fluorescence of E^2GFP and LSSmKate2 measured at the isosbestic point and in the absence of Chloride is reported in

Tbl. 1.1.

4.2.4 In vivo delivery of the LSSmClopHensor

To ensure a long-lasting expression *in vivo*, LSSmClopHensor was cloned in an expression vector under the CAG promoter. Plasmids were electroporated *in utero* in mouse at embryonic day 15.5 to transfect neuronal progenitors of pyramidal cells committed to layers II/III of the visual cortex (Fig. 4.8, panels A and B).

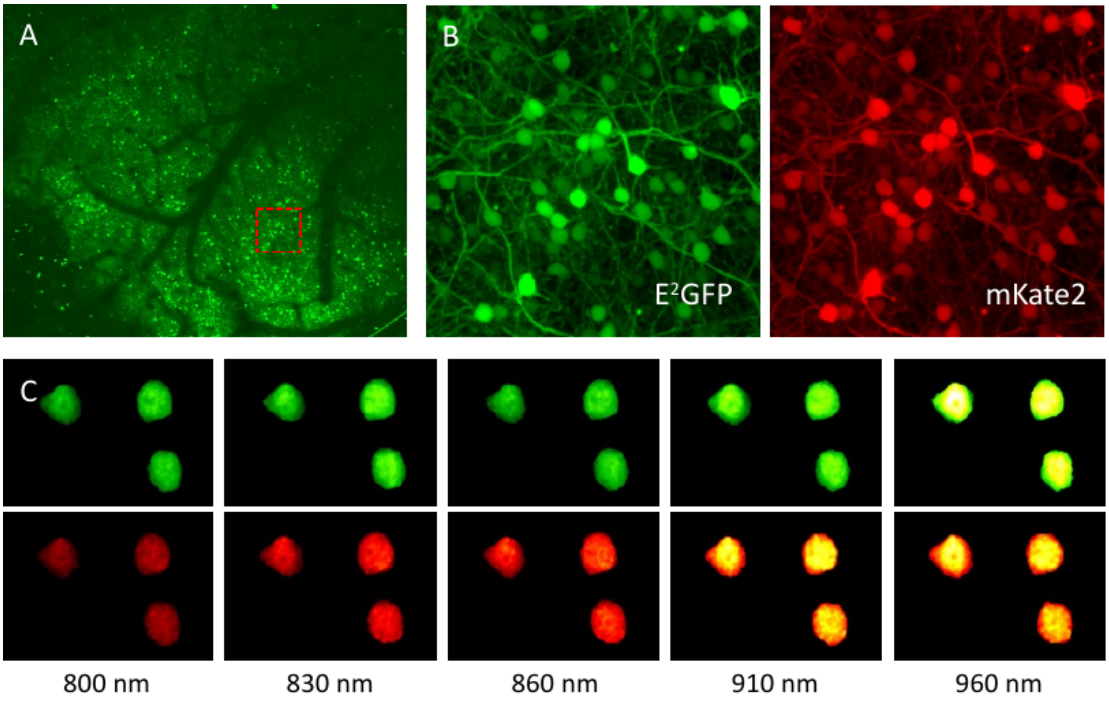

Figure 4.8: **Expression of LSSmClopHensor in vivo after in utero electroporation.** A) Two-photon wide field imaging of the visual cortex in a P32 mouse. The image is a maximum projection of a 250 m stack obtained with a low magnification objective (Olympus, 10X, 0.3 NA, excitation at 910 nm) and shows the entire extension of a 2 mm wide craniotomy. B) Magnified image of the boxed area from panel A showing the E2GFP (green) and LSSmKate2 (red) fluorescence after correction for bleed-through. Field width 200 m, Olympus 60X 1.00 NA. A gamma transform (g=0.5) was applied to the images of A and B to improve visualization of dendrites and cell bodies. C) Example of a spectral series for a P10 mouse. Calibration bar 20 m. D) Quantification of the raw fluorescence of the five cell bodies indicated by the arrowheads (calibration bar 20 m.). Data have only been corrected for flat field illumination and background. E) Spectral measurement of one cell after correction of bleed-through (symbols and line), compared to the raw fluorescence without bleed-through correction (thin lines).

Moreover, collaborators in Pisa verified that the product of expression of the plas-

mid was an intact E^2GFP-LSSmKate2 dimer by performing two independent controls based on *in vivo* FRAP and on the measure of the cross-correlation spectra of fluorescence fluctuations (FCCS).

In vivo studies were performed in adult mice (P18-P60) by acquiring images at several wavelengths under a constant power at the brain surface. A representative example of a spectral series is shown in Fig. 4.8, C. The spectral series were corrected for field illumination and bleed-through before data analysis. In spite of careful data processing, we noticed that the spectra observed *in vivo* showed a clear mismatch with regard of the calibrations. We ruled out any influence of bleaching occurring during the scan in our experimental conditions (Supplementary Methods and figure S5). Owing to spectra distortion, the calculated values of pH and chloride concentration turned out to be very dispersed and showed a pronounced dependency on imaging depth. This suggested that data were affected by wavelength-dependent scattering/absorption of excitation and emission by brain tissue [140].

4.2.5 Effects of brain tissue on sensor spectroscopy

In order to investigate this distortion, we used a mouse line expressing YFP in a sparse population of cortical pyramidal cells line H,). Fig. 4.9, panel A shows the ratio of the fluorescence emitted by YFP when excited at 960 and 910 nm (F960 and F910 respectively). The color-coded transverse section demonstrates that, as the imaging depth increased, F910 decreased compared to F960. These data clearly show that there was a progressive loss of power available at the focal plane with decreasing wavelength, and that this effect increased with imaging depth (Fig. 4.9, panel B). This implies that also the emitted fluorescence undergoes some extinction while propagating from the imaging plane to the brain

surface, with the green fluorescence experiencing more loss than the red one. We obtained a quantitative assessment of this process in the YFP mice. If we measure the fluorescence of recombinant YFP or after expression in cultured cells, the emission spectrum is not altered by extinction: in these conditions, the fluorescence of YFP was distributed in the green and red channels with a ratio R/G = 0.116 (SD = 0.006, n = 10 cells). Then, we recorded the fluorescence in YFP mice in the red and green channels and computed the R/G ratio at various focal depths. As expected, the ratio R/G changed with depth, as shown in Fig. 4.9, panel C, which reports qualitatively the R/G ratio normalized to the R/G value for the isolated protein. Thus, the detected fluorescence underwent an apparent red shift with increasing depth, as quantitatively shown in Fig. 4.9, panel D, that reports the measured R/G ratio at different depths normalized to the R/G value for the isolated protein.

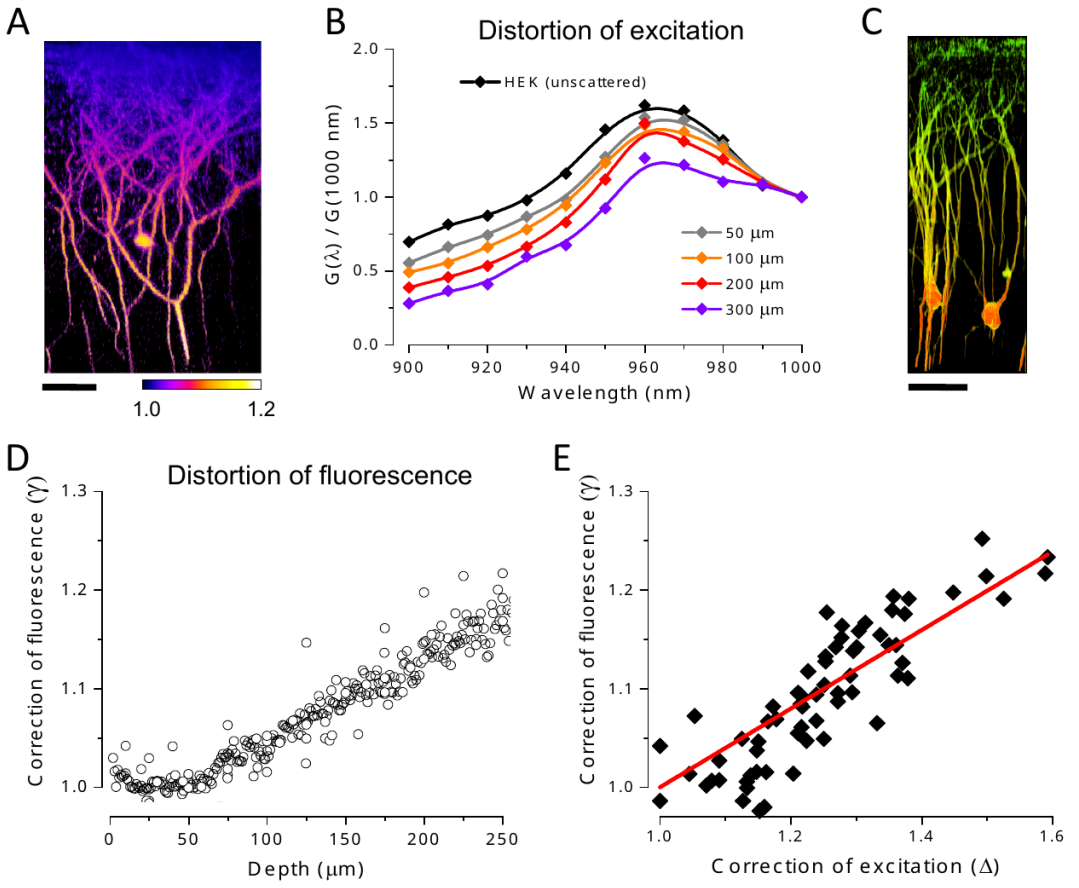

Figure 4.9: **The excitation and emission spectra of intracellular fluorescence are altered when imaging in a thick tissue.** A) Imaging of a YFP expressing mouse demonstrates the wavelength-dependent loss of excitation in vivo. The reconstructed transverse section depicts the ratio of the fluorescence emitted in response to excitation at 960 and 910 nm. The ratio has been normalized to the value measured at zero scattering and the image shows that, as the imaging depth increases, excitation at 960 nm is less attenuated. Calibration bar 50 m. B) Excitation spectra of YFP imaged at different depth in the cortex of one adult YFP-expressing mouse. As a zero-scattering reference, the spectra of YFP recorded in HEK cells is also shown. Spectra have been normalized to the fluorescence measured at 1000 nm. At increasing imaging depth, shorter wavelengths are scattered more and more and less power is delivered at the focal plane with a consequent decrement of fluorescence. Similar results have been obtained in 5 additional mice. C) Effects of imaging depth on the color of recorded fluorescence. The image is a reconstructed transverse section from a YFP expressing mouse. The look-up table codifies for the ratio of the fluorescence recorded in the G and R channels. In HEK cells, the emitted fluorescence is distributed between the G and R channels with a rate of 1 to 0.116. With increasing depth the green fluorescence undergoes more extinction than the red and the rate decreases from 1 to 0.38. Calibration bar 50 m. D) Quantification of the progressive red shift of detected fluorescence with imaging depth. Data collected from 6 YFP-expressing adult mice. E) Correlation between differential excitation scattering (parametrized by D) and fluorescence red shift g (R2=0.73).

Next, we verified whether, for a given focal plane, we could establish a relationship between excitation scattering and emission extinction. Fig. 4.9, D shows the correlation between these two effects as quantified by the measured Δ- pairs at different depths. Δ(z) yields the relative loss of fluorescence excited at 960 and 910 nm, as defined by:

$$(z) = \frac{\mathrm{YFP}_{960}\,(z)}{\mathrm{YFP}_{910}\,(z)}\ \frac{\mathrm{YFP}_{910}\,(0)}{\mathrm{YFP}_{960}\,(0)} \tag{4.5}$$

where the subscripts indicate the excitation wavelength and z indicates the imaging depth. Depth zero corresponds to the fluorescence measured in the absence of scattering and Δ=1 implies that there is no wavelength-dependent loss of excitation power. (z) is defined by:

$$\gamma\,(z) = \frac{R_{\mathrm{YFP}}(z)}{G_{\mathrm{YFP}}(z)}\ \frac{G_{\mathrm{YFP}}(0)}{R_{\mathrm{YFP}}(0)} \tag{4.6}$$

where z is the imaging depth. The value of (z) is 1 in absence of differential

extinction of the fluorescence detected in the R and G channels. Fig. 4.9, E shows that there is a linear relationship between the extinction of emission and the excitation scattering and that it is similar in different mice. Thanks to this finding, if Δ(z) is known the parameter for differential emission extinction can be readily estimated using the empirical relationship:

$$\gamma = 1 + \mu \ ((z) - 1) \tag{4.7}$$

with μ = 0.040 ± 0.02 (n = 66, 6 mice; figure 3E).

4.2.6 In vivo measurements of pH and chloride concentration

To plot the in vivo spectra together with the calibration spectra, we normalized the spectral sequence with the value of the fluorescence of LSSmKate2 at 910 nm. Figure 4A shows the steps of the computation of the steady-state intracellular pH and chloride concentration. The fluorescence of each pixel in the cell body outline was measured and the resulting fluorescence was calibrated and corrected for bleed-through to produce a spectral series for the R and G channels. The fluorescence averaged in a cell body is reported in figure 4A. As explained above, the spectral series must be corrected for excitation scattering before computing the pH values. We performed this correction knowing that R*(ƒ) is pH and chloride independent. Therefore, any divergence between R*(λ) and the LSSmKate2 spectra must be due to excitation scattering. Thus, we computed the correction factors φ(λ) defined as:

$$\varphi_z(\lambda) = \frac{R_{*0}(\lambda)}{R_{*z}(\lambda)} \tag{4.8}$$

where R_{*0} indicates the mKate2 excitation spectra corrected for bleed-through and at depth 0 (no scattering) and R_{*z} indicate the spectral series obtained from the neurons imaged at depth z. We used this set of coefficients to correct the E^2GFP spectra:

$$G_{\prime}\left(\lambda\right) = G_{*z}\left(\lambda\right)\ \varphi_z(\lambda) \tag{4.9}$$

where G_{*_z} indicates the E^2GFP spectra obtained from each imaged neuron at depth z. Fig. 4.10, panel A shows that the effect of excitation scattering on the sensor spectra was very strong. After computation of pH_i by means of the linear decomposition described above, R (Eq:gix_pH) provides a readout of the quality of the pH estimate for each pixel of the image. $[Cl^-]_i$ was then computed using the correction for the extinction of emission Eq. 4.7 and Sec. 1.5. Fig. 4.10, panel B compares the residues R, and the pH and chloride estimates of each neuron acquired in an imaging run. We computed these parameters on the raw data, after correction for bleed-through only, and after correction for excitation scattering and extinction of emission. Strikingly, the dispersion of the pH and $[Cl^-]_i$ estimates and the magnitude of the fit residues decreased radically after correction for scattering and extinction.Fig. 4.10, panels C and D show the chloride and pH maps and the uncertainties (see Supplemental Experimental Procedures for details) of the pH and chloride measurements at each pixel in the outlines of the cell bodies. During acquisition of spectroscopic series, the wavelength presentation was randomized to exclude any bias due to photobleaching. However, in control experiment we verified that the effects of photobleaching on the spectroscopic data was negligible.

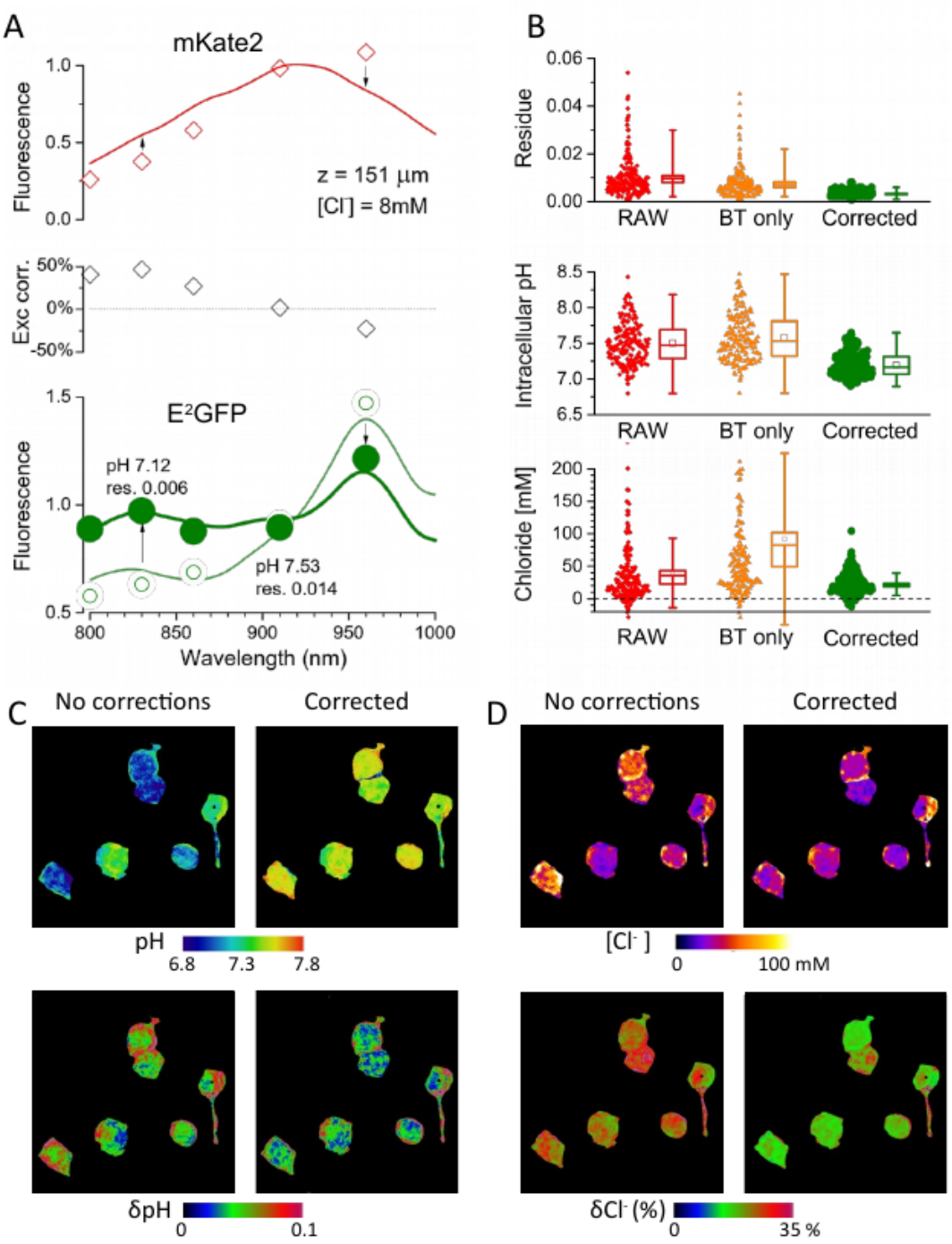
A
mKate2
Fluorescence
1.0
0.5
0.0
z = 151 µm
[Cl] = 8mM
Exc corr.
50%
0%
-50%
E²GFP
pH 7.12
res. 0.006
pH 7.53
res. 0.014
1.5
1.0
0.5
800
850
900
950
1000
Wavelength (nm)
B
Residue
0.06
0.04
0.02
0.00
RAW
BT only
Corrected
Intracellular pH
8.5
8.0
7.5
7.0
6.5
Chloride [mM]
200
150
100
50
0
C
No corrections
Corrected
pH
6.8
7.3
7.8
δpH
0
0.1
D
[Cl⁻]
0
100 mM
δCl⁻ (%)
0
35 %

Figure 4.10: **Raw imaging data and computation of pH_i and $[Cl]_i$.** A) Open symbols: excitation spectrum of LSSmKate2 observed in a field at the depth of 150 m in a P22 mouse. The red line is the LSSmKate2 spectrum obtained in the absence of excitation scattering. As expected there is more loss of fluorescence at shorter excitation wavelength. The middle panel reports the ratio between the reference and the observed spectra. This correction is applied on the E2GFP spectrum, as shown in the lower panel: the open symbols are the original data (after bleed-through correction) and the filled symbols have been corrected for excitation scattering. The lines show the results of best fitted liner decomposition, without (thin line) and with correction (thick line). The corresponding pH and fit residuals are also reported. It is apparent that the distortion of the excitation spectrum causes a shift of the estimate of pH_i towards more alkaline values. B) Each symbol represents the fit residue of a neuron, computed from the raw data of adult mice, with correction for bleed-through only (BT) and fully corrected for excitation and emission scattering. The corrections improve the fit of the spectra thus decreasing the residues. Furthermore, dispersion of the computed pH_i and [Cl]i diminishes. C-D) The pH (C) and chloride maps (D) computed before and after correction for excitation and emission scattering show the decrease of data variability which is also mirrored by the decrement of the uncertainties computed on each pixel (lower maps, see supplementary methods for details). Images have been obtained at an imaging depth of 200 m in a P32 mouse (calibration bar: 25 m).

4.2.7 Scattering-independent measurement of pH by means of E^2GFP fluorescence lifetime

We also wondered whether we could use the fluorescence lifetime as an alternative method to measure pH since this approach would be independent of excitation scattering and of the procedure used to correct the spectroscopic measure of pH for the cellular environment. Fig. 4.11, panel A shows the fluorescence decay of the sensor solution excited at 910 nm. At this wavelength, we measured a mix of the protonated and unprotonated lifetimes yielding a relationship between the time course of fluorescence decay and pH. As previously done, we established a calibration curve between pH and lifetime, both in protein solution and in cells (Fig. 4.11, panel B). Then, we imaged a spectral series *in vivo* for the spectroscopic computation of pH_i. At the end of the spectral acquisition, we measured the fluorescence decay at 910 nm. In this way, we estimated the pH_i of each imaged cell by two independent methods, only one of which was affected by the scattering effects. Fig. 4.11, panels D and E show an excellent agreement of the

two pH measurements.

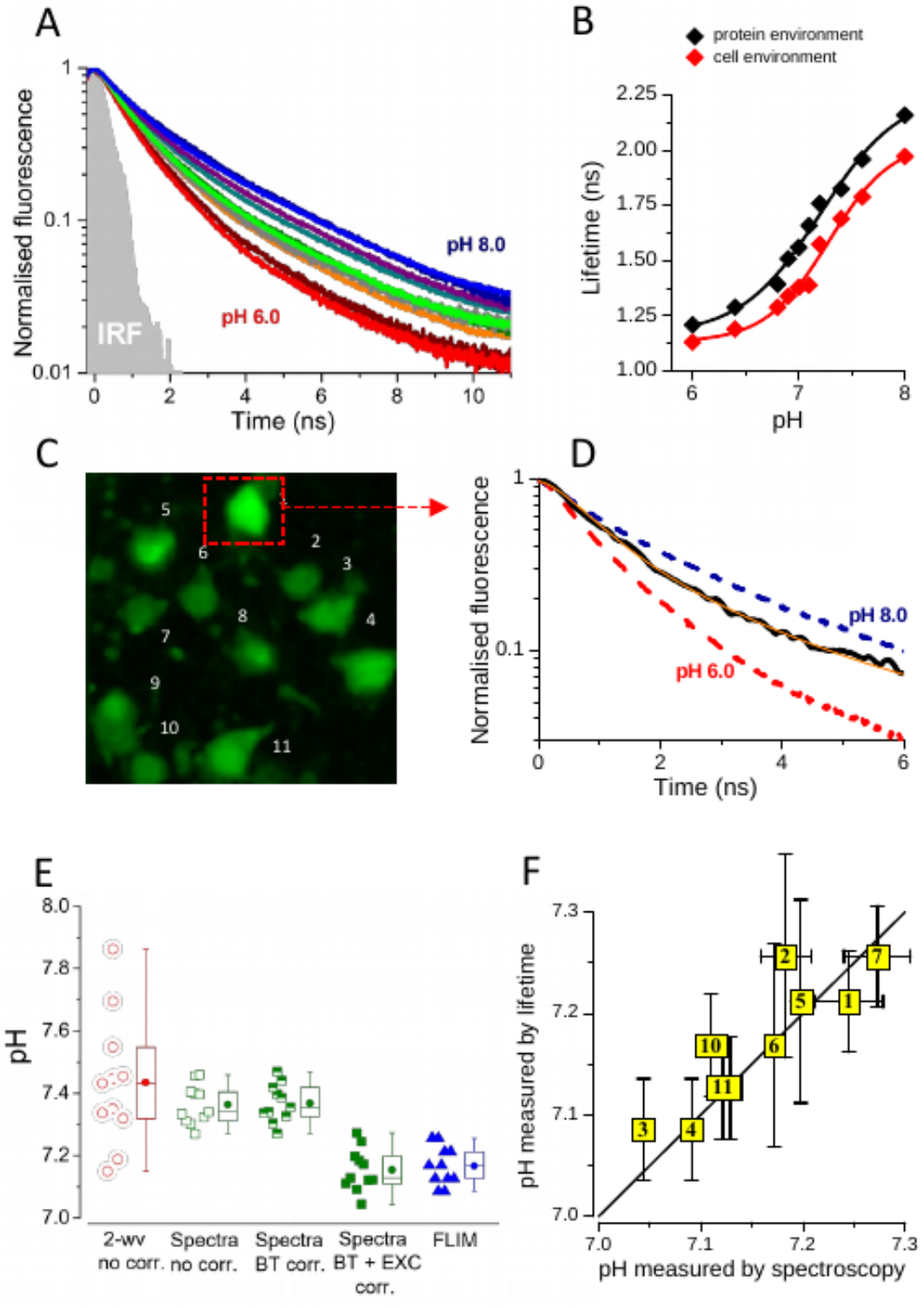

Figure 4.11: **Scattering-independent lifetime measurement of pH.** The lifetime of E2GFP fluorescence can be used to measure pH in a scattering-independent way and to verify the efficacy of the corrections for excitation scattering and intracellular environment. A) Set of lifetime calibration data obtained in cells held in zero chloride and at the specified pH value in the presence of ionophores. For each pH value at least 30 cells were measured. Fluorescence decays have been obtained at pH 6.0, 6.4, 6.8, 6.9, 7.0, 7.1, 7.2, 7.4, 7.6, 8.0. Labels have been omitted for clarity. B) Calibration curves showing the average lifetime of E2GFP vs pH in purified protein solution and in cells demonstrating a difference due to the different environments. C) Two-photon imaging of a field placed at 150 m of depth. The intracellular pH was determined for each labelled neuron by both spectroscopy and lifetime analysis. Calibration bar 15 m. D) Decay of fluorescence as measured in the boxed neuron in (C) (black line) and its fit (orange line). For reference the fluorescence decays at pH 8 and 6 are also shown. E) Comparison of pH values (for of each cell labelled in panel C) in the field as obtained from spectroscopy analysis-without and with different degrees of correction- and from lifetime analysis. From the left: pH computed with a conventional ratiometric method with two excitation wavelengths (910 and 960 nm) and no correction neither for bleed-through nor for excitation scattering; pH computed by spectral decomposition without any correction; pH computed by spectral decomposition and correction for bleed-through only; pH computed by spectral decomposition and correction for bleed-through and excitation scattering. All these data have been corrected for the effect of intracellular environment on spectral properties. The rightmost data set shows the pH measured by FLIM. E) Correlation between the pH measured by spectroscopy and by lifetime shows an excellent agreement between the two estimates after the data are fully corrected for scattering and intracellular environment.

4.2.8 Developmental maturation of chloride homeostasis

We collected spectral series from CD1 mice at three temporal points: P4-5 (10 mice, 650 neurons), P8-10 (n = 8, 591) and from older mice, in the age range P18–P51 (n = 5, 274). From each spectral series we obtained the chloride and pH maps, as shown in Fig. 4.12, panels A and B. This analysis was limited to the cell bodies that provided a better signal following strict criteria for data weighting and exclusion (see Methods). We did not detect any change in pH during development (Fig. 4.12, panel C), while the developmental maturation of chloride concentration was quite obvious. The data pooled from the three groups showed that the median $[Cl]_{i,}$ decremented from 65 ± 25 mM (median ± SD) at p4-5, 45.3 ± 34 at P8-10 down to 11.6 ± 8 mM in the adult group (fig. 6D). These values neatly falls within the range defined by the equilibrium chloride concentration of the prevalent cotransporters: 4 mM for KCC2 and 90 mM for NaKCC1 [13].

According to this view, the high chloride concentration in immature neurons is maintained by the influx of Cl^- ions driven by the symporter NaKCC1. To test this hypothesis, we superfused the cortex of P4-5 mice (n = 7) with the NaKCC1 inhibitor Bumetanide (55 µM) in correspondence of the craniotomy. Imaging was performed immediately after sealing the coverslip and imaging was started. The treatment caused a large decrement of intracellular chloride from 52 mM to 18.5 ± 9 mM, 7 mice, n = 938), confirming the crucial role of NKCC1 in determining the high $[Cl]_i$ in the immature brain (Fig. 4.12, panels E and F).

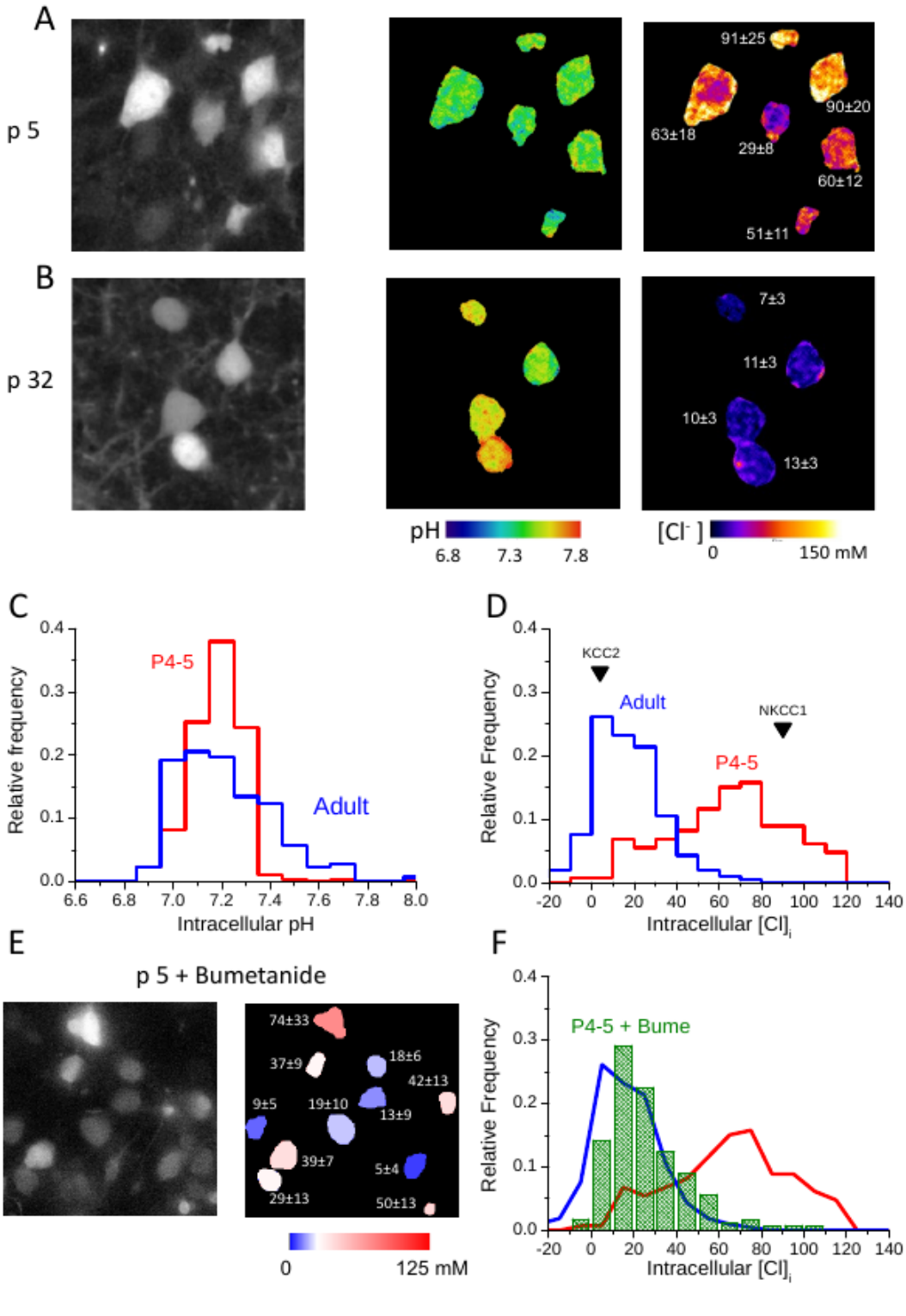
A
p 5
91±25
90±20
63±18
29±8
60±12
51±11
B
p 32
7±3
11±3
10±3
13±3
pH
6.8
7.3
7.8
[Cl⁻]
0
150 mM
C
P4-5
Adult
Relative frequency
Intracellular pH
D
KCC2
Adult
NKCC1
P4-5
Relative Frequency
Intracellular [Cl]i
E
p 5 + Bumetanide
74±33
37±9
18±6
42±13
9±5
19±10
13±9
39±7
5±4
29±13
50±13
0
125 mM
F
P4-5 + Bume
Relative Frequency
Intracellular [Cl]i

Figure 4.12: **Measurement of steady-state intracellular pH and chloride in vivo.** A,B) Two-photon imaging fields in an immature mouse (A) and in an adult (B). Calibration bar 15 m. The color images show the computed pH and $[Cl]_i$ maps for each cell in the field. C,D) Distributions of intracellular pH and $[Cl]_i$ in three different age group. The developmental shift of chloride concentration is obvious. Data pooled from 10 P4-5 mice (650 neurons), 8 P8-10 mice (610 neurons) and 5 mice aged P18-P51 (274 neurons). The arrows indicate the Cl equilibrium concentrations for the cotransporters KCC2 and NKCC1. E) Imaging as in A and B after local application of the inhibitor of NKCC1 bumetanide. This treatment caused a drastic reduction of intracellular chloride to values comparable to adulthood, showing that the elevated $[Cl]_i$ in new born mice is maintained by the operation of NKCC1. The white point in the color scale, corresponds to $[Cl]_i = 25$ mM. Calibration bar 25 m. F) Distribution of intracellular chloride at P4-5 after treatment with bumetanide, compared to the adult and P4-5 control distribution. Treatment did not affect pH (7.23 $\pm$ 0.08, meand $\pm$ SD). Data pooled from 7 treated mice aged P4-5 (938 neurons).

4.3 Glioblastoma chloride and osmotic homeostasis

This part of the work was conducted in collaboration with Professor Anders I. Persson, University of California, San Francisco and Professor Dandan Sun, University of Pittsburgh, Pittsburgh.

Glioblastoma represents the most common and aggressive primary brain tumor with a median survival of 12-15 months post-diagnosis [141]. Each year in the United States, approximately 12,000 new cases are diagnosed with GBM [142]. Inhibition of sodium-potassium-chloride co-transporter NKKC1 reduces proliferation and invasion of GBM cells. We found that compression promotes GBM cell proliferation, an effect antagonized by bumetanide or antisecretory factor (AF). Poor brain penetration and side-effects limit the use of the NKCC1 inhibitor bumetanide in patients. As a solid tumor, GBM is associated with elevated interstitial fluid pressure (IFP) as a result of vascular leakiness and drainage resistance via increased cell density, stromal cell mediated synthesis, and contraction of the interstitial matrix [143]. Fluid accumulation compresses the tumor and surrounding normal tissue, and promotes osmotic swelling of tumor cells. Although studies have clarified the role of IFP on vascular remodeling, it is still

unclear how osmotic changes and mechanical stresses regulate tumor cell biology.

NKCC1 is a major regulator of cell volume under osmotic challenges in mature astrocytes and oligodendrocyte progenitor cells (OPCs), the origins of GBM in mice [144,145] . NKCC1 potently reduced migration and tumor invasion of human GBM cells [146,147]. Cell volume changes caused by accumulation of chloride ions are necessary for cell proliferation and migration of GBM cells [148,149]. Recently was demonstrated that the FDA-approved NKCC1 inhibitor bumetanide (BMT) abrogated restoration of volume increase (RVI; Fig. 4.13) and potentiated TMZ-induced cytotoxicity of primary human GBM cells [150]. However, side-effects from the highly potent diuretic effect of BMT limit its chronic use and it shows poor brain penetrance [151–154].

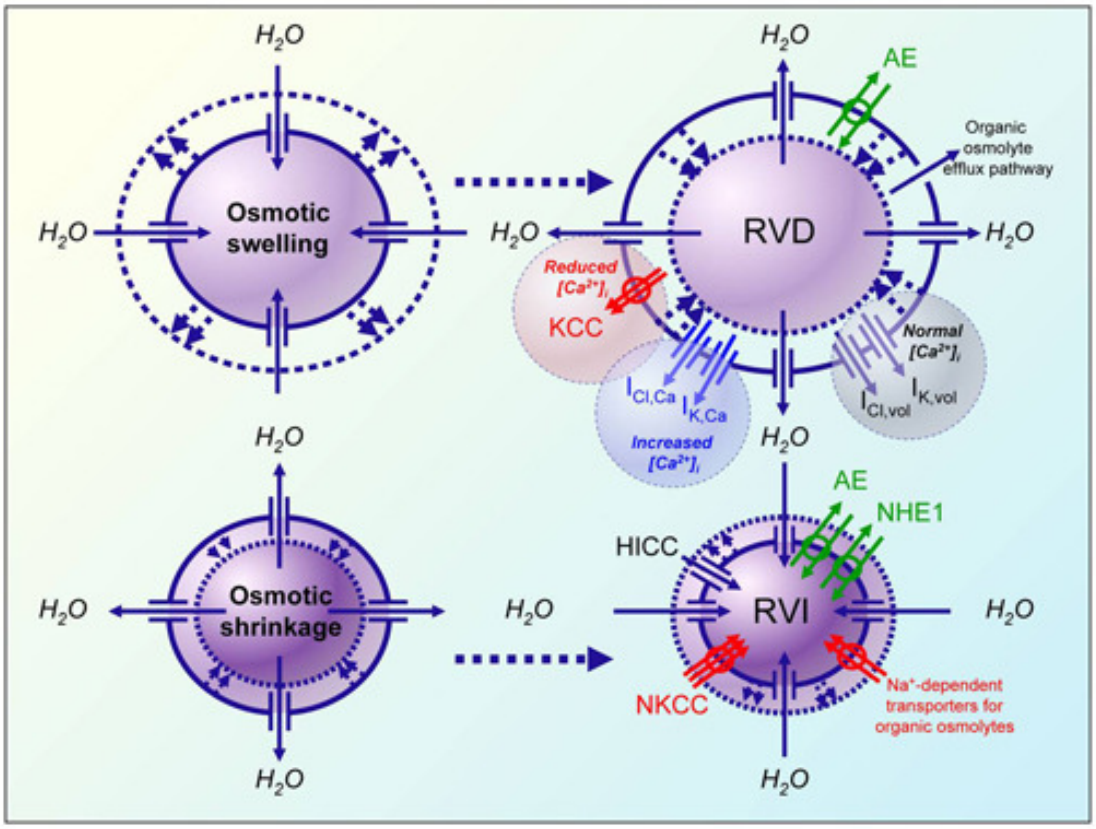

Figure 4.13: **Restoration of volume increase.**

Efforts to identify agents that prevent cholera toxin-induced hypersecretion from intestine lead to the identification of a protein in intestinal organs that demonstrated antisecretory properties [155]. Purification of this antisecretory factor (AF) matched the 41-kDa non-ATPase subunit of the 19S proteasome (AF, PSMD4, Sn5, Rpn10) in a larger 26S polyribosome complex [156–158]. The eight-amino acid N-terminal sequence (aa 35-42) of AF display antisecretory properties in higher vertebrates and humans [159–161]. A specially processed cereal (SPC) induced endogenous AF protein within days following treatment in animals and humans [163,164]. For a more immediate effect, oral administration of AF-rich egg yolk (Salovum, B221) or nasal uptake of AF peptide produced more immediate effects [165–168]. As a naturally occurring protein, endogenous or exogenous induction of AF protein showed no side-effects in animals and patients [163,165]. More recent studies show that AF can regulate fluid dysregulation, including intracranial pressure, in the brain and other organs [164,168–172]. The mechanism of action remains largely unknown but it has been linked to molecular targets known to regulate fluid homeostasis, including the NKCC1 channel [173,174]. Its ability to reduce intracranial pressure in the injured brain, lower IFP in subcutaneous tumors, and increase drug uptake in solid subcutaneous tumors suggest that it might also be effective in GBM.

Expression of NKCC1 increases with glioma grade [175]. Collaborators found that high expression of total and activated NKCC1 in human GBMs. To measure IFP in intracranial tumors of mice, they repurposed telemetry-based methodology to remotely and continuously record IFP during tumor progression in human GBM xenografts. Using a force bioreactor, then they demonstrated that compression increased expansion of human GBM tumorspheres in 3D cultures, provocative results suggesting that tumor pressure reinforces tumor growth. AF peptide, BMT, or NKCC1 knockdown similarly normalized compression-induced

proliferation and the transcriptional phenotype in cultured GBMs.

Elevated intracranial pressure in GBM patients contributes to neuronal degeneration and a plethora of symptoms [176]. Indirect measurement of intracranial pressure in the cerebrospinal fluid space showed elevated pressure (10-100 mmHg) in high-grade glioma patients compared to matched controls (0-5 mmHg) [177,178].

Notably, elevated IFP is also known as a barrier for uptake of chemotherapeutics in solid cancers [143,179]. In this work it was hypothesized that IFP-reducing strategies that inhibit osmotic swelling of tumor cells rather than targeting the tumor vasculature should have fundamentally different effects on drug uptake and GBM biology.

4.3.1 Prevention of restoration of cell volume and chloride permeability

NKCC1 is a major cell volume regulatory protein under normal physiological conditions and plays an essential role to achieve restoration of volume increase (RVI) in response to osmotic stress in glioma cells [150,180]. To test whether AF induction similar to BMT regulates cell volume in GBM cells, 3D imaging was used to analyze tumor cell volume following administration of SPC diet in GBM43 xenografts. Staining of tumors with Phalloidin (to selectively label F-actin) following administration of SPC or control diet showed that AF induction in tumor cells reduced the tumor cell size at terminal stages compared to control mice. A close correlation between total cell volume and nuclear size was found. Tumor cells in SPC-treated mice displayed reduced total cell volume and nuclear size compared to controls.

To study RVI of GBM cells in vitro, we loaded cultured GBM43 cells with cell-permeable calcein dye (calcein-AM), an established marker of intracellular cell volume [119]. Hypertonic exposure led to cell shrinkage in both BMT (10 μM) and AF peptide (5 μg/ml) treated cells and no RVI response was detected within 20 min of hypertonic exposure, implying that both BMT and AF were effective in inhibiting RVI in these cells. Tumor cells incubated with AF peptide failed to surpass the baseline when returned to isotonic conditions and cells where apoptotic compared to cells treated with BMT (Fig. 4.14).

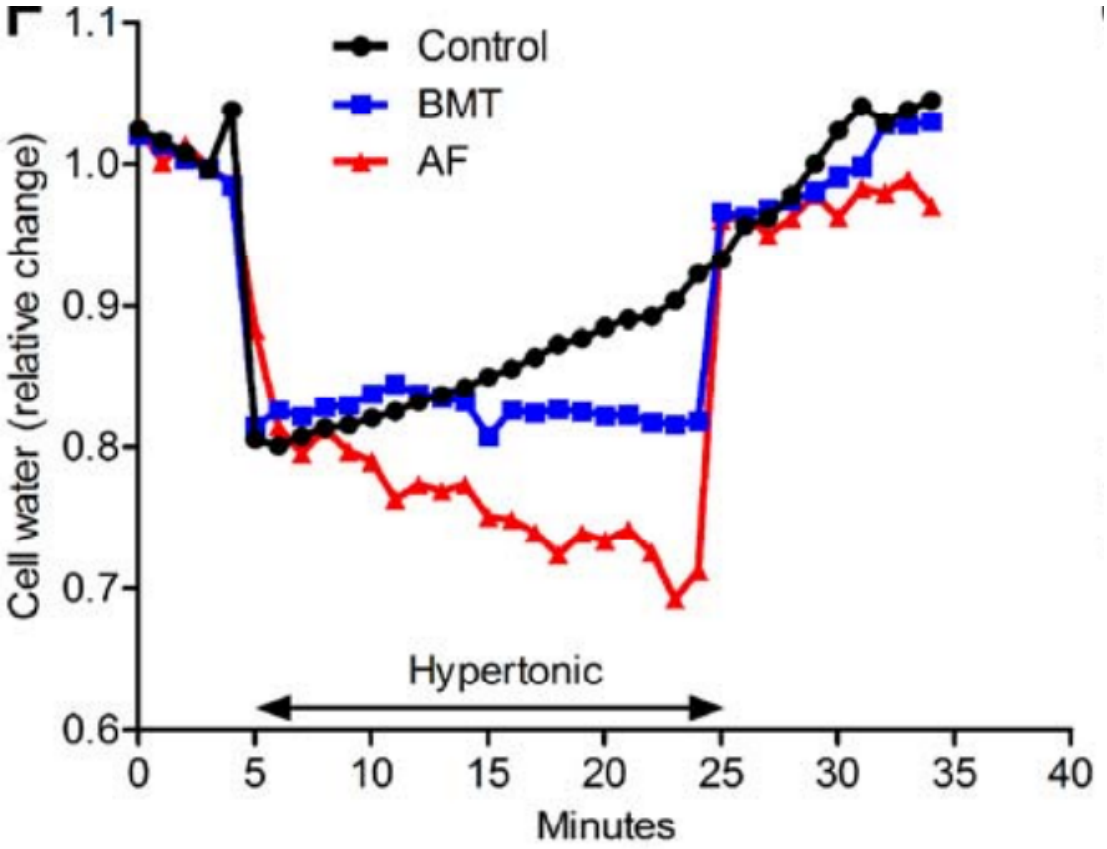

Figure 4.14: **Restoration of GBM cells volume.** Cell shrinkage was induced with hypertonic exposure in both BMT and AF peptide treated cell with no RVI response recorded within 20 minutes of hypertonic exposure.

We have previously demonstrated that BMT regulates chloride permeability in human GBM cells [150]. Thus we electroporated GBM43 cells with ClopHensor (Fig. 4.15) to demonstrate that AF and bumetanide reduced chloride perme-

ability when tumor cells were transferred to hypertonic conditions (Fig. 4.16). Thus AF and BMT similarly prevented adaptation of tumor cells to osmotic challenges, providing a rationale for reduced survival of tumor cells in AF-treated GBM xenografts.

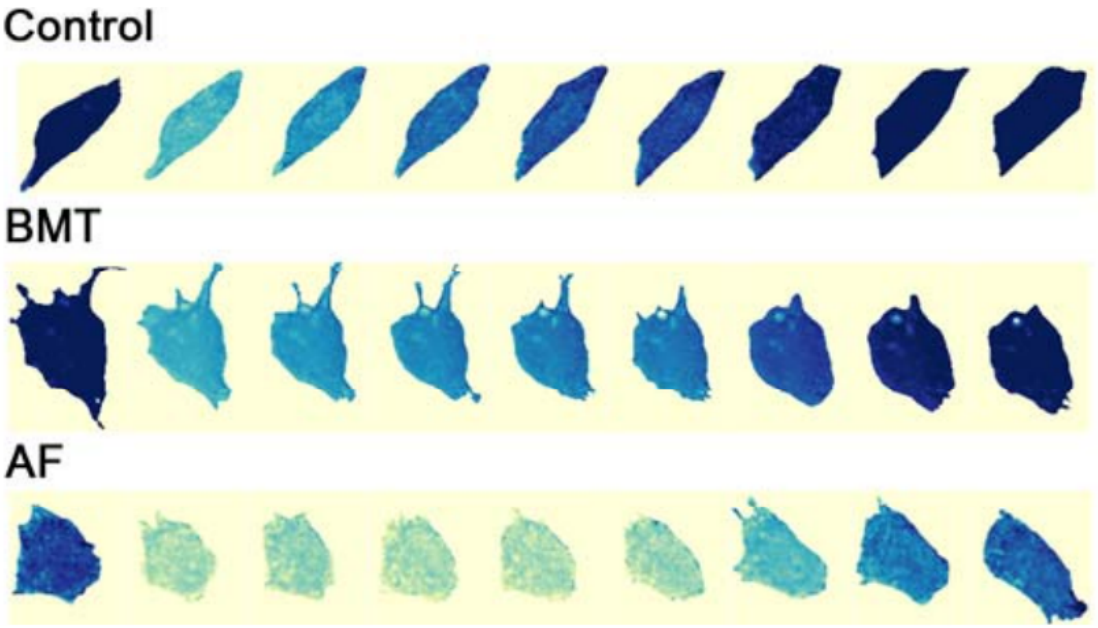

Figure 4.15: Time-lapse recordings of intracellular chloride concentrations in GBM14 cells in the presence of BMT or AF peptide. Cell shrinkage was induced with hypertonic exposure in both BMT and AF peptide treated cell with no RVI response recorded within 20 minutes of hypertonic exposure.

Intriguingly, our collaborators showed that mice administered a combination of SPC diet and TMZ ceased tumor growth and completely prevented tumor recurrence in GBM43 xenografts. Thus, AF therapy effectively increased cellular uptake of chemotherapeutics, resulting in reduced tumor growth and prevention of tumor recurrence in GBM xenografts.

4.3.2 Discussion

Hydrostatic and osmotic pressures contribute to high IFP in solid tumors. AF completely reversed compression-induced proliferation in GBM tumor spheres,

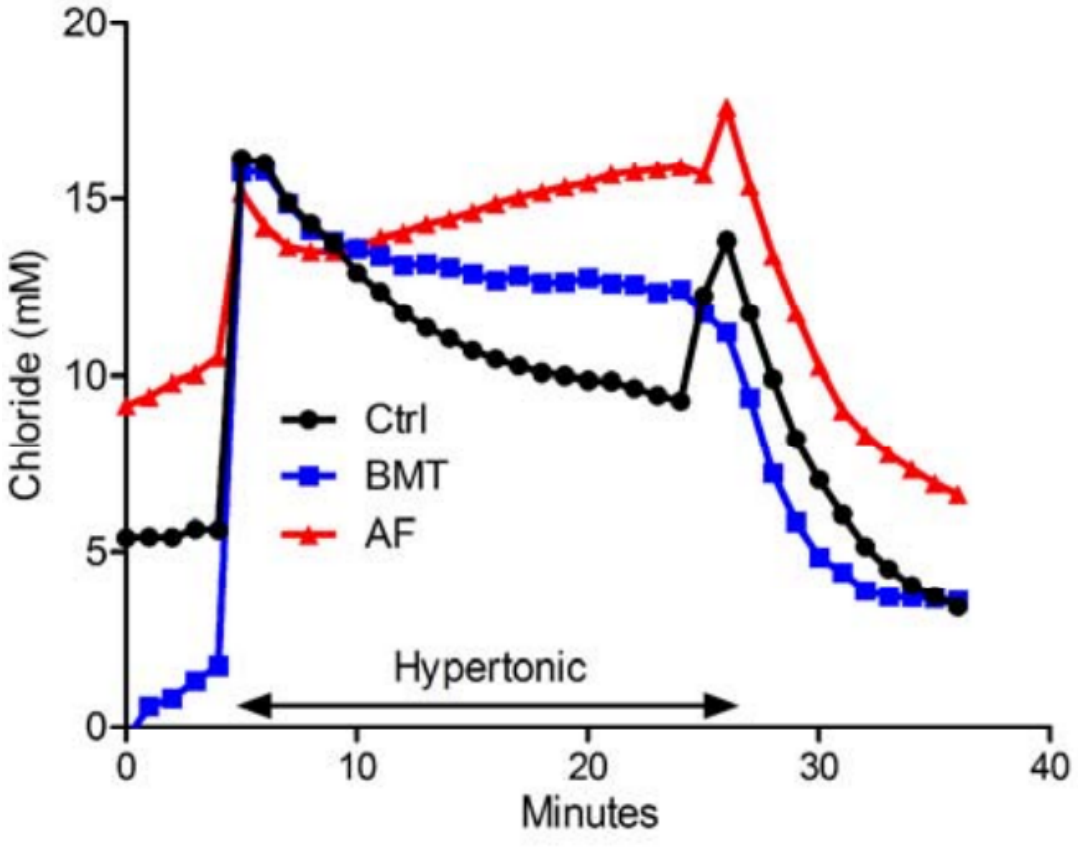

Figure 4.16: **Chloride permeability under hyperosmolar conditions.** Quantifications following adjustment for pH changes showing changes in $[Cl^-]$ following incubation with BMT or AF peptide versus control (PBS). $P < 0.05$.

an effect also achieved using BMT or NKCC1 knockdown. Interestingly, AF peptide had no effect on proliferation when GBM cells were grown under atmospheric pressure.

AF peptide and BMT prevented RVI and chloride permeability in GBM cells grown under hyperosmotic conditions. AF therapy lowered IFP in tumors, reduced tumor growth, and increased the overall survival in mice xenografted with human GBM cells. Fluid accumulation compresses the tumor and surrounding normal tissue, and promotes osmotic swelling of tumor cells as a second barrier to cellular uptake in solid tumors. Lowering of IFP reduced tumor cell proliferation in carcinoma xenografts [181,182]. Invading GBM cells have been shown to maximally decrease their cell volume 30-35%, a value that represents all free unbound

cytoplasmic water [183]. Any volume reduction beyond this value is expected to compromise the viability of glioma cells [184]. In fact, we observed an approximately 40% reduction in cell volume along with massive apoptosis of GBM cells. Reduced cell density was found to increase uptake of doxorubicin and other cytotoxic agents in solid tumors [185]. Our data suggest that AF-mediated inhibition of RVI in tumor cells provides an explanation for the compromised survival of tumor cells and increased intracellular uptake of chemotherapeutic agents in GBM xenografts.

Cell volume regulation is critical for biological processes such as cell proliferation [186–188], migration [189,190], and apoptosis [149,191,192]. Glial cells use several mechanisms to achieve osmotic balance of water, ions, and solutes between the extracellular and intracellular spaces. Cortical astrocytes and neural stem cells (NSCs) give rise to GBM in mice [193,194]. In astrocytes the regulation of chloride fluxes is complex involving a large number of exchangers, transporters, and ion channels, where NKCC1 is a major regulator [144,195,196]. The activity of NKCC1 is strongly stimulated by cell swelling in astrocytes [197]. Although both the NKCC1 and anion exchangers contribute to elevated intracellular chloride levels in neuronal progenitors, only NKCC1 inhibition reduced proliferation of progenitors [198]. NKCC1 knockdown reduced gamma-amino butyric acid type A receptor GABAAR-induced depolarization in NSCs that resulted in reduced proliferation and neuron production [199]. GABA is not only a neurotransmitter but also regulate osmotic swelling in glial cells and neural stem cells (NSCs) through GABAAR signaling [200]. Very low levels of AF peptide (10-13 M) reduced GABA diffusion and Cl- permeation across cell membranes [171,174]. Previous electrophysiological studies indicate that AF modulates GABAAR-mediated responses, but it does not appear to be a general GABA antagonist or agonist [174]. In glioma, cell proliferation was dependent on cell volume in a bell-shaped man-

ner, where shrinkage or osmotic swelling reduced proliferation, and shrinkage also induced apoptosis in tumor cells [187]. Interestingly, functional GABAARs were suggested to be lost in GBM cell lines, but restored when tumor cells were xenografted [201]. Instead, we observed high expression of NKCC1 in cultured GBM cells. Although we are unable rule out other mechanisms of action, our data suggest that AF is directly or indirectly regulating NKCC1 function in GBM cells.

5

Discussion and Conclusion

In this thesis I presented the development of genetically encoded fluorescent biosensors and analysis methods for the quantification of intracellular Cl^- concentrations in living neurons in time-lapse with subcellular resolution.

New sensing elements with improved Cl^- affinity or reduced pH-dependence were identified through rational design and random library screening. A new protein design was engineered exploiting the spectral properties of a long Stokes' shift fluorescent protein (LSS-mKate2) achieving the first LSS-based Cl^- biosensor, LSSmClopHensor, in which a single wavelength is able to excite both green and red biosensor moieties. This was a crucial step that allowed us to extend quantitative chloride imaging to the realm of intact brains and 2-photon microscopy.

Often Cl^- changes are coupled to proton fluxes mediated by chloride-transporting proteins [8,202,203] or by the concomitant activation of different synaptic receptors [32]. Therefore, only approaches that accounts for the local changes of pH can be used for accurate measurements of Cl^- changes or, in other words, for quantitative chloride imaging as this work has shown. The concomitant variation in the intracellular pH and Cl^- level, which is ineludible particularly in neurons, have plagued many previous attempts to develop Cl^- biosensors based on chloride-sensitive fluorescent proteins [51,98]. We overcome this limitation by the introduction of a dual ratio simultaneous quantification of pH and Cl^- levels which requires the acquisition of three images at distinct excitation wavelengths. The savings of an excitation wavelength in LSSmClopHensor allowed the extension of this method to the 2-photon microscopy and – to the best of our knowledge – the first quantification of the decrease of Cl^- concentration from the young to the adult brain; a surprising fact considering that Clomeleon mice have been available for several years. Indeed, we have highlighted how light scattering can substantially perturb ratiometric imaging in brain tissue as confirmed also in a recent report [204].

We have seen how intracellular Cl^- concentration ($[Cl^-]_i$) is a critical determinant for synaptic transmission events. Postsynaptic target neurons can be either excited or inhibited by GABA or glycine release depending on the level of $[Cl^-]_i$ [205,206]. Therefore, chloride imaging represents the only tool currently available for imaging inhibition dynamics in the neurons of the adult brain at low level of $[Cl^-]_i$.

Finally, our quantitative chloride imaging methods were demonstrated also in time-lapse microscopy; in a mouse model following epileptic like discharges and in primary glioblastoma cells following osmotic stress changes. So, Cl^- elevation

during ictogenesis was accurately quantified after measuring also the concurrent local acidification in ex vivo. While in patient-derived GBM cultures, chloride imaging helped to elucidate the mechanism of action of a novel anti-tumor therapy. In particular, it was proved that inhibition of the Cl^- extruder NKCC1 or AF therapy inhibit osmotic adaptation. The consequent disruption of the regulatory volume increase (RVI) mechanism explained the observed induction of apoptosis and reduced proliferation.

As our knowledge on the molecular determinants of Cl^- binding in GFP accumulates, we will be able to engineer even improved biosensor variants that will optimally match $[Cl^-]_i$ and subcellular pH values. In the presence of concomitant pH changes – for instance bicarbonate flux associated to GABA activity – more accurate measurements of $[Cl^-]$ can be based on GFP variants with pH-independent Cl^- binding that we have identified by random mutagenesis.

Ion homeostasis is governed by a highly dynamic metastable equilibrium in which ion distributions balances electrochemical forces. The identification of the cellular determinants of ion homeostasis processes demands new tools of investigation allowing us to scrutinize disputed concepts as the effect of extracellular charges on the distribution of Cl^- within neuronal cells [38]. As occurred in the field of calcium imaging, the development of tools to measure Cl^- in vivo, where neural circuitry are fully preserved, will represent a dramatic improvement in our under- standing of Cl^- regulation and of the mechanisms of GABAA mediated inhibitory activity considering that slice preparation and maintenance procedures affects profoundly Cl^- regulation [103,207]. In vivo imaging might reveal more subtle Cl^- fluxes that are activated in dendrites or in the soma by physiological activity. Compartmentalization within the dendritic tree and the cell body can originate from localized changes in ion homeostasis [208,209] and might differ-

entially affect the inhibitory inputs from different neuronal compartments.

Chloride imaging is playing a growing role in the understanding of brain diseases. Epilepsy is the most obvious pathology that involves alterations in GABAergic transmission. Studies that inspect Cl^- regulation during seizures are accumulating [14,52,134,138,210,211]. All these studies were performed in slices. New studies will be performed in experimental models with intact neuronal circuits; possibly by imaging *in vivo* the hippocampus [212,213]. While epilepsy and Cl^- homeostasis is certainly a very important field, it is becoming clear that the involvement of Cl^- regulation in brain physiopathology is far more extensive. The spectrum of brain diseases associated with defective inhibition is broad and includes both acute conditions like ischemia or traumatic injury [103,214] and chronic conditions like fragile X and autism [215–218]. Dysregulation of Cl^- homeostasis might play an important part in any pathology associated to a defective equilibrium between excitation and inhibition. The availability of diuretics that alter the activity of Cl^- cotransporters and have a long clinical track record makes the modulation of Cl^- homeostasis an attractive target for pharmacological intervention [152,219]. In vivo imaging will likely offer a powerful pre-translational tool for the direct testing of drugs acting on Cl^- homeostasis in different models of brain diseases.

5.1 Future work

Alteration of chloride fluxes plays physiological roles in many tissue homeostasis and cellular processes as well as pathological roles in many diseases. Therefore, several hypothesis can be formulated as further development in the field. For example, chloride ion fluxes can regulate cell migration by exerting housekeeping

functions such as setting membrane potential, intracellular pH, cell volume [22]. While apoptosis affects ions homeostasis by decreasing cell volume, cancer cells are able to interrupt the apoptosis pathways by modulating the expression of chloride and potassium channels on the plasma membrane [192,220]. Chloride homeostasis can thus be considered as a prominent player in the biology of tumor cells; and it can be hypothesized that altered functionality of chloride channels and chloride fluxes are responsible for disrupting the apoptosis pathways and promoting cell migration.

In gliomas, the $Na^+/K^+/2Cl^-$ cotransporters NKCC1 accumulates chloride ions up to the concentration of 100–140 mM, which is about 10 fold higher than in physiological conditions [148]. It means that for chloride ions to function as the energetic driving force for volume decreases, an outward-directed gradient has to be maintained. A hydrodynamic cell invasion model was described for glioma cells where the flux of chloride ions across the plasma membrane is the key determinant of the cellular volume changes and ultimately of invasion [183]. Invading glioma cells would maximally decrease their volume by expelling all free (unbound) water molecules from the cytoplasm; a process powered by the driving force provided by the concomitant Cl^- efflux. Other migratory cells may use similar hydrodynamic mechanism to sustain their migration, where chloride currents are used for cell volume changes. One of the grand challenges of ion channel research is to identify the specific subtype of ion channels that plays a pathogenic role in cancer e.g. oncogenesis [221], progression and cell cycle checkpoints [222], metastasis and angiogenesis, and to develop specific blockers (or openers) for the channel as tumor suppressants [223]. Different kinds of chloride channels, classified according to their activation mechanism (ligandgated, Ca2+dependent and voltagegated), are involved in cancer processes in different cell lines [12]. Yet, the types and subtypes of chloride channels involved are still largely unknown; their

identification is likely to be the subject of future research.

In the near future, it will also be feasible to screen different murine models of brain pathologies for alterations in the development of chloride regulation resolving image chloride compartmentalization between dendritic tree and cell body. Furthermore, sensory cortices offer the opportunity to study incoming GABAergic activity in response to physiological stimuli in regions where the functional architecture is well known.

Another intriguing hypothesis is to consider Cl^- as a **second messenger**. For example, in the CFTR signalling mechanism involved in the expression of CFTR-dependent genes was shown that Cl^- concentration can regulate the expression of specific genes [224]. In particular, the identified the gene RPS27, which encodes the multifunctional ribosomal protein RPS27, suggest an association between Cl^- homeostasis and protein translation regulations, especially in highly differentiated and polarized cells such as neurons. Indeed, dysregulation in the maturation of messenger RNA and in the translation machinery have been associated to the onset of numerous neuron pathologies; in the case of fragile X syndrome a direct link was observed [225].

Finally, Cl^- homeostasis may play a role also in neurodegenerative diseases. By altering osmotic condition of the cells, Cl^- dysregulation could establish environment conditions promoting and sustaining protein misfolding and aggregation and thus cell toxicity. So, the modulation of Cl^- metabolism is emerging as a novel therapeutic target for a variety of neurological diseases.

In conclusion, the methods here presented hold out the promise of disentangling the tight physiological role of bicarbonate, proton and Cl^- in fully preserved neuron circuitry and in a wider range of biological processes.

6

Appendix

6.1 Effects of ionic strength on protein pK_a

Application of the Hendersson-Hasselbalch equation to the studied equilibrium of E^{2}GFP at near-physiological pH provides:

$$pK_a^{app} = pK_a + \log \frac{f_A}{f_N} - \log a_{H_2O} \tag{6.1}$$

where f_N and f_A denote the activity coefficients of the neutral and the anion of E^{2}GFP, respectively, and a_{H_2O} is the water activity.

A semi-empirical function based on the extended Debye-Hückel equation could be used to relate f_i with μ. Using this approach the activity coefficients may be represented as:

$$\log f_i = \frac{-A_{DH} z_i^2 \sqrt{\mu}}{1 + \dot{a}_i B \sqrt{\mu}} + L_i \mu \tag{6.2}$$

In this equation, also called the Truesdell-Jones equation, L_i is an adjustable parameter, typical values for A_{DH} and B at room temperature and atmospheric pressure are 0.51 and 0.33, respectively, $\dot{a}_i$ stands for the ionic radius in Angstroms, and z_i is the ionic charge. Substituting Eq. 6.1 into Eq. 6.2 and assuming a similar radius for N and A states, we can derive Eq. 6.3.

$$pK_a^{app} = pK_a - A_{DH}(z_A^2 - z_N^2)\frac{\sqrt{\mu}}{1 + \dot{a}B\sqrt{\mu}} - L^*\mu - \log a_{H_2O} \tag{6.3}$$

6.2 Sequences

Sequence data are shown as annotated graphic, which were created using [226] TEXshade.

6.2.1 LSSmKate2 codon-optimized DNA sequence

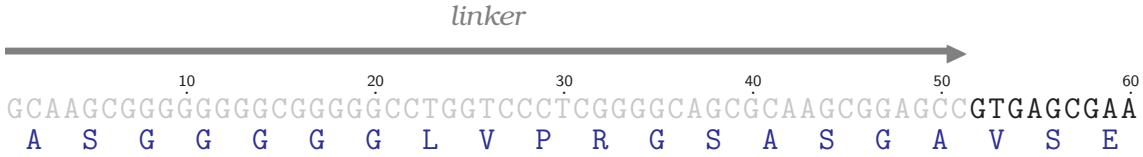

```
                70                  80                  90                 100                 110                 120
CTGATTAAGGAGAATATGCACATGAAGCTGTACATGGAGGGGACAGTGAACAATCACCAT
 L   I   K   E   N   M   H   M   K   L   Y   M   E   G   T   V   N   N   H   H

               130                 140                 150                 160                 170                 180
TTCAAGTGCACTTCCGAGGGCGAAGGAAAACCATATGAAGGCACTCAGACCATGCGAATC
 F   K   C   T   S   E   G   E   G   K   P   Y   E   G   T   Q   T   M   R   I

               190                 200                 210                 220                 230                 240
AAGGTGGTCGAGGGAGGACCACTGCCTTTCGCATTTGACATTCTGGCCACCTCTTTCATG
 K   V   V   E   G   G   P   L   P   F   A   F   D   I   L   A   T   S   F   M

               250                 260                 270                 280                 290                 300
TACGGCAGTTATACCTTTATCAACCACACACAGGGAATTCCTGACTTCTTTAAACAGTCT
 Y   G   S   Y   T   F   I   N   H   T   Q   G   I   P   D   F   F   K   Q   S

               310                 320                 330                 340                 350                 360
TTCCCAGAAGGCTTCACCTGGGAGCGGGTCACCACATACGAAGATGGGGGCGTGCTGACA
 F   P   E   G   F   T   W   E   R   V   T   T   Y   E   D   G   G   V   L   T

               370                 380                 390                 400                 410                 420
GCAACTCAGGACACATCACTGCAGGATGGGTGTCTGATCTATAATGTCAAGATTCGCGGA
 A   T   Q   D   T   S   L   Q   D   G   C   L   I   Y   N   V   K   I   R   G

               430                 440                 450                 460                 470                 480
GTGAACTTTACTAGCAATGGGCCCGTCATGCAGAAGAAAACTCTGGGGTGGGAGGCTGGC
 V   N   F   T   S   N   G   P   V   M   Q   K   K   T   L   G   W   E   A   G

               490                 500                 510                 520                 530                 540
ACCGAAATGCTGTACCCTGCAGACGGAGGGCTGGAGGGACGAAGTGACGATGCTCTGAAG
 T   E   M   L   Y   P   A   D   G   G   L   E   G   R   S   D   D   A   L   K
```

Figure 6.1: LSSmKate2 codon-optimized DNA sequence.

6.2.2 Sequences of LSSmClopHensor constructs

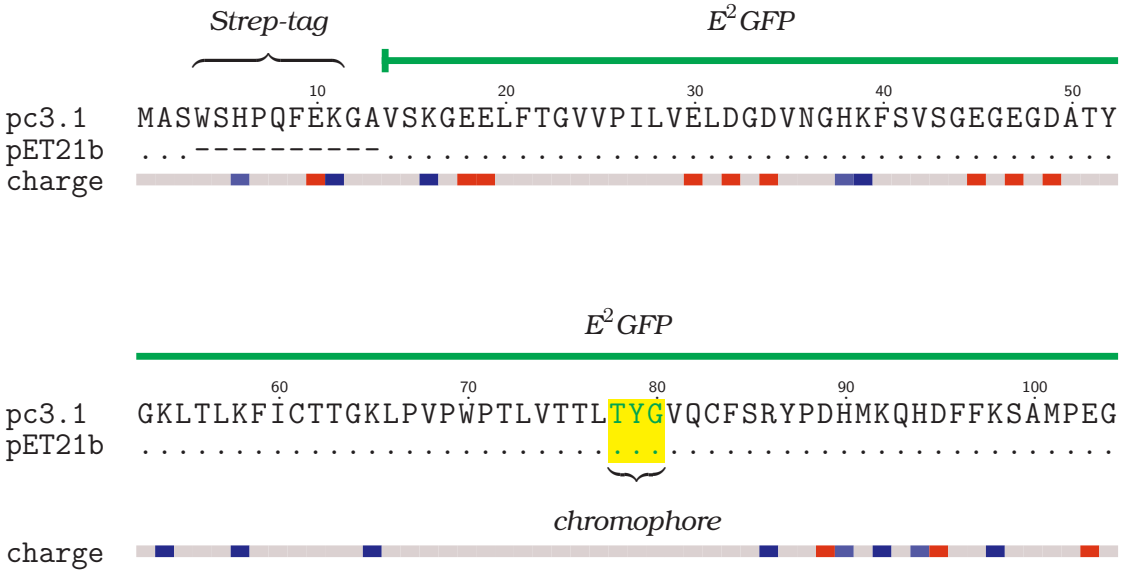

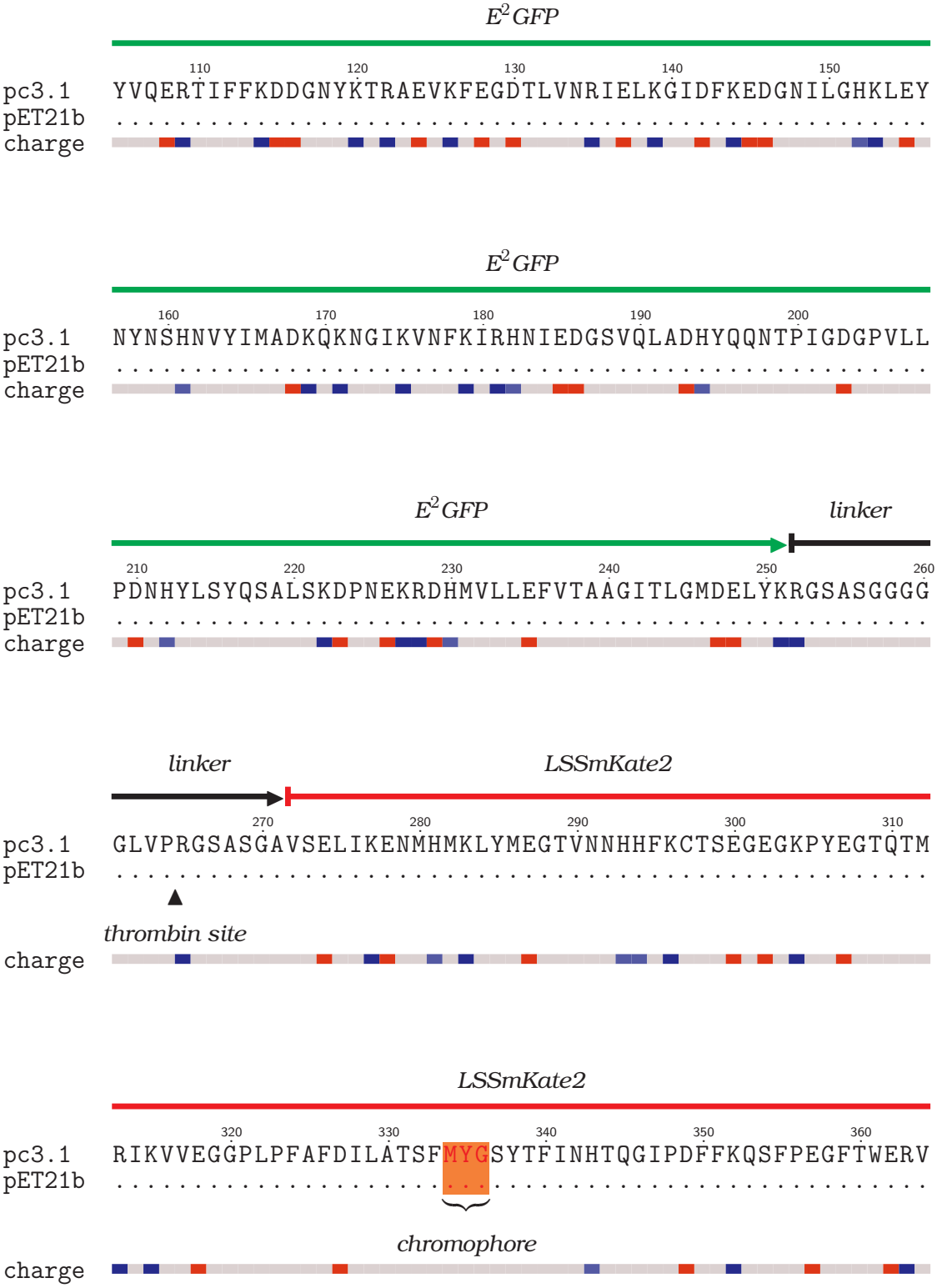
E2 GFP
110 120 130 140 150
pc3.1 YVQERTIFFKDDGNYKTRAEVKFEGDTLVNRIELKGIDFKEDGNILGHKLEY
pET21b
charge
E2 GFP
160 170 180 190 200
pc3.1 NYNSHNVYIMADKQKNGIKVNFKIRHNIEDGSVQLADHYQQNTPIGDGPVLL
pET21b
charge
E2 GFP
linker
210 220 230 240 250 260
pc3.1 PDNHYLSYQSALSKDPNEKRDHMVLLEFVTAAGITLGMDELYKRGSASGGGG
pET21b
charge
linker
LSSmKate2
270 280 290 300 310
pc3.1 GLVPRGSASGAVSELIKENMHMKLYMEGTVNNHHFKCTSEGEGKPYEGTQTM
pET21b
thrombin site
charge
LSSmKate2
320 330 340 350 360
pc3.1 RIKVVEGGPLPFAFDILATSFMYGSYTFINHTQGIPDFFKQSFPEGFTWERV
pET21b
chromophore
charge

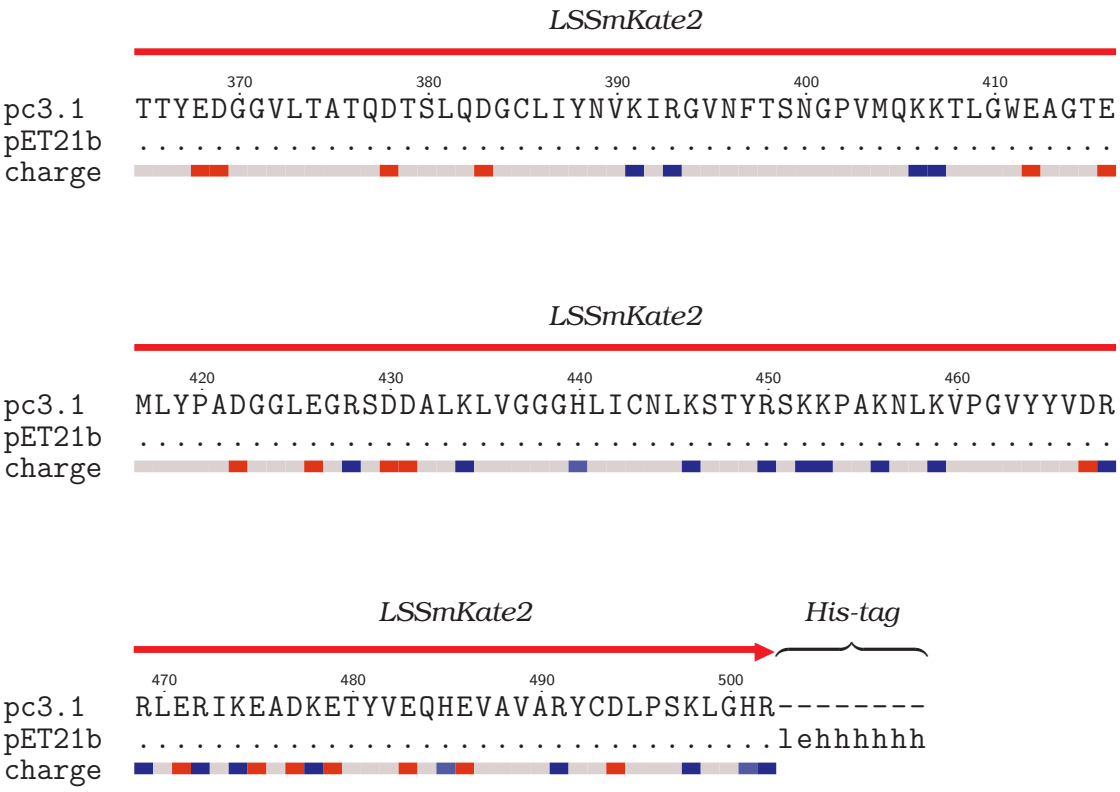

Figure 6.2: Sequences of LSSmClopHensor constructs. Matching residues in pET21b construct are blanked out, mismatches are shown in lowercase. Amino acid charge is reported as color scale: red (negative) and blue (positive). The chromophore-forming residues are color-shaded.

Acknowledgement

It is an honor for me to express my gratitude to Professor Paolo Macchi, whose encouragement and support have been crucial to pursue this dissertation. Likewise I extend my thank you to Mauro Dalla Serra for his support being my tutor. All members of the CNR Institute of Biophysics at Trento and FBK Labssah group have contributed immensely to my personal and professional time. I want also to thank all the CIBIO community for time spent together in science and fun, and the Referees for letting my defense be an enjoyable moment, and for your brilliant comments and suggestions, thanks to you.

I would like to extend thanks to the many people, in many places, who so generously contributed to the work presented in this thesis. Lastly, I offer my thanks to all of those who supported me in any respect during the completion of this adventure.

7

References

[1] G. Zifarelli and M. Pusch, *Reviews of Physiology, Biochemistry and Pharmacology*, Vol. 158, Springer Berlin Heidelberg, Berlin, Heidelberg, 2007.

[2] A.R. Graves, P.K. Curran, C.L. Smith and J.A. Mindell, *The Cl-/H+ antiporter ClC-7 is the primary chloride permeation pathway in lysosomes*, Nature 453 (2008), pp. 788–792.

[3] T.J. Jentsch, *Chloride and the endosomal–lysosomal pathway: Emerging roles of CLC chloride transporters*, The Journal of physiology 578 (2007), pp. 633.

[4] V. Faundez and H.C. Hartzell, *Intracellular Chloride Channels: Determinants of Function in the Endosomal Pathway*, Sci. STKE 2004 (2004), pp. re8.

[5] M. Pedersen, M. Carmosino and B. Forbush, *Intramolecular and intermolecular fluorescence resonance energy transfer in fluorescent protein-tagged Na-K-Cl cotransporter (NKCC1): Sensitivity to*

regulatory conformational change and cell volume, J. Biol. Chem 283 (2008), pp. 2663–2674.

[6] H. Miyazaki, A. Shiozaki, N. Niisato and Y. Marunaka, *Physiological significance of hypotonicity-induced regulatory volume decrease: Reduction in intracellular Cl- concentration acting as an intracellular signaling*, Am J Physiol Renal Physiol 292 (2007), pp. F1411–F1417.

[7] T.-Y. Chen and T.-C. Hwang, *CLC-0 and CFTR: Chloride channels evolved from transporters*, Physiol. Rev 88 (2008), pp. 351–387.

[8] T.J. Jentsch, *CLC chloride channels and transporters: From genes to protein structure, pathology and physiology*, Crit. Rev. Biochem. Mol. Biol 43 (2008 Jan-Feb2008 Jan-Feb), pp. 3–36.

[9] P. Blaesse, M.S. Airaksinen, C. Rivera and K. Kaila, *Cation-Chloride Cotransporters and Neuronal Function*, Neuron 61 (2009), pp. 820–838.

[10] P. Bregestovski and D. Arosio, *Green Fluorescent Protein-Based Chloride Ion Sensors for In Vivo Imaging*, in *Fluorescent Proteins II*, G. Jung, ed., Springer Berlin Heidelberg, Berlin, Heidelberg, 2011, pp. 99–124.

[11] R. Planells-Cases and T.J. Jentsch, *Chloride channelopathies*, Biochimica et Biophysica Acta (BBA) - Molecular Basis of Disease 1792 (2009), pp. 173–189.

[12] A.S. Verkman and L.J. Galietta, *Chloride channels as drug targets*, Nature Reviews Drug Discovery 8 (2009), pp. 153–171.

[13] K. Kaila, T.J. Price, J.A. Payne, M. Puskarjov and J. Voipio, *Cation-chloride cotransporters in neuronal development, plasticity and disease*, Nat Rev Neurosci 15 (2014), pp. 637–654.

[14] K. Kaila, E. Ruusuvuori, P. Seja, J. Voipio and M. Puskarjov, *GABA actions and ionic plasticity in epilepsy*, Current Opinion in Neurobiology 26 (2014), pp. 34–41.

[15] K.J. Treharne, R.M. Crawford and A. Mehta, *CFTR, chloride concentration and cell volume: Could mammalian protein histidine phosphorylation play a latent role?*, Experimental physiology 91 (2006), pp. 131.

[16] C.A. Reid, S.F. Berkovic and S. Petrou, *Mechanisms of human inherited epilepsies*, Progress in neurobiology 87 (2009), pp. 41–57.

[17] M. Poët, U. Kornak, M. Schweizer, A.A. Zdebik, O. Scheel, S. Hoelter et al., *Lysosomal storage disease upon disruption of the neuronal chloride transport protein ClC-6*, Proceedings of the National

Academy of Sciences 103 (2006), pp. 13854–13859.

[18] D. Kasper, R. Planells-Cases, J.C. Fuhrmann, O. Scheel, O. Zeitz, K. Ruether et al., *Loss of the chloride channel ClC-7 leads to lysosomal storage disease and neurodegeneration*, The EMBO journal 24 (2005), pp. 1079–1091.

[19] K.T. Kahle, K.J. Staley, B.V. Nahed, G. Gamba, S.C. Hebert, R.P. Lifton et al., *Roles of the cation–chloride cotransporters in neurological disease*, Nature Clinical Practice Neurology 4 (2008), pp. 490–503.

[20] M. Pusch, A. Liantonio, A. De Luca and D. Conte Camerino, *Pharmacology of CLC chloride channels and transporters*, Advances in Molecular and Cell Biology 38 (2006), pp. 83–107.

[21] S.F. Pedersen and C. Stock, *Ion Channels and Transporters in Cancer: Pathophysiology, Regulation, and Clinical Potential*, Cancer Research 73 (2013), pp. 1658–1661.

[22] A. Schwab, A. Fabian, P.J. Hanley and C. Stock, *Role of Ion Channels and Transporters in Cell Migration*, Physiological Reviews 92 (2012), pp. 1865–1913.

[23] M. Peretti, M. Angelini, N. Savalli, T. Florio, S.H. Yuspa and M. Mazzanti, *Chloride channels in cancer: Focus on chloride intracellular channel 1 and 4 (CLIC1 AND CLIC4) proteins in tumor development and as novel therapeutic targets*, Biochimica et Biophysica Acta (BBA)-Biomembranes 1848 (2015), pp. 2523–2531.

[24] K. Obata, M. Oide and H. Tanaka, *Excitatory and inhibitory actions of GABA and glycine on embryonic chick spinal neurons in culture*, Brain research 144 (1978), pp. 179–184.

[25] Y. Ben-Ari, E. Cherubini, R. Corradetti and J.L. Gaiarsa, *Giant synaptic potentials in immature rat CA3 hippocampal neurones.*, J Physiol 416 (1989), pp. 303–325.

[26] E. Cherubini, C. Rovira, J.L. Gaiarsa, R. Corradetti and Y.B. Ari, *GABA mediated excitation in immature rat CA3 hippocampal neurons*, International Journal of Developmental Neuroscience 8 (1990), pp. 481–490.

[27] W.L. Wu, L. Ziskind-Conhaim and M.A. Sweet, *Early development of glycine- and GABA-mediated synapses in rat spinal cord*, J. Neurosci. 12 (1992), pp. 3935–3945.

[28] K. Kandler and E. Friauf, *Development of glycinergic and glutamatergic synaptic transmission*

in the auditory brainstem of perinatal rats, J. Neurosci. 15 (1995), pp. 6890–6904.

[29] I. Ehrlich, S. Löhrke and E. Friauf, *Shift from depolarizing to hyperpolarizing glycine action in rat auditory neurones is due to age-dependent Cl– regulation*, The Journal of Physiology 520 (1999), pp. 121–137.

[30] Y. Ben-Ari, *Excitatory actions of gaba during development: The nature of the nurture*, Nat Rev Neurosci 3 (2002), pp. 728–739.

[31] E. Delpire, *Cation-Chloride Cotransporters in Neuronal Communication*, Physiology 15 (2000), pp. 309–312.

[32] C.A. Hubner and K. Holthoff, *Anion transport and GABA signaling*, Front Cell Neurosci 7 (2013),.

[33] M.D. Plotkin, E.Y. Snyder, S.C. Hebert and E. Delpire, *Expression of the Na-K-2Cl cotransporter is developmentally regulated in postnatal rat brains: A possible mechanism underlying GABA's excitatory role in immature brain*, J. Neurobiol. 33 (1997), pp. 781–795.

[34] G.H. Clayton, G.C. Owens, J.S. Wolff and Roderic L. Smith, *Ontogeny of cation–Cl– cotransporter expression in rat neocortex*, Developmental Brain Research 109 (1998), pp. 281–292.

[35] J. Lu, M. Karadsheh and E. Delpire, *Developmental regulation of the neuronal-specific isoform of K-CL cotransporter KCC2 in postnatal rat brains*, J. Neurobiol. 39 (1999), pp. 558–568.

[36] C. Rivera, J. Voipio, J.A. Payne, E. Ruusuvuori, H. Lahtinen, K. Lamsa et al., *The K+/Cl|[Minus]| co-transporter KCC2 renders GABA hyperpolarizing during neuronal maturation*, Nature 397 (1999), pp. 251–255.

[37] J. Glykys, V. Dzhala, K. Egawa, T. Balena, Y. Saponjian, K.V. Kuchibhotla et al., *Local Impermeant Anions Establish the Neuronal Chloride Concentration*, Science 343 (2014), pp. 670–675.

[38] J. Glykys, V. Dzhala, K. Egawa, T. Balena, Y. Saponjian, K.V. Kuchibhotla et al., *Response to Comments on "Local impermeant anions establish the neuronal chloride concentration"*, Science 345 (2014), pp. 1130–1130.

[39] M. Canepari, F. Mammano, S.G. Kachalsky, R. Rahamimoff and E. Cherubini, *GABA- and glutamate-mediated network activity in the hippocampus of neonatal and juvenile rats revealed by*

fast calcium imaging, Cell Calcium 27 (2000), pp. 25–33.

[40] K. Ganguly, A.F. Schinder, S.T. Wong and M.-m. Poo, *GABA Itself Promotes the Developmental Switch of Neuronal GABAergic Responses from Excitation to Inhibition*, Cell 105 (2001), pp. 521–532.

[41] M. Canepari, S. Willadt, D. Zecevic and K.E. Vogt, *Imaging Inhibitory Synaptic Potentials Using Voltage Sensitive Dyes*, Biophysical Journal 98 (2010), pp. 2032–2040.

[42] J. Bormann, O.P. Hamill and B. Sakmann, *Mechanism of anion permeation through channels gated by glycine and gamma-aminobutyric acid in mouse cultured spinal neurones.*, J Physiol 385 (1987), pp. 243–286.

[43] K. Kaila, J. Voipio, P. Paalasmaa, M. Pasternack and R.A. Deisz, *The role of bicarbonate in GABAA receptor-mediated IPSPs of rat neocortical neurones.*, J Physiol 464 (1993), pp. 273–289.

[44] P.B. Guthrie, M. Segal and S.B. Kater, *Independent regulation of calcium revealed by imaging dendritic spines*, Nature 354 (1991), pp. 76–80.

[45] W. Müller and J.A. Connor, *Dendritic spines as individual neuronal compartments for synaptic Ca2+ responses*, Nature 354 (1991), pp. 73–76.

[46] D. Smetters, A. Majewska and R. Yuste, *Detecting Action Potentials in Neuronal Populations with Calcium Imaging*, Methods 18 (1999), pp. 215–221.

[47] R. Yuste and W. Denk, *Dendritic spines as basic functional units of neuronal integration*, Nature 375 (1995), pp. 682–684.

[48] R. Yuste, A. Majewska, S.S. Cash and W. Denk, *Mechanisms of Calcium Influx into Hippocampal Spines: Heterogeneity among Spines, Coincidence Detection by NMDA Receptors, and Optical Quantal Analysis*, J. Neurosci. 19 (1999), pp. 1976–1987.

[49] J. Noguchi, M. Matsuzaki, G.C.R. Ellis-Davies and H. Kasai, *Spine-Neck Geometry Determines NMDA Receptor-Dependent Ca2+ Signaling in Dendrites*, Neuron 46 (2005), pp. 609–622.

[50] T. Kuner and G.J. Augustine, *A Genetically Encoded Ratiometric Indicator for Chloride:: Capturing Chloride Transients in Cultured Hippocampal Neurons*, Neuron 27 (2000), pp. 447–459.

[51] K. Berglund, W. Schleich, P. Krieger, L.S. Loo, D. Wang, N.B. Cant et al., *Imaging synaptic inhibition in transgenic mice expressing the chloride indicator, Clomeleon*, Brain Cell Biol 35 (2006),

pp. 207–228.

[52] J. Glykys, V.I. Dzhala, K.V. Kuchibhotla, G. Feng, T. Kuner, G. Augustine et al., *Differences in Cortical versus Subcortical GABAergic Signaling: A Candidate Mechanism of Electroclinical Uncoupling of Neonatal Seizures*, Neuron 63 (2009), pp. 657–672.

[53] G. Perea, M. Navarrete and A. Araque, *Tripartite synapses: Astrocytes process and control synaptic information*, Trends in Neurosciences 32 (2009), pp. 421–431.

[54] A. Araque, G. Carmignoto, P.G. Haydon, S.H.R. Oliet, R. Robitaille and A. Volterra, *Gliotransmitters Travel in Time and Space*, Neuron 81 (2014), pp. 728–739.

[55] S. Kirischuk, V. Parpura and A. Verkhratsky, *Sodium dynamics: Another key to astroglial excitability?*, Trends in Neurosciences 35 (2012), pp. 497–506.

[56] R. Zorec, A. Araque, G. Carmignoto, P.G. Haydon, A. Verkhratsky and V. Parpura, *Astroglial excitability and gliotransmission: An appraisal of Ca^{2+} as a signalling route*, ASN NEURO 4 (2012), pp. 103–119.

[57] K. Egawa, J. Yamada, T. Furukawa, Y. Yanagawa and A. Fukuda, *Cl– homeodynamics in gap junction-coupled astrocytic networks on activation of GABAergic synapses*, The Journal of Physiology 591 (2013), pp. 3901–3917.

[58] S. Jayaraman, J. Biwersi and A.S. Verkman, *Synthesis and characterization of dual-wavelength Cl–Sensitive fluorescent indicators for ratio imaging*, Am J Physiol 276 (1999), pp. C747–57.

[59] A. Fukuda, M. Tanaka, Y. Yamada, K. Muramatsu, Y. Shimano and H. Nishino, *Simultaneous optical imaging of intracellular Cl– in neurons in different layers of rat neocortical slices: Advantages and limitations*, Neuroscience Research 32 (1998), pp. 363–371.

[60] J.R. Inglefield and R.D. Schwartz-Bloom, *Confocal imaging of intracellular chloride in living brain slices: Measurement of GABAA receptor activity*, Journal of Neuroscience Methods 75 (1997), pp. 127–135.

[61] T. Nakamura, H. Kaneko and N. Nishida, *Direct measurement of the chloride concentration in newt olfactory receptors with the fluorescent probe*, Neuroscience Letters 237 (1997), pp. 5–8.

[62] L.-L. Zhang, H.R. Pathak, D.A. Coulter, M.A. Freed and N. Vardi, *Shift of Intracellular Chloride Concentration in Ganglion and Amacrine Cells of Developing Mouse Retina*, J Neurophysiol 95 (2006),

pp. 2404–2416.

[63] W.B. Thoreson, E.J. Bryson and K. Rabl, *Reciprocal Interactions Between Calcium and Chloride in Rod Photoreceptors*, Journal of Neurophysiology 90 (2003), pp. 1747–1753.

[64] N. Chub, G.Z. Mentis and M.J. O'Donovan, *Chloride-sensitive MEQ fluorescence in chick embryo motoneurons following manipulations of chloride and during spontaneous network activity*, J Neurophysiol 95 (2006), pp. 323–330.

[65] H.S. White, S.D. Brown, J.H. Woodhead, G.A. Skeen and H.H. Wolf, *Topiramate enhances GABA-mediated chloride flux and GABA-evoked chloride currents in murine brain neurons and increases seizure threshold*, Epilepsy Research 28 (1997), pp. 167–179.

[66] J.R. Inglefield and R.D. Schwartz-Bloom, *Optical Imaging of Hippocampal Neurons with a Chloride-Sensitive Dye: Early Effects of In Vitro Ischemia*, Journal of Neurochemistry 70 (1998), pp. 2500–2509.

[67] R. Sah and R.D. Schwartz-Bloom, *Optical Imaging Reveals Elevated Intracellular Chloride in Hippocampal Pyramidal Neurons after Oxidative Stress*, J. Neurosci. 19 (1999), pp. 9209–9217.

[68] Y. Yamada, A. Fukuda, M. Tanaka, Y. Shimano, H. Nishino, K. Muramatsu et al., *Optical imaging reveals cation–Cl– cotransporter-mediated transient rapid decrease in intracellular Cl– concentration induced by oxygen–glucose deprivation in rat neocortical slices*, Neuroscience Research 39 (2001), pp. 269–280.

[69] Y. Isomura, M. Sugimoto, Y. Fujiwara-Tsukamoto, S. Yamamoto-Muraki, J. Yamada and A. Fukuda, *Synaptically Activated Cl– Accumulation Responsible for Depolarizing GABAergic Responses in Mature Hippocampal Neurons*, Journal of Neurophysiology 90 (2003), pp. 2752–2756.

[70] N. Marandi, A. Konnerth and O. Garaschuk, *Two-photon chloride imaging in neurons of brain slices*, Pflugers Arch - Eur J Physiol 445 (2002), pp. 357–365.

[71] Y. Kovalchuk and O. Garaschuk, *Two-Photon Chloride Imaging Using MQAE In Vitro and In Vivo*, Cold Spring Harb Protoc 2012 (2012), pp. pdb.prot070037.

[72] H. Kaneko, I. Putzier, S. Frings and T. Gensch, *Determination of intracellular chloride concentration in dorsal root ganglion neurons by fluorescence lifetime imaging*, Calcium-activated chloride

channels (2002), pp. 167–189.

[73] H. Kaneko, I. Putzier, S. Frings, U.B. Kaupp and T. Gensch, *Chloride accumulation in mammalian olfactory sensory neurons*, Journal of Neuroscience 24 (2004), pp. 7931.

[74] D. Gilbert, C. Franjic-Würtz, K. Funk, T. Gensch, S. Frings and F. Möhrlen, *Differential maturation of chloride homeostasis in primary afferent neurons of the somatosensory system*, International Journal of Developmental Neuroscience 25 (2007), pp. 479–489.

[75] K. Funk, A. Woitecki, C. Franjic-Würtz, T. Gensch, F. Möhrlen and S. Frings, *Modulation of chloride homeostasis by inflammatory mediators in dorsal root ganglion neurons*, Molecular Pain 4 (2008), pp. 32.

[76] M. Chalfie, Y. Tu, G. Euskirchen, W.W. Ward and D.C. Prasher, *Green fluorescent protein as a marker for gene expression*, Science 263 (1994), pp. 802–805.

[77] A.B. Cubitt, R. Heim, S.R. Adams, A.E. Boyd, L.A. Gross and R.Y. Tsien, *Understanding, improving and using green fluorescent proteins*, Trends Biochem Sci 20 (1995), pp. 448–55.

[78] R. Heim, A.B. Cubitt and R.Y. Tsien, *Improved green fluorescence*, Nature 373 (1995), pp. 663–664.

[79] R. Heim and R.Y. Tsien, *Engineering green fluorescent protein for improved brightness, longer wavelengths and fluorescence resonance energy transfer*, Curr. Biol 6 (1996), pp. 178–182.

[80] M.A. Rizzo, M.W. Davidson and D.W. Piston, *Fluorescent Protein Tracking and Detection: Fluorescent Protein Structure and Color Variants*, Cold Spring Harb Protoc 2009 (2009), pp. pdb.top63.

[81] R.N. Day and M.W. Davidson, *The fluorescent protein palette: Tools for cellular imaging*, Chem. Soc. Rev. 38 (2009), pp. 2887–2921.

[82] D.M. Chudakov, M.V. Matz, S. Lukyanov and K.A. Lukyanov, *Fluorescent Proteins and Their Applications in Imaging Living Cells and Tissues*, Physiological Reviews 90 (2010), pp. 1103–1163.

[83] R.M. Wachter and S.J. Remington, *Sensitivity of the yellow variant of green fluorescent protein to halides and nitrate*, Curr. Biol 9 (1999), pp. R628–629.

[84] A. Arvey, P. Agius, W.S. Noble and C. Leslie, *Sequence and chromatin determinants of cell-type–*

specific transcription factor binding, Genome Res. 22 (2012), pp. 1723–1734.

[85] R. Krapf, C.A. Berry and A.S. Verkman, *Estimation of intracellular chloride activity in isolated perfused rabbit proximal convoluted tubules using a fluorescent indicator*, Biophysical Journal 53 (1988), pp. 955–962.

[86] R.M. Wachter, D. Yarbrough, K. Kallio and S. Remington, *Crystallographic and energetic analysis of binding of selected anions to the yellow variants of green fluorescent protein1*, Journal of Molecular Biology 301 (2000), pp. 157–171.

[87] L.J. Galietta, P.M. Haggie and A.S. Verkman, *Green fluorescent protein-based halide indicators with improved chloride and iodide affinities*, FEBS Lett 499 (2001), pp. 220–224.

[88] O. Griesbeck, G.S. Baird, R.E. Campbell, D.A. Zacharias and R.Y. Tsien, *Reducing the Environmental Sensitivity of Yellow Fluorescent Protein*, Journal of Biological Chemistry 276 (2001), pp. 29188–29194.

[89] T. Nagai, K. Ibata, E.S. Park, M. Kubota, K. Mikoshiba and A. Miyawaki, *A variant of yellow fluorescent protein with fast and efficient maturation for cell-biological applications*, Nature biotechnology 20 (2002), pp. 87–90.

[90] S. Jayaraman and A.S. Verkman, *Quenching mechanism of quinolinium-type chloride-sensitive fluorescent indicators*, Biophys. Chem 85 (2000), pp. 49–57.

[91] S. Jayaraman, P. Haggie, R.M. Wachter, S.J. Remington and A.S. Verkman, *Mechanism and cellular applications of a green fluorescent protein-based halide sensor*, J. Biol. Chem 275 (2000), pp. 6047–6050.

[92] L.J.V. Galietta, M.F. Springsteel, M. Eda, E.J. Niedzinski, K. By, M.J. Haddadin et al., *Novel CFTR Chloride Channel Activators Identified by Screening of Combinatorial Libraries Based on Flavone and Benzoquinolizinium Lead Compounds* , Journal of Biological Chemistry 276 (2001), pp. 19723–19728.

[93] L.V. Galietta, S. Jayaraman and A.S. Verkman, *Cell-based assay for high-throughput quantitative screening of CFTR chloride transport agonists*, Am. J. Physiol., Cell Physiol 281 (2001), pp. C1734–1742.

[94] R. De La Fuente, W. Namkung, A. Mills and A.S. Verkman, *Small-molecule screen identifies*

inhibitors of a human intestinal calcium-activated chloride channel, Mol. Pharmacol 73 (2008), pp. 758–768.

[95] K.J. Rhoden, S. Cianchetta, V. Stivani, C. Portulano, L.J. Galietta and G. Romeo, *Cell-based imaging of sodium iodide symporter activity with the yellow fluorescent protein variant YFP-H148Q/I152L*, American Journal of Physiology- Cell Physiology 292 (2007), pp. C814.

[96] S.D. Watts, K.L. Suchland, S.G. Amara and S.L. Ingram, *A Sensitive Membrane-Targeted Biosensor for Monitoring Changes in Intracellular Chloride in Neuronal Processes*, PLoS ONE 7 (2012), pp. e35373.

[97] A. Bullen and P. Saggau, *Optical Recording from Individual Neurons in Culture*, in *Modern Techniques in Neuroscience Research*, Springer, Berlin, 1999,.

[98] K. Berglund, W. Schleich, H. Wang, G. Feng, W.C. Hall, T. Kuner et al., *Imaging synaptic inhibition throughout the brain via genetically targeted Clomeleon*, Brain Cell Biol 36 (2008), pp. 101–118.

[99] M. Lorenz, H. Yamaguchi, Y. Wang, R. Singer and J. Condeelis, *Imaging sites of N-wasp activity in lamellipodia and invadopodia of carcinoma cells*, Current biology 14 (2004), pp. 697–703.

[100] M. Jose, D.K. Nair, C. Reissner, R. Hartig and W. Zuschratter, *Photophysics of Clomeleon by FLIM: Discriminating excited state reactions along neuronal development*, Biophysical journal 92 (2007), pp. 2237–2254.

[101] M. Jose, D.K. Nair, C. Reissner, R. Hartig and W. Zuschratter, *Comparison of FRET in the Chloride Indicator Clomeleon with neuronal development*, 2007,.

[102] J. Duebel, S. Haverkamp, W. Schleich, G. Feng, G.J. Augustine, T. Kuner et al., *Two-photon imaging reveals somatodendritic chloride gradient in retinal ON-type bipolar cells expressing the biosensor Clomeleon*, Neuron 49 (2006), pp. 81–94.

[103] V. Dzhala, G. Valeeva, J. Glykys, R. Khazipov and K. Staley, *Traumatic alterations in GABA signaling disrupt hippocampal network activity in the developing brain*, J Neurosci 32 (2012), pp. 4017–4031.

[104] O. Markova, M. Mukhtarov, E. Real, Y. Jacob and P. Bregestovski, *Genetically encoded*

chloride indicator with improved sensitivity, J Neurosci Methods 170 (2008), pp. 67–76.

[105] L. Batti, M. Mukhtarov, E. Audero, A. Ivanov, R.C. Paolicelli, S. Zuborg et al., *Transgenic mouse lines for non-invasive ratiometric monitoring of intracellular chloride*, 2013,.

[106] J.S. Grimley, L. Li, W. Wang, L. Wen, L.S. Beese, H.W. Hellinga et al., *Visualization of Synaptic Inhibition with an Optogenetic Sensor Developed by Cell-Free Protein Engineering Automation*, J. Neurosci. 33 (2013), pp. 16297–16309.

[107] D.P. Arosio, *Heterotropic Linkage between Halide and Proton ion binding to a GFP-based halide indicator for in vivo study.*, Biophys. J. (2007), pp. 386A–386A.

[108] D. Arosio, G. Garau, F. Ricci, L. Marchetti, R. Bizzarri, R. Nifosi et al., *Spectroscopic and structural study of proton and halide ion cooperative binding to GFP*, Biophys. J. 93 (2007), pp. 232–244.

[109] G. Grynkiewicz, M. Poenie and R.Y. Tsien, *A new generation of Ca2+ indicators with greatly improved fluorescence properties.*, Journal of Biological Chemistry 260 (1985), pp. 3440.

[110] J.V. Raimondo, A. Irkle, W. Wefelmeyer, S.E. Newey and C.J. Akerman, *Genetically encoded proton sensors reveal activity-dependent pH changes in neurons*, 2012,.

[111] J.V. Raimondo, B. Joyce, L. Kay, T. Schlagheck, S.E. Newey, S. Srinivas et al., *A genetically-encoded chloride and pH sensor for dissociating ion dynamics in the nervous system*, Front Cell Neurosci 7 (2013),.

[112] D. Arosio, F. Ricci, L. Marchetti, R. Gualdani, L. Albertazzi and F. Beltram, *Simultaneous intracellular chloride and pH measurements using a GFP-based sensor*, Nat. Methods 7 (2010), pp. 516–U44.

[113] R. Bizzarri, C. Arcangeli, D. Arosio, F. Ricci, P. Faraci, F. Cardarelli et al., *Development of a novel GFP-based ratiometric excitation and emission pH indicator for intracellular studies*, Biophys. J. 90 (2006), pp. 3300–3314.

[114] J. Sambrook, E.F. Fritsch, T. Maniatis and others, *Molecular Cloning*, Vol. 2, Cold spring harbor laboratory press New York, 1989.

[115] D. Arosio, *GFP-based fluorescence Sensing and Tracking*, 2010–15BC,.

[116] M. dal Maschio, D. Ghezzi, G. Bony, A. Alabastri, G. Deidda, M. Brondi et al., *High-*

performance and site-directed in utero electroporation by a triple-electrode probe, Nat Commun 3 (2012), pp. 960.

[117] S.V. Gaitonde, W. Qi, R.R. Falsey, N. Sidell and J.D. Martinez, *Morphologic Conversion of a Neuroblastoma-derived Cell Line by E6-mediated p53 Degradation*, Cell Growth Differ 12 (2001), pp. 19–27.

[118] D. Arosio and G.M. Ratto, *Twenty years of fluorescence imaging of intracellular chloride*, Front. Cell. Neurosci. 8 (2014), pp. 258.

[119] B. Lenart, D.B. Kintner, G.E. Shull and D. Sun, *Na-K-Cl Cotransporter-Mediated Intracellular Na+ Accumulation Affects Ca2+ Signaling in Astrocytes in an In Vitro Ischemic Model*, J. Neurosci. 24 (2004), pp. 9585–9597.

[120] R. Dutzler, *A structural perspective on ClC channel and transporter function*, FEBS Letters 581 (2007), pp. 2839–2844.

[121] M.A. Elsliger, R.M. Wachter, G.T. Hanson, K. Kallio and S.J. Remington, *Structural and spectral response of green fluorescent protein variants to changes in pH*, Biochemistry 38 (1999), pp. 5296–5301.

[122] G.T. Hanson, T.B. McAnaney, E.S. Park, M.E.P. Rendell, D.K. Yarbrough, S. Chu et al., *Green fluorescent protein variants as ratiometric dual emission pH sensors. 1. Structural characterization and preliminary application*, Biochemistry 41 (2002), pp. 15477–15488.

[123] R. Heim, D.C. Prasher and R.Y. Tsien, *Wavelength mutations and posttranslational autoxidation of green fluorescent protein.*, Proc Natl Acad Sci U S A 91 (1994), pp. 12501–12504.

[124] M. Ormo, A.B. Cubitt, K. Kallio, L.A. Gross, R.Y. Tsien and S.J. Remington, *Crystal structure of the Aequorea victoria green fluorescent protein*, Science 273 (1996), pp. 1392–5.

[125] K.D. Piatkevich, J. Hulit, O.M. Subach, B. Wu, A. Abdulla, J.E. Segall et al., *Monomeric red fluorescent proteins with a large Stokes shift*, Proceedings of the National Academy of Sciences 107 (2010), pp. 5369–5374.

[126] K.D. Piatkevich, V.N. Malashkevich, S.C. Almo and V.V. Verkhusha, *Engineering ESPT Pathways Based on Structural Analysis of LSSmKate Red Fluorescent Proteins with Large Stokes Shift*,

Journal of the American Chemical Society 132 (2010), pp. 10762–10770.

[127] N.C. Shaner, P.A. Steinbach and R.Y. Tsien, *A guide to choosing fluorescent proteins*, Nature methods 2 (2005), pp. 905–909.

[128] N. Boens, W. Qin, N. Basarić, A. Orte, E.M. Talavera and J.M. Alvarez-Pez, *Photophysics of the fluorescent pH indicator BCECF*, J Phys Chem A 110 (2006), pp. 9334–9343.

[129] J.M. Paredes, L. Crovetto, R. Rios, A. Orte, J.M. Alvarez-Pez and E.M. Talavera, *Tuned lifetime, at the ensemble and single molecule level, of a xanthenic fluorescent dye by means of a buffer-mediated excited-state proton exchange reaction*, Phys. Chem. Chem. Phys. 11 (2009), pp. 5400–5407.

[130] R.A. Ross, B.A. Spengler and J.L. Biedler, *Coordinate Morphological and Biochemical Interconversion of Human Neuroblastoma Cells*, JNCI J Natl Cancer Inst 71 (1983), pp. 741–747.

[131] S. Acosta, C. Lavarino, R. Paris, I. Garcia, C. de Torres, E. Rodríguez et al., *Comprehensive characterization of neuroblastoma cell line subtypes reveals bilineage potential similar to neural crest stem cells*, BMC Developmental Biology 9 (2009), pp. 12.

[132] *Nuovo mutante di GFP sensibile al pH e alla concentrazione di anioni, proteina chimerica comprendente tale mutante e procedimento di determinazione combinata del pH e della concentrazione di anioni*, 2007,.

[133] P. Bregestovski, T. Waseem and M. Mukhtarov, *Genetically encoded optical sensors for monitoring of intracellular chloride and chloride-selective channel activity*, Front Mol Neurosci 2 (2009), pp. 15.

[134] V.I. Dzhala, K.V. Kuchibhotla, J.C. Glykys, K.T. Kahle, W.B. Swiercz, G. Feng et al., *Progressive NKCC1-Dependent Neuronal Chloride Accumulation during Neonatal Seizures*, Journal of Neuroscience 30 (2010), pp. 11745.

[135] G. Losi, M. Cammarota, A. Chiavegato, M. Gomez-Gonzalo and G. Carmignoto, *A new experimental model of focal seizures in the entorhinal cortex*, Epilepsia 51 (2010), pp. 1493–1502.

[136] M. Gómez-Gonzalo, G. Losi, A. Chiavegato, M. Zonta, M. Cammarota, M. Brondi et al., *An excitatory loop with astrocytes contributes to drive neurons to seizure threshold*, PLoS biology 8

(2010), pp. 800.

[137] M. Cammarota, G. Losi, A. Chiavegato, M. Zonta and G. Carmignoto, *Fast spiking interneuron control of seizure propagation in a cortical slice model of focal epilepsy*, The Journal of physiology 591 (2013), pp. 807–822.

[138] K.P. Lillis, M.A. Kramer, J. Mertz, K.J. Staley and J.A. White, *Pyramidal cells accumulate chloride at seizure onset*, Neurobiology of Disease 47 (2012), pp. 358–366.

[139] A.D. Kummer, C. Kompa, H. Niwa, T. Hirano, S. Kojima and M.E. Michel-Beyerle, *Viscosity-Dependent Fluorescence Decay of the GFP Chromophore in Solution Due to Fast Internal Conversion*, J. Phys. Chem. B 106 (2002), pp. 7554–7559.

[140] M. Brondi, S.S. Sato, L.F. Rossi, S. Ferrara and G.M. Ratto, *Finding a Needle in a Haystack: Identification of EGFP Tagged Neurons during Calcium Imaging by Means of Two-Photon Spectral Separation*, Frontiers in Molecular Neuroscience 5 (2012),.

[141] R. Stupp, W.P. Mason, M.J. van den Bent, M. Weller, B. Fisher, M.J. Taphoorn et al., *Radiotherapy plus Concomitant and Adjuvant Temozolomide for Glioblastoma*, New England Journal of Medicine 352 (2005), pp. 987–996.

[142] O. Gallego, *Nonsurgical treatment of recurrent glioblastoma*, Curr Oncol 22 (2015), pp. e273–281.

[143] C.-H. Heldin, K. Rubin, K. Pietras and A. Östman, *High interstitial fluid pressure — an obstacle in cancer therapy*, Nat Rev Cancer 4 (2004), pp. 806–813.

[144] A.R. Jayakumar and M.D. Norenberg, *The Na–K–Cl Co-transporter in astrocyte swelling*, Metab Brain Dis 25 (2010), pp. 31–38.

[145] P. Fu, R. Tang, Z. Yu, S. Huang, M. Xie, X. Luo et al., *Bumetanide-induced NKCC1 inhibition attenuates oxygen–glucose deprivation-induced decrease in proliferative activity and cell cycle progression arrest in cultured OPCs via p-38 MAPKs*, Brain Research 1613 (2015), pp. 110–119.

[146] B.R. Haas and H. Sontheimer, *Inhibition of the Sodium-Potassium-Chloride Cotransporter Isoform-1 Reduces Glioma Invasion*, Cancer Res 70 (2010), pp. 5597–5606.

[147] B.R. Haas, V.A. Cuddapah, S. Watkins, K.J. Rohn, T.E. Dy and H. Sontheimer, *With-No-Lysine Kinase 3 (WNK3) stimulates glioma invasion by regulating cell volume*, American Journal of

Physiology - Cell Physiology 301 (2011), pp. C1150–C1160.

[148] C.W. Habela, N.J. Ernest, A.F. Swindall and H. Sontheimer, *Chloride Accumulation Drives Volume Dynamics Underlying Cell Proliferation and Migration*, Journal of Neurophysiology 101 (2008), pp. 750–757.

[149] N.J. Ernest, A.K. Weaver, L.B.V. Duyn and H.W. Sontheimer, *Relative contribution of chloride channels and transporters to regulatory volume decrease in human glioma cells*, American Journal of Physiology - Cell Physiology 288 (2005), pp. C1451–C1460.

[150] J. Algharabil, D.B. Kintner, Q. Wang, G. Begum, P.A. Clark, S.-S. Yang et al., *Inhibition of Na+-K+-2Cl– Cotransporter isoform 1 Accelerates Temozolomidemediated Apoptosis in Glioblastoma Cancer Cells*, Cell Physiol Biochem 30 (2012), pp. 33–48.

[151] W. Flamenbaum and R. Friedman, *Pharmacology, Therapeutic Efficacy, and Adverse Effects of Bumetanide, A New "Loop" Diuretic*, Pharmacotherapy: The Journal of Human Pharmacology and Drug Therapy 2 (1982), pp. 213–222.

[152] W. Löscher, M. Puskarjov and K. Kaila, *Cation-chloride cotransporters NKCC1 and KCC2 as potential targets for novel antiepileptic and antiepileptogenic treatments*, Neuropharmacology 69 (2013), pp. 62–74.

[153] K. Töllner, C. Brandt, M. Töpfer, G. Brunhofer, T. Erker, M. Gabriel et al., *A novel prodrug-based strategy to increase effects of bumetanide in epilepsy*, Ann Neurol. 75 (2014), pp. 550–562.

[154] M. Töpfer, K. Töllner, C. Brandt, F. Twele, S. Bröer and W. Löscher, *Consequences of inhibition of bumetanide metabolism in rodents on brain penetration and effects of bumetanide in chronic models of epilepsy*, Eur J Neurosci 39 (2014), pp. 673–687.

[155] I. Lönnroth and S. Lange, *Purification and characterization of the antisecretory factor: A protein in the central nervous system and in the gut which inhibits intestinal hypersecretion induced by cholera toxin*, Biochimica et Biophysica Acta (BBA) - General Subjects 883 (1986), pp. 138–144.

[156] K. Ferrell, Q. Deveraux, S. van Nocker and M. Rechsteiner, *Molecular cloning and expression of a multiubiquitin chain binding subunit of the human 26S protease*, FEBS Letters 381 (1996), pp. 143–148.

[157] E. Johansson, I. Lönnroth, S. Lange, I. Jonson, E. Jennische and C. Lönnroth, *Molecular*

Cloning and Expression of a Pituitary Gland Protein Modulating Intestinal Fluid Secretion, J. Biol. Chem. 270 (1995), pp. 20615–20620.

[158] H. Kawahara, M. Kasahara, A. Nishiyama, K. Ohsumi, T. Goto, T. Kishimoto et al., *Developmentally regulated, alternative splicing of the Rpn10 gene generates multiple forms of 26S proteasomes*, The EMBO Journal 19 (2000), pp. 4144–4153.

[159] P. Hanner, H. Rask-Andersen, S. Lange and E. Jennische, *Antisecretory factor-inducing therapy improves the clinical outcome in patients with Ménière's disease*, Acta Oto-Laryngologica 130 (2010), pp. 223–227.

[160] E. Johansson, S. Lange and I. Lönnroth, *Identification of an active site in the antisecretory factor protein*, Biochimica et Biophysica Acta (BBA) - Molecular Basis of Disease 1362 (1997), pp. 177–182.

[161] S. Lange and I. Lönnroth, *The antisecretory factor: Synthesis, anatomical and cellular distribution, and biological action in experimental and clinical studies*, B.I.R. of Cytology, ed., Academic Press, 2001, pp. 39–75.

[162] C. Ulgheri, B. Paganini and F. Rossi, *Antisecretory factor as a potential health-promoting molecule in man and animals*, Nutrition Research Reviews 23 (2010), pp. 300–313.

[163] A. Eriksson, M. Shafazand, E. Jennische, I. Lönnroth and S. Lange, *Antisecretory Factor-induced Regression of Crohn's Disease in a Weak Responder to Conventional Pharmacological Treatment*, Inflammatory Bowel Diseases 9 (2003),.

[164] E. Johansson, M. Al-Olama, H.-A. Hansson, S. Lange and E. Jennische, *Diet-induced antisecretory factor prevents intracranial hypertension in a dosage-dependent manner*, British Journal of Nutrition 109 (2013), pp. 2247–2252.

[165] A. Eriksson, M. Shafazand, E. Jennische and S. Lange, *Effect of antisecretory factor in ulcerative colitis on histological and laborative outcome: A short period clinical trial*, Scandinavian Journal of Gastroenterology 38 (2003), pp. 1045–1049.

[166] N.H. Alam, H. Ashraf, M. Olesen, M.A. Salam, N. Gyr and R. Meier, *Salovum Egg Yolk Containing Antisecretory Factor As an Adjunct Therapy in Severe Cholera in Adult Males: A Pilot Study*, J

Health Popul Nutr 29 (2011), pp. 297–302.

[167] S. Lange, I. Bosaeus, E. Jennische, E. Johansson, B.K. Lundgren and I. Lönnroth, *Food-induced antisecretory factor activity is correlated with small bowel length in patients with intestinal resections*, APMIS 111 (2003), pp. 985–988.

[168] A. Laurenius, B. Wängberg, S. Lange, E. Jennische, B.K. Lundgren and I. Bosaeus, *Anti-secretory factor counteracts secretory diarrhoea of endocrine origin*, Clinical Nutrition 22 (2003), pp. 549–552.

[169] M. Al-Olama, A. Wallgren, B. Andersson, K. Gatzinsky, R. Hultborn, A. Karlsson-Parra et al., *The peptide AF-16 decreases high interstitial fluid pressure in solid tumors*, Acta Oncologica 50 (2011), pp. 1098–1104.

[170] E. Jennische, T. Bergström, M. Johansson, K. Nyström, A. Tarkowski, H.-A. Hansson et al., *The peptide AF-16 abolishes sickness and death at experimental encephalitis by reducing increase of intracranial pressure*, Brain Research 1227 (2008), pp. 189–197.

[171] S. Lange, I. Lönnroth and E. Skadhauge, *Effects of the antisecretory factor in pigs*, Pflügers Archiv - European Journal of Physiology 409 (1987), pp. 328–332.

[172] I. Lönnroth, S. Lange, E. Jennische, E. Johansson, I. Jonson and J. Torres, *Cholera toxin protects against action by Clostridium difficile toxin A*, APMIS 111 (2003), pp. 969–977.

[173] E. Johansson, I. Jonson, M. Bosaeus and E. Jennische, *Identification of flotillin-1 as an interacting protein for antisecretory factor*, Regulatory Peptides 146 (2008), pp. 303–309.

[174] M. Kim, P. Wasling, M.-Y. Xiao, E. Jennische, S. Lange and E. Hanse, *Antisecretory factor modulates GABAergic transmission in the rat hippocampus*, Regulatory Peptides 129 (2005), pp. 109–118.

[175] T. Garzon-Muvdi, P. Schiapparelli, C. ap Rhys, H. Guerrero-Cazares, C. Smith, D.-H. Kim et al., *Regulation of Brain Tumor Dispersal by NKCC1 Through a Novel Role in Focal Adhesion Regulation*, PLOS Biol 10 (2012), pp. e1001320.

[176] E.C. Kaal and C.J. Vecht, *The management of brain edema in brain tumors*, Current Opinion in Oncology 16 (2004),.

[177] E. Alberti, A. Hartmann, H.J. Sch tz and F. Schreckenberger, *The effect of large doses of*

dexamethasone on the cerebrospinal fluid pressure in patients with supratentorial tumors, Journal of Neurology 217 (1978), pp. 173–181.

[178] G.A. Rosenberg, W.T. Kyner and E. Estrada, *Bulk flow of brain interstitial fluid under normal and hyperosmolar conditions*, American Journal of Physiology - Renal Physiology 238 (1980), pp. F42–F49.

[179] A.V. Salnikov, V.V. Iversen, M. Koisti, C. Sundberg, L. Johansson, L.B. Stuhr et al., *Lowering of tumor interstitial fluid pressure specifically augments efficacy of chemotherapy*, FASEB J 17 (2003), pp. 1756–1758.

[180] W. Zhu, G. Begum, K. Pointer, P.A. Clark, S.-S. Yang, S.-H. Lin et al., *WNK1-OSR1 kinase-mediated phospho-activation of Na+-K+-2Cl- cotransporter facilitates glioma migration*, Mol Cancer 13 (2014), pp. 31.

[181] M. Hofmann, M. Guschel, A. Bernd, J. Bereiter-Hahn, R. Kaufmann, C. Tandi et al., *Lowering of Tumor Interstitial Fluid Pressure Reduces Tumor Cell Proliferation in a Xenograft Tumor Model*, Neoplasia 8 (2006), pp. 89–95.

[182] M. Hofmann, M. Schultz, A. Bernd, J. Bereiter-Hahn, R. Kaufmann and S. Kippenberger, *Long-term lowering of tumour interstitial fluid pressure reduces Ki-67 expression*, Journal of Biomechanics 40 (2007), pp. 2324–2329.

[183] S. Watkins and H. Sontheimer, *Hydrodynamic Cellular Volume Changes Enable Glioma Cell Invasion*, Journal of Neuroscience 31 (2011), pp. 17250–17259.

[184] N.J. Ernest, C.W. Habela and H. Sontheimer, *Cytoplasmic condensation is both necessary and sufficient to induce apoptotic cell death*, Journal of Cell Science 121 (2008), pp. 290–297.

[185] J.L.S. Au, S.H. Jang, J. Zheng, C.T. Chen, S. Song, L. Hu et al., *Determinants of drug delivery and transport to solid tumors*, Journal of Controlled Release 74 (2001), pp. 31–46.

[186] O. Bussolati, J. Uggeri, S. Belletti, V. Dall'Asta and G.C. Gazzola, *The stimulation of Na,K,Cl cotransport and of system A for neutral amino acid transport is a mechanism for cell volume increase during the cell cycle.*, FASEB J 10 (1996), pp. 920–926.

[187] J.-M. Dubois and B. Rouzaire-Dubois, *The influence of cell volume changes on tumour cell*

proliferation, Eur Biophys J 33 (2003), pp. 227–232.

[188] M.L. McManus, K.B. Churchwell and K. Strange, *Regulation of Cell Volume in Health and Disease*, New England Journal of Medicine 333 (1995), pp. 1260–1267.

[189] C.B. Ransom, J.T. O'Neal and H. Sontheimer, *Volume-Activated Chloride Currents Contribute to the Resting Conductance and Invasive Migration of Human Glioma Cells*, J. Neurosci. 21 (2001), pp. 7674–7683.

[190] L. Soroceanu, T.J. Manning and H. Sontheimer, *Modulation of glioma cell migration and invasion using Cl- and K+ ion channel blockers*, The Journal of neuroscience 19 (1999), pp. 5942–5954.

[191] T. Lang, *Imaging ca(2+)-triggered exocytosis of single secretory granules on plasma membrane lawns from neuroendocrine cells.*, Methods Mol Biol 440 (2008), pp. 51–59.

[192] E. Maeno, Y. Ishizaki, T. Kanaseki, A. Hazama and Y. Okada, *Normotonic cell shrinkage because of disordered volume regulation is an early prerequisite to apoptosis*, Proceedings of the National Academy of Sciences 97 (2000), pp. 9487–9492.

[193] J. Chen, Y. Li, T.-S. Yu, R.M. McKay, D.K. Burns, S.G. Kernie et al., *A restricted cell population propagates glioblastoma growth after chemotherapy*, Nature 488 (2012), pp. 522–526.

[194] P. Shannon, N. Sabha, N. Lau, D. Kamnasaran, D.H. Gutmann and A. Guha, *Pathological and Molecular Progression of Astrocytomas in a GFAP:12V-Ha-Ras Mouse Astrocytoma Model*, The American Journal of Pathology 167 (2005), pp. 859–867.

[195] H.K. Kimelberg, *Active accumulation and exchange transport of chloride in astroglial cells in culture*, Biochimica et Biophysica Acta (BBA) - Biomembranes 646 (1981), pp. 179–184.

[196] W. Walz, *Chloride/anion channels in glial cell membranes*, Glia 40 (2002), pp. 1–10.

[197] H. Chen, J. Luo, D.B. Kintner, G.E. Shull and D. Sun, *Na+-dependent chloride transporter (NKCC1)-null mice exhibit less gray and white matter damage after focal cerebral ischemia*, Journal of Cerebral Blood Flow & Metabolism 25 (2005), pp. 54–66.

[198] L. Sun, Z. Yu, W. Wang and X. Liu, *Both NKCC1 and anion exchangers contribute to Cl– accumulation in postnatal forebrain neuronal progenitors*, European Journal of Neuroscience 35

(2012), pp. 661–672.

[199] S.Z. Young, M.M. Taylor, S. Wu, Y. Ikeda-Matsuo, C. Kubera and A. Bordey, *NKCC1 Knockdown Decreases Neuron Production through GABAA-Regulated Neural Progenitor Proliferation and Delays Dendrite Development*, J. Neurosci. 32 (2012), pp. 13630–13638.

[200] T. Cesetti, F. Ciccolini and Y. Li, *GABA not only a neurotransmitter: Osmotic regulation by GABAAR signaling*, Front. Cell. Neurosci. 6 (2012), pp. 3.

[201] C. Labrakakis, S. Patt, J. Hartmann and H. Kettenmann, *Functional GABAA receptors on human glioma cells*, European Journal of Neuroscience 10 (1998), pp. 231–238.

[202] A.A. Zdebik, G. Zifarelli, E.-Y. Bergsdorf, P. Soliani, O. Scheel, T.J. Jentsch et al., *Determinants of Anion-Proton Coupling in Mammalian Endosomal CLC Proteins*, Journal of Biological Chemistry 283 (2007), pp. 4219–4227.

[203] T.J. Jentsch, I. Neagoe and O. Scheel, *CLC chloride channels and transporters*, Current Opinion in Neurobiology 15 (2005), pp. 319–325.

[204] R.N. Day, W. Tao and K.W. Dunn, *A simple approach for measuring FRET in fluorescent biosensors using two-photon microscopy*, Nat. Protocols 11 (2016), pp. 2066–2080.

[205] O.P. Hamill, J. Bormann and B. Sakmann, *Activation of multiple-conductance state chloride channels in spinal neurones by glycine and GABA*, Nature 305 (1983), pp. 805–808.

[206] A. Marty and I. Llano, *Excitatory effects of GABA in established brain networks*, Trends Neurosci 28 (2005), pp. 284–289.

[207] M. Puskarjov, F. Ahmad, K. Kaila and P. Blaesse, *Activity-Dependent Cleavage of the K-Cl Cotransporter KCC2 Mediated by Calcium-Activated Protease Calpain*, J. Neurosci. 32 (2012), pp. 11356–11364.

[208] J. Szabadics, C. Varga, G. Molnár, S. Oláh, P. Barzó and G. Tamás, *Excitatory effect of GABAergic axo-axonic cells in cortical microcircuits*, Science 311 (2006), pp. 233–235.

[209] S. Khirug, J. Yamada, R. Afzalov, J. Voipio, L. Khiroug and K. Kaila, *GABAergic depolarization of the axon initial segment in cortical principal neurons is caused by the Na-K-2Cl cotransporter NKCC1*, J. Neurosci 28 (2008), pp. 4635–4639.

[210] V.I. Dzhala, D.M. Talos, D.A. Sdrulla, A.C. Brumback, G.C. Mathews, T.A. Benke et al.,

NKCC1 transporter facilitates seizures in the developing brain, Nat Med 11 (2005), pp. 1205–1213.

[211] J.M. Paredes, A.I. Idilli, L. Mariotti, G. Losi, L.R. Arslanbaeva, S.S. Sato et al., *Synchronous Bioimaging of Intracellular pH and Chloride Based on LSS Fluorescent Protein*, ACS Chem. Biol. 11 (2016), pp. 1652–1660.

[212] A. Mizrahi, J.C. Crowley, E. Shtoyerman and L.C. Katz, *High-Resolution In Vivo Imaging of Hippocampal Dendrites and Spines*, J. Neurosci. 24 (2004), pp. 3147–3151.

[213] M. Navarrete, G. Perea, D.F. de Sevilla, M. Gómez-Gonzalo, A. Núñez, E.D. Martín et al., *Astrocytes Mediate In Vivo Cholinergic-Induced Synaptic Plasticity*, PLoS Biol 10 (2012), pp. e1001259.

[214] B.B. Pond, K. Berglund, T. Kuner, G. Feng, G.J. Augustine and R.D. Schwartz-Bloom, *The chloride transporter Na(+)-K(+)-Cl- cotransporter isoform-1 contributes to intracellular chloride increases after in vitro ischemia*, J Neurosci 26 (2006), pp. 1396–406.

[215] Q. He, T. Nomura, J. Xu and A. Contractor, *The Developmental Switch in GABA Polarity Is Delayed in Fragile X Mice*, J. Neurosci. 34 (2014), pp. 446–450.

[216] R. Tyzio, R. Nardou, D.C. Ferrari, T. Tsintsadze, A. Shahrokhi, S. Eftekhari et al., *Oxytocin-Mediated GABA Inhibition During Delivery Attenuates Autism Pathogenesis in Rodent Offspring*, Science 343 (2014), pp. 675–679.

[217] R. Pizzarelli and E. Cherubini, *Alterations of GABAergic Signaling in Autism Spectrum Disorders*, Neural Plasticity 2011 (2011), pp. e297153.

[218] G. Deidda, I.F. Bozarth and L. Cancedda, *Modulation of GABAergic transmission in development and neurodevelopmental disorders: Investigating physiology and pathology to gain therapeutic perspectives.*, Frontiers in Cellular Neuroscience 8 (2014),.

[219] M. Puskarjov, K.T. Kahle, E. Ruusuvuori and K. Kaila, *Pharmacotherapeutic targeting of cation-chloride cotransporters in neonatal seizures*, Epilepsia 55 (2014), pp. 806–818.

[220] N. Prevarskaya, R. Skryma and Y. Shuba, *Ion channels and the hallmarks of cancer*, Trends in Molecular Medicine 16 (2010), pp. 107–121.

[221] A. Arcangeli, *Ion channels and transporters in cancer. 3. Ion channels in the tumor cell-microenvironment cross talk*, American Journal of Physiology - Cell Physiology 301 (2011), pp.

C762–C771.

[222] A. Becchetti, *Ion channels and transporters in cancer. 1. Ion channels and cell proliferation in cancer*, American Journal of Physiology - Cell Physiology 301 (2011), pp. C255–C265.

[223] E.K. Hoffmann, *Ion channels involved in cell volume regulation: Effects on migration, proliferation, and programmed cell death in non adherent EAT cells and adherent ELA cells*, Cellular Physiology and Biochemistry 28 (2011), pp. 1061–1078.

[224] .G. Valdivieso, M. Clauzure, M. Massip-Copiz and T.A. Santa-Coloma, *The Chloride Anion Acts as a Second Messenger in Mammalian Cells - Modifying the Expression of Specific Genes*, Cellular Physiology and Biochemistry 38 (2016), pp. 49–64.

[225] J.C. Darnell, S.J. Van Driesche, C. Zhang, K.Y.S. Hung, A. Mele, C.E. Fraser et al., *FMRP Stalls Ribosomal Translocation on mRNAs Linked to Synaptic Function and Autism*, Cell 146 (2011), pp. 247–261.

[226] E. Beitz, *TeXshade: Shading and labeling of multiple sequence alignments using LaTeX2e*, Bioinformatics 16 (2000), pp. 135–139.